Water Oxidation with Multinuclear Ruthenium Catalysts

Dissertation zur Erlangung des

naturwissenschaftlichen Doktorgrades

der Julius-Maximilians-Universität Würzburg

vorgelegt von

Dorothee Schindler

aus Heidelberg

Würzburg 2021

Eingereicht bei der Fakultät für Chemie und Pharmazie am:

12. Januar 2021

Gutachter der schriftlichen Arbeit:

Gutachter: Prof. Dr. Frank Würthner

Gutachter: Prof. Dr. Udo Radius

Prüfer des öffentlichen Promotionskolloquiums:

Prüfer: Prof. Dr. Frank Würthner

Prüfer: Prof. Dr. Udo Radius

Prüfer: Priv.-Doz. Dr. Florian Beuerle

Datum des öffentlichen Promotionskolloquiums:

12. März 2021

Doktorurkunde ausgehändigt am:

_____

Abbreviations

3-D	3-dimensional
ADP	adenosine diphosphate
AFM	atomic force microscopy
ATP	adenosine triphosphate
bda	2,2'-bipyridine-6,6'-dicarboxylate
biqa	(1,1'-biisoquinoline)-3,3'-dicarboxylate
bnda	2,2’-bi(nicotinic acid)-6,6-dicarboxylate
bpb	1,4-bis(pyridin-3'-yl)benzene
bpHc	2,2′-bipyridine-6-phosphonate-6′-carboxylate
bpy	2,2‘-bipyridine
BSE	backscattered electrons
CAN	cerium(IV) ammonium nitrate
CB	conduction band
CE	counter electrode
CNT	carbon nanotubes
CPE	controlled potential electrolysis
CV	cyclic voltammetry
DFT	density functional theory
DOSY	diffusion ordered spectroscopy
DPV	differential pulse voltammetry
DS-PEC	dye-sensitized photoelectrochemical cell
EDX	energy dispersive X-ray spectroscopy
eq	equation
equiv.	equivalent
ESI	electrospray ionization
FOWA	Foot of the Wave Analysis
FTO	fluorine-doped tin oxide
GC	glassy carbon
GPC	gel permeation chromatography
H_4tPa	2,2′:6′,2″-terpyridine-6,6″-diphosphonic acid
HEC	hydrogen evolving catalyst
HER	hydrogen evolution reaction
HOMO	highest occupied molecular orbital
HOPG	highly oriented pyrolytic graphite
I2M	interaction of two M-O units
*i*Prpy	2-isopropylpyridine

ITO	indium tin oxide
LFSE	ligand field stablization energy
LUMO	lowest unoccupied molecular orbital
MWCNT	multi-walled carbon nanotubes
$NADP^+$	nicotinamide adenine dinucleotide phosphate
NADPH	reduced nicotinamide adenine dinucleotide phosphate
NHE	normal hydrogen electrode
NMR	nuclear magnetic resonance
OEC	oxygen evolving complex
OEG	oligoethylene glycol (here: triethylene glycol)
PCET	proton-coupled electron transfer
pda	1,1'-phenanthroline-2,9-dicarboxylate
pdc	pyridyl-2,6-dicarboxylate
PEC	photoelectrochemical cell
phtz	phthalazine
pic	picoline
POM	polyoxometallates
PS	photosensitizer
PSI	photosystem I
PSII	photosystem II
PVE	photovoltaic-coupled electrolyzers
py	pyridine
RE	reference electrode
SC	semiconductor
SEA	sacrificial electron acceptor
SEM	scanning electron microscopy
tda	[2,2':6',2''-terpyridine]-6,6''-dicarboxylate
terpy	2,2';6',2"-terpyridine
TFE	2,2,2-trifluoroethanol
UV	ultraviolet
VB	valence band
VE	valence electrons
vis	visible
WE	working electrode
WNA	water nucleophilic attack
WO	water oxidation
WOC	water oxidation catalyst

Variables and constants

k_B	Boltzman constant
E	potential
F	Faraday constant
I	current
j	current density
N_A	Avogadro constant
q	fundamental electron charge
R	universal gas constant
r_1, r_2	rate constants in ligand exchange process
T	Tesla
Δ	energy splitting of d-orbitals
η	overpotential
$\varkappa$	denticity of a ligand
v	speed
λ	wavelength

Table of Contents

Chapter 1

—

Introduction and Aim of the Thesis

One of the greatest challenges our society is facing today is providing an environmental and climate friendly energy supply.[1] In a world populated by 7.8 billion people[2] with an expected continuous growth and improving standards of living thanks to technological progress, our energy demand will increase annually.[3] For the last 100 years and still today, humans have been covering over 80% of their power by finite fossil fuels such as oil, coal or natural gas (Figure 1a).[4-6] Nowadays, humankind is confronted with the consequences of the long term dependency on this resource. Large quantities of harmful emissions (mainly CO_2) as the predominant origin of global warming have urgently to be reduced to preserve our planet for future generations (Figure 1b).[7-8]

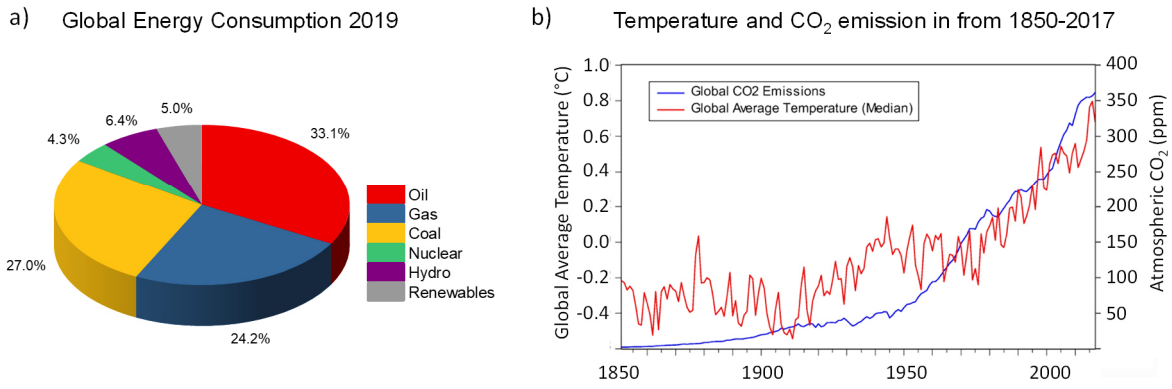

Figure 1: a) Contribution of sources to total global energy consumption in 2019.[9] b) Dependency of global mean temperature on level of atmospheric CO_2 from 1850-2017. Adapted and reprinted with Permission of Springer Nature B.V., Copyright 2020.[10-11]

However, today's challenge is not only to provide environmentally benign renewable energy sources, but also the development of flexible storage solutions to be independent of un-controllable environmental factors.[12-14] As in many groundbreaking inventions, inspiration has been taken from nature. Life on our planet is only possible due to production of hydrocarbons

by plants using solar energy in a process known as natural photosynthesis.[15-18] While photovoltaic cells convert energy of the sun directly into electricity, it comes with the issue of being unevenly distributed, diffuse and intermittent at the Earths' surface, so energy production and consumption sites might be far apart.[19-20] Even though research on battery technology has made enormous progress during the last years, they still possess a relatively low energy density and inefficiency in long term storage compared to traditional fossil fuels.[21-24] In contrast, the concept of artificial photosynthesis includes the transformation of energy of the sun in chemical bonds of energy rich molecules.[25-26] These so called "solar fuels" seem to be the ideal solution and became a goal of scientists a long time ago.[27] French science fiction author Jules Verne envisioned in 1874 in his book "The Mysterious Island" a world where "water will one day be employed as fuel, that hydrogen and oxygen which constitute it, used singly or together, will furnish an inexhaustible source of heat and light, of an intensity of which coal is not capable", which is the holy grail where scientists still put plenty of efforts in for replicating nature.

The process of oxygenic photosynthesis which nature started to perfectionize for its purpose over 2.4 billion years ago comprises the splitting of water applying energy provided by the sun.[28] Being the most abundant and inexhaustible energy source on our planet, solar illumination that strikes Earth in one hour is greater than the worldwide energy consumption of a whole year.[29-30] To benefit from this, an artificial approach of photosynthesis would apply solar energy to split water in its components, namely oxygen and hydrogen, and the latter would serve as sustainable solar fuel which can be burned resulting in harmless water as a product.[31] Hydrogen as energy carrier has the advantage of a very high energy density compared to other fuels,[32] and additionally, it can provide long-term and large-scale storage.[33] However, until now, hydrogen makes up less than 1% of Europe's energy supply and is mainly produced by carbon-emitting pathways, primarily from natural gas. Accordingly, this so-called "gray hydrogen" does not contribute to decarbonization. Besides "blue hydrogen", which is a more environmentally friendly version as carbon emissions are captured and stored or reused, "green hydrogen" is the ultimate goal. Without producing harmful emissions in the first place, "green hydrogen" is produced either by water electrolysis using energy from renewable energy sources such as solar power, or by direct water splitting in photoelectrochemical cells.[34]

The process of reducing protons to hydrogen is technically feasible in large scale. However, the main reason why this concept is not applied in an industrial scale yet is the challenge of the water oxidation reaction.[35] Efficient catalysts are needed to overcome the thermo-dynamically uphill reaction comprising a four electron transfer to generate one molecule of oxygen.[36-37]

Fujishima and Honda presented the first water splitting photoelectrochemical device in 1972, and the timing was perfect as just one year later, the first oil crisis draw even more attention to alternative energy sources.[38] Since this fundamental breakthrough, much research has been devoted to water splitting during the last 50 years. To enable more efficient systems, research on molecular water oxidation catalysts (WOCs) has been initiated by Meyer and co-workers who reported the so-called “blue dimer” as a WOC in 1982.[39] Since then, a significant number of WOCs have been synthesized and investigated in their ability to catalyze the water oxidation (WO) reaction. The most outstanding performance was found for the class of Ru(bda) catalysts (bda: [2,2’-bipyridine]-6,6’-dicarboxylate) presented in 2009 by Sun and co-workers.[40] Besides the intrinsic features of the equatorial bda ligand which make this unit suitable for water oxidation catalysis, it provides large flexibility as axial ligands can easily be replaced and various redundant modifications have been investigated in the last decade.[41] Würthner and co-workers presented 2016 a trinuclear WOC by incorporating the catalytically active Ru(bda) unit in a supramolecular structure. The Ru centers were connected by bidentate axial ligands and this so-called **MC3** WOC (Figure 2b) has been studied in detail.[42] Activities comparable to the ones of the oxygen evolving complex (OEC) in nature have been observed and DFT calculations suggested that a pre-organized water network within the cavity creates a unique coordination environment which is beneficial for the proton-coupled electron transfer steps in the catalytic cycle.[42-44] These interesting findings encouraged our group to extend the research on supramolecular Ru(bda)-based water oxidation catalysts.

In this thesis, ligand exchange processes have been analyzed to gain insights into kinetic and thermodynamic product formation in the synthesis of multinuclear macrocyclic WOCs. Based on the knowledge acquired by these studies, new multinuclear cyclic Ru complexes have been synthesized and their catalytic efficiencies in homogeneous water oxidation have been investigated (Figure 2a). One step further for setting up functional devices is the immobilization of molecular WOCs on conducting or semiconducting supporting materials. **MC3** seemed to be an ideal candidate and direct anchoring on carbon nanotubes generated a promising materials for further applications (Figure 2b).

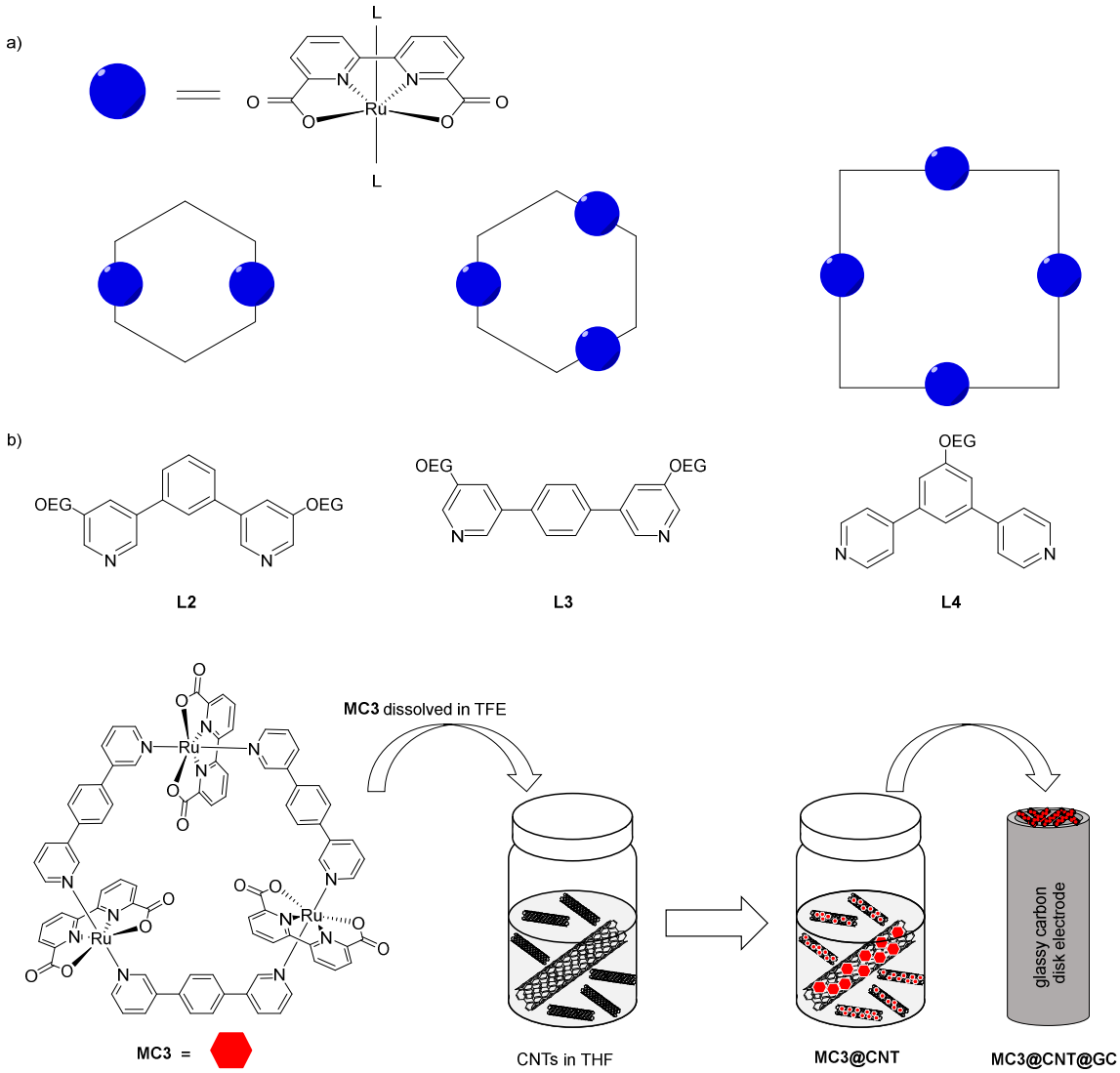

Figure 2: a) Schematic illustration of di-, tri- and tetranuclear Ru(bda)-based water oxidation catalysts investigated in this work. b) Anchoring procedure of **MC3** on carbon nanotubes (CNTs) and preparation of glassy carbon electrodes as hybrid anodes. Investigations of this new material are discussed in *Chapter 5*.

Chapter 2 of this thesis provides an overview on the development of artificial photosynthesis following the example of nature. Details about the water splitting reaction with focus on the oxidation part are discussed and recent developments on systems mimicking the natural photosynthesis are presented. Water oxidation catalysis is analyzed comparing heterogeneous and homogeneous systems as well as oxygen bond formation mechanisms and techniques for the investigation of catalysts. The development of Ru-based WOCs, the generation of active species during catalysis, supramolecular water oxidation catalysts and the immobilization of molecular WOCs is introduced.

Chapter 3 presents investigations on the kinetic and thermodynamic pathway in the formation of **MC3**-type macrocycles. Studies on axial ligand exchange processes in Ru(bda) complexes in mononuclear model systems are also presented in this chapter. The mechanism of the ligand

exchange was investigated and conditions under which thermodynamic product formation is enabled have been analyzed.

The acquired knowledge of conditions of fast ligand exchange was applied in supramolecular macrocyclization of Ru(bda) units with axial chelating ligands in *Chapter 4* for the synthesis of a dinuclear and tetranuclear Ru(bda) macrocycle. Both new complexes have been characterized and studied in comparison on their catalytic activities in chemical as well as photochemical water oxidation to a trinuclear **MC3** derivative.

Chapter 5 describes the immobilization of the **MC3** WOC on carbon nanotubes for anchoring the hybrid material on glassy carbon electrodes. This new hybrid anode has been investigated by atomic force microscopy and absorption spectroscopy as well as electrochemically in regard to activation process, maximum current densities, Faraday efficiency, stability and catalytic activities in heterogeneous water oxidation.

Chapter 6 presents a summary of the obtained results in English.

Chapter 7 summarizes of the obtained results in German.

Chapter 8 comprises the experimental section, including materials, methods, synthesis and characterization of new compounds.

Chapter 9 contains the appendix with additional experimental data for the research presented in *Chapters 3, 4* and *5*.

Chapter 2

—

Literature Survey

2.1 Natural and Artificial Photosynthesis

2.1.1 Photosynthesis in nature

Absorption of solar light and its utilization for the conversion of low-energy molecules into energy-rich compounds during natural photosynthesis is the key process which makes life of eukaryotic organisms on our planet possible. This process, generally known as photo-synthesis, consists of several light-driven reactions where electrons are extracted and used to generate higher energetic molecules. Different electron donators (like Fe^{2+}, NO_2^-, S, H_2S, $S_2O_3^{2-}$, H_2)[45-46] were used in the earliest form of anoxygenic photosynthesis developed over 3.5 billion years ago in some bacteria.[45-46] Oxygenic photosynthesis started about 1.1 billion years later and is performed by green plants, algae and cyanobacteria.[47] In this light-driven process, water is used to reduce carbon dioxide to carbohydrates while oxygen is generated as a by-product which enabled the development of an oxygen atmosphere and revolutionized the development of higher species on the Earth.[48] The oxygenic photosynthesis (from now on termed as 'photosynthesis') can be summarized as in the following equation:

$$12\ H_2O + 6\ CO_2 \xrightarrow{h\nu} C_6H_{12}O_6 + 6\ O_2 + 6\ H_2O$$

Photosynthesis in green plants takes place in the chloroplasts (Figure 3), where two fundamental processes are differentiated.[49] On the one hand, light dependent reactions in the thylakoid membrane are taking place in PS I (photosystem I) and PS II (photosystem II), where water is oxidized and the released protons and electrons are used for generating reduced nicotinamide adenine dinucleotide phosphate (NADPH) from $NADP^+$. At the same time, energy

gained by proton gradients and the electron transport chain is used to convert adenosine diphosphate (ADP) to adenosine triphosphate (ATP), which provides energy to living cells. On the other hand, the so-called dark reactions in the Calvin cycle use NADPH and ATP to produce carbohydrates from CO_2.

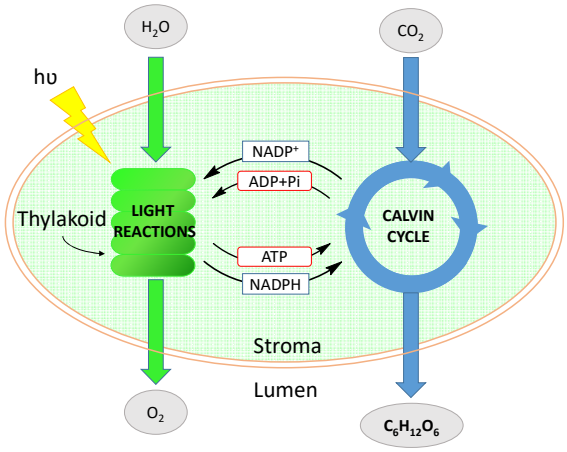

Figure 3: Schematic presentation of a chloroplast with key steps of light reaction and Calvin cycle taking place during photosynthesis.

The light dependent reactions of photosynthesis (Figure 4) start with the absorption of sunlight by chlorophyll complexes located in PS II.[50] To make this process more efficient, PS II is surrounded by light-harvesting complexes (LHC).[51-52] Those chromophore assemblies consisting of different dye molecules such as carotenoids and chlorophyll derivatives absorb light and channel photons towards the reaction centers.[53-54] This leads to the excitation of chlorophyll complex P680 in PS II, which is responsible for a first charge separation.[55] Electrons delivered from the water oxidation reaction with oxygen as a by-product which takes place in the thylakoid lumen catalyzed by the oxygen evolving complex (OEC) fill the electron holes. For each absorbed photon, one electron is taken from a water molecule. The excited electrons are transferred to the second reaction center in PS I by an electron transfer chain with different quinone and cytochrome carriers.[56] Energy provided by this process together with a resulting proton gradient across the chloroplast membrane is used by the enzyme ATP synthase to produce ATP.[57] Electrons are used to refill holes that result from photon absorption in PS I, where the enzyme NADP reductase generates NADPH.[58] To obtain carbohydrates for storing the collected energy from the sun, several light-independent reactions take place during the Calvin cycle in the stroma of the chloroplast.[59] The reducing powers of ATP and NADPH are used in a stepwise process of carbon fixation, reduction and Ribulose 1,5-bisphosphate (RuBP) regeneration reactions.[60-61]

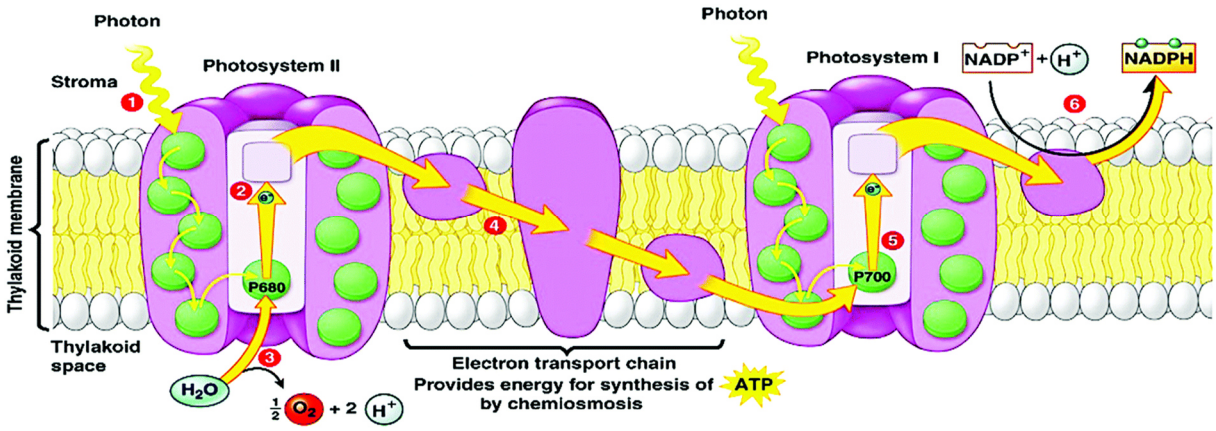

Figure 4: Schematic illustration of light-dependent processes during photosynthesis is plants: 1: absorption of photons, 2: excitation of P680 in PS II, 3: refill of electrons provided by water oxidation, 4: electron transfer chain with ATP synthesis, 5: excitation of P700 in PS I, 6: generation of NADPH. Reprinted with permission of Pearson Education, Copyright 2006.[62]

Te efficiency of photosynthesis can be described by taking into account the energy needed for the production of 1 mol of glucose from CO_2 in the Calvin cycle and the energy needed to provide NADPH and ATP to perform this reaction. Considering that only specific wavelengths of the solar spectrum are used, the photosynthetic efficiency for the conversion of light into chemical energy under optimal conditions can be estimated to be around 11-20% (more realistic conditions including factors like poor absorption due to reflection, the need for optimum solar radiation level or respiration requirements of photosynthesis leads to efficiencies around 3-6%[63]).[64-65] The total global energy captured by photosynthesis is approximately 130 terawatts[66-68] and about 100-115 billion tons of carbon are converted into biomass per year.[69-70]

Focusing on the water splitting reaction, the natural OEC is especially of interest as it catalyzes this rather challenging four electrons and four protons abstraction process with high efficiencies. In catalysis, activity is measured by the turnover frequency (TOF), which gives the number of catalytic cycles that a catalyst performs in a given time, while stability is determined by the turnover numbers (TON) as the total number of catalytic cycles that one molecule of catalyst can perform. Water oxidation by OEC is performed with a TOF of 500 cycles per second.[71-72] A stability for about 30 min has been reported, which results in a TON in the range of 10^6.[73-74] Nature chose a calcium-manganese cluster for this purpose as first row transition metal ions are widely available and able to perform a diverse redox chemistry.[75-76] Additionally, Mn ions in +III and +IV oxidation states are able to stabilize O^{2-} ions by π-bonding and form robust metal-oxo species which arise as intermediates during the water oxidation cycle.[75] The Mn_4CaO_5 cluster is built up of a distorted heterocubane structure with an attached di-μ-oxo-bridged manganese atom (Figure 5).[77-78]

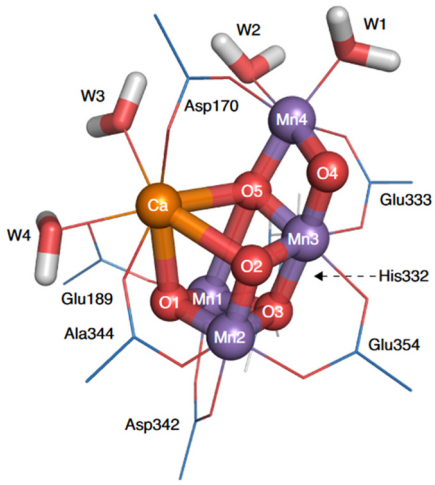

Figure 5: Model of OEC in its natural environment of amino acids. Reprinted with permission from ref. [79]. Copyright 2015 Elsevier.

The OEC is embedded in a protein environment which has been found to be essential for its performance.[79] Therefore, the replication of a functional Ca-Mn-cluster as WOC is rather complex.[80-81] The unique surrounding of the OEC assists a fast diffusion of water to the reaction center by preorganizing a long-range coupled hydrogen-bonded water network.[79, 82] Moreover, these water channels also play a role in proton translocation, oxygen evacuation and reassembly of the OEC.[82] The mechanism of the water oxidation reaction is described in the Kok cycle.[83] However, no experimental data demonstrating the exact process of the O-O bond formation has been presented so far. While some groups propose a water nucleophilic attack type (WNA) mechanism in which water attacks a Mn^{V}-oxo species,[84-86] others believe in a intramolecular radical coupling of two Mn^{IV}-oxyl units in an I2M (interaction of two M-O units) type mechanism.[87-88] Some other mechanistic pathways are discussed as well,[89-90] but further studies are needed to finally elucidate the key steps in water oxidation by natural OEC.

2.1.2 Water splitting reaction

Water splitting describes the reaction where a water molecule is split into oxygen and hydrogen. To do so, four O-H bonds need to be broken in order to generate one O=O double bond, while four protons and four electrons have to be removed and recombined to form hydrogen. The required breaking and forming of multiple new bonds involved in this reaction make it highly complex. The water splitting reaction can be examined in two separate steps: the oxidation of water at the anode and the reduction of protons at the cathode. Conditions for electrolysis of water at pH 0 under standard conditions (25.0 °C, 1.013 bar, reported vs NHE) are shown below which demonstrate that water splitting is a thermodynamically highly disfavored process.[91]

$$2\ H_2O \rightarrow O_2 + 4\ H^+ + 4\ e^- \qquad E^0_{anode} = +1.23\ V$$

$$4\ H^+ + 4\ e^- \rightarrow 2\ H_2 \qquad E^0_{cathode} = 0.00\ V$$

$$2\ H_2O \rightarrow O_2 + 2\ H_2$$

With the standard potential of the hydrogen reduction being set to be zero under standard conditions,[92] the potential of water electrolysis in a cell can be calculated as shown below and give E^0_{cell} = -1.23 V.

$$E^0_{cell} = E^0_{cathode} - E^0_{anode} \qquad \text{eq. 1}$$

The Nernst equation correlates reduction potentials of electrochemical half reactions to their standard potential at the applied temperature and activities of the species taking part in the respective process.[93] For the process

$$Ox + z^*e^- \rightarrow Red$$

the following equation is given:

$$\Delta G = \Delta G^{\Theta} + RT \ln Q_r \qquad \text{eq. 2}$$

where ΔG is the actual Gibbs free energy, ΔG^{Θ} is the standard Gibbs free energy, R is the universal gas constant, T is the temperature and Q_r is the reaction quotient. The decrease of the Gibbs free energy per coulomb of transferred charge defines the cell potential E of an electrochemical reaction and can be described by the following relationship:

$$\Delta G = -zFE \qquad \text{eq. 3}$$

with z being the number of electrons transferred and F the Faraday constant, representing the magnitude of electric charge per moles of electrons. Combining eq. 2 and eq. 3 leads to the Nernst equation:

$$E_{red} = E^{\Theta}_{red} - \frac{RT}{zF} \ln Q_r = E^{\Theta}_{red} - \frac{RT}{zF} \ln \frac{a_{red}}{a_{ox}} \qquad \text{eq. 4}$$

where a stands for the chemical activity of the relevant species. According to this equation, the overall cell potential (meaning the difference between E^0_{red} and E^0_{ox}) remains the same (-1.23 V) when varying the pH value. However, the standard potentials of the oxidation and reduction half reactions will vary. A shift of -59 mV per pH unit can be observed. Due to this fact, water oxidation reactions are favored at basic pH for having a lower standard potential, in contrast to water reduction which is favored at lower pH values.[94-95]

Applying eq. 3, the Gibbs free energy for the water splitting reaction can be determined. For the generation of 1 mol of oxygen out of two moles of water, ΔG = +474 kJ are needed at standard conditions (ΔG = +237 kJ per 1 mol water). This theoretical thermodynamic value, however, only gives the minimum energy required and does not reflect real experimental findings. The amount of increase of potential needed to drive the reaction is termed "overpotential" (η) and accounts for any kind of loss and non-ideality in the process, as outlined in Figure 6. It can originate from different factors such as activation barriers, temperature, concentration effects, ion mobility, surface hindrance including bubbles or voltage drops due to material-dependent wire resistance.[96] Thus, overpotential is a kinetic phenomenon which can be lowered by smart choice of materials and the addition of catalysts for driving the water splitting reaction.[97]

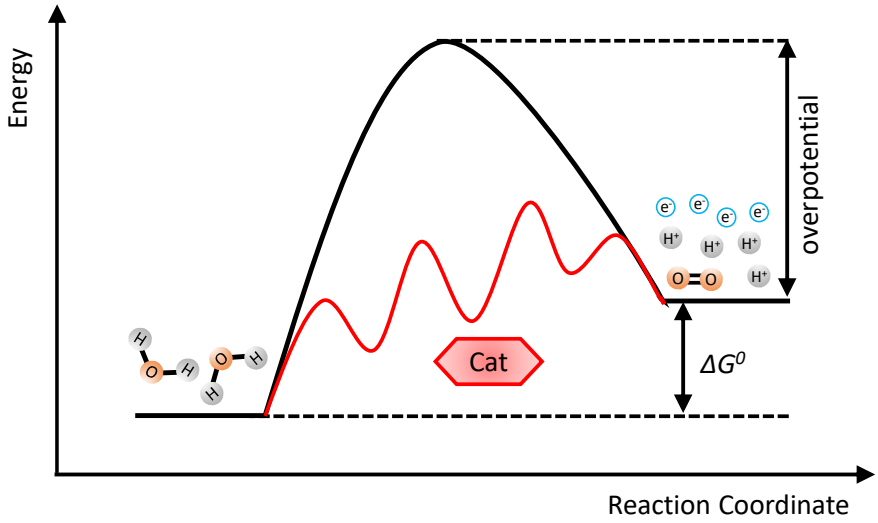

Figure 6: Schematic representation of the energy profile of the uncatalyzed (black line) and catalyzed (red line) reaction of oxidizing water to dioxygen.

Especially for the water oxidation reaction, which is considered to be the bottleneck of the water splitting process, catalysts that are able to accumulate four oxidative charges and capable of operating at potentials close to the thermodynamic potential of the water oxidation are necessary for overcoming high overpotentials. These catalysts largely determine both energy efficiency and chemical selectivity needed to make the reaction suitable for industrial production of solar fuel hydrogen.[98]

2.1.3 Artificial photosynthesis

An enormous quantity of about $13.8*10^8$ km^3 of water are estimated to exist on the Earth surface.[99] Undoubtedly, an exact mimicking of nature's photosystem for converting water to

energy by sunlight is still illusive due to its complex structure, however, artificial photosynthesis systems comprising similar components have been developed in the last years.[100] To realize the ambitious goal of solar-driven water splitting, artificial photosynthesis devices require four essential parts: (1) a light-harvesting antenna to capture and channel the solar energy, (2) a photosensitizer for light-induced charge separation into electrons and holes, (3) an oxygen evolving catalyst to gain the reducing equivalents and (4) a hydrogen evolving catalyst to generate molecular hydrogen from the obtained protons.[101] With the Gibbs free energy of ΔG = +474 kJ/mol needed to generate one mole of dioxygen, light of the visible solar spectrum should be sufficient to perform this reaction. However, keeping in mind the overpotentials, application of additional energy needs to be considered.[102]

Artificial photosynthesis systems are commonly divided into two types of devices: photovoltaic-coupled electrolyzers (PVE) and photoelectrochemical cells (PEC), as illustrated in Figure 7.

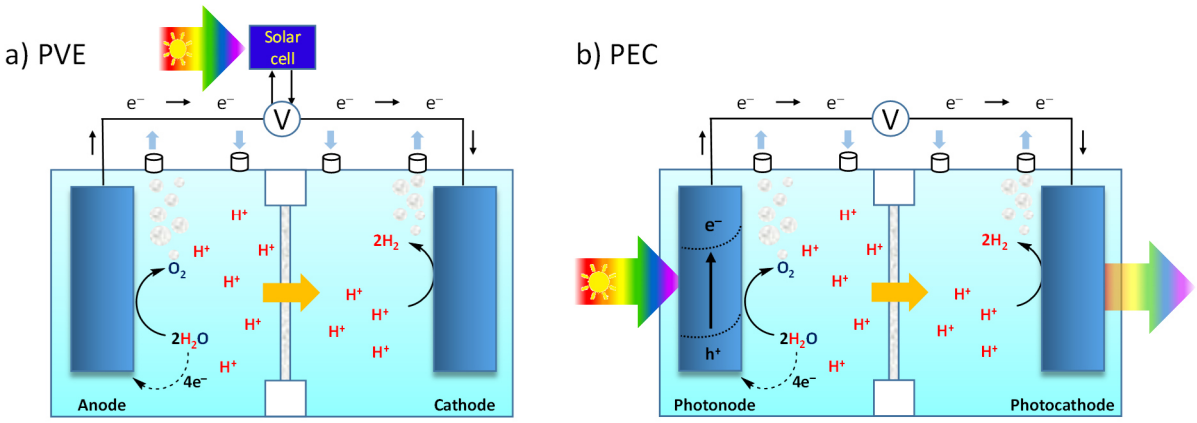

Figure 7: Illustration of a) a photovoltaic-coupled electrolyzer (PVE) and b) a photoelectrochemical cell (PEC) as the two major types of artificial photosynthesis systems. Adapted from ref. [100].

Photovoltaic-coupled electrolyzers (PVE) are the more simple systems for artificial photo-synthesis consisting of a photovoltaic cell and an electrolyzer (Figure 7). Light is absorbed by the solar cell where a charge separation occurs and electric power is generated. Typical silicon-based solar cells generate a voltage between 0.5 and 0.7 V.[103] Accordingly, for a typical electrolyzer which conventionally requires about 2 V,[104-105] at least three in series connected solar cells are necessary. However, cells applying multiple stacked absorber materials, so called “tandem” solar cells, are able to generate higher voltages (even over 2 V). Jaramillo and co-workers presented a water splitting system consisting of a triple-junction solar cell with III-V semiconductors coupled to two electrolyzers connected in series.[106] A maximum cell voltage output of 2.9 V was achieved under the irradiation of concentrated sunlight and an average solar-to-hydrogen efficiency of 30% over a period of 48 hours was demonstrated. Although it is one of the most efficient PVE systems today, industrial application under real conditions is still too expensive for commercial application.[106]

Very first approaches to a photoelectrochemical cells (PEC) have been launched already in the early 1970's by Fujishima and Honda, reporting of the feasibility of photocatalytic water splitting.[38] PECs are able to directly convert solar light into energy without external solar cells. Using a two chamber cell consisting of a semiconducting TiO_2 photoanode and a platinum cathode, UV-irradiation was applied and anodic current flow was observed. Oxygen evolution was confirmed by several analytic measurements. Photons with wavelengths shorter than 415 nm (3 eV) were needed in the experiment, which corresponds to the band gap of TiO_2. The observations can be explained by the following processes:

$$TiO_2 + 2\ x\ h\upsilon \rightarrow 2\ e^- + 2\ p^+$$

$$2\ p^+ + H_2O \rightarrow 0.5\ O_2 + 2\ H_2$$

$$2\ e^- + 2\ H^+ \rightarrow H_2$$

$$H_2O + 2\ x\ h\upsilon \rightarrow H_2 + 0.5\ O_2$$

The first step is the excitation of TiO_2 by light as the valence band (VB) to conduction band (CB) gap of n-type anatase TiO_2 is about 3 eV.[107-108] The photo-generated electron holes are able to drive the water oxidation reaction at the anode, while electrons wander to the cathodic platinum electrode and reduce the resulting protons to hydrogen. The setup of the first water splitting cell and an energy schema of the processes taking place are presented in Figure 8.

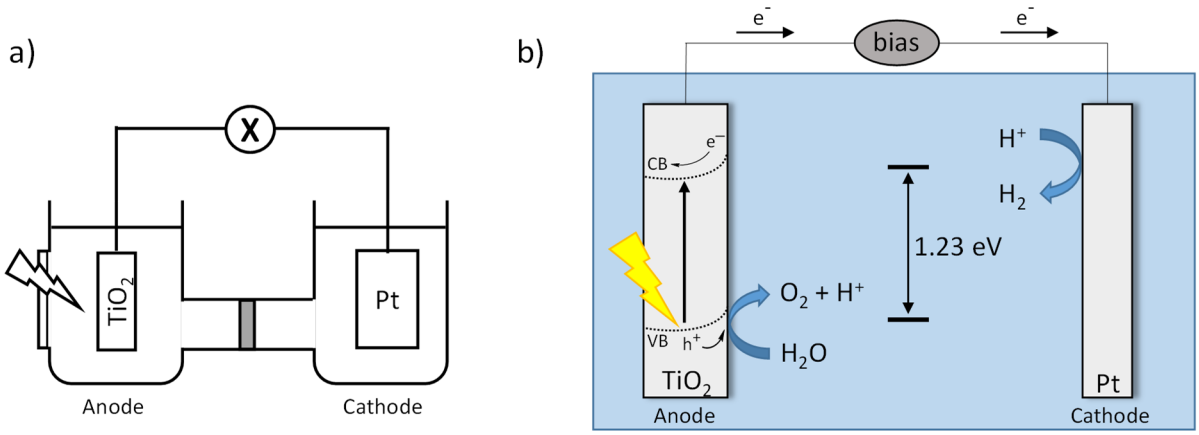

Figure 8: a) Schematic presentation of the first PEC by Fujishima and Honda. b) Fundamental principle of a PEC based on semiconducting TiO_2 anode. Adapted from refs. [38] and [109].

However, further improvement of the underlying components in terms of stability, long-lived charge seperated states, band gaps and costs are essential to meet requirements for potential industrial applications.[110-111] Besides only applying semiconducting electrodes, further approach on PECs is the design of dye-sesitized photoelectrochemical cells (DS-PEC).[109, 112-114] In DS-PEC, molecular photosensitizers are attached to the electrodes to extend the

absorption of wide band gap semiconductors (SC) to make them more responsive to the solar spectrum. In contrast to inorganic SC oxides, fine tuning of the energy levels (HOMO and LUMO) of organo-metal complexes and organic dyes is much easier through specific modifications of their molecular structures.[41] An ideal DS-PEC consists of the following three main components: (1) an anode compartment where the electrode is equiped with dye molecules and water oxidation catalysts, either based on metal oxides or on anchored molecular catalysts, (2) a cathode compartment comprising a photosensitive dye molecule and a hydrogen evolving catalyst (HEC) attached to a (p-type) electrode and (3) a membrane junction to separate both compartments and prevent unwanted charge recombination. Proton flow must be ensured while avoiding a mixing of the reaction products.[101]

Key steps for the operation of DS-PECs start with the photoexcitation of the dye molecules, where an electron-hole pair is generated. In the anodic compartment, electrons from the excited dye are injected in the CB of the electrode (ideally a n-type material), while the WOC accumulates four positive charges to perform water oxidation. Resulting electrons regenerate the photosensitizer, while emerging molecular oxygen is released into the gas phase and protons are transferred through the membrane to the cathodic department driven by the arising concentration gradient. To avoid charge accumulation, resulting electrons migrate from the anode through an external circuit to the cathode. Photoexcitation of the dyes in the cathodic compartment provides electrons to reduce the HEC, which leads to the conversion of protons into molecular hydrogen. Currents initiated by the water oxidation fill the electron holes. However, one of the main problems in artificial molecular photosynthetic systems is the fast charge recombination following the photoinduced charge separation leading to deactivation without energy storage.[109, 115-119]

Since most research groups have specialized on the development of either water oxidation or hydrogen evolving catalysts, many publications focus on either the anodic or the cathodic half reaction.[120] One of the first examples of a functional DS-PEC was presented by Mallouk and co-workers.[121] The photoanode consists of a $Ru(bpy)_3^{2+}$ derivate anchored to nanocrystalline TiO_2 film on fluorine doped tin oxide (FTO) with an $IrO_2 \cdot nH_2O$ WOC attached to the photosensitizer. A platinum electrode was used as cathode for proton reduction. A small voltage had to be applied, but overall water splitting with visible light was demonstrated. However, quantum efficiencies were rather low due to back electron transfer from TiO_2 to the dye. In the following years, Spiccia and co-workers presented a DS-PEC with a bioinspired manganese water oxidation catalyst embedded in a Nafion membrane and combined with a sensitizer-supported TiO_2 anode.[122] Water oxidation using visible light without any external bias was demonstrated, while the hydrogen evolution reaction (HER) took place at a platinum electrode. Sun and co-workers also published different approaches for photoanodes. In one

cell, the WOC was also embedded in a Nafion membrane,[123] while others comprise the direct anchoring of the catalyst on a TiO_2 surface,[124-125] anchoring of photosensitizer-catalyst dyads to the anode,[126-127] embedding the WOC in a poly(methyl methacrylate) (PMMA) membrane[114] or electropolymerization of the water oxidizing catalyst on a photosensitizer-TiO_2 film.[128] Very recently, Meyer and co-workers presented a DS-PEC with a photoanode and demonstrated solar-to-hydrogen efficiencies up to 1.5%.[129] In all cases, proton reduction was performed on a platinum cathode. Cells focusing on photocathodes have also been presented,[130-133] however, while proton reduction also takes place without HEC, complete cells without a WOC are not efficient for water splitting. Much more interest is devoted to tandem systems comprising both WOCs and HECs. Examples of Sun and co-workers present platinum-free tandem cells with the combination of cobalt-based HRC at the cathode and Ru-based WOC at the anode that are able to perform light-driven water splitting. However, such cells are not very effective yet as a Faraday efficiency of only 55% was achieved.[134-135]

While only the water splitting will be discussed in this work, the concept of these photosynthetic devices can also be applied for the generation of different solar fuels like NH_3 or hydrocarbons. In all cases, water oxidation is the crutial reaction to deliver the reducing equivalents, while various reduction reactions are possible at the cathode. Accordingly, the development of WOCs and (photo)anodes for performing this reaction are highly desired.

Ideally, DS-PECs would be used for testing activities of newly designed water oxidation catalysts. However, too many factors influence the system and optimization would be too time-consuming and costly to perform for all new WOCs. Fast screening of activities is, therefore, studied in less complicated set-ups independently from the HER applying sacrificial electron acceptors. The simplest way of evaluating a WOC is in a chemically driven approach. Oxidants activate the catalyst and trigger the water oxidation reaction. Furthermore, one step closer to artificial photosynthesis devices is the use of photosensitizers to trigger the reaction and oxidize the catalyst, while electron acceptors are applied for termination of the reaction. Electrochemically-driven water oxidation has also been used extensively to study the performance of WOCs, as simple setups allow for fast analysis of activities and stabilities. These techniques will be further discussed in *Chapter 2.2.2*.

2.2 Water Oxidation Catalysis

2.2.1 Homogeneous versus heterogeneous WOCs

As mentioned before, for water splitting, efficient catalysts are required to lower the kinetic barriers due to high overpotentials of the water oxidation reaction. Heterogeneous electrocatalysts are usually applied in electrolyzers, however, very different operating conditions of such devices require specific properties of the catalysts.[136-137] Various earth abundant metals as heterogeneous WOCs have been demonstrated to catalyze the water oxidation reaction, most efficiently in alkaline or neutral environment. For example, bismuth vanadate ($BiVO_4$) shows stability against photocorrosion in a pH range from 3 to 13 and has a low band gap of 2.4 eV, however, catalytic efficiency is limited by poor charge-transport properties and high electron-hole recombination.[138-140] Other metal oxides have also received considerable attention during the last years. Nanostructured manganese oxides (Mn_2O_3), cobalt oxide (CoO_x), nickel oxide (NiO_x) and cooper-based materials (Cu/CuO or $Cu(OH)_2$) as water oxidation catalysts have also been reported.[141] One of their drawbacks, however, is their poor electroconductivity.[142]

Oxides of noble metals like RuO_2 and IrO_2 have been shown to be among the most active catalysts in water oxidation because of their inherent electronic properties and relatively high stability, granting high electronic conduction by their crystallographic structure.[143-145] It has been found that independent of the applied electrode, RuO_2 is always more active than IrO_2, whereas electrode stability of IrO_2 is better compared to RuO_2, as the latter can degrade by the formation of soluble RuO_4 oxides. In both cases, dissolution increased drastically in basic environment, while high activities were obtained in acidic media.[146] Kokoh and co-workers reported investigations on a highly active mixed core-shell IrO_2@RuO_2 material in acidic media consisting of 75% Ru and 25% Ir. A remarkable stability of 97% of the initial charge remained after 1000 repetitive CV cycles.[147] Similar findings were also reported by Qiao and co-workers, who prepared a Ru@IrO_x electrode and demonstrated high activity and stability.[148] However, the main drawbacks of noble metal oxides are their poor availability and high costs, which make them unattractive for large scale applications.

The group of polyoxometallates (POMs) consists of anionic metal oxo clusters, which are most commonly based on early, high-valent transition metals such as molybdenum, tungsten or vanadium. They can contain between 5 and 50 metal centers and their unusual high oxidative stability makes high-valent states of the metal atoms easily accessible. These transition metal oxyanions are linked by shared oxygen atoms to form 3-D frameworks, whereas the outer shell of the cluster is stabilized by strong metal-oxo bonds.[137] Very recently, studies on activities of

water oxidation catalysts by Wada and co-workers demonstrated a significant enhancement of catalytic activity of a tetra-ruthenium polyoxometalat WOC by radio frequence stimuli. Best efficiency was obtained by electromagnetic waves of 200 MHz with an increase of catalytic current by a factor of 3.6 compared to experiments with no external stimuli, presumably due to acceleration of important proton transfer steps in the catalytic cycle.[149] Another ground-breaking way of enhancing the catalytic activity of a POM was presented by the groups of Galán-Mascarós and López.[150] A $NiZnFe_4O_x$ WOC anode in alkaline media was exposed to a moderate external magnetic field of ≤ 450 mT and doubled current density was observed compared to experiments without the influence of the magnetic field. This could be explained by spin polarization which might favor parallel spin alignment of the oxygen atoms during the water oxidation and therefore improve efficiencies of the process.[150]

Heterogeneous materials offer advantages for technical application and are needed for setting up functional devices, even though they often lack in economy of the metal since in most cases only a low percentage of the materials is active towards water oxidation.[151] Straight-forward synthesis of bulk material allows simple upscaling and, additionally, heterogeneous WOCs are often superior to homogeneous catalysts both in chemical stability and catalytic durability.[141, 152] However, gaining a deeper understanding on mechanistic pathways of catalysis and its underlying principles is required to improve and further develop WOCs. Such exploration is more difficult in heterogeneous than in homogeneous systems. Molecular catalysts are advantageous for understanding fundamentals of structure-activity relationships due to the following reasons: (1) they are of defined structure and well characterized by different analytical, spectroscopic and electrochemical methods; (2) active sites can be identified and mechanistic investigations can be performed; (3) rational ligand design and modifications of steric and electronic properties allow insight into critical steps of the reaction; (4) studies of intermediates can contribute to solve the complexity of catalytic water splitting and (5) theoretical simulations to support experimental results can be more accurate for small molecular species.[41, 153] Considering these aspects, profound studies on molecular water oxidation catalysts are essential for advancing the development of efficient water splitting systems and will therefore be the topic of this thesis.

2.2.2 Techniques to analyze efficiencies of molecular WOCs

To study the water oxidation reaction separated from the proton reduction step, different methods can be applied depending on the catalyst and the desired purpose. Depending on the solubility of the WOC, acetonitrile or trifluoroethanol can be used as a co-solvent. Three techniques will be applied in this work that are discussed in the following section.

1) Chemically induced water oxidation

Chemically induced water oxidation is considered to be the method of choice for a fast, inexpensive and uncomplicated screening of WOCs. Sacrificial electron acceptors are being applied to bring the catalysts to higher oxidation states and enable them to initiate the water oxidation reaction. The main drawback of this method, however, is that it does not resemble conditions which would be found in functional artificial photosynthesis cells. Nevertheless, obtained results give an indication on stability and activities of investigated WOCs and allow for an easy comparison between different systems. It can be seen as a preliminary indication of efficiency and suitability for further application in devices.[154]

The most commonly applied chemical oxidant is cerium(IV) ammonium nitrate (CAN). It is a strong one-electron acceptor which is commercially available. However, CAN is only stable in acidic environment of around pH 1, but at higher pH, insoluble cerium oxides are formed.[154] The need for acidic solutions limits application to catalysts that are stable under these conditions and also obstructs the desire to perform catalysis at neutral or high pH in order to minimize voltage required to oxidize water. A reduction potential of CAN of 1.75 V vs NHE at pH 1 gives a relatively high overpotential of about 570 mV for the water oxidation reaction.[154] CAN is considered to be innocent towards water oxidation, but while the high overpotential is beneficial for driving catalysts with relatively high activation barriers, it also increases the possibility of side reactions and degradation of the WOC.[154] The following reactions take place in a Ru catalyst operating by WNA mechanism. First, three equivalents of CAN are needed to oxidize the catalyst to Ru^{V}=O and a fourth equivalent is responsible for further oxidation after the second water molecule attacks and a Ru^{III}–OOH species is formed:

$$Ru^{II} + Ce^{IV} + H_2O \rightarrow Ru^{III}–OH_2 + Ce^{III}$$

$$Ru^{III}–OH_2 + Ce^{IV} \rightarrow Ru^{IV}–OH + Ce^{III} + H^+$$

$$Ru^{VI}–OH + Ce^{IV} \rightarrow Ru^{V}=O + Ce^{III} + H^+$$

$$Ru^{V}=O + H_2O \rightarrow Ru^{III}–OOH + H^+$$

$$Ru^{III}–OOH + Ce^{IV} \rightarrow Ru^{IV}– O_2 + Ce^{III} + H^+$$

$$Ru^{IV}–O_2 \rightarrow Ru^{II} + O_2$$

To analyze the evolving oxygen, the reactions are carried out at a constant temperature (T) in air-tight vessels of a known volume (V) connected to pressure sensors. The increase of pressure (Δp) is attributed to the transformation of gaseous oxygen out of water and the amount of oxygen (Δn) can be calculated applying the ideal gas law (R is the universal gas constant):

$$\Delta n = \frac{\Delta p\, V}{R\, T} \qquad \text{eq. 5}$$

To exclude the possibility of an increase in pressure originating from an oxidative degradation of the ligands of the WOC to CO_2, as it has been reported before in some Ru based catalysts,[155-156] gas chromatography analysis of the head-space is performed at the end of the water oxidation reaction. The detected amount of oxygen should be in agreement with the results from the increase in pressure.

2) Photocatalytic water oxidation

Photocatalytic investigations of water oxidation reaction are mimicking more similar conditions to the ones which can be found in DS-PECs and are, therefore, closer to a real application. A set-up usually consists of three components comprising a photosensitizer (PS), a WOC and a sacrificial electron acceptor (SEA). In most studies, ruthenium trisbipyridine $Ru^{II}(bpy)_3^{2+}$ is applied as PS (E^0 = 1.26 V) and sodium persulfate ($Na_2S_2O_8$) as SEA. Several reactions occur in this three component system as shown below.

$$PS + h\nu \rightarrow PS^*$$

$$PS^* + S_2O_8^{2-} \rightarrow PS^+ + SO_4^{2-} + SO_4^{\bullet-}$$

$$PS + SO_4^{\bullet-} \rightarrow PS^+ + SO_4^{2-}$$

$$PS^+ + WOC^{n+} \rightarrow PS + WOC^{(n+1)+}$$

$$2\ H_2O + WOC^{(n+1)+} \rightarrow O_2 + 4\ H^+ + 4\ e^-$$

After a photoexcitation of the PS, the persulfate splits into a sulfate anion and a sulfate radical. The latter can oxidize another PS molecule and the oxidized PS^+ is able to extract electrons from the WOC and thus initiate the water oxidation.[157-158] One of the advantages of this technique is the neutral pH under which the system operates. Additionally, the use of a Clark electrode for oxygen detection makes it more sensitive than pressure changes in the chemically induced reaction. Accordingly, lower amounts of catalyst are needed in investigations compared to chemical WO. The Clark electrode is applied in solution and detects solely dissolved oxygen by an electrocatalytic reduction on a platinum cathode, while AgCl is formed with the conducting KCl solution on the silver anode:

$$O_2 + 4\ e^- + 2\ H_2O \rightarrow 4\ OH^-$$

$$4\ Ag + 4\ Cl^- \rightarrow 4\ AgCl + 4\ e^-$$

The responsive current is proportional to the partial pressure of oxygen in solution. However, as solubility of gas strongly depends on the temperature, experiments need to be carried out under stable conditions to obtain comparable results.

3) Electrochemical water oxidation

To test reactivity of WOCs under conditions close to real applications, electrochemical methods are the most suited ones. Investigations of catalysts in homogeneous phase are more complicated as only the diffusion layer around the electrode is taken into consideration. Applying hybrid anodes with anchored WOCs, the total amount of catalyst present is taking part in the reaction. The loading of catalyst on the electrode is therefore an important factor, as it has direct impact on the achievable maximum currents of the system. Since solubility is not a point of concern for anchored catalysts, pure water can be used without any organic co-solvent. However, the ion product of water is very low (K_w = 10^{-14}) and thus, it conducts electrical current very poorly with only 0.055 µS/cm.[159] Much higher concentrations of conducting salts or buffer are required to enable the continuous flow of electricity.[160]

Maximum currents at defined potentials give an indication on the activity of catalysts anchored to anode materials and are one of the most important parameters for molecular oxygen evolving anodes. High currents result from an increased flow of electrons due to water oxidation taking place at the anode and the resulting electrons move to the counter electrode and through the circuit. Currents can be converted to current density for a known surface area of the electrode. To compare various WOCs in terms of efficiency, the overpotential at the operating pH value is an important factor. Anodes with high current densities and low overpotentials are highly desired. The TOF can be determined as the activity at the foot of the catalytic wave at the very beginning of the water oxidation process by FOWA analysis (see *Chapter 5.4*).[161] However, this number gives only a theoretical value and is much higher as the real TOF observed in experiments. To calculate the latter, the amount of evolved oxygen in a controlled potential electrolysis experiment can be measured by Clark electrode and the TOF is obtained by dividing by the amount of active catalyst on the surface.

To investigate stability of hybrid materials, a constant current of a potential above the onset potential of the respective WOC is applied for a particular time. In this controlled potential electrolysis experiment (CPE), a constant flow of electrons is expected for a strongly attached and stable catalyst when no degradation is observed. A decrease in current indicates a loss of activity or detachment of the WOC. Assuming that all electrons are participating in the water oxidation reaction, the amount of evolved oxygen can be calculated from the current passing through the system.

The Faraday efficiency is a measure for how efficiently the electrons flowing in the system are taking part in an observed electrochemical reaction.[162] It was initially observed by Michael Faraday and described in his laws of electrolysis in 1833.[163] Systems with low Faraday efficiency lose energy in unwanted side reactions, which can be detected by the formation of side-products or heat. To determine the Faraday efficiency, a CPE experiment in inert atmosphere can be performed and the amount of evolved oxygen observed by a Clark electrode is compared to the maximal theoretical amount of oxygen possible according to the amount of electrons flowing through the system.

2.2.3 Mechanisms of water oxidation

During the last years, significant knowledge on reaction mechanisms of the catalytic water oxidation cycle has been gained thanks to combined electrochemical, spectroscopic and ^{18}O labelling experiments as well as complementary computational studies. Since catalysts should remove multiple protons and electrons from H_2O, a number of transition metal complexes are worth to be considered for catalytic water oxidation. Most intensive research was performed with ruthenium complexes and various reaction pathways have been proposed. Focus was hereby put in the crucial step of the oxygen-oxygen bond formation. Two main mechanisms are being differentiated today: the water-nucleophilic attack (WNA) mechanism and the I2M (interaction of two M-O units) mechanism (Figure 9), which can also be applied to other transition metal complexes besides ruthenium.[164]

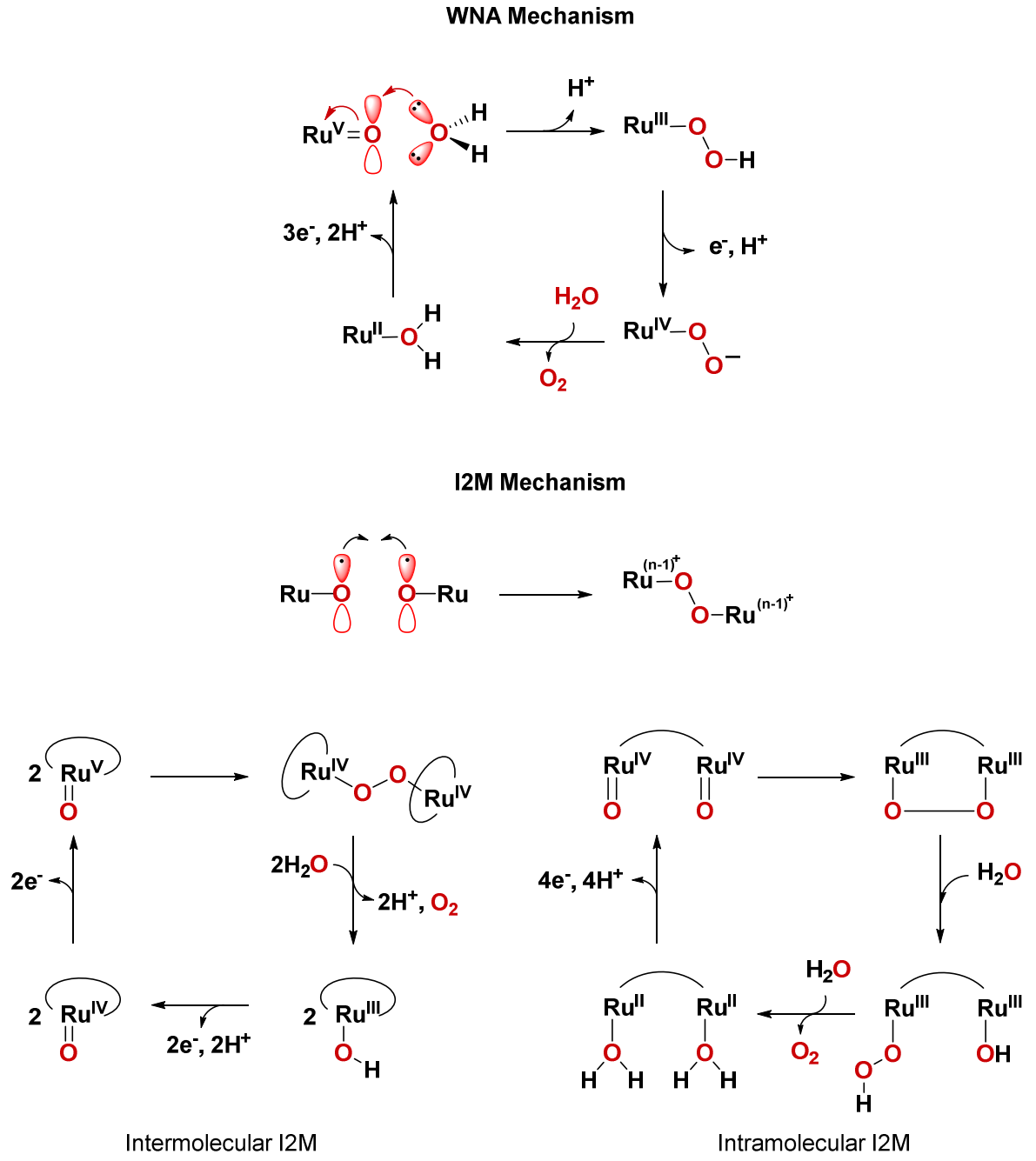

Figure 9: Mechanisms of oxygen-oxygen bond formation in water splitting with homogeneous catalysts.

In the WNA mechanism, several consecutive oxidation steps partly coupled to proton extraction lead to the formation of a highly reactive Ru^{V}=O species. Water acts as a nucleophile and attacks the electrophilic oxygen atom of Ru^{V}=O, followed by proton abstraction and the formation of a Ru^{III}-O-O-H hydroperoxo species. A proton-coupled electron transfer (PCET) step affords a Ru^{IV}-O-O^{-} intermediate. The attack of another water molecule regenerates the starting compound by the abstraction of two protons and three electrons and generates molecular oxygen.[164]

The bimolecular I2M mechanism can occur in an intermolecular or an intramolecular fashion. In the intermolecular way, two Ru^{V}=O species couple to generate a Ru^{IV}-O-O-Ru^{IV} peroxo compound. Molecular oxygen evolves and two water molecules re-coordinate, which leads to several proton and electron abstractions and the regeneration of the starting complex. In the intramolecular pathway, two Ru^{IV}=O species of the same molecule couple to form the peroxo compound, followed by the attack of one water molecule to form a Ru^{III}-OH hydroxyl and a Ru^{III}-O-OH peroxo species. The attack of a second water molecule leads to the formation of oxygen and the initial compound is recovered after the abstraction of four protons and four electrons.

Interestingly, investigations have shown that only minor variations (see Figure 10) in the second coordination sphere of Ru(bda) complexes (bda: 2,2'-bipyridine-6,6'-dicarboxylate) can induce a change of mechanism. Very recently, Sun and co-workers have reported investigations on the impact of sterical hindrance, flexibility and hydrophilicity on water oxidation mechanism under acidic conditions.[165] Ru(bda)$(pic)_2$ complex **1** (pic: picoline) oxidizes water in a I2M fashion, and so does Ru(bnda)$(pic)_2$ complex **2** (bnda: 2,2'-bi(nicotinic acid)-6,6'-dicarboxylate). TOFs of 19 s^{-1} and 10 s^{-1} were obtained, respectively. In contrast, complexes Ru(pda)$(pic)_2$ **3** (pda: 1,1'-phenanthroline-2,9-dicarboxylate) and Ru(biqa)$(pic)_2$ **4** (biqa: (1,1'-biisoquinoline)-3,3'-dicarboxylate) operate by WNA mechanism with much lower activities of 0.1 s^{-1} and 0.6 s^{-1}.

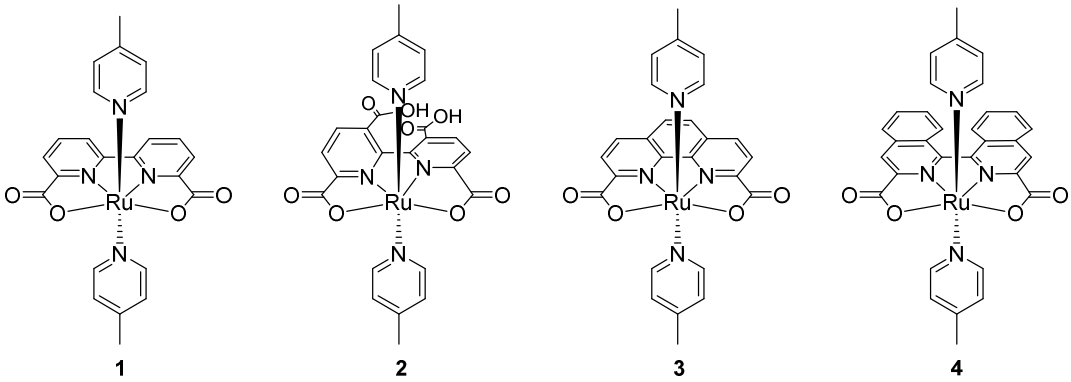

Figure 10: Homogeneous Ru WOCs studied by Sun and co-workers.[165]

Spin densities and radical character of the oxygen atom in Ru^{V}=O as well as activation free energies for the formation of a [Ru^{V}=O···O=Ru^{V}] transition state have been compared by DFT calculations, but no significant differences were observed. It is being hypothesized that the main factor for the resulting mechanisms and efficiencies of Ru(bda) catalysts is the formation of a pre-reactive state from solvated Ru^{V}=O monomers and their intermolecular interaction in aqueous solution.[165]

2.3 Ruthenium-based Water Oxidation Catalysts

2.3.1 Molecular ruthenium water oxidation catalysts

Due to its rich coordination chemistry and ability to access various oxidation states from +2 to +8, ruthenium has been widely applied in studies of water oxidation.[166] Six-fold coordination of most Ru^{II} WOCs leads to octahedral low spin complexes with d^6 configuration, whereas heptacoordinated complexes in Ru^{IV} state or higher form pentagonal bipyramidal geometries.[167] The 7th coordination provides additional electron density and leads to a lowering of the d_{xz} and d_{yz} orbitals and hence, stabilizes the electron-deficient higher oxidation states, which leads to a reduction of the overall redox potentials and facilitates catalysis. The splitting of the d-orbitals is depicted in Figure 11a. Fully occupied orbitals of octahedral low spin d^6 and pentagonal bipyramidal d^4 complexes result in diamagnetic species, while d^3 and d^5 intermediates are paramagnetic.

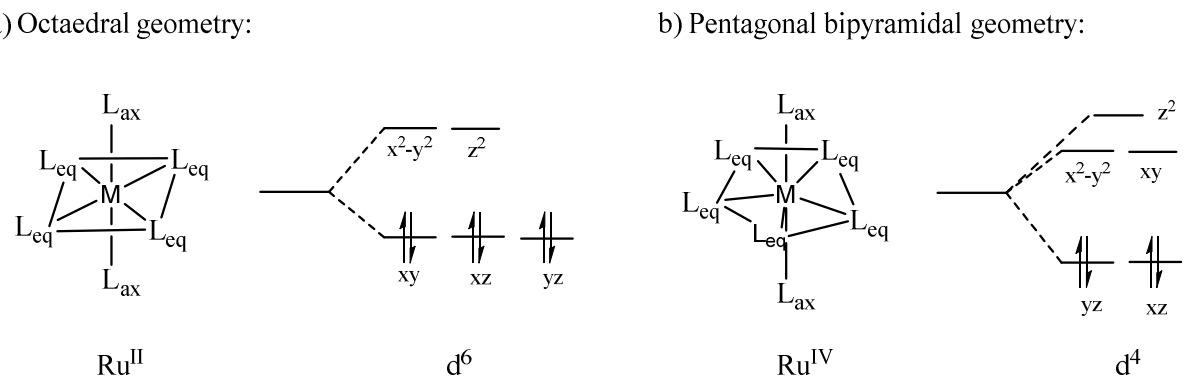

Figure 11: Schematic illustration of geometries and energy splitting diagram of d-orbitals in a) octahedral low spin and b) pentagonal bipyramidal complexes.

Research in the field of molecular ruthenium WOCs was initiated by pioneering work of Meyer and co-workers, who presented their discovery of a μ-oxo-bridged dinuclear Ru complex active in water oxidation catalysis in 1982.[39] This *cis,cis*-$[Ru^{II}(bpy)_2(H_2O)](\mu\text{-}O)^{4+}$ complex **5** (Figure 12), which is also known as the "blue-dimer" due to its characteristic blue color, has been the earliest well-characterized molecular WOC able to oxidize water chemically as well as electrochemically. This Ru complex has been extensively studied and is one of the best understood WOCs to date.[168-170] Taking inspiration from its discovery, scientists have been working on further improvement of catalytic activities and design of WOCs with high efficiencies and fast reaction kinetics. Besides Ru, complexes of different other metals such as Mn,[122, 171] Fe,[172-175] Co,[176-178] Ni,[179-181] Cu[182-184] or Ir[185-187] have been shown to catalyze water oxidation. However, only Ru-based systems will be discussed in this work.

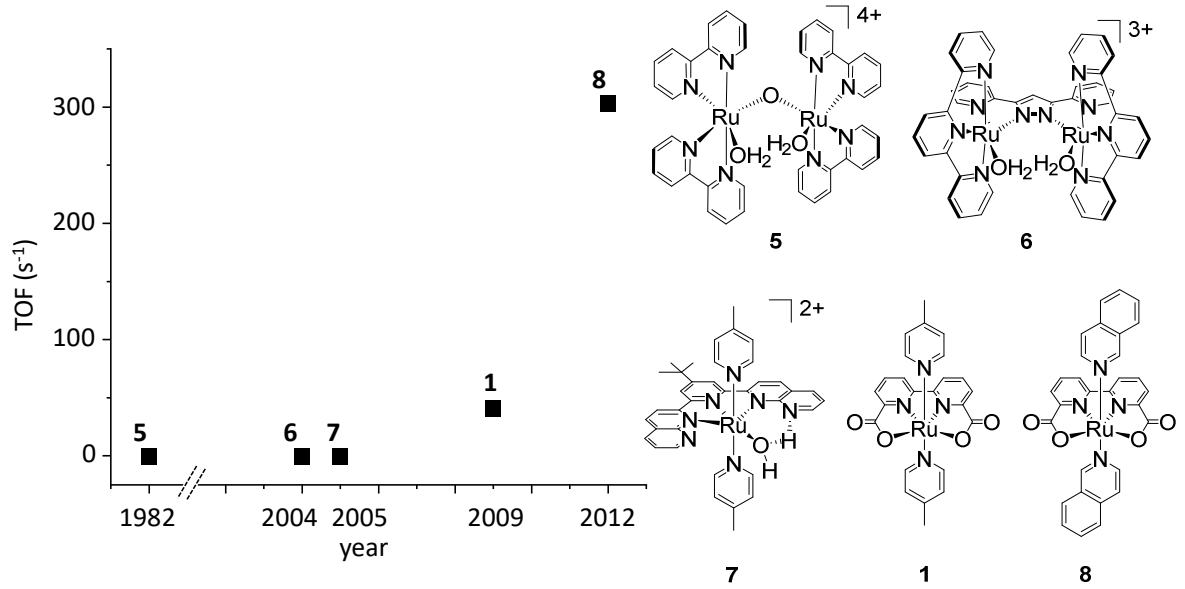

Figure 12: Improvement of catalytic activities of Ru based WOCs since the discovery of the "blue dimer" **5** in 1982 in terms of TOF values obtained in chemically induced water oxidation using CAN as an oxidant.

Studies on the "blue dimer" **5** revealed a TOF of 0.004 s^{-1} and only 13.2 turnovers in chemically induced water oxidation.[39] Subsequent investigations in the following years by extensive kinetic and DFT studies revealed that the rather unstable μ-oxo-bridge breaks down during catalysis, leading to inactive monomers which might be the reason for low efficiencies of **5**.[188-191] Mechanistic studies have demonstrated that the complex operates by a WNA mechanism, forming $Ru^{V}ORu^{IV}$ and $Ru^{V}ORu^{V}$ species as intermediates.[192-194] Due to the high oxidation states observed in the "blue dimer", it was assumed that two Ru centers would be necessary to give WOCs which are stable enough to accumulate four oxidizing equivalents and reach high oxidation states needed for this reaction. Following this assumption, the design of new WOCs has mainly been focused on multinuclear complexes at that time.

In 2004, Llobet and co-workers presented dinuclear Ru WOC **6** (Figure 12), replacing the instable μ-oxo-bridge by a conjugated pyrazol bridge between the two Ru centers.[195] Activity of this catalyst has been investigated in chemically induced water oxidation and a TOF of 0.014 s^{-1} was obtained. The relatively low TON of 18.6 with an efficiency of 70% with regard to Ce^{IV} could be increased to 512 with a much higher excess of oxidant. ^{18}O kinetic studies and theoretical investigations revealed an I2M mechanism for this catalyst.[196-198]

A real breakthrough in the field of molecular WOCs was achieved by Thummel and co-workers in 2005.[199] They have shown that mononuclear WOC **7** can accomplish the four-electron transfer process necessary for water oxidation with only one ruthenium center.[199] The complex bearing a tridentate polypyridyl ligand and two picoline ligands was found to obtain the same TOF of 0.014 s^{-1} as reported for dinuclear Ru complex **6** in chemical water oxidation with a

TON of 260. It has been only in 2008 that Meyer and co-workers published a mechanistic study and revealed a WNA mechanism for **7**.[200]

Since the revolutionary discovery that single-site catalysts are indeed able to perform a series of H^+/e^- transfer processes needed to oxidize H_2O to O_2, the much easier and straight-forward synthesis of mononuclear WOCs led to a rapid increase in publications in this field. Several examples of $Ru(terpy)(bpy)_2(OH_2)$ complexes with derivatives of terpy (terpy: 2,2';6',2"-terpyridine) and bpy or different bidentate ligands have been reported in the following years, however, no significant increase in efficiency could be achieved.[199, 201-202]

A major improvement in catalytic efficiency of WOCs was obtained in 2009, when Sun and co-workers introduced the dianionic bda ligand and showed that $Ru(bda)(pic)_2$ catalyst **1** was able to perform water oxidation using CAN as an oxidant with a TOF of 41 s^{-1} and TON of 2000. These remarkably high activity and stability were assigned to the dianionic nature the bidentate bda ligand in the equatorial plane. Mechanistic studies demonstrated an I2M mechanism for the mononuclear Ru complex **1**.[40, 203] The exchange of axial picoline with isoquinoline ligands resulted in WOC **8**, which exhibited a record TOF value of 303 s^{-1} and TON of 8000 in chemical water oxidation.[204] This was explained by intramolecular π-π interactions of the axial ligands that bring two Ru centers in close proximity and promoting reaction rates of the bimolecular mechanism in aqueous environment.

An overview of the best-performing WOCs in chemical, light-induced and electrochemical water oxidation is shown in Figure 13.

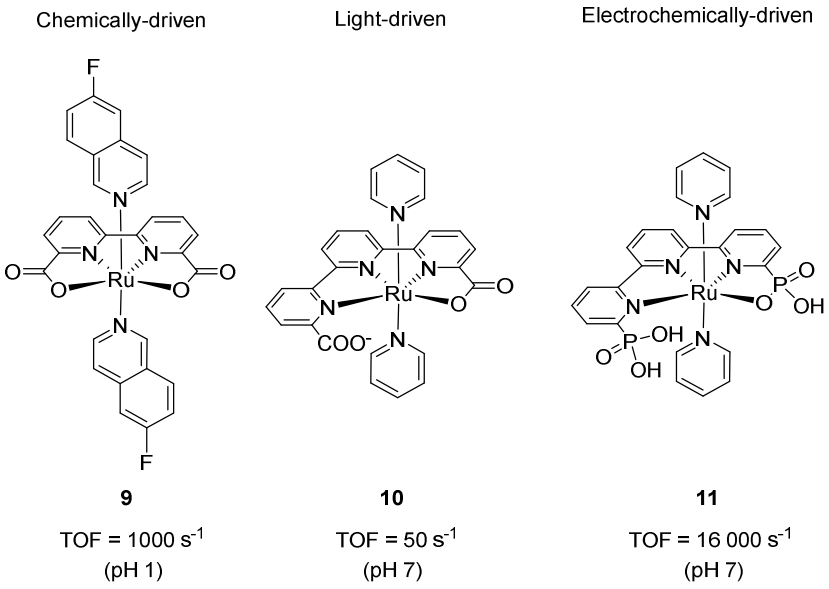

Figure 13: Best performing WOCs in chemical, light-induced and electrochemical water oxidation known to date**.**

Straight forward synthesis of neutral Ru(bda) complexes using easily exchangeable axial ligands with different *N*-heterocycles makes them attractive for various applications, from mechanistic studies of the influence of modified ligands as well as implementation in supramolecular structures and introduction of anchoring groups for heterogeneous catalysis.[100] The dianionic bda ligand allows for easy access to high oxidation states and facilitates the formation of Ru^{IV} and Ru^{V} intermediates in the catalytic cycle. Due to the wide O-O angle of 123° in the equatorial plane of Ru^{II}(bda), an open site for heptacoordination in higher oxidation states is accessible. While more than 50 WOCs with Ru(bda) scaffold are reported in literature, Ru(bda)(6-bromophtz)$_2$ (phtz: phthalazine) is the most stable Ru WOC in chemically induced catalysis driven by CAN at pH 1. Also working by I2M mechanism, the TOF of 380 s^{-1} of this WOC is similar to that of Ru complex **8**, however, with an impressive TON of 101 000, the stability is significantly improved. This is explained by DFT calculations, claiming that the high HOMO of phtalazine is leading to complexes with high durability. The fastest catalyst reported in literature is Ru(bda)(6-fluoroisoquinoline)$_2$ **9** (Figure 13), which performs up to 1000 cycles per second (TON = 24 000). The increased hydrophobicity favors the dimer formation and therefore, accelerates reaction rates.[204-205]

The best performing Ru WOC in light-induced water oxidation was reported by the groups of Llobet and Durrant.[206-207] They have shown that Ru(tda)(py)$_2$ (tda: [2,2':6',2''-terpyridine]-6,6''-dicarboxylate) **10** gets activated in situ and efficiently catalyzes photochemical water oxidation with a TOF of 50 s^{-1} when applying Ru(bpy)(bpy-COOEt)$_2^{2+}$ as photosensitizer and sodium persulfate as electron acceptor at pH 7. Due to the relatively high potential of the $Ru^{V/IV}$=O redox couple, the ethyl ester derivative of the standard ruthenium tris(bipyridine) photosensitizer with a higher redox potential (E^0 = 1.62 V) had to be applied. Interestingly, this catalyst does not show any activity in chemically driven water oxidation at pH 1 due to the inability to form the catalytically active species in acidic environment. This aspect will be further discussed in *Chapter 2.3.2*.[206-207]

The $Ru^{II}(H_3tPa\text{-}\kappa\text{-}N^3O)(py)_2^+$ complex **11** (H_4tPa: 2,2′:6′,2″-terpyridine-6,6″-diphosphonic acid) is actually a precursor and has to be transformed into the active catalyst by electrochemical activation. The resulting species is able to oxidize water with a TOF of 16 000 s^{-1} at an overpotential of 530 mV under neutral conditions. DFT and electrochemical studies suggest a WNA mechanism for **11**.[208] Interestingly, WOC **10** is also very active in electrochemically driven water oxidation with a remarkable TOF at 8000 s^{-1} at pH 7 which can be boosted to TOF = 50 000 s^{-1} at pH 11 after activation.[207]

2.3.2 Active species of Ru catalysts

Catalysts synthesized and applied in water oxidation are often only precursors and do not represent the catalytically active species. Some of them show already catalytic activity after simple oxidation of the Ru center, while others are inactive prior to specific activation, particularly by electrochemical processes.

In Figure 14a, the generation of catalytically active species from a pre-catalyst by electrochemical process is shown as an example.[207] Activation of Ru(tda)(py)$_2$ **10** is performed by coordination of a hydroxide anion to the metal center either by repetitive CV cycling or by applying a constant potential. Presumably due to the much higher concentration of hydroxyl-ions, activation by CPE in basic environment is much faster than at pH 7. Further oxidation of the formed species combined with proton-coupled electron transfer leads to Ru^{V}(O(tda-*κ*-N^3O))$(py)_2^+$ **10-B** as the real catalyst. Water attacks in a WNA mechanism and intermediates **10-C** and **10-D** are stabilized by hydrogen bonds to the dangling deprotonated carboxy group. The attack of a second water molecule on **10-D** regenerates the activated pre-catalyst in oxidation state II under release of molecular oxygen as shown in Figure 14b.

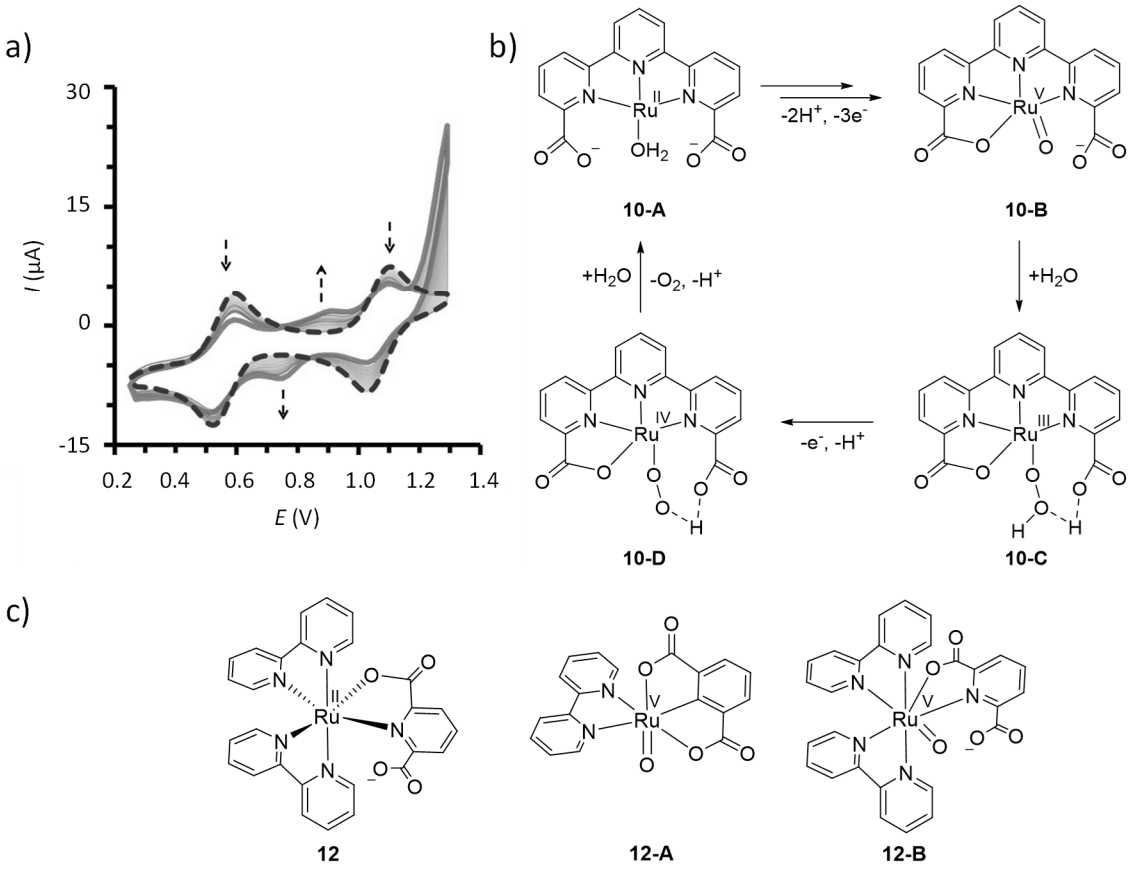

Figure 14: a) Repetitive CV cycles of pre-catalyst **10** lead to formation of active Ru(tda)-aqua species. b) Relevant steps of water oxidation catalyzed by activated Ru(tda)-aqua species **10-B**. Axial ligands are omitted for clarity. c) Structure of pre-catalyst **12** and activated species **12-A** and **12-B**. Figure 14a) adapted and reprinted with permission from ref. [207]. Copyright 2015 American Chemical Society.

Another example of activated aqua species is shown in Figure 14c. $Ru^{II}(pdc\text{-}\kappa\text{-}N^1O^1)(bpy)_2$ **12** (pdc: pyridyl-2,6-dicarboxylate) was activated by 100 consecutive CV cycles, which lead to the formation of Ru-aqua complex **12-A** and **12-B** (shown in Ru^V state).[209] The latter was found to be the more active one in the mixture with an estimated maximum TOF of about 3400 s^{-1} analyzed electrochemically by FOWA. When **12** loses one bpy ligand during the attack of one water molecule on the Ru^{IV} state, **12-A** is generated after further oxidation. In contrast, in a second pathway, the attack of water leads to the detachment of one carboxylic arm and **12-B** is formed. Interestingly, both complexes oxidize water but **12-A** involves a six-coordinated Ru center in the active catalyst, while **12-B** is seven coordinated. It is proposed that both catalysts operate by WNA mechanism.[209]

Very recently, the transformation of a further pre-catalyst **11** (see Figure 13) to an active species has been reported.[208] The application of a constant voltage of 1.3 V to complex **11** for 110 min leads to the activation process shown in Figure 15. While **11-A** shows a dynamic behavior with spontaneous coordination and decoordination of the dangling carboxy group at basic or neutral pH, both of them are bonded to the metal center in a heptacoordinated complex upon oxidation to the Ru^{IV} state (**11-B**). Nucleophilic attack of a water molecule with loss of a proton leads to the detachment of one pyridine group resulting in species **11-C**. Further proton-coupled one-electron oxidation results in **11-D** which is then transformed into **11-F** by oxygen insertion to the uncoordinated pyridyl group and subsequent deprotonation. The nature of the highly active species **11-F** has been confirmed by crystal structure analysis (TOF of 16000 s^{-1} electrochemically-driven).[208]

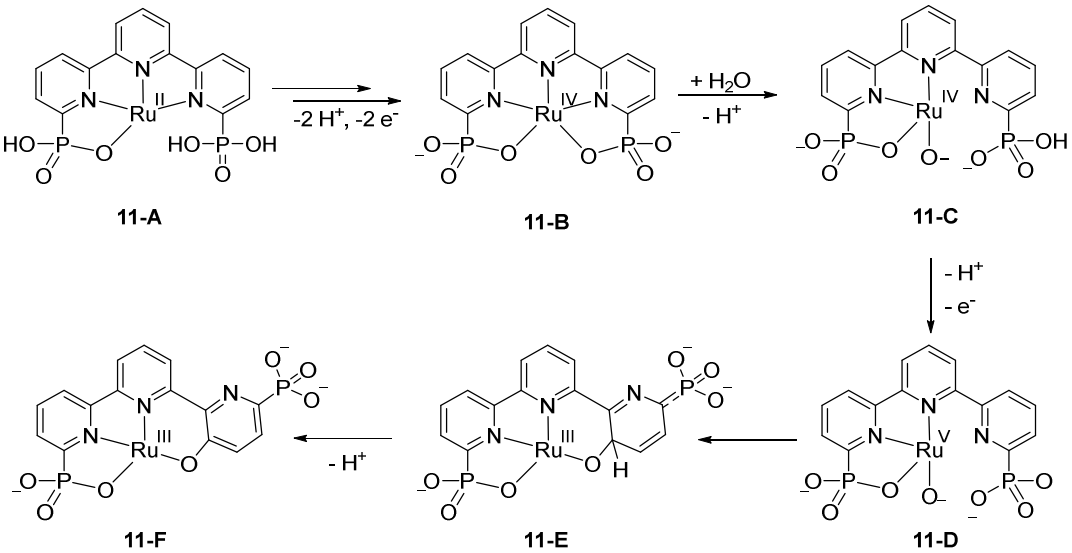

Figure 15: Activation pathway of **11** by exogenous OH^- coordination leading to intramolecular aromatic O insertion forming the active species **11-F**. Axial ligands are omitted for clarity.

2.3.3 Influence of the second coordination sphere

Making use of the second coordination sphere in the design of homogeneous WOCs can be a powerful tool for improving catalytic activities. Second coordination sphere effects describe, for example, the influence of ligands or functional groups that are not directly coordinated to the metal center but assist in a subtle way in enhancing the efficiency of water oxidation catalysts. Strategies comprise the use of accessible pendant bases, supramolecular π-π interactions, hydrogen bonding or steric effects.[210] All of them can play an important role in kinetics and activation and even influence the mechanism of the water oxidation reaction.

As shown in Figure 14b, $Ru(tda)(py)_2$ **10** benefits from the dangling carboxy group in the equatorial tda ligand. After the nucleophilic attack of water to the activated species **10-B**, intramolecular hydrogen bonds between the deprotonated carboxylic acid and the protons of water in **10-C** lead to a reduced activation barrier during the proton abstraction process and O-O bond formation.[207] Similar effects were reported by Concepcion and co-workers, who replaced one of the carboxylic acid groups in the bda ligand with phosphonic acid to give $Ru(bpHc)(pic)_2$ **13** (bpHc: 2,2′-bipyridine-6-phosphonic acid-6′-carboxylate) (Figure 16).[211] With deprotonated phosphonic acid groups, this molecule is negatively charged and high oxidation states are easily accessible. An almost three-fold increase in TOF in chemical water oxidation compared to $Ru(bda)(pic)_2$ was observed for **13** (TOFs are 20 s^{-1} and 58 s^{-1}, respectively). A WNA mechanism was proposed with stabilized intermediates by the deprotonated phosphonic acid group acting as pendant base and thus, significantly lower activation barriers.[211]

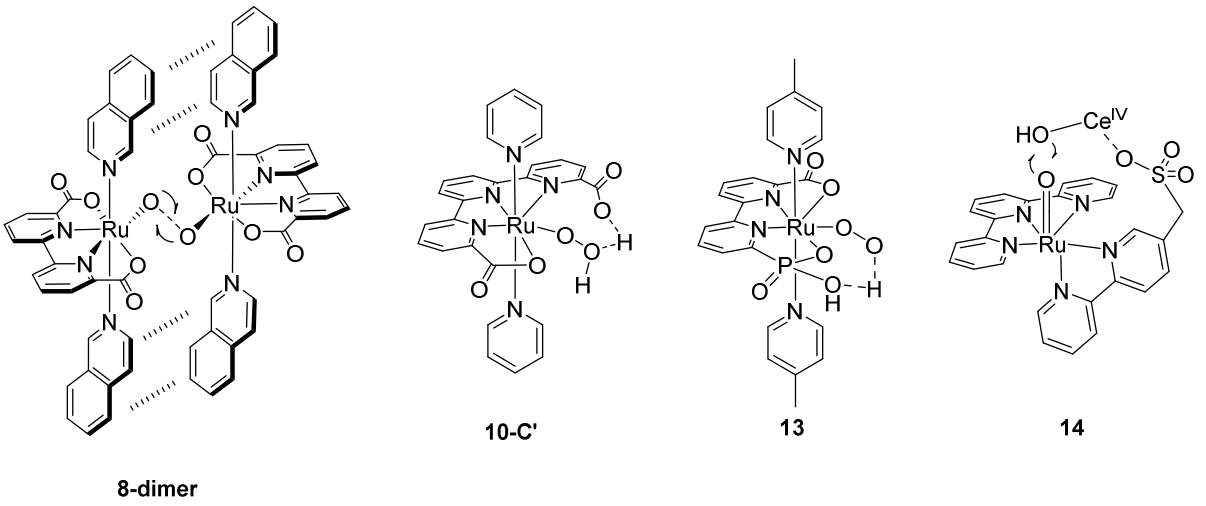

Figure 16: Examples of second coordination sphere design which accelerates rates in water oxidation catalysis.

Another example for the influence of the second coordination sphere is the previously mentioned dimer formation of **8** due to π-π interactions between the axial aromatic ligands, leading to a self-assembly of the catalytically active units and, therefore, faster rates in the bimolecular reaction mechanism.[204, 212]

A different approach for accelerating reaction rates with the help of the second coordination sphere was reported by Masaoka and co-workers.[210] A heterometallic reaction center for the oxygen-oxygen bond formation was designed by bringing a Ce^{IV}-OH ion in close proximity to the reactive Ru^{V}=O center in Ru(terpy)(bpyms) **14** (bpyms: 2,2'-bipyridine-5,5'-bis(methane-sulfonate)). Sulfonate group has been chosen as a functional unit with strong ability to coordinate to Lewis-acidic metal ions and placed on a strategically chosen position in the pyridyl ligand to assist the O-O bond formation. Complex **14** shows higher activities compared to the same WOC without methansulfonate group in chemical water oxidation at low concentrations of CAN. The effect is negligible at a large excess of Ce^{IV}, presumably due to the fact that no assistance is needed to bring Ce^{IV}-OH ions close to the reaction center. Interestingly, control experiments showed that addition of *p*-toluenesulfonic acid to the reaction mixture leads to decreased reaction rates due to competitive binding and blocking of Ce^{IV}-OH.[210]

Further examples of second coordination sphere effects have been demonstrated on supramolecular WOCs, which offer good possibilities for investigation of hydrogen bonding and influences of sterical hinderance as will be addressed in the next subchapter.

2.3.4 Supramolecular Ru-based WOCs

In order to accelerate reaction rates in catalytic water oxidation with mononuclear Ru(bda) WOCs working via I2M mechanism, Sun and co-workers designed supramolecular WOCs in which the Ru centers would be in close proximity to facilitate the dimerization step.[213] Ru(bda)-dimer **15** (Figure 17) with terminal picoline ligands and a bridging bidentate benzylic ligand having pyridine units attached to the Ru showed no evidence for any communication between the Ru centers and onset potentials of catalysis are comparable to those of the parent compound $Ru(bda)(pic)_2$ **1** in electrochemical studies.[213] However, chemically induced water oxidation with **15** using CAN gave an impressive TON of 44 412 during only one hour of reaction time, which is a seven-fold increase compared to $Ru(bda)(pic)_2$ (TON = 1 550 measured at doubled concentration) taking into account the number of Ru centers present. It was found that the WO reaction follows a first-order dependency on the catalyst concentration with a TOF of 68 s^{-1}. The first order behavior leads to the assumption that only one molecule is involved in the rate-determining step, and accordingly, an intramolecular I2M mechanism

was proposed for **15**.[213] Taking advantage of these mechanistic changes, the Sun group functionalized the benzene bridge in a similar bidentate ligand with phosphonic groups and immobilized the respective WOC on TiO_2/FTO surfaces for application in heterogeneous catalysis, resulting in improved activities compared to an anchored derivative of the mononuclear complex **1**.[124] Comparing **15** with trinuclear Ru(bda) WOC **16**, an even higher TON of 86 500 was observed for the latter with a TOF of 126 s^{-1}. Even considering the TON and TOF values per Ru center, both values are still higher for the trinuclear than for the dinuclear complex. This was explained by the fact that in case of loss of one of the catalytically active centers from the bridging ligand, **16** is still able to perform water oxidation in intramolecular fashion with the two remaining subunits, while this pathway is not available for **15** anymore.[214]

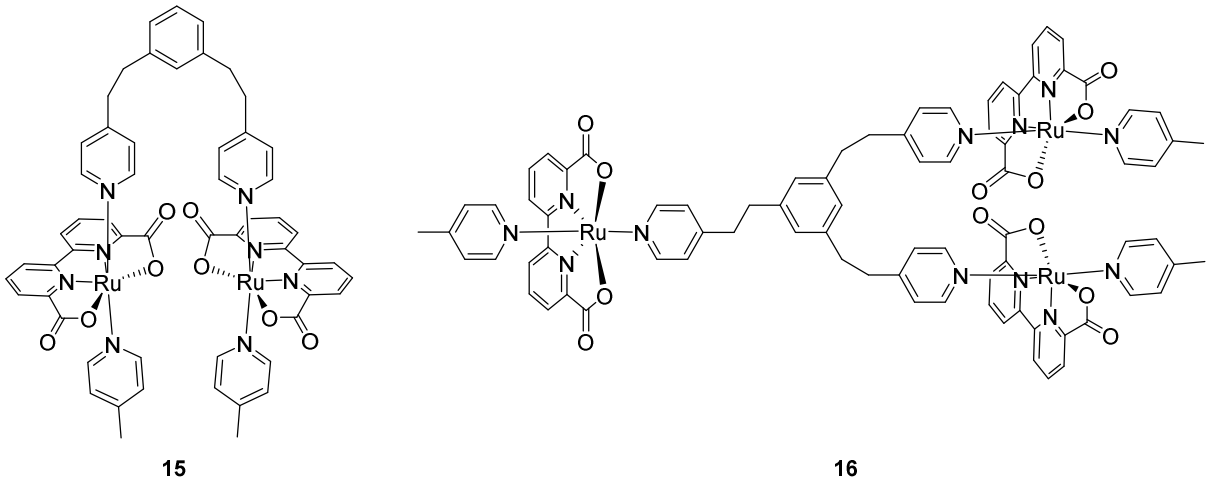

Figure 17: Structures of di- and trinuclear Ru(bda) complexes **15** and **16**.

The linearity of the Ru(bda)L_2 WOC combined with easy exchangeable axial ligands allows for the integration of Ru(bda) not only in open systems, but also in closed macrocyclic structures. Indeed, this strategy was first applied by Würthner and co-workers in 2016 and trinuclear macrocycle **MC3** was reported as highly efficient WOC (Figure 18a). The preorganization of catalytically active units in a macrocyclic structure benefits from an increased stability due to the presence of three bidentate ligands, preventing easy axial ligand dissociation known as one main degradation pathway in mononuclear Ru(bda) WOCs.[204] Additionally, self-oxidation is minimized due to sterics, which allow only small molecules like water to reach the reaction center.[215] Water oxidation by **MC3** was performed in water/acetonitrile mixtures (4:6) to circumvent poor solubility in pure water due to its large size. In chemically induced experiments, significantly improved activities compared to the Ru(bda)$(pic)_2$ parent compound **1** were reported with an impressive TON of 7 400 and a TOF of 150 s^{-1}.[42] Variations of the bridging ligands resulted in trinuclear macrocycles of smaller and larger size. These macrocycles were studied in chemically induced water oxidation revealing that the medium

size **MC3** is the most active one.[43] For increasing solubility in aqueous media, trialkylamin and triethylenglycol groups were introduced in the axial ligands. This allowed for a reduction of acetonitrile as a co-solvent to only 20%, while maintaining comparable catalytic activities.[215]

The macrocyclic arrangement is also responsible for a change in WO mechanism: while the Ru(bda)(pic)$_2$ parent compound operates via I2M, formation of bimolecular intermediates is suppressed in **MC3**. Detailed kinetic studies and ^{18}O labeling experiments confirmed a WNA mechanism for **MC3** by indicating the attack of a water molecule on a Ru^{V}=O species.[42] As one of the most active Ru(bda) WOCs operating by WNA mechanism, it is especially interesting to have a closer look at the cooperative effects between the catalytic centers facilitated by the macrocyclic arrangement. Molecular dynamics simulations suggest the presence of a highly ordered network of hydrogen-bonded water molecules within the cavity of **MC3** to be responsible for fast reaction rates (Figure 18b). Reduced reaction barriers in proton-coupled electron transfer steps through cooperative proton abstraction between the Ru centers are proposed to be the reason for accelerated reaction rates. This Grotthuss-type mechanism for efficient proton transfer is graphically depicted in Figure 18c.[43, 216] Recently, Würthner and co-workers presented first experimental evidence for these water networks in a crystal structure obtained from fluoro-substituted derivative ***m*-F-MC3** (see Figure 18d).[216]

The introduction of substituents in different positions of the bridging ligands that influence the steric features in macrocycles has demonstrated the importance of the water network. Accordingly, conformational changes resulting from modification of the macrocycles in the *para*-position relative to the *N*-atom of the axial ligands led to a more restricted access of water molecules to the reaction center and limited access to the inner preorganized water network.[216]

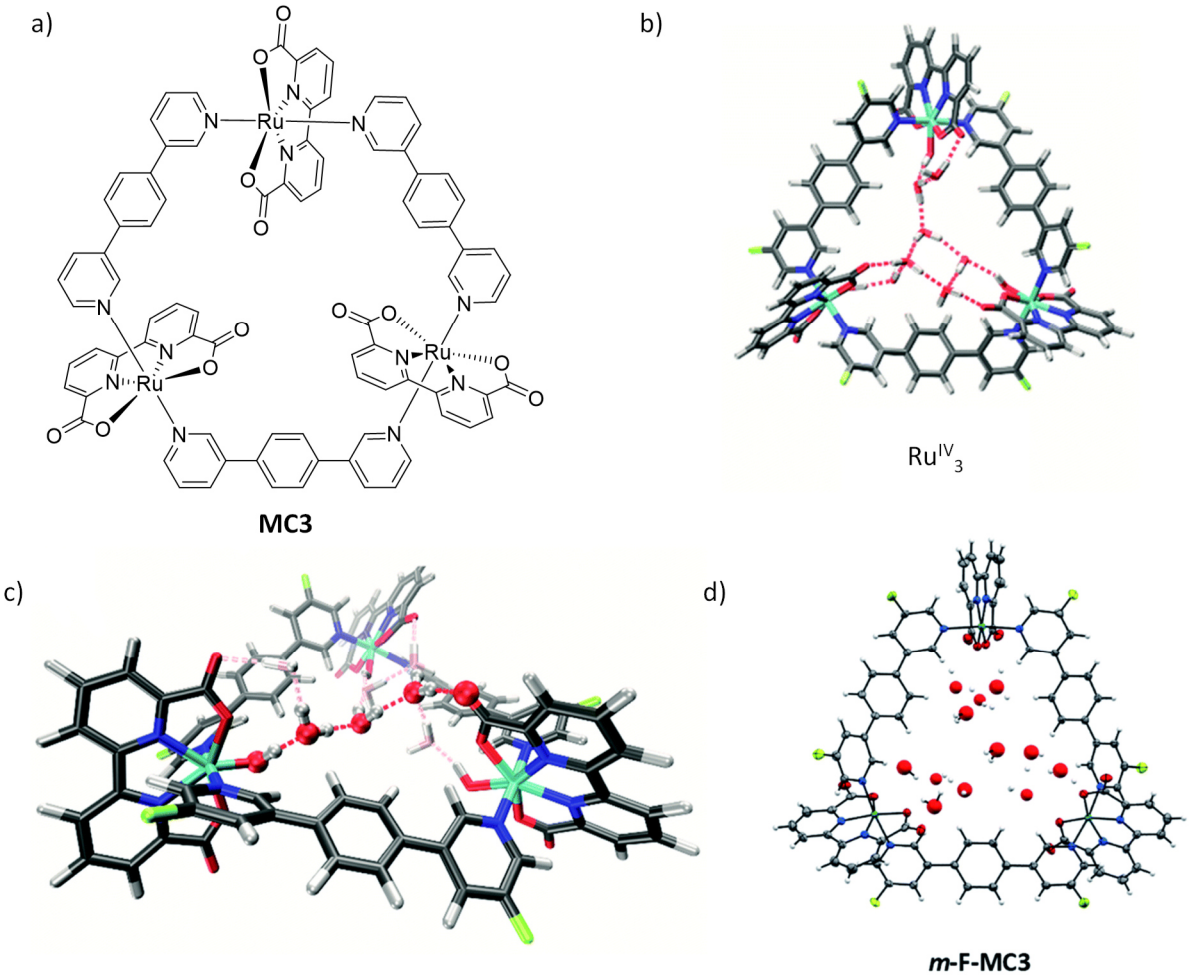

Figure 18: a) Structure of **MC3** macrocycle. b) DFT-optimized structure of the water network inside the cavity of ***m*-F-MC3** in the oxidation state Ru_3^{IV}. c) Perspective view on three water molecules connecting two Ru centers DFT-optimized in Ru_3^{IV} state. d) Crystal structure of ***m*-F-MC3** determined by single crystal X-ray diffraction provides first experimental evidence for water networks in the macrocyclic cavity. Figure 18b)-d) are reprinted with permission from ref. [216]. Copyright 2020 Royal Society of Chemistry.

2.3.5 Immobilization strategies for molecular WOCs

Molecular ruthenium catalysts not only belong to the earliest WOCs, they are also the most extensively studied class of catalysts possessing high efficiencies for water oxidation. Anchoring these well-understood catalysts onto surfaces is one auspicious way of generating well-performing electroanodes, benefitting not only from a better atomic economy but also from fast hole transfer to the respective electrode preventing charge recombination. Catalysts which have demonstrated to operate via WNA mechanism in solution are the most promising candidates. Immobilizing WOCs on surfaces that operate by I2M can result in higher over-potentials by enforcing the catalyst to switch to WNA mechanism.[217] For the anchoring of catalysts on a conducting surface, mainly two different strategies have been employed that are discussed below.

Anchoring on surfaces via covalent bonds

Direct anchoring of WOCs has been performed by incorporation of specific functional groups into the ligands to attach them to anode materials. Metal oxide surfaces such as indium tin oxide (ITO), FTO or nanoparticles of TiO_2, In_2O_3 or SnO_2 are usually applied to immobilize the functionalized catalysts.[218] The functionalization of the outer ligand scaffold of the molecular catalyst for interacting with the surface is advantageous as it preserves the intrinsic properties of the WOC. Most studies have been performed with silane and phosphonate functionalized WOCs, while other approaches of direct anchoring comprise the use of thiophene or carboxylate anchoring groups in ligands.[219-220] Disadvantages of anchoring by these groups is the relatively poor stability in aqueous solutions. While carboxylate groups are moderately stable at pH < 4, phosphonate groups are more robust at pH < 7 than carboxylates, whereas silane groups have a strong affinity to metal oxides over a wide pH range.[221-222]

Meyer and co-workers presented Ru(bda) WOC **17** with axial 4-(6-(triethoxysilyl)hexyl)pyridine ligands anchored to nano-ITO (Figure 19a).[223] Decorated electrodes were obtained by soaking the nano-ITO electrodes into a solution of **17** for 3.5 days. These electrodes demonstrated to be stable at pH 7 and only minimal detachment of catalyst was observed after 250 repetitive CV cycles when oxidizing up to the $Ru^{III/II}$ couple. However, cycling to higher potentials of 1.6 V where catalysis takes place resulted in significant loss of **17** with less than 5% of intact catalyst remaining on the electrode.[223] Similar results were obtained at pH 1 with marginally higher stability. The groups of Meyer and Sun presented several examples of Ru catalysts anchored to surfaces by phosphonate-functionalized axial ligands.[124, 224-227] Meyer group reported that electroanodes were prepared by first anchoring the functionalized pyridine ligands to the metal oxide surface and in a second step immobilizing the catalyst by axial ligand exchange.[227] A maximum current density of 27.5 μA/cm^2 was obtained with the resulting catalyst **18** (Figure 19a) at pH 1. Studies were mostly conducted in acidic environment due to potential hydrolysis at higher pH. Stability was investigated by 400 consecutive CV cycles around the $Ru^{III/II}$ redox couple, where only minimal loss was reported. However, no data for stability at higher potentials was provided.

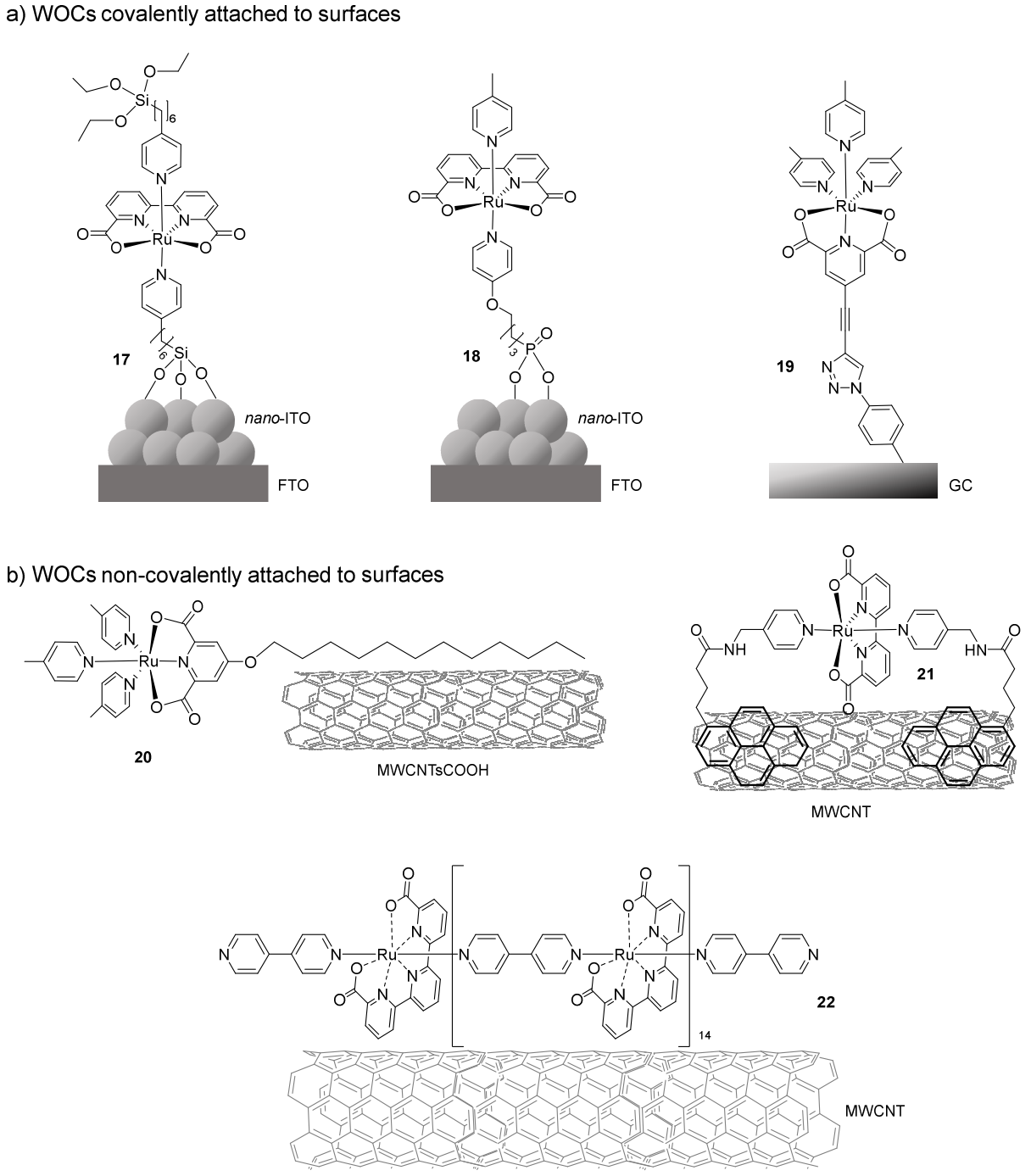

Figure 19: a) Schematic illustration of molecular WOCs anchored on solid supports or electrode surfaces by a) covalent interactions and b) non-covalent interactions.

Besides linkage by ester-type bonds to metal oxides, covalent attachment of $Ru(pdc)(pic)_3$ **19** (pdc: 2,6-pyridine dicarboxylate) (Figure 19a) to a glassy carbon substrate has been presented by Sun and co-workers.[228] Glassy carbon (GC) materials offer excellent electronical conductivity and are widely used in electrochemistry.[229] A 4-azidobenzene diazonium salt has been grafted to the GC surface by electroreduction and an acetylene-functionalized WOC was attached by click reaction to form a robust triazol linker which is resistant to high oxidation potentials. A maximum current density of 2.5 mA/cm^2 was observed when applying 1.45 V at

pH 7. However, no long term investigations on stability were performed. It should be noted that Llobet and co-workers reported a Ru(bda)(4-phenylpyridine)$_2$ WOC covalently anchored to a glassy carbon electrode which progressively decomposed to RuO_2 upon repetitive CV cycles up to 1.2 V.[228]

Anchoring on surfaces via non-covalent linkage

Besides covalently anchoring to a surface, another strategy reported to immobilize molecular WOCs on surfaces is through electrostatic or π-π-stacking interactions. Sun and co-workers functionalized Ru(pdc)(pic)$_3$ WOC **20** with a dodecyloxy group and attached it to carboxyl-functionalized multi-walled carbon nanotubes (MWCNTs) by hydrophobic interactions of the aliphatic chain (Figure 19b). CNTs are widely used due to their high surface area, high thermal and chemical stability and great conductivity. A current density of 12.5 mA/cm^2 was obtained at neutral pH at 1.75 V by an anode covered by **20** immobilized on CNTs.[230]

A similar approach has been reported by Concepcion and co-workers, who functionalized metal oxide surfaces with long alkyl chains (self-assembled monolayers) and immobilized catalysts that are functionalized with dodecyl chains by non-covalent interactions (self-assembled bilayers).[231] Applying this strategy, they also developed self-assembled chromophore-catalyst bilayers for DSPECs by covalently anchoring Ru(bpy-$(PO_3H_2)_2)_2$(bpy-$2C_nH_{2n+1})^{2+}$ (n = 6,7,9) on a TiO_2/nanoSnO_2 surface and providing catalysts functionalized with pentyl chains for non-covalent interactions with the photosensitizer.[232]

Sun and co-workers presented the functionalization of a Ru(bda) WOC with pyrene units on the axial ligands (Figure 19b, complex **21**). An ITO electrode coated with MWCNTs was soaked in a solution of **21** in methanol overnight. The catalyst was anchored to the surface of the CNTs by π-π interactions and generated a current density of 720 μA cm^{-2}. Long term electrolysis over 7 h at 1.4 V showed only minor loss and demonstrated the stable anchoring of the catalyst.[233]

Making use of non-covalent interactions, Llobet and co-workers have reported very recently that an oligomer (4,4'-bpy)[Ru(tda)(4,4'-bpy)]$_{15}$ **22** complex can be anchored to MWCNTs by CH-π interactions between the protons of the equatorial tda ligand and the graphitic surface (Figure 19b).[234] Interestingly, the strong attachment was only observed for oligomers, but the corresponding monomer did not adhere on the CNTs surface. Electrodes have been prepared by anchoring the decorated CNTs to GC electrodes. An impressive maximum current density of 240 mA/cm^2 was obtained at 1.45 V with practically no decay during CPE experiments. Therefore, this hybrid anode with immobilized molecular WOCs is one of the most efficient ones reported until now.[234]

Chapter 3

—

Mechanistic studies on ligand exchange processes in Ru(bda) complexes

Summary: Thermodynamic control over ligand exchange processes is the key for designing large metallosupramolecular structures. Here NMR investigations on the formation of trinuclear Ru(bda) macrocycle **MC3** are reported, which indicate kinetic product formation under the reaction conditions previously applied in synthetic procedure. Mechanistic investigations on ligand exchange processes of Ru(bda)L_2 model systems by ^{1}H NMR spectroscopy revealed a dissociative mechanism for these complexes and the possibility of thermodynamic product formation in the synthesis of supramolecular Ru(bda) macrocycles by ligand exchange reaction at higher temperature.

3.1 Introduction

The successful synthesis of supramolecular macrocyclic Ru(bda) (bda: 2,2'-bipyridine-6,6'-dicarboxylate) complexes containing three Ru centers by ligand exchange reaction of precursor Ru(bda)$(dmso)_2$ with differently substituted 1,4-bis(pyrid-3-yl) benzene (bpb) axial ligands resulted in efficient water oxidation catalysts (WOCs) as reported during the last years by Würthner and co-workers.[42-43, 215-216] In light of the observed high yield (55%)[42] for the parent trinuclear macrocycle **MC3** without further substituents in the bpb ligand and much lower yields (as low as down to 21%)[216] for derivatives of **MC3** with functionalized axial bpb ligands (Figure 20), the question of dynamic exchange process of pyridyl axial ligands under applied reaction conditions arises. To explore whether the complexes formed under the synthetic

procedure reported previously[42, 216] are kinetic or thermodynamic products, further studies on the ligand exchange process are highly desirable. Since coordination bonds exhibit a bond strength of 60-200 kJ/mol,[235] reversible exchange of axial ligands should be achievable under suitable conditions without breaking the stronger covalent bonds of other parts of the molecule, as typical single covalent bond strength is about 250-500 kJ/mol.[235]

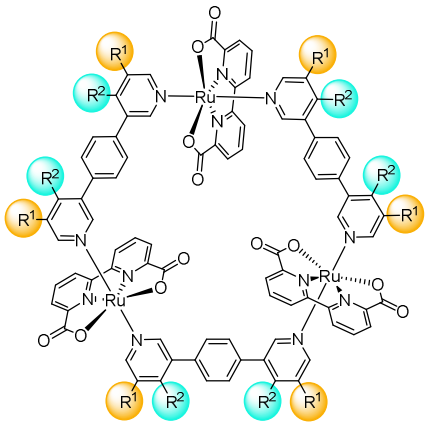

electronics / sterics:

MC3	$R^1 = R^2 = H$	
***m*-R^1-MC3**	R^1 = OMe, Me, F	$R^2 = H$
***p*-R^2-MC3**	R^2 = OMe, Me, F	$R^1 = H$

Figure 20: Overview of derivatives of trinuclear macrocyclic Ru(bda) WOC **MC3** with tuned electronic and steric properties reported by Würthner group.[216]

The concept of dynamic covalent chemistry (DCvC) to enable the synthesis of large supramolecular structures from small building blocks was initially introduced by Jean-Marie Lehn.[236] In this strategy, chemists take advantage of reversible bond formation in imine condensation reaction, boronic ester formation or metathesis reaction.[237] In dynamic reactions, multiple (semi-)stable intermediates and products coexist in the reaction mixture in equilibrium. Due to lower activation barriers, kinetic intermediates and products are present in higher concentrations at the very beginning of the reaction. However, if the reaction follows a thermodynamic pathway, intermediates and kinetic products re-equilibrate with time towards the thermodynamic product since the latter is more stable than the starting components and any kinetically formed intermediate. Theoretical calculations have shown that, if an appropriate ratio of the building blocks is provided, thermodynamically controlled reactions in most cases lead to the formation of highly symmetrical structures.[238] This is the result of reversibility enabling proof-reading, error-checking and self-healing processes in non-favored structures which facilitate the formation of well-defined and ordered supramolecular architectures out of smaller building blocks in one pot reactions with relatively high yields.[239]

For the synthesis of Ru(bda) WOCs, the commonly used precursor Ru(bda)(dmso)$_2$ is obtained by heating $RuCl_2(dmso)_4$ overnight at a moderate temperature of 65 °C in the presence of 2,2'-bipyridine-6,6'-dicarboxylic acid and triethylamine. The base promotes deprotonation of the carboxyl groups and enables a tetradentate κ-N^2O^2 coordination of this ligand in

$Ru(bda)(dmso)_2$. Product formation is highly favored due to the introduction of the chelating bda ligand, which leads to the release of four ligands from the first coordination sphere of $RuCl_2(dmso)_4$ resulting in an entropy gain of $Ru(bda)(dmso)_2$ and four free ligands compared to the initial RuL_6 complex and bda. This chelate effect is also responsible for the observation that even a small deviation from the optimal 1:1 ratio of Ru precursor to bda ligand by an excess of the latter leads to the formation of a catalytically inactive $Ru(bdaH)_2$ complex.[240] The next step in the synthesis of Ru(bda) WOCs containing pyridyl axial ligands is the substitution reaction of dmso in $Ru(bda)(dmso)_2$ by stronger coordinating pyridyl ligands. As described in literature,[241] dmso ligands have a much lower influence on the energy splitting of the d-orbitals (Δ) and are therefore considered to be much weaker ligands than pyridyl ligands.[242] Accordingly, the replacement of dmso ligands by stronger binding pyridyl ligands is a fast exergonic process.

Previous kinetic studies on the substitution of the axial dmso ligands of $Ru(bda)(dmso)_2$ by pyridyl ligands have shown that for this reaction an activation energy of E_a = 81 kJ/mol is required.[240] Due to a strong kinetic trans-effect of dmso,[243] the first exchange process with pyridine ligands is fast. However, due to the thermodynamic trans-influence of pyridine after substitution of one dmso ligand, thermodynamic destabilization of the remaining dmso ligand results in fast substitution of the latter.[244-246] In other words, the gain in LFSE (ligand field stabilization energy) resulting from the σ-donor character of the pyridine ligands is the main driving force for this reaction.[247-248] In contrast, the exchange of pyridine ligands by pyridine-d_5 in a oxo-bridged trinuclear ruthenium complex does not benefit from any energetic gain in LFSE and an activation energy in the range of 100-110 kJ/mol has been reported.[249-250]

To elucidate whether the supramolecular trinuclear Ru(bda) macrocycles obtained by previously reported synthetic procedure[42, 216] are formed by kinetic or thermodynamic pathway and to gain more insight into the ligand exchange process of Ru(bda) complexes, detailed ^{1}H NMR spectroscopic studies have been performed. These investigations indicated that under the previously applied reaction conditions, the supramolecular macrocycles are formed by kinetic pathway. These studies have also shown that the ligand exchange process of mononuclear $Ru(bda)L_2$ complexes follows a dissociative mechanism and thus, at higher temperatures, thermodynamic product formation should be possible.

3.2 Results

3.2.1 Thermodynamic versus kinetic product formation

To elucidate whether the macrocyclization of the reported **MC3** Ru complexes (Figure 20)[42, 216] is governed by kinetic or thermodynamic pathway, the formation of macrocycles under similar conditions as applied previously has been studied by ^{1}H NMR spectroscopy. For this purpose, starting materials Ru(bda)(dmso)$_2$ **23** (1 equiv.) and the respective axial bpb ligand (0.9 equiv.) were suspended in a NMR tube in CD_2Cl_2/MeOD (5:1) and ethylene carbonate **24** was added as an internal standard to quantify the formed products. The reaction scheme is exemplarily shown for the macrocycle ***p*-F-MC3** (Figure 21). NMR studies were performed in CD_2Cl_2/MeOD at 55 °C, instead of in a solvent mixture of chloroform and methanol at 60 °C as previously used in synthesis,[216] to avoid residual signal of deuterated chloroform in the aromatic region where significant signals of the axial ligands also appear and thus hampers reliable product analysis.

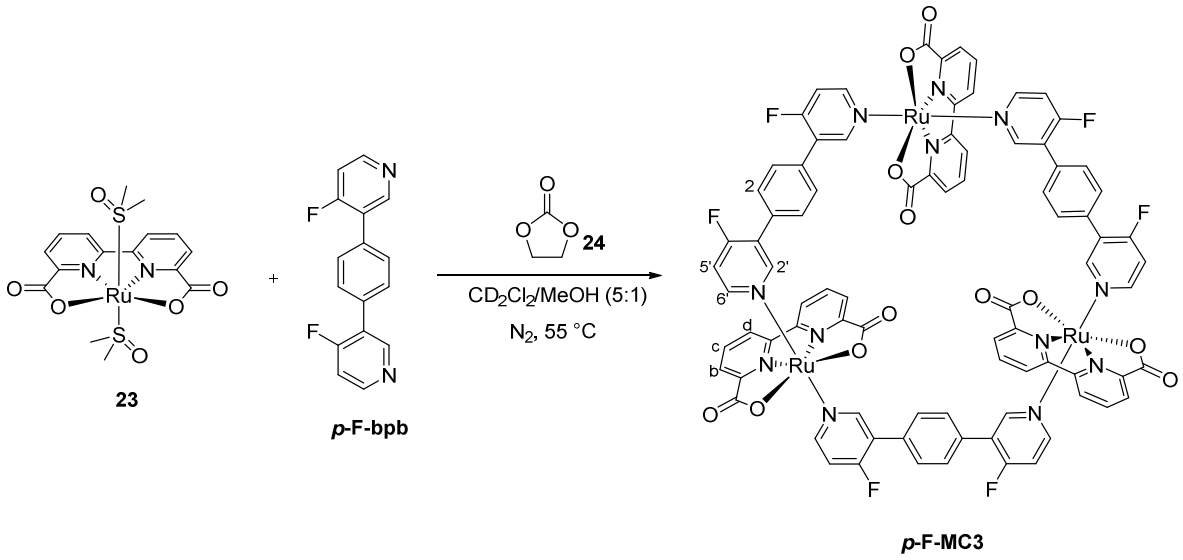

Figure 21: Formation of trinuclear macrocycle ***p*-F-MC3** as an example monitored by ^{1}H NMR spectroscopy.

One NMR spectrum was recorded at the very beginning before putting the sealed tube in an oil bath at 55 °C. After defined periods of time, the tube was removed from the oil bath and the reaction was terminated by immediately cooling the reaction mixture to 0 °C with an ice bath. NMR spectra were then recorded at room temperature and the tube was brought back to reaction temperature to continue the reaction. Time-dependent changes in the ^{1}H NMR spectra for the formation of ***p*-F-MC3** as an example are displayed in Figure 22.

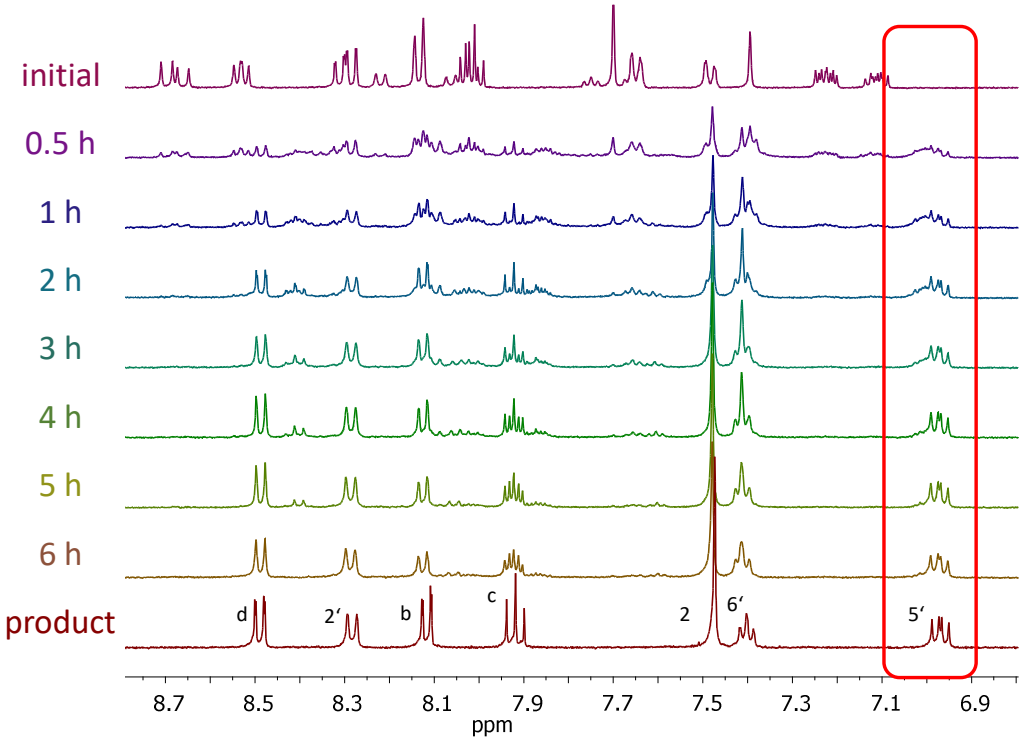

Figure 22: Time-dependent ^{1}H NMR spectra (400 MHz) following the formation of ***p*-F-MC3** in CD_2Cl_2/MeOD (5:1) at 55 °C. Reaction was performed in an NMR tube in an oil bath at 55 °C, NMR spectra were recorded at room temperature. Signals highlighted in red square (proton 5', see Figure 21) were used to analyze product formation. The inclusion of oligomeric fragments can not be fully excluded.

A comparison of ^{1}H NMR spectra during the reaction course with that of the isolated product ***p*-F-MC3** (bottom spectrum) clearly indicates the formation of the trinuclear macrocycle. Product signals could be observed already after 30 min and a rapid increase was observed up to about 4 h while the reaction was completed after about 6 h since no more product was generated on prolonged time up to 18 h (Figure 23). These observations indicate a kinetic control of the reaction. The product formation was analyzed by integration of the product signals at around 7 ppm in reference to the signal of the internal standard.

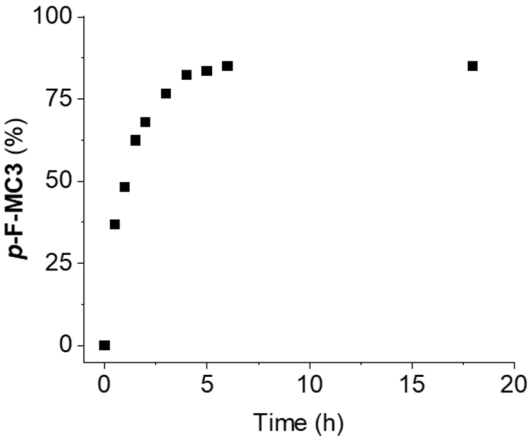

Figure 23: Time-dependent formation of ***p*-F-MC3** analyzed by ^{1}H NMR spectroscopy using ethylene carbonate **24** as internal standard. ^{1}H NMR spectra (400 MHz) were recorded at rt in CD_2Cl_2/MeOD (5:1). Signal 5' highlighted in the red square in Figure 22 was used for evaluation.

The formation of side products such as polymeric chains cannot be detected by NMR due to the low solubility of such large products. Apparently, the applied reaction temperature of 55 °C is not sufficient to convert such possibly precipitated polymers to macrocyclic products. Macrocyclization reactions of other **MC3** derivatives derivatives have also been studied under identical conditions as applied for ***p*-F-MC3** (Figures S1 - S7) and the results are summarized in Table 1.

Table 1: Comparison of product formation for **MC3** derivatives.[a]

MC3 derivative	maximal product yield[b] after 6 h according to NMR analysis	maximal isolated product yield[216] after a reaction time of 16.5 h
***m*-F-MC3**	94% (after 3 h)	38%
***p*-F-MC3**	85%	55%
***m*-Me-MC3**	68%	29%
***p*-OMe-MC3**	62%	32%
MC3	61%	55%[42] (after 14 h)
***m*-OMe-MC3**	60%	36%
***p*-Me-MC3**	26%	21%

[a] The product formation was analyzed by comparison to an internal standard by recording ^{1}H NMR spectra at rt (400 MHz) after certain time intervals during the reaction in an NMR tube.
[b] The yield is referred to the amount of axial bpb ligand used in the reaction.

Although for both *meta*- and *para*-fluorinated macrocycles highest amounts of products are formed, no clear trend depending on the substituents of axial ligands is observed as isolated yields of Me- and MeO-substituted derivatives are in the same range as of the parent compound **MC3**, except for ***p*-Me-MC3** with the lowest yield of 26%. Indeed, for the latter macrocycle, an isolated yield of 21% was reported, being the lowest in the series.[216]

The time-dependent NMR studies under similar reaction conditions as previously applied in synthetic scale reactions indicated that the **MC3** macrocycles are formed under kinetic control. Detailed studies on the ligand exchange mechanism to explore the conditions for thermodynamic equilibrium, which may enable the synthesis of larger supramolecular structures than cyclic trimers, have been performed with a series of monomeric Ru(bda)L_2 model systems.

3.2.2 Ligand Exchange in Ru(bda)L_2 complexes

To gain insight into the ligand exchange mechanism of Ru(bda) complexes and elucidate the influence of sterics and excess of the ligand on the exchange process, a series of mononuclear Ru(bda)L_2 model complexes (Figure 24) containing different axial ligands were synthesized and the exchange process has been investigated by ^{1}H NMR spectroscopy.

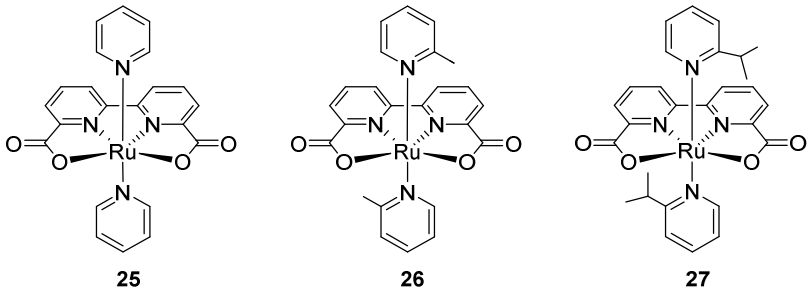

Figure 24: Ru(bda)L_2 model compounds for the investigation of axial ligand exchange process.

For this purpose, time-dependent ^{1}H NMR spectra of the complexes in deuterated pyridine (py-d_5) were monitored at variable temperatures. In all cases, no ligand exchange was observed at room temperature upon stirring the respective complex in py-d_5 for one week. The ligand exchange process of Ru(bda)(2-picoline)$_2$ complex **26** dissolved in py-d_5 is shown in Figure 25 as an example.

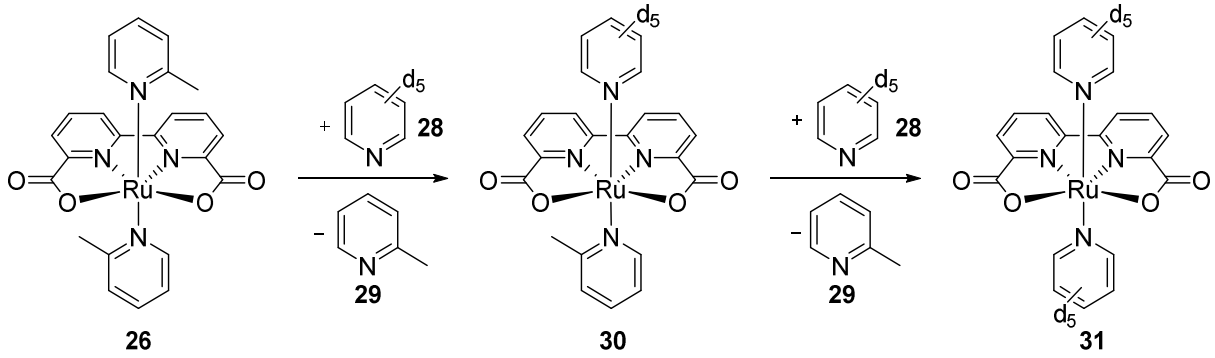

Figure 25: Ligand exchange process of Ru(bda)(2-picoline)$_2$ **26** in pyridine-d_5 monitored by ^{1}H NMR spectroscopy. Exchange of 2-picoline **29** in **26** by pyridine-d_5 solvent molecules was monitored.

At room temperature, no exchange of 2-picoline ligand was observed and the complex remained stable even after several days. However, upon increasing the temperature of NMR measurements, the ligand exchange reaction was initiated (Figure 26). The time-dependent ligand exchange process was monitored in intervals of 15 or 30 min for over 12 h at 85 °C and 104 °C. After the NMR tube was brought into the spectrometer, some minutes were needed for equilibration of the temperature and the magnetic field before a first spectrum could be measured after 15 min. A second NMR spectrum was recorded after another 15 min (30 min

after being exposed to the set temperature in the spectrometer) and further spectra were recorded every 30 min for 12 h (Figure 26).

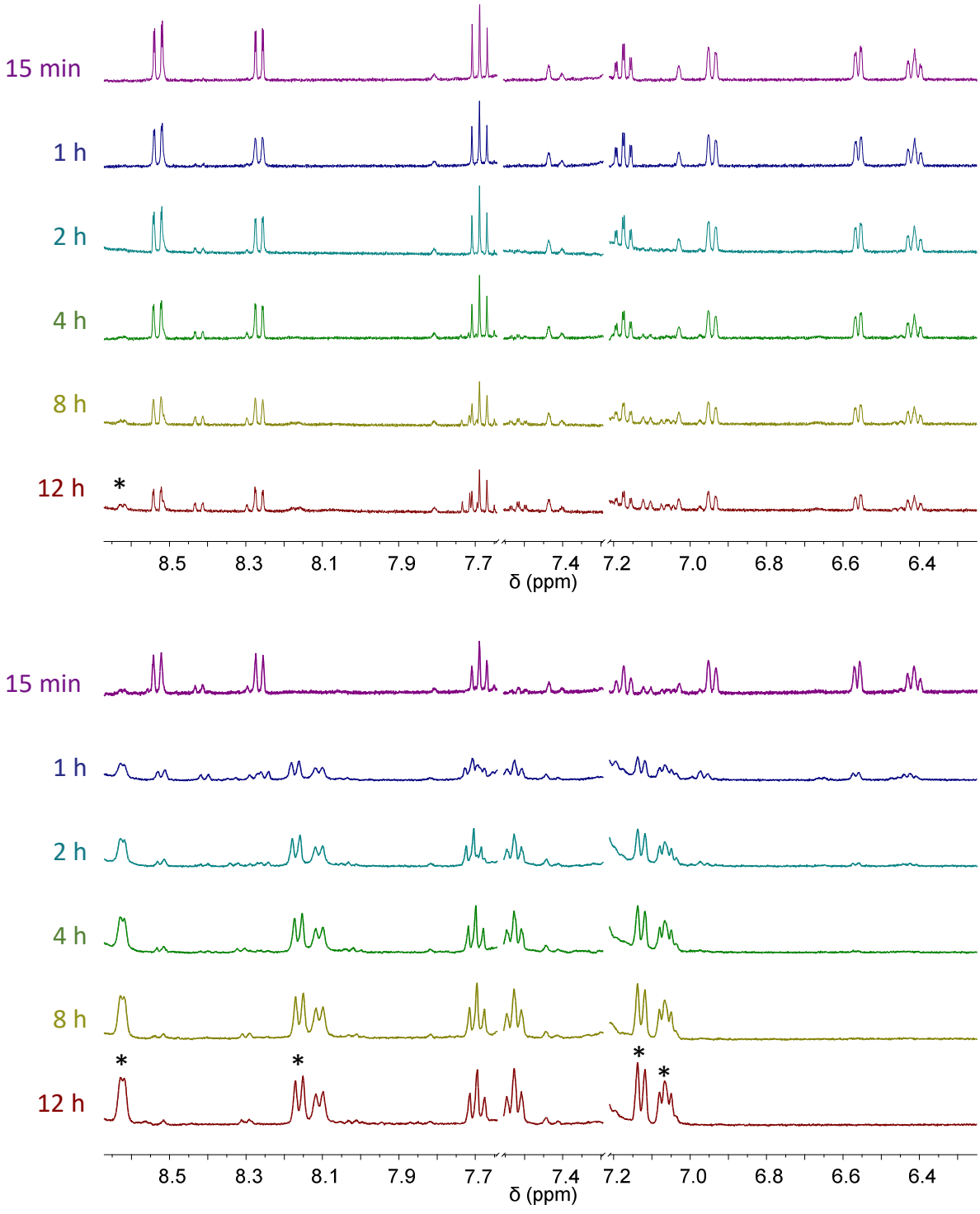

Figure 26: Aromatic region of time-dependent ^{1}H NMR spectra of Ru(bda)(2-picoline)$_2$ **26** in py-d$_5$ at a) 85 °C and b) 104 °C. Signals of the free ligand 2-picoline **29** are marked with (*) and residual solvent signals of deuterated pyridine are not shown for clarity.

^{1}H NMR analysis at 85 °C (Figure 26a) shows a rather slow ligand exchange process at this temperature, as the signals between 6.4 and 6.6 ppm, which belong to the initial complex **26**,

decreased only slightly in intensity even after ca. 8 h, while new rather weak signals emerged between 7.0 and 7.2 ppm as well as at 8.1 and 8.6 ppm, that belong to the free 2-picoline ligand **29**. After 12 h, the signals of free ligand **29** increased appreciably indicating considerable ligand exchange. In contrast, rapid significant changes in the ^{1}H NMR spectra were observed at 104 °C as the signals between 6.4 and 6.6 ppm vanished almost completely only after 2 h and the emerged new signals can be clearly assigned to Ru(bda)(py-d_5)$_2$ complex **31** and free 2-picoline ligand **29** (Figure 26b).

For describing kinetics and activation energies in ligand exchange reactions, which are dependent on the applied temperatures, the empirical Arrhenius equation (equation 6) can be used.[251-252]

$$k = A \cdot \exp\left(\frac{-E_a}{R \cdot T}\right) \qquad \text{(eq. 6)}$$

Here, k is the rate constant, A is a pre-exponential factor, E_a is the activation energy for the reaction, R is the universal gas constant and T the temperature at which the reaction is monitored.

Taking the natural logarithm, equation 6 can be transformed to equation 7.

$$\ln(k) = \ln(A) - \frac{E_a}{R \cdot T} \qquad \text{(eq. 7)}$$

By considering two different temperatures (T_1 and T_2), equation 7 can be expressed as shown in equation 8 and the activation energy can be determined according to equation 9, where k_1 and k_2 are the rate constants at the two different temperatures.

$$\ln\left(\frac{k_2}{k_1}\right) = -\frac{E_a}{R} \cdot \left(\frac{1}{T_2} - \frac{1}{T_1}\right) \qquad \text{(eq. 8)}$$

$$E_a = R \cdot \ln\left(\frac{k_2}{k_1}\right) \cdot \frac{T_1 \cdot T_2}{T_2 - T_1} \qquad \text{(eq. 9)}$$

The reaction rate of the ligand exchange process can be determined from the plot of time-dependent changes of the concentration of the initial species at each temperature (Figure 27a). To obtain kinetic data, signals of the starting complex at 6.4 ppm (belong to the 2-picoline ligand of Ru(bda)(2-picoline)$_2$) were integrated. Notably, integration of the methyl signal of the picoline ligand could not be used due to the overlap with the signal of residual water in py-d_5.

The respective reaction rates can be obtained from the slope of the plot of the natural logarithm of the concentration versus the time according to equation 9 (Figure 27b).

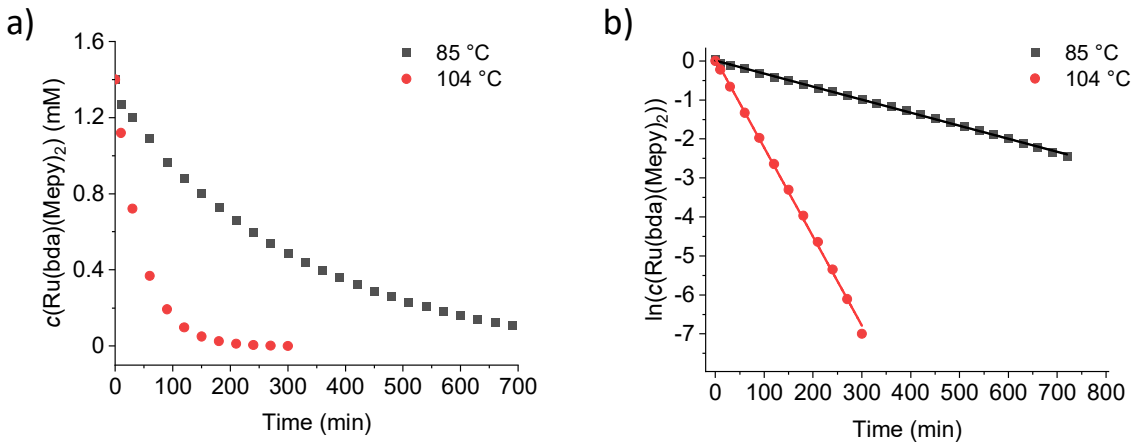

Figure 27: a) Concentration dependent decay of Ru(bda)(2-picoline)$_2$ **26** upon exchange of 2-picoline ligand in py-d$_5$ at 85 °C and 104 °C. Since no initial spectra at the reaction temperature could be obtained for the first minute, the obtained curve was extrapolated and normalized to the initial concentration. b) Arrhenius plot with linear regression curves for the determination of individual reaction rates (k_1, k_2) and activation energy (E_a).

The temperature-dependency of the ligand exchange rates can be clearly identified in Figure 27a as the concentration of the initial complex decays much faster at 104 °C (red dots) than at 85 °C (black squares). Rate constants at these two temperatures (k_1, k_2) were obtained by plotting the natural logarithm of the concentration of the starting compound versus the time (equation 9) and analyzing the slope of the calculated linear regression. Rate constants of k_1 = 2.76 x 10^{-3} min^{-1} and k_2 = 22.8 x 10^{-3} min^{-1} at T_1 = 85 °C and T_2 = 104 °C, respectively, are obtained from this analysis leading to an activation energy of E_a = 109 kJ/mol for Ru(bda)(2-picoline)$_2$ **26**. Previously, a much higher activation energy of E_a = 124 kJ/mol was reported for the exchange of py-d$_5$ in Ru(bda)(py)$_2$ **25** in this solvent.[240] This implies a significant steric effect by methyl group of 2-picoline axial ligands on the exchange process in Ru(bda)(2-picoline)$_2$. To further confirm that bulkier ligands indeed accelerate ligand exchange, NMR analysis under similar conditions was performed with Ru(bda)(2-isopropylpyridine)$_2$ **27** that contains larger substituent at pyridine than complex **26** (Figures S8 – S10). Notably, a much faster ligand exchange process with an activation energy of E_a = 92 kJ/mol was observed for this complex (Table 2). Further ligand exchange experiments were performed with Ru(bda)(2-picoline)$_2$ in the presence of defined amounts of py-d$_5$ in deuterated DMF to elucidate the concentration effect of incoming ligand py-d$_5$ on ligand exchange process (Figures S11 – S14). As shown in Figure 28 and Table 2, very similar results were obtained with only 5 and 10 equivalents of py-d$_5$ as those observed in py-d$_5$ as solvent.

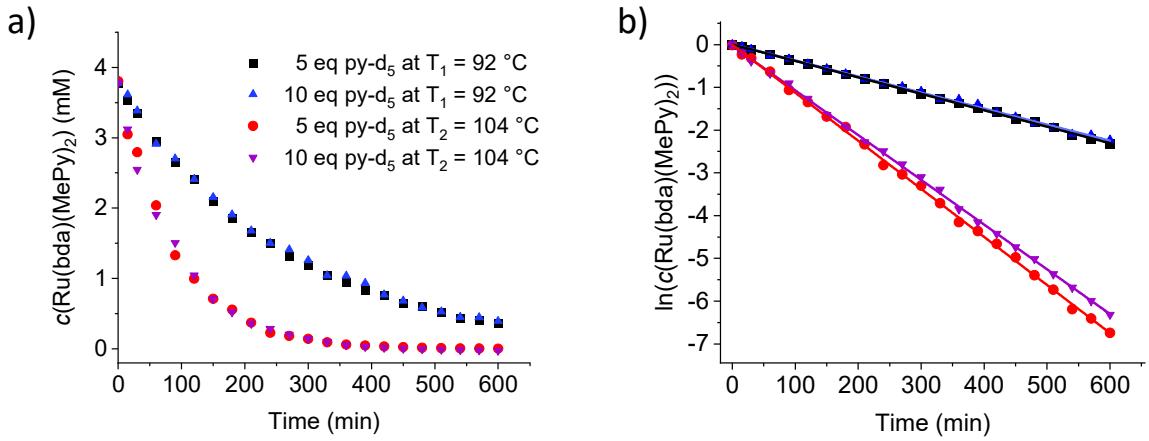

Figure 28: a) Concentration dependent decay of Ru(bda)(2-picoline)$_2$ **26** in reactions with 5 and 10 equivalents of py-d$_5$ in DMF-d$_7$ at 92 °C and 104 °C. Since no initial spectra at the reaction temperature could be obtained for the first minute, the obtained curve was extrapolated and normalized to the initial concentration. b) Determination of the individual reaction rates k_1 and k_2 at two temperatures and the activation energy (E_a).

Rate constants at 92 °C of k_1 = 3.85 x 10^{-3} min^{-1} and 3.75 x 10^{-3} min^{-1} were obtained for 5 and 10 equivalents of py-d$_5$, respectively, while at 104 °C, a faster exchange with rates of k_2 = 11.24 x 10^{-3} min^{-1} and 10.53 x 10^{-3} min^{-1} was observed. The activation energies summarized in Table 2 clearly show that the ligand exchange process in complexes with sterically bulky axial ligands (**26** and **27**) is more favored than in reference complex Ru(bda)(py)$_2$ **25** and the exchange process is not dependent on the amount of incoming ligand py-d$_5$.

Table 2: Summary of ligand exchange processes of Ru(bda)L$_2$ complexes studied by ^{1}H NMR and the respective activation energies.[a]

Starting complex	Exchange ligand	Solvent	E_a (kJ/mol)[b]
Ru(bda)(py)$_2$ **25**	py-d$_5$	py-d$_5$	124 ± 4[240]
Ru(bda)(2-picoline)$_2$ **26**	py-d$_5$	py-d$_5$	109 ± 4
Ru(bda)(*i*Prpy)$_2$ **27**	py-d$_5$	py-d$_5$	92 ± 5
Ru(bda)(2-picoline)$_2$ **26**	py-d$_5$ (5 equiv.)	DMF-d$_7$	112 ± 3
Ru(bda)(2-picoline)$_2$ **26**	py-d$_5$ (10 equiv.)	DMF-d$_7$	108 ± 4

[a] Determined by ^{1}H NMR studies at two different temperatures and different concentrations of exchanging ligands (py-d$_5$).
[b] Standard deviations were determined from the linear fit of ln[WOC] vs time plot.

3.3 Discussion

The formation of **MC3** macrocycles by ligand exchange process has been studied by monitoring the reaction progress by ^{1}H NMR spectroscopy in a mixture of CD_2Cl_2/MeOD to

avoid residual signals of deuterated chloroform in the aromatic region which impede reliable product analysis since significant signals of the axial ligand also appear in this region (see Figure 22). In previously reported synthesis procedure for **MC3** macrocycles, $CHCl_3$ and MeOH were used as solvents and the reaction was conducted at 60 °C.[42, 215-216] Due to the lower boiling point of dichloromethane compared to chloroform, the NMR experiments were carried out at a temperature of 55 °C. These studies have shown that the maximal amount of trinuclear macrocycle products were formed after 6 h and no further increase in product could be detected even after running the experiment for additional 12 h. The latter observation implies that oligomeric chains possibly formed as side products could not be further transformed into the desired product even after very long reaction times. These results indicate that formation of macrocycles under applied reaction conditions is not taking place in a thermodynamic equilibrium. Thus, obtained **MC3** macrocycles are the result of kinetic product formation. To explore the conditions for thermodynamic equilibrium with dynamic ligand exchange in Ru(bda)L_2 complexes and get more insight into the ligand exchange mechanism, ^{1}H NMR experiments have been performed with mononuclear model compounds **26** and **27** (see Figure 24) bearing pyridyl axial ligands with different substituents and compared to previously reported with Ru(bda)$(py)_2$ **25**.[240] No axial ligand exchange was observed for these complexes in deutero-pyridine (py-d_5) at room temperature even after stirring for 7 days. However, at higher temperatures, exchange of the pyridine ligands with py-d_5 could be clearly observed as the NMR spectra changed significantly. ^{1}H NMR experiments at two different temperatures allowed the determination of activation energy E_a of the exchange process by applying the Arrhenius equation.[251-252] For Ru(bda)$(py)_2$, an activation energy of E_a = 124 kJ/mol for the ligand exchange in py-d_5 solvent was reported based on data acquired at 92 and 104 °C.[240] Interestingly, the ligand exchange in Ru(bda)(2-picoline)$_2$, which contains sterically bulky picoline axial ligands, with py-d_5 is much faster than in Ru(bda)$(py)_2$. For the former, a full conversion to Ru(bda)(py-d_5)$_2$ was observed after 4 h at 104 °C while the conversion of Ru(bda)$(py)_2$ was not completed even after 12 h at this temperature. Indeed, an activation energy of E_a = 109 kJ/mol was obtained for Ru(bda)(2-picoline)$_2$ based on NMR data at 85 and 104 °C. When the bulkiness of the substituent in the *ortho*-position of the pyridy axial ligand is increased by replacing 2-picoline with 2-isopropylpyridine in Ru(bda)(*i*Prpy)$_2$ **27**, a much faster ligand exchange was observed. In this case, reaction temperatures had to be decreased to 71 °C and 81 °C because otherwise the ligand exchange is too fast to determine the activation energy. A remarkably lower activation energy of E_a = 92 kJ/mol was observed for this complex.

Two major ligand exchange mechanisms have been discussed in literature for octahedral complexes (Figure 29).[253-254] In a dissociative mechanism, the first step involving the release of one ligand from the first coordination sphere in a ML_6 complex is usually the rate determining step. The resulting five-coordinated intermediate with a trigonal bipyramidal or square

pyramidal structure is less stable and thus the coordination of a free exchanging ligand X to regenerate the six-coordinated octahedral complex will occur much faster. Therefore, the overall substitution reaction in a dissociative mechanism is only dependent on the concentration and nature of the initial complex, while the incoming ligand will have no influence on the rate of the process.

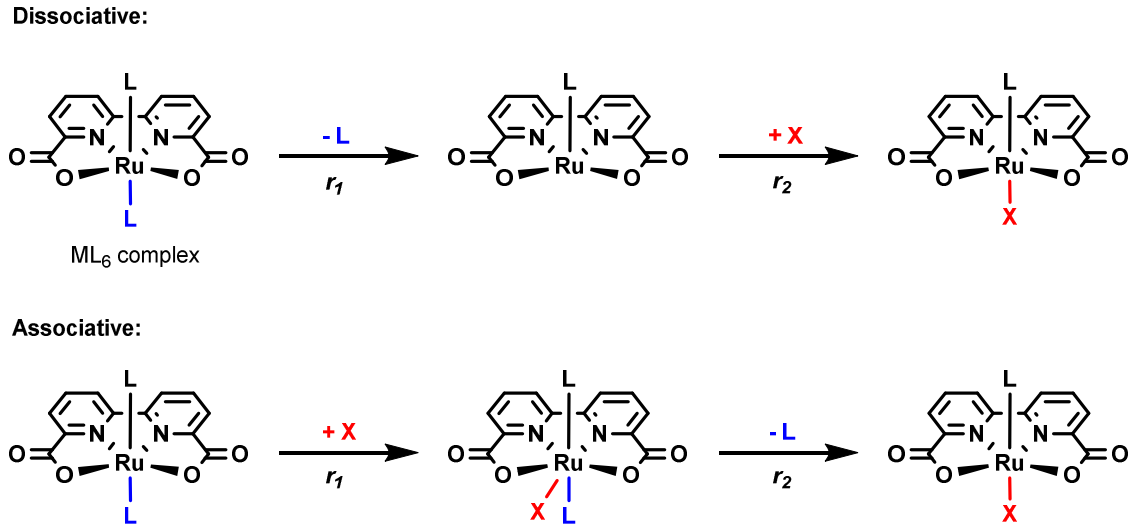

Figure 29: Schemes of dissociative and associative ligand exchange mechanism for octahedral Ru(bda) complexes.

Assuming that $r_2 << r_1$, the rate of the dissociative ligand exchange reaction can be described as $v = r_1 [ML_6]$.[255] In contrast, in an associative mechanism the first step, which is mostly rate-determining, comprises the addition of a free substituting ligand X to the ML_6 complex to form the respective ML_6X complex. Since the subsequent dissociation of initial ligand L is fast, the rate can be described as $v = r_1 [ML_6][X]$. In the presence of a large excess of ligand X, the kinetics of the associative ligand exchange change to a pseudo-first order mechanism and is therefore no longer distinguishable from those of the dissociative mechanism. However, individual features of the initial ligands L such as the presence of sterically bulky groups can be helpful to differentiate between both mechanisms, since sterically encumbered groups reduce the possibility for seven-coordination in an associative fashion and rather favor the dissociative mechanism.[256] Notably, a concerted interchange mechanism with no observable kinetic intermediates is also possible and often reported for solvent exchange reactions.[254] For example, ligand substitution in a $Ru(H_2O)_6^{2+}$ complex was found to proceed by a slow interchange-dissociative type mechanism.[257-260]

As mentioned above, bulkier axial ligands in initial complex favor the ligand exchange process in a dissociative mechanism. Since for the initial complexes **26** and **27** with bulkier axial ligands significantly lower activation energies compared to that of reference complex **25** were

observed, a dissociative mechanism is proposed for these complexes. To verify that the ligand exchange in Ru(bda)L_2 complexes is independent of the amount of incoming ligand py-d_5 which would also support a dissociative mechanism, experiments were also performed in DMF-d_7 in presence of 5 or 10 equivalents of py-d_5 with Ru(bda)(2-picoline)$_2$. These studies revealed similar activation energies as observed with a large excess of py-d_5 used as solvent. As discussed above, the amount of incoming ligand would affect the kinetics in associative mechanism, but not in dissociative one. The fact that very similar activation energies are observed for ligand exchange in Ru(bda)(2-picoline)$_2$ in the presence of 5 and 10 equivalents of py-d_5 as well as in pure py-d_5 (see Table 2) excludes an associative ligand exchange mechanism in this complex. Faster ligand exchange in the case of bulkier ligands in the initial compounds as revealed by higher rate constants also support a dissociative ligand exchange mechanism for the investigated Ru(bda)L_2 complexes.

3.4 Conclusions

Insights into the mechanism of ligand exchange is essential for designing large multinuclear matallosupramolecular structures. ^{1}H NMR spectroscopic investigations on the synthetic process of trinuclear Ru(bda) macrocycles revealed that the product formation under applied conditions follows a kinetic pathway. To assess the conditions of thermodynamic equilibrium for the synthesis of larger structures, studies with mononuclear model compounds were performed. The independency of the activation energy E_a on the concentration of the incoming ligand as well as the faster ligand exchange observed for complexes with bulky axial ligands demonstrate the presence of a dissociative ligand exchange mechanism in Ru(bda)L_2 complexes. The detailed investigations revealed that the ligand exchange process is rather slow at moderate temperatures of 85 °C, however, a fast ligand exchange could be initiated at a higher temperature of 104 °C. The observed independency of the kinetics on the amount of incoming ligand should be beneficial for the formation of thermodynamic products since no excess of the incoming ligand is necessary for fast ligand exchange process in dissociative mechanism. Based on the results of ligand exchange studies it can be concluded that a temperature of around 100 °C may facilitate a thermodynamic equilibrium between all species present in the reaction of Ru(bda)(dmso)$_2$ with bipyridyl chelating ligands for the synthesis of supramolecular macrocycles to enable the formation of thermodynamically most stable products.

Chapter 4

—

Synthesis of di- and tetranuclear Ru(bda) macrocycles and their catalytic activities in water oxidation

Summary: Highly efficient catalysts are indispensable for the generation of renewable fuels by water oxidation. A comparative study on chemical and photochemical water oxidation with a homologous series of di-, tri-, and tetranuclear macrocyclic Ru(bda) catalysts is reported here. These investigations have shown that the catalytic activities are dependent on the size of the macrocycle with highest efficiencies for the largest tetranuclear complex. Thus, a deeper understanding of structure-activity relationship for this class of water oxidation catalysts could be gained.

4.1 Introduction

Since the discovery of Ru(bda)$(pic)_2$ (bda: 2,2'-bipyridine-6,6'-dicarboxylate, pic: picoline) as a highly efficient water oxidation catalyst by Sun and co-workers in 2009, several studies have been reported on diverse Ru(bda)-based catalysts bearing modified axial and equatorial ligands.[40-41] In the last years, oligomeric and polymeric as well as macrocyclic structures have been obtained by assembly of multiple Ru(bda) units and axial ligands.[219, 240, 261-262] A family of supramolecular macrocycles containing three Ru(bda) centers have recently been developed by Würthner and co-workers and reported as highly efficient water oxidation catalysts (WOCs) (Figure 30).[42-44, 215-216] Notably, the reduced flexibility of the trinuclear macrocycle **MC3** (Figure 30) resulted in an enhanced stability as well as high TOF and TON

values in chemical water oxidation, comparable to those of the OEC of PS II in nature.[72] Detailed mechanistic studies confirmed a WNA mechanism for the water oxidation for the **MC3** macrocycle, in contrast to mononuclear complexes such as Ru(bda)(pic)$_2$ that operate by binuclear I2M mechanism.[41] The unequivocally confirmed WNA mechanism of macrocyclic Ru(bda) complexes makes them particularly interesting for applications under high dilution conditions and upon anchoring on surfaces. Based on theoretical calculations, a preorganized hydrogen-bonded water network in the macrocyclic cavity of **MC3** was proposed to explain its high catalytic activity in water oxidation.[43] Very recently, experimental evidence for the formation of such water networks has been obtained by X-ray crystal structure analysis and X-ray absorption studies performed on functionalized **MC3** derivatives (see Figure 20, *Chapter 3*).[216] Accordingly, efficient water oxidation by **MC3** is most likely the result of cooperative proton abstraction during catalysis which leads to significant reduction of activation barriers for the key proton-coupled electron transfer processes.[42, 216]

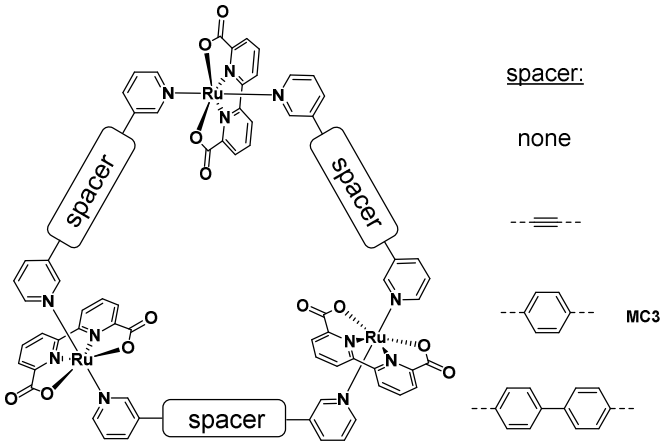

Figure 30: Overview of size variations by introduction of different spacer units in trinuclear macrocyclic Ru(bda) WOCs reported by Würthner group.[43]

Previous studies on the effect of spacer length of bipyridyl axial ligands on the size of resulting macrocycles (Figure 30) and their catalytic activities have shown that the optimum size and highest catalytic efficiency can be obtained for a medium size macrocycle with a benzene spacer (**MC3**) in the axial ligands.[43] Additionally, water solubility of **MC3** macrocycles could be significantly increased by introducing solubilizing oligoethylene glycol (OEG) chains and amine groups in axial ligands and comparable activities as observed for the parent **MC3** have been obtained with water soluble derivatives in chemically driven catalysis studies.[215]

With Ru(bda) as a unique functional unit, the question raised in this thesis was how the number of active centers within a macrocycle affects its catalytic efficiency. Therefore, hitherto unknown di- and tetranuclear Ru(bda) macrocycles having bipyridyl benzyl axial ligands should be constructed by using non-linear derivatives of the bridging ligands of **MC3** and the catalytic activities of the homologeous series of di-, tri-, and tetranuclear complexes should be studied

in a comparative manner. OEG chains should be introduced in macrocycles to enhance solubility, especially in the larger tetranuclear structure. Although the catalytic performance of **OEG-MC3** (Figure 32) has previously been studied in chemical water oxidation,[215] its photocatalytic activities remained unexplored and thus should be investigated in this work.

Detailed studies have shown that the catalytic efficiencies of the present series of macrocycles in chemical as well as photochemical water oxidation increases with the increasing size of the macrocycle with the highest TOF value of 42 s^{-1} in chemical and 23 s^{-1} in photochemical experiments for the tetranuclear WOC **OEG-MC4**. Thus, for the first time, a structure-activity relationship has been established for this class of Ru(bda) WOCs.

4.2 Results

4.2.1 Synthesis of ligands and multinuclear cyclic Ru(bda) complexes

For the synthesis of macrocyclic Ru(bda) WOCs with different size, axial bidentate ligands **L2** and **L4** having non-linear arrangements of terminal pyridyl units with *meta* and *para* connectivity, respectively, at a benzene center, were synthesized (Figure 31). As reported for large matallosupramolecular structures, solubility decreases significantly with increasing the size of the metallocycle.[215] Therefore, solubilizing OEG chains were introduced to the axial ligands to facilitate the formation of the desired product.

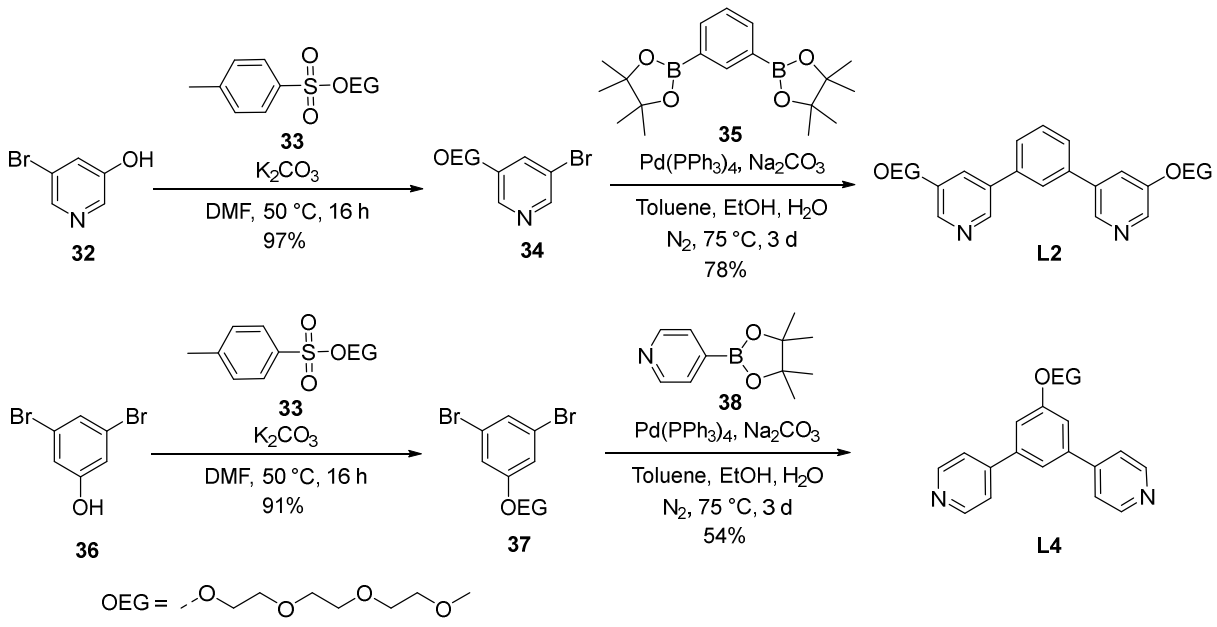

Figure 31: Synthesis of ligands **L2** and **L4**.

Ligand **L2** was synthesized by the reaction of commercially available 3-bromo-5-hydroxypyridine **32** with OEG-tosylate **33** by a procedure adapted from literature[263] and subsequent Suzuki-Miyaura cross-coupling reaction of OEG-functionalized 3-bromopyridine **34** with 1,3-benzenediboronic acid bis(pinacol) ester **35**. Ligand **L4** was prepared by the reaction of OEG-tosylate **33** with 1,3-dibromphenol **36** to afford **37**, which was then coupled with commercially available 4-pyridineboronic acid pinacol ester **38**.

In previously established procedure for the synthesis of **MC3** and its derivatives,[42-43, 215-216] respective axial 1,4-bis(pyrid-3-yl) benzene (bpb) ligand and Ru(bda)(dmso)$_2$ precursor **23** were stirred under reflux (ca. 60 °C) in a $CHCl_3$/MeOH (5:1) mixture for 16 h as shown in Figure 32 for **OEG-MC3**.[215] However, in the reactions of **L2** and **L4** with precursor **23** under these standard conditions only mixtures of small oligomeric open chain products could be obtained. Therefore, these reaction conditions for kinetic product formation (see previous *Chapter 3.1*) should be changed for the formation of thermodynamically controlled products.

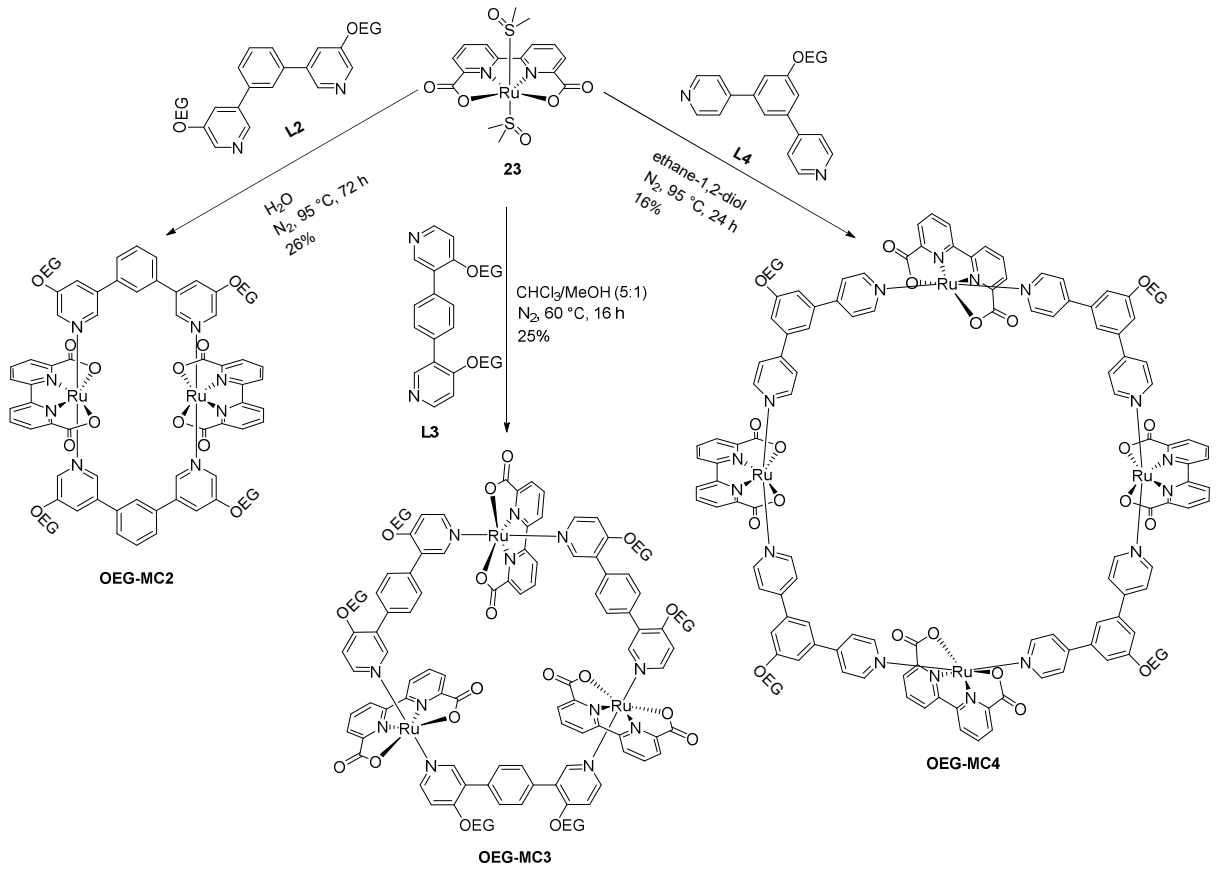

Figure 32: Synthesis of literature-known trimeric macrocycle **OEG-MC3**[215] and new dimeric and tetrameric macrocycles **OEG-MC2** and **OEG-MC4**.

Indeed, the reaction of Ru(bda)(dmso)$_2$ **1** with pyridyl *meta*-substituted axial ligand **L2** in a 1:1 ratio under nitrogen atmosphere in water at a higher temperature of 95 °C for 3 days afforded

the dimeric Ru(bda) macrocycle **OEG-MC2** (Figure 32). Likewise, the assembly of *para*-substituted **L4** and Ru(bda)(dmso)$_2$ **23** under nitrogen atmosphere in ethylene glycol at 95 °C for 24 h led to the formation of larger tetranuclear macrocycle **OEG-MC4**. Both macrocycles are assumed to be formed under thermodynamic control since a sufficiently fast exchange of the axial ligand at temperatures of around 100 °C had been confirmed in previous studies (see *Chapter 3.1*). The separation of macrocyclic products from insoluble larger polymeric chains was achieved by column chromatography over Al_2O_3 and smaller oligomeric open chain side products could be removed by several size exclusion chromatography cycles over BioBeads SX1 or SX3 and GPC. Pure **OEG-MC2** and **OEG-MC4** were obtained in acceptable isolated yields of 26% and 16%, respectively, for such macrocyclizations. Detailed characterization of the new ligands and macrocycles by NMR spectroscopy, mass spectrometry and CV analysis can be found in *Chapter 9* (Figures S15 – S39).

4.2.2 Characterization of di- and tetranuclear Ru(bda) WOCs

The new Ru(bda) macrocycles were first characterized by ^{1}H NMR spectroscopy. Traces of paramagnetic and NMR silent Ru^{3+} species were reduced to Ru^{2+} by addition of small amounts of ascorbic acid to NMR tube to obtain high resolution spectra as exemplarily shown for **OEG-MC4** (Figure 33).

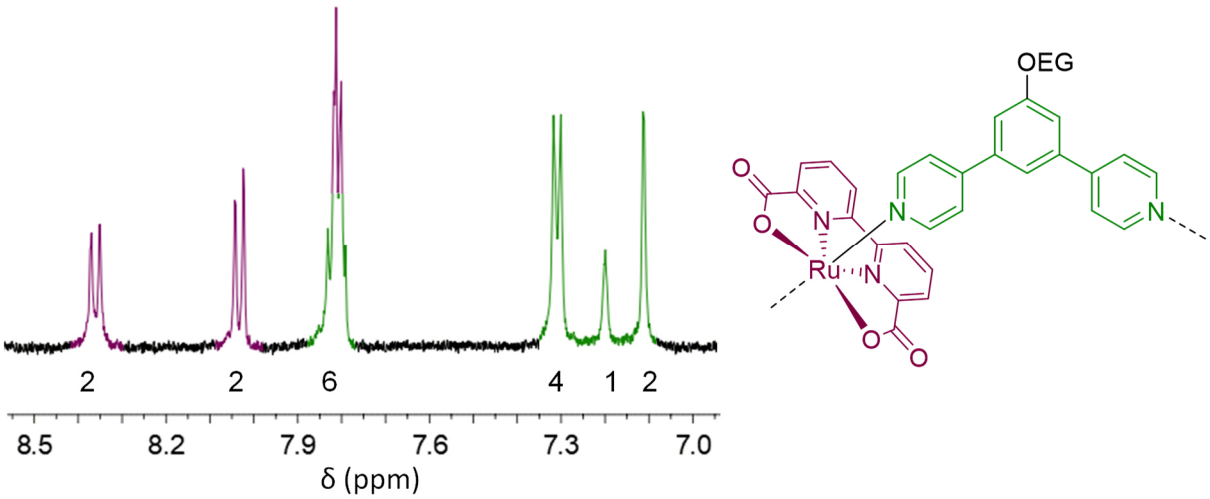

Figure 33: Aromatic region of ^{1}H NMR spectrum of tetrameric **OEG-MC4** in CD_2Cl_2/MeOD/CF_3CD_2OD 5:3:2 (400 MHz, rt), along with the structure of a monomeric repeat unit of this macrocycle. Numbers given under the signals correlate to the numbers of protons associated with each signal as determined by integration of the respective signal area. Colors of the signals correspond to bda (purple) and bpb (green) as highlighted in the structure.

One single set of nicely resolved signals for the aromatic protons of the **L4** (shown in green) and equatorial bda ligands (shown in purple) of the tetrameric macrocycle are observed, thus excluding the presence of open chain side products. The fact that the pyridine protons of the

axial ligands show only one set of signals clearly confirms the high symmetry and therefore cyclic structure of **OEG-MC4**. In case of linear oligomeric structures, multiple signals would arise and additional signals of the non-coordinated terminal pyridine rings or terminal Ru(bda) protons were to expect. The absence of such additional signals in the proton NMR spectra of **OEG-MC2** as well as **OEG-MC4** confirms the formation of macrocyclic structures (Figure S17, Figure S21). The smaller macrocycle **OEG-MC2** could be further characterized by high-resolution mass spectrometry. A mass peak was observed for $[M+Na]^+$ with *m/z* = 1823.4219 (calculated 1823.4204), confirming the dimeric structure. Unfortunately, due to fragmentation of **OEG-MC4** it was not possible to obtain a clean mass spectrum for the tetrameric macrocycle. Upon deconvolution of signals, the product peak could be detected as a weak signal, however, the intensity was not sufficient to enable analysis of the isotopic pattern.

Analytical GPC chromatograms of the purified products demonstrate the successful separation of macrocycles from smaller oligomeric side products as well as larger polymers and clearly reflect the different size of the new macrocycles compared to the literature-known WOCs **MC3** and **OEG-MC3** (Figure 34). For GPC analysis, purified samples of di- and tetrameric OEG-Ru(bda) WOCs were dissolved in a $CHCl_3$/MeOH (9:1) mixture and injected on an analytical GPC system with a SDV column (SDV: styrol-divinylbenzol-copolymer network). A comparison of the chromatograms of **MC3** and **OEG-MC3** reveals a significant influence of the OEG chains on the size of the macrocycle. The retention time of the **OEG-MC3** with 5.3 min is about half that of **MC3** without any functionalization (*t* = 11.3 min). GPC analysis further confirms a slightly larger size of the new macrocycle **OEG-MC4** as the retention time (*t* = 4.4 min) of the latter is shorter than that of **OEG-MC3** (*t* = 5.3 min), while **OEG-MC2** exhibits a longer retention time of 6.5 min. The observed trend in retention times is in agreement with the expected increasing size from dinuclear to tetranuclear macrocycle as obtained by molecular modelling (MM2 optimization, Spartan'14, see Figure 35).

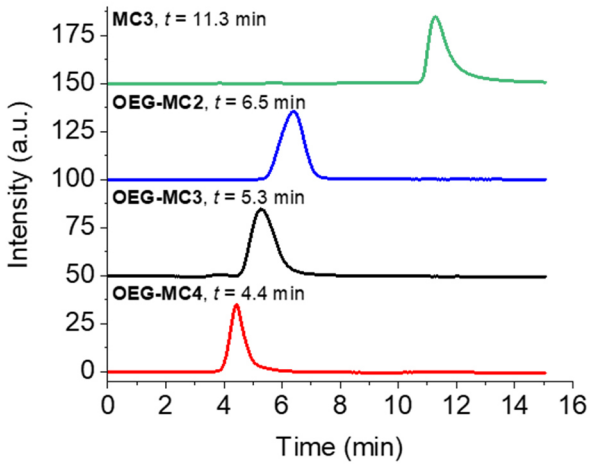

Figure 34: Analytical GPC chromatograms of **MC3** (green line), **OEG-MC2** (blue line), **OEG-MC3** (black line) and **OEG-MC4** (red line).

To gain further confirmation of the structures of the macrocycles, DOSY NMR spectroscopy of **OEG-MC2**, **OEG-MC3** and **OEG-MC4** was performed (Figure 35).

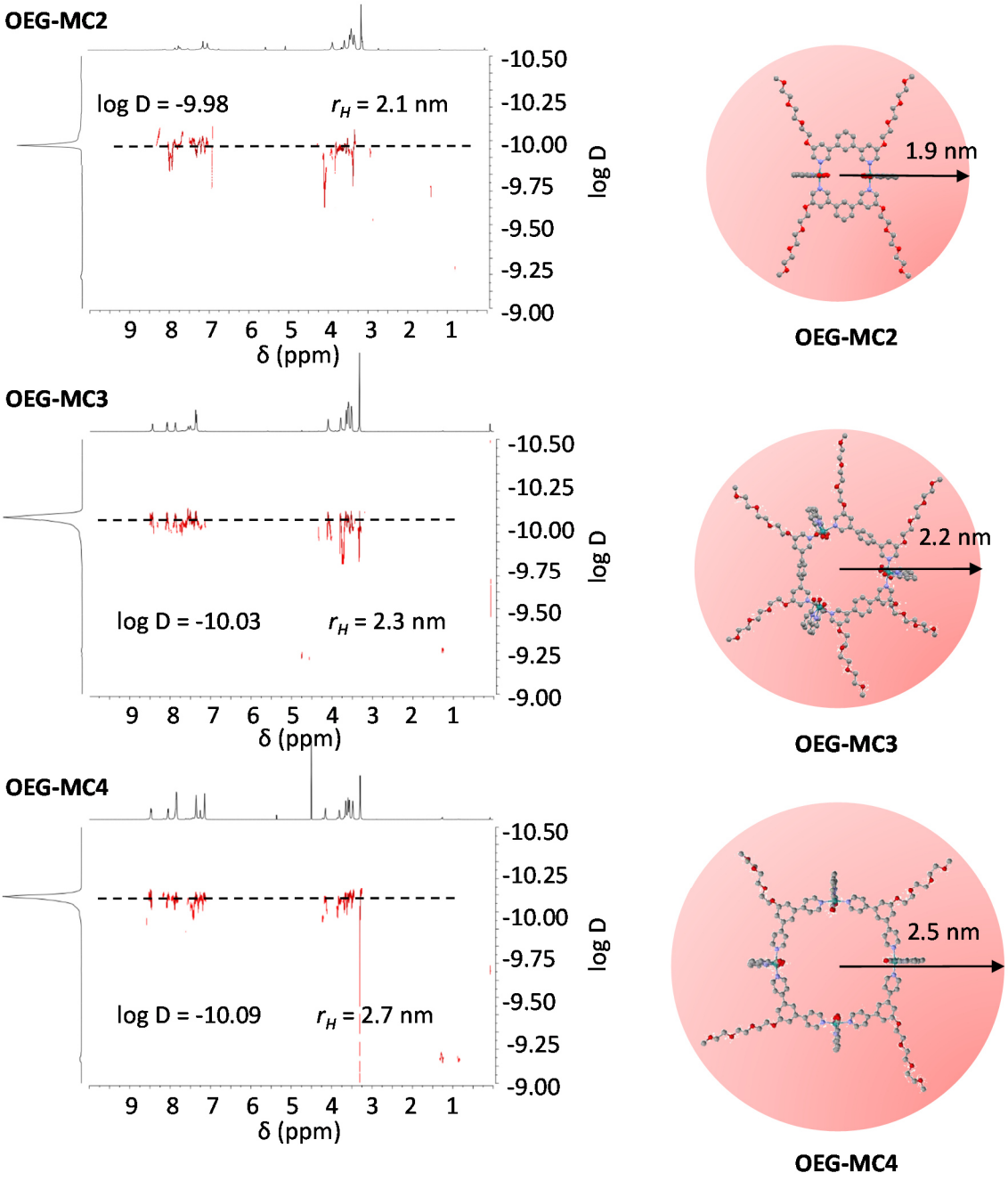

Figure 35: Left: DOSY NMR (400 MHz, rt) of **OEG-MC2, OEG-MC3** and **OEG-MC4** in CD_2Cl_2/MeOD/ TFE-d_3 (3:7:10). Right: Modelled structures and diameters of these compounds.

The obtained DOSY spectra show decreasing diffusion coefficients with the increasing size of the macrocycles from di-, tri- to tetranuclear WOCs. According to the Stokes-Einstein equation (equation 10), diffusion coefficients were used to calculate the hydrodynamic radius (r_H) for each macrocycle.[264]

$$D = \frac{k\,T}{6\,\pi\,\eta\,r_H} \qquad \text{(eq. 10)}$$

Here, D is the diffusion coefficient which was determined from the DOSY experiments, k is the Boltzman constant, T is the temperature and η is the dynamic viscosity. Assuming a nearly spherical particle, the diffusion coefficient of D = -10.09 m^2s^{-1} for **OEG-MC4** results in a hydrodynamic radius of r_H = 2.7 nm (diameter d_H = 5.4 nm). Smaller hydrodynamic radii of 2.1 and 2.3 nm were obtained for **OEG-MC2** and **OEG-MC3**, respectively. The size of the macrocycles estimated from DOSY experiments corroborates very well with the trends obtained by molecular modelling (Figure 35), thus again confirming the macrocyclic structure of the Ru(bda) complexes.

4.2.3 Optical and redox properties

UV/vis absorption spectra of the new di- and tetrameric macrocycles at different oxidation states were investigated in phosphate buffer/TFE (1:1) at pH 7. Figure 36 displays spectro-electrochemical properties of **OEG-MC2** and **OEG-MC4**. Experimental data for **OEG-MC3** can be found in Figure S40 which shows similar intensities and transitions reported in literature for **MC3**.[216]

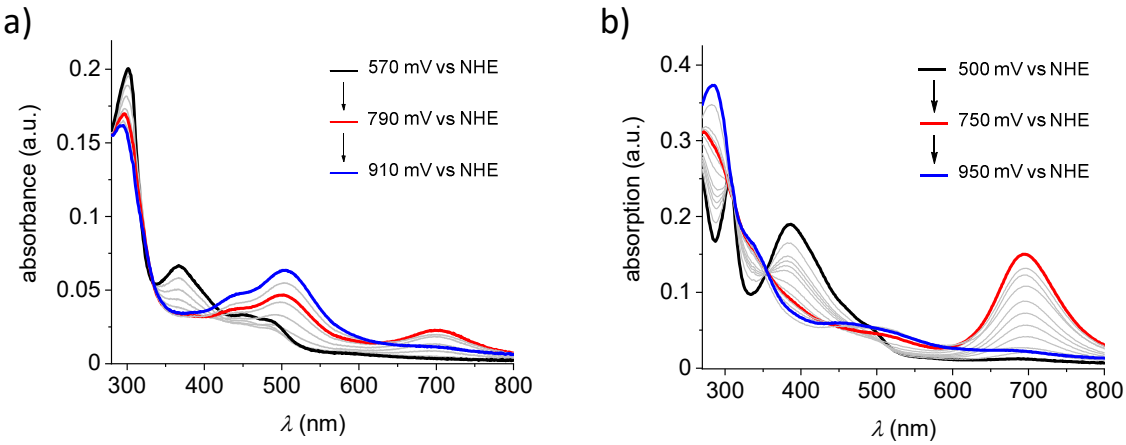

Figure 36: Spectroelectrochemical studies of a) **OEG-MC2** (*c* = 219 µM) and b) **OEG-MC4** (*c* = 250 µM) in a 1:1 mixture of H_2O/TFE (phosphate buffer, pH 7, 0.1 M).

The UV/vis absorption spectrum of **OEG-MC2** at Ru^{II} state (Figure 36a, black line) shows a relatively intense sharp band at 300 nm, which is typical for Ru complexes and attributed to the axial ligand-centered π-π* transition.[265] The two broad bands at higher energies at about 340 nm and 540 nm correspond to metal-to-ligand charge transfer (MLCT) transitions from the Ru-d orbital to the π* orbitals of the axial and bda ligand.[170, 265] Calculations have shown that

the Ru-d to bda-π* MLCT bands appear at lower energies compared to Ru-d to L-π*.[266] Similar transitions can be observed for **OEG-MC4**, where the axial ligand-centered π-π* transition appears at about 310 nm. In this case, Ru-d to L-π* transitions are not distinguishable from Ru-d to bda-π* due to overlapping of the signals and are detected as one broad band from 340 nm to 530 nm with a maximum intensity at 385 nm. It is known that each Ru oxidation state has a distinctive UV/vis absorption spectrum.[43] By applying an increasing voltage, stepwise oxidation of the Ru centers from Ru^{II} to Ru^{IV} could be observed in these complexes. Changes in the UV/vis spectra were observed during the transformation to the Ru^{III} state by a significant decrease in intensity of the MLCT transition between 340 nm and 430 nm of both macrocycles. Additionally, a new band arises at 700 nm, which is of lower intensity in the case of the dinuclear macrocycle and much more distinct for the tetranuclear one. This absorption band was also observed for the macrocycle **MC3**, for which calculations revealed that this band can be assigned to the Ru(bda)-σ to Ru(bda)-σ* transition in the Ru^{III} state.[44] In addition, it has been reported that the strong absorption at 700 nm depends on the distance of a coordinated aqua / hydroxyl molecule to the Ru center.[43] It is assumed that due to an equilibrium between $[Ru^{III}]^+$ and $[Ru^{III}\text{-}OH_2]^+$ species,[267] the existence of this band and its intensity depends on whether the six or seven coordinated form is favored. Simulations for the monomeric $Ru(bda)(pic)_2$ complex demonstrated that no transition appears at 700 nm as the arrangement of the axial ligands is blocking the 7th coordination site at the Ru center and making it difficult for a water molecule to access the metal center. In contrast to monomeric $Ru(bda)(pic)_2$, macrocycle **MC3** has a relatively fixed axial ligand which facilitates the coordination of water as reflected in the intense absorption band at 700 nm.[43] Furthermore, a water network within the macrocyclic cavity of **MC3** was presumed to increase the intensity of this band due to readily accessible water molecules coordinating to the Ru centers. Comparing **OEG-MC2** and **OEG-MC4**, it becomes apparent that the possible influence of a water network is much more distinct in the tetramer than in the dimer. The band at around 700 nm decreases upon further oxidation and finally vanishes completely when reaching the Ru^{IV} state at 920 mV or 950 mV.

The redox properties of the macrocycles were studied by CV and DPV in a 1:1 phosphate buffer/trifluoroethanol (TFE) mixture at pH 7 (Figures S27 – S29). The addition of the non-coordinating co-solvent TFE was needed to circumvent the poor solubility in pure water and is reported to have no significant effect on the redox potentials.[43] For **OEG-MC2**, three redox events are observed at +0.66 V, +0.82 V and +1.07 V that can be assigned to the Ru^{III}_2/Ru^{II}_2, Ru^{IV}_2/Ru^{III}_2, and Ru^{V}_2/Ru^{IV}_2 oxidation processes, respectively. For comparison, **OEG-MC4** shows redox processes at +0.67 V, +0.84 V and +1.03 V. The redox potentials of di- and tetranuclear macrocycles are compared to those of trinuclear macrocycles with and without OEG chains in Table 3. The nearly identical oxidation potentials of all macrocycles indicate

that the different spatial arrangement of the Ru(bda) units in a di-, tri- or tetranuclear complex as well as the introduction of OEG chains have only a minor effect on the redox properties of the Ru center. Importantly, since the Ru^{V}/Ru^{IV} oxidation potential of the macrocyclic WOCs appears below the Ru^{III}/Ru^{II} oxidation potential of $Ru(bpy)_3^{2+}$ (E = +1.26 V vs NHE),[268] they appear properly suited for photocatalytic water oxidation driven by $Ru(bpy)_3^{2+}$ as a photosensitizer.

Table 3: Redox properties of macrocyclic WOCs **MC3**, **OEG-MC2**, **OEG-MC3** and **OEG-MC4** under neutral conditions.[a]

WOC	E vs NHE (V)		
	$Ru^{III/II}$	$Ru^{IV/III}$	$Ru^{V/IV}$
MC3[216]	+0.66	+0.82	+1.00
OEG-MC2	+0.66	+0.82	+1.07
OEG-MC3	+0.67	+0.81	+1.01
OEG-MC4	+0.67	+0.84	+1.03

[a] Data extracted from DPV experiments in 1:1 mixture of H_2O/TFE (phosphate buffer, pH 7, 0.1 M), c(WOC) = 0.25 mM.

4.2.4 Chemical water oxidation

The catalytic performance of new di- and tetranuclear Ru(bda) macrocycles was first studied in chemical water oxidation using ceric ammonium nitrate (CAN) as a sacrificial electron acceptor. Although the use of a sacrificial oxidant to drive the water oxidation reaction does not mimic conditions that are required for artificial photosynthesis, it allows for an initial comparison of trends in catalytic activities of WOCs. In general, water oxidation is known to be favored at higher pH which enables reduction of overpotentials.[95] However, chemical water oxidation is commonly performed applying the strong oxidant CAN which is only stable in acidic media, particularly at pH 1.[154] Measurements of the OEG-WOCs presented in this work were performed in air-tight Schlenk flasks attached to pressure sensors and equipped with a septum for injection of the catalyst. A fresh solution of excess CAN was prepared in acidic aqueous mixtures (triflic acid) containing 50% acetonitrile as a co-solvent, which has been reported to be robust in highly oxidizing environments.[43]

Oxygen evolution curves at different concentrations for **OEG-MC4** are depicted exemplarily in Figure 37a (see Figure S41 for **OEG-MC2**). For both catalysts, an increase in pressure was observed immediately after addition of CAN. Initial rates of the water oxidation were determined in the first two seconds of catalysis and a linear dependency of the rate on the concentration of the catalyst was observed (Figure 37b). This first order kinetics is typically found in catalyst

operating via WNA mechanism as previously demonstrated for trinuclear WOC **MC3**.[42] In contrast, for catalysts working via I2M mechanism, e.g. monomer Ru(bda)(pic)$_2$, an increase of rate with higher catalyst concentrations is observed.[42, 269]

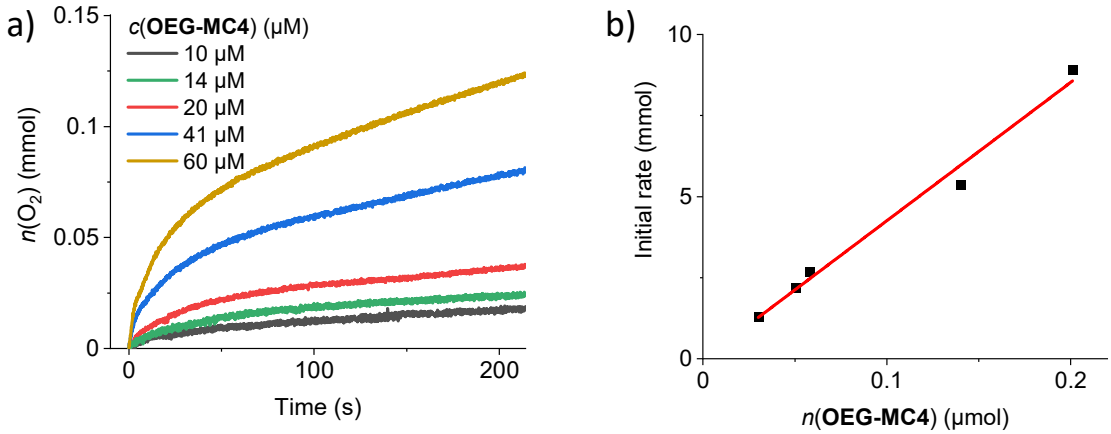

Figure 37: a) Concentration-dependent water oxidation experiments with **OEG-MC4** as WOC in H_2O/ MeCN 1:1 (pH 1, triflic acid). b) Plot of initial rates vs catalyst amount with linear regression for the determination of TOF.

Average TOF values per macrocyclic catalyst were calculated from the slope of the linear regression of the initial rates vs catalyst concentration. A TON was determined at each concentration and the reported value represents the maximal TON obtained for each catalyst. For **OEG-MC4**, an average TOF of 42 s^{-1} was obtained for **OEG-MC4**, which is slightly higher than the reported TOF of 26 s^{-1} for **OEG-MC3**,[215] while **OEG-MC2** showed a lower activity with TOF = 12 s^{-1}. Thus, a clear trend in increasing catalytic activities with increased size of the macrocycles is revealed, with TOFs per Ru of 6 s^{-1}, 8.7 s^{-1} and 10.5 s^{-1} for the di-, tri- and tetranuclear macrocycles. However, the stability reflected in TON is similar for **OEG-MC3** and **OEG-MC4** (2200 and 2870, respectively), whereas **OEG-MC2** exhibits a much lower value of only 200. Analysis of the headspace of the reaction vessel by gas chromatography was performed to determine the gas composition after each experiment (Figures S42 and S43). For both macrocycles **OEG-MC2** and **OEG-MC4**, the amount of oxygen detected by gas chromatography is in agreement with the amount calculated from the pressure sensor detection. These findings demonstrate that under the conditions applied in catalytic water oxidation with these WOCs only oxygen and no other gaseous by-products are generated (Figures S42 and S43).

4.2.5 Photocatalytic water oxidation

One step closer to mimicking natural photosynthesis in an artificial approach is the investigation of WOCs in photocatalytic water oxidation. A typical light-driven experiment for studying the

catalytic activities of WOCs requires the use of a three component system consisting of the WOC, a photosensitizer (PS) and a sacrificial electron acceptor (EA) (Figure 38). The process starts with the absorption of solar irradiation by the PS. As the PS transfers an electron to an EA, it increases its oxidizing power and is able to activate the catalyst.

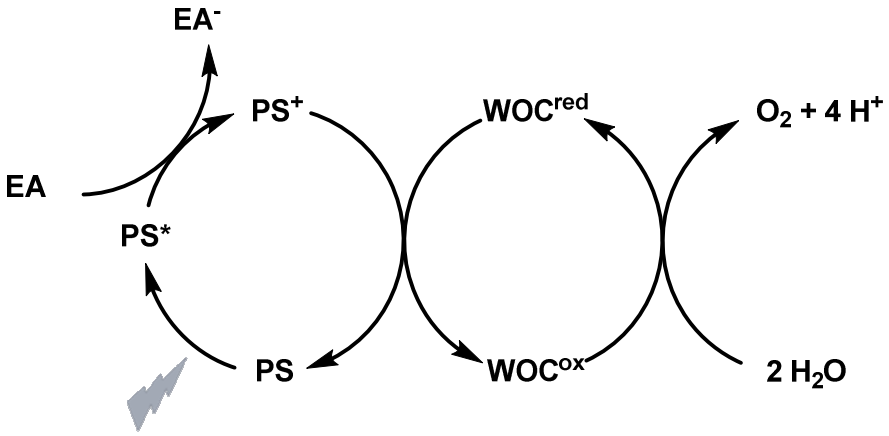

Figure 38: Schematic illustration of photocatalytic water oxidation using a one-electron transferring PS, a sacrificial EA and a WOC.

The catalytic activities of the OEG-functionalized macrocycles **OEG-MC2**, **OEG-MC3** and **OEG-MC4** were investigated using $Ru(bpy)_3^{2+}$ as PS and $Na_2S_2O_8$ as EA under neutral conditions (pH 7). As mentioned before, chemically driven catalytic water oxidation of **OEG-MC3** has been previously investigated,[215] but its photocatalytic activities remained unexplored. Thus, this macrocycle is also included to these studies. To generate the mild oxidant $Ru(bpy)_3^{3+}$ (PS^+) in situ from $Ru(bpy)_3^{2+}$, the PS is exposed to light, leading to the formation of the excited ^{3}MLCT state PS*.[270] By one-electron transfer to the EA, PS^+ is generated and $Na_2S_2O_8$ is converted into SO_4^{2-} anion and $SO_4^{\bullet-}$ radical. The latter can react with another PS molecule in the ground state and generate an additional PS^+. With the $Ru^{III/II}$ redox potential at +1.26 V vs NHE,[268] the oxidative power of PS^+ is sufficient to enable consecutive oxidation of the WOCs to the Ru^V state where water oxidation is initiated and the PS is regenerated.

Light-driven water oxidation experiments were performed at 20 °C in a temperature-controlled transparent reaction chamber, which was connected to a Clark electrode set-up for the detection of generated oxygen. For irradiation of the samples, a xenon lamp with calibrated intensity of sunlight at the earth surface (100 mW/cm^2)[271] was employed. To overcome the poor solubility of the WOCs in pure water, acetonitrile was chosen as co-solvent due to its stability in oxidative environments.[43] Experiments were performed at pH 7 in a phosphate buffer/MeCN mixture (1:1) under identical conditions to ensure reliable comparability.[216] Concentrations of PS (1.5 mM) and sodium persulfate as EA (37 mM) were kept constant in

all experiments, while the concentration of the WOC was varied. In a standardized procedure, PS and EA were mixed with the particular amount of WOC in the dark and irradiation was started after 50 s. While the solution was mixing in the dark, no oxygen was generated. However, after illumination of the sample and a short induction period of about 1-2 s, an increase in oxygen concentration was clearly detected by the Clark electrode. Oxygen evolution curves at different concentrations of the WOC, as shown for **OEG-MC4** in Figure 39a, were observed for all the investigated macrocycles. Experiments for **OEG-MC2** and **OEG-MC3** can be found in Figures S44 and S45.

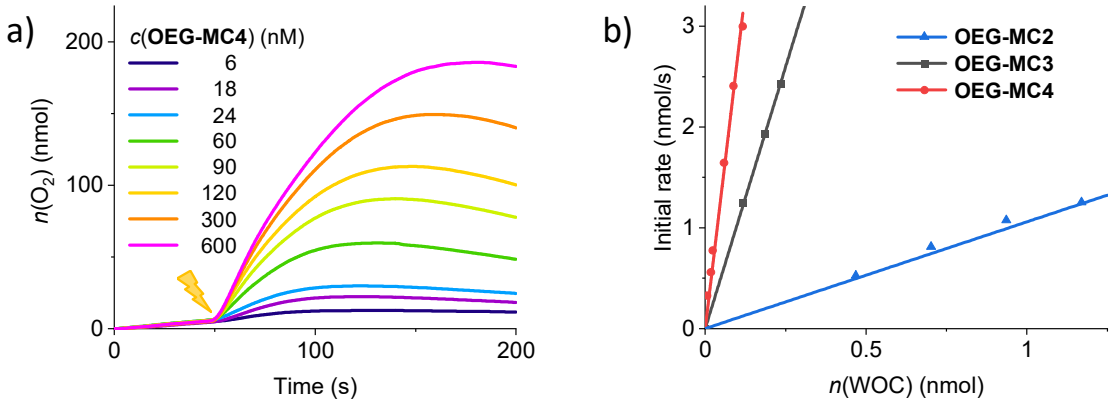

Figure 39: a) Oxygen evolution curves of **OEG-MC4** at different concentrations in H_2O/MeCN 1:1 (pH 7, phosphate buffer), *c*(PS) = 1.5 mM, *c*($Na_2S_2O_8$) = 37 mM. The lighting symbol indicates the start of sample irradiation at *t* = 50 s. b) Plots of initial rates vs concentrations of macrocycles studied here with linear regression for the determination of averaged TOF.

After the rate of oxygen production subsides, a plateau is observed since a maximal value of dissolved O_2 in solution is reached. A slight decrease in the oxygen evolution curves is then observed as some of the dissolved oxygen is released into the gas phase. By increasing the concentration of the catalyst, a higher amount of photo-generated O_2 is detected and steeper curves are observed (Figure 39a). Initial rates for each measurement at different concentrations were determined from the linear increase of the oxygen evolution curves in the first 10 to 15 s of catalysis (for further details see *Chapter 8* – Experimental Section). A linear dependency of the rates on the amount of WOC was observed for all the macrocycles (Figure 39b). By linear regression in the plot of initial rates at different concentrations an average TOF value was obtained for each catalyst. TON values were calculated from the maximum amount of oxygen detected at each concentration. The reported TON reflects the highest value obtained for each catalyst. Table 4 summarizes the photocatalytic activities of the OEG-functionalized WOCs in comparison to unfunctionalized macrocycle **MC3** previously investigated under identical conditions.

Table 4: Efficiencies of macrocyclic WOCs in photocatalytic water oxidation.[a]

WOC	TOF [s^{-1}]	TOF [s^{-1}] / Ru	TON
OEG-MC2	1.1	0.6	36
OEG-MC3	10	3.3	400
OEG-MC4	23	5.8	500
MC3[216]	11	3.7	430

[a] Photochemical water oxidation in H_2O:MeCN 1:1 (pH 7, phosphate buffer), *c*(PS) = 1.5 mM, *c*($Na_2S_2O_8$) = 37 mM, *c*(WOC) = 6 nM - 6 µM.

Tetrameric macrocycle **OEG-MC4** is the most active catalyst among the present series as evident from its much steeper linear regression in Figure 39b. Oxygen evolution was already detected at remarkably low catalyst concentration of 6 nM. With a TOF of 23 s^{-1}, this tetranuclear complex is more than twice as active as trimeric **OEG-MC3** with a TOF of 10 s^{-1}, whereas dimeric **OEG-MC2** shows with TOF = 1.1 s^{-1} one order of magnitude lower activity than the lager macrocycles. TOFs per Ru (see Table 4) reflect the same trend of increasing activity in the larger macrocycles. Additionally, a TON of 36 indicates the lower stability of **OEG-MC2** compared to **OEG-MC3** and **OEG-MC4** (TON = 400 and 500, respectively), which are in a similar range as the unfunctionalized macrocycle **MC3**.[216] As observed for chemical oxidation, the efficiencies of OEG-functionalized macrocyclic WOCs in photocatalytic water oxidation increased with increasing size and thus, a clear structure-activity relationship is given.

4.3 Discussion

Following the successful synthesis of di- and tetranuclear Ru(bda) macrocycles **OEG-MC2** and **OEG-MC4**, the catalytic performance of these WOCs, along with the previously reported trinuclear **OEG-MC3**, in chemical and light-driven water oxidation has been explored. Albeit water oxidation starts at higher voltages at acidic pH, chemically induced water oxidation at pH 1 is a useful tool for gaining first information on activities of catalysts.[154] However, it should be noted that WOCs display different activities under various conditions and low activities in chemically driven water oxidation might not rule out high performances in photocatalysis or electrocatalysis. New macrocycles **OEG-MC2** and **OEG-MC4** show TOFs of 12 s^{-1} and 42 s^{-1} in chemical oxidation at pH 1, which meets the expectation of higher activities in catalysts with more active centers. Interestingly, TOFs per Ru(bda) unit also reveal the same trend as TOF values of 6 s^{-1}, 8.7 s^{-1} and 10.5 s^{-1} were obtained for the di-, tri- and tetranuclear OEG-WOCs, respectively. TONs, which represent stability, are not increased with the size of the macrocycle

as similar TON values were observed for the tri- and tetranuclear WOCs **OEG-MC3** and **OEG-MC4** (TON = 2200 and 2870), while dinuclear **OEG-MC2** showed much lower TON of 200.

A comparison of **OEG-MC2** with axial-bridged but open dimeric $[Ru(bda)(pic)]_2L$ (L = dipyridyl bridging ligand) **42** and trimeric $[Ru(bda)(pic)]_3L$ (L = tripyridyl bridging ligand) shows that higher stabilities with a TON up to 86500 have been observed applying CAN at pH 1 (see Table S1 and Figure S48 for further comparison with different Ru based WOCs).[213-214] A high TOF of 126 s^{-1} was reported for the trinuclear WOC, while no activity was reported for the dinuclear one.[214] Lower TONs in the here presented WOCs might be due to instability of the OEG chains in the harsh conditions of chemical water oxidation. This is supported by the fact that TON as well as TOF values of **MC3** are significantly higher than in **OEG-MC3** (see Table S1).[216] Very few macrocyclic WOCs with multiple Ru centers active in water oxidation are described in literature. A very recently reported macrocyclic calix[4]arene-based dinuclear Ru(bda) catalyst **43** oxidizes water with a TON of 820 and TOF of 19 s^{-1}, displaying comparable activities per Ru center as tri- and tetranuclear macrocyclic WOCs presented in this chapter.[272]

Similar trends were observed in photocatalytic water oxidation at neutral pH. The catalytic activity of **OEG-MC4** is among the highest reported for a Ru(bda) complex in photocatalysis, being only outperformed by a Ru^{IV}=O(tda) complex, which reaches a TOF of 50 s^{-1}.[206] To put this into context, the values should be compared to those of $Ru(bda)(pic)_2$ and the unsubstituted **MC3**.[216] A TOF of 11 s^{-1} was reported for the latter, which is comparable to the activity of the trinuclear macrocycle with the identical basic framework exhibiting a TOF of 10 s^{-1}. For the monomeric $Ru(bda)(pic)_2$ complex, a TOF of 0.6 s^{-1} was observed (Figure S46). Considering the presence of two Ru(bda) active centers in **OEG-MC2**, the catalytic activity of this dinuclear complex with TOF of 1.1 s^{-1} (0.6 s^{-1} per Ru unit) is nearly identical with that of monomeric $Ru(bda)(pic)_2$. Therefore, no gain in catalytic performance could be achieved by macrocyclic arrangement in dimer. Thus, it can be assumed that each catalytically active Ru center in **OEG-MC2** functions independently. On the other hand, the TOFs per Ru center for **OEG-MC4** (5.8 s^{-1}) and **OEG-MC3** (3.3 s^{-1}) are significantly higher than that of monomeric $Ru(bda)(pic)_2$ and **OEG-MC2**, indicating beneficial preorganization in larger macrocycles leading to higher catalytic activities. Notably, activities in a similar range in photocatalysis have been reported for an axially bridged dimeric $[Ru(bpy)(py)(H_2O)]_2$(pyrazole)-type WOC **39** and for dinuclear macrocyclic calix[4]arene-based Ru(bda) WOC **43** with TOFs of 5.5 s^{-1} and 6.5 s^{-1} per Ru unit, respectively (see Figure S48 and Table S5 for further information).[272-273]

Interestingly, **OEG-MC2** shows a higher TON per Ru unit (TON = 18) than $Ru(bda)(pic)_2$ (TON = 13), indicating that the dimeric macrocycle is more stable than the monomer. This can presumably be attributed to the rigid nature of the bridging ligand. Due to the chelating effect of **L2**, axial pyridyl ligand dissociation, which is known to be one of the main degradation

pathways for molecular Ru(bda) WOCs,[204] can be diminished as self-healing processes take place by a re-association. Both tri- and tetranuclear complexes **OEG-MC3** and **OEG-MC4** feature similar stabilities as **MC3** with TONs of 133, 125 and 143 per Ru center, respectively, that are remarkably higher than those of dinuclear **OEG-MC2** and monomeric Ru(bda)$(pic)_2$. These results imply a significant gain in stability by the macrocyclic effect compared to the monomer.

4.4 Conclusions

Mononuclear water oxidation catalysts containing Ru(bda) as an active unit have been studied extensively during the last decade. However, not many reports on multinuclear Ru(bda) WOCs are known. In this work, new dinuclear and tetranuclear macrocyclic WOCs **OEG-MC2** and **OEG-MC4** were synthesized with implemented Ru(bda) units and triethylene glycol chains in axial ligands to enhance solubility of the metallosupramolecular structures in aqueous media. ^{1}H NMR spectra of **OEG-MC2** and **OEG-MC4** revealed a highly symmetric structure of these compounds, demonstrating the absence of open chain ends. The different size of the macrocycles compared with the previously reported **OEG-MC3** was confirmed by analytical GPC and DOSY NMR spectroscopy. Redox properties and catalytic activities of the macrocyclic WOCs in chemically- and light-driven water oxidation have been investigated. While the redox potentials of these macrocycles for the oxidation of the Ru centers from Ru^{II} to Ru^{IV} are rather similar, changes between the macrocycles could be observed in spectroelectrochemical experiments. Here, intense signals at 700 nm, which are associated with the influence of a hydrogen-bonded water network within the cavity as reported previously for **MC3**,[43] were also observed for **OEG-MC3** and **OEG-MC4**. Whilst only a very weak band was observed in the case of **OEG-MC2**, this corroborates our hypothesis that the intensity of this band relates to the catalytic activity for water oxidation because the activity indeed increased from di- to tetranuclear complex with TOFs per Ru center of 6 s^{-1}, 8.7 s^{-1} and 10.5 s^{-1} using CAN as an oxidant at pH 1 in 50 % water / MeCN. TON values show a similar trend with the highest TON of 2870 observed for **OEG-MC4**, but comparison with the unubstitued **MC3**[216] indicates that the harsh conditions in acidic solution are disadvantageous for the OEG-substituted WOCs and presumably lead to oxidative degradation. In light-driven catalytic water oxidation under neutral conditions (pH 7) similar trends were observed as for chemical water oxidation. **OEG-MC2** performed with similar efficiency per Ru unit as the monomeric reference catalyst Ru(bda)$(pic)_2$. Pleasingly, much better performances were observed for tri- and tetranuclear WOCs. **OEG-MC4** with a TOF of 23 s^{-1} (5.8 s^{-1} per Ru unit) belongs to the best performing homogeneous Ru(bda) WOCs in photocatalytic water oxidation.

Chapter 5

—

Trinuclear macrocycle in heterogeneous catalytic water oxidation[1]

Summary: Catalytic water splitting is a viable process for the generation of renewable fuels. Here it is reported for the first time that a trinuclear supramolecular Ru(bda) catalyst, anchored on multi-walled carbon nanotubes and subsequently immobilized on glassy carbon electrodes, shows outstanding performance in heterogeneous water oxidation.

5.1 Introduction

Anchoring of well-characterized and understood molecular WOCs on the surface of electrodes is an attractive strategy for the generation of hybrid materials for heterogeneous water splitting.[274-276] Such hybrid materials are highly versatile for setting up (photo-)electrochemical cells.[114, 121, 123, 225] For the immobilization of homogeneous WOCs onto electrodes, mainly two strategies have been employed. One of them is based on covalent attachment of molecular catalysts to electrode surfaces by silane-, carboxylate- or phosphonate-functionalized ligands.[124-125, 128, 134, 225, 277] Another approach is a supramolecular one, comprising introduction of aromatic groups to the WOCs to facilitate non-covalent π-π interactions between the catalyst and a supporting material like carbon nanotubes (CNTs).[233, 278-279]

[1] This chapter was partly communicated in: D. Schindler, M. Gil-Sepulcre, J. O. Lindner, V. Stepanenko, D. Moonshiram, A. Llobet, F. Würthner, *Adv. Energy Mater.* **2020**, 2002329. (Reproduced with permission, Copyright 2020 by John Wiley & Sons).

Due to their large surface area as well as high conductivity and stability,[280-283] CNTs are properly suited for immobilization of catalysts on electrodes. Cao and co-workers compared different linking strategies of Co corroles on CNTs and reported improved activities and the importance of fast electron transfer for high efficiencies.[284-285] Indeed, Sun and co-workers have shown that a derivative of Ru(bda)(pic)$_2$ WOC containing axial pyridyl ligands that are functionalized with pyrene groups through amide linkers, can be immobilized on multi-walled carbon nanotubes (MWCNTs).[233] Recently, also Llobet and co-workers have successfully anchored a Ru(tda) (tda: ([2,2':6',2''-terpyridine]-6,6''-dicarboxylate)) catalyst bearing pyrene-functionalized axial ligands on MWCNTs by π-π interactions and demonstrated heterogeneous water oxidation for this hybrid material.[278] It has been reported in literature that immobilization of molecular Ru(bda) catalysts, which operate by I2M (interaction of two M-O units) mechanism[164] in homogeneous phase on electrodes, leads to adverse effects on their catalytic activity in heterogeneous catalysis[228, 286] due to restricted mobility, associated with a switch to the WNA (water nucleophilic attack) mechanism.[164] This implies that Ru-based WOCs functioning through the latter mechanism are favorable for heterogeneous catalysis.[161, 287]

Therefore, macrocyclic WOCs bearing three Ru(bda) units such as **MC3** (highly soluble in a CH_2Cl_2/MeOH (5:3) mixture but not in pure water, for structure see Figure 40) should be a promising candidate for heterogeneous water oxidation as **MC3** exhibits high catalytic efficiency in homogeneous water oxidation via a WNA mechanism[42, 44] and benefits from the supramolecular arrangement.[43] As this metallomacrocycle comprises three bipyridyl phenyl linear ligands, in addition to the three bda units, it might be possible that **MC3** could anchor in a similar way on CNTs by non-covalent CH-π interactions by orientating the bda-backbone towards the graphene-like surface without further functionalization as described recently by Llobet and co-workers for a related oligomer based on Ru(tda) subunits.[234] Here it is shown that **MC3** indeed adheres to CNTs as confirmed by electrochemical techniques and atomic force microscopy (AFM). More importantly, CNT-anchored **MC3** immobilized on glassy carbon electrodes performed outstanding catalytic activity in electrochemically driven water oxidation underlining its potential for device application.

5.2 Results

5.2.1 Preparation and characterization of hybride anode

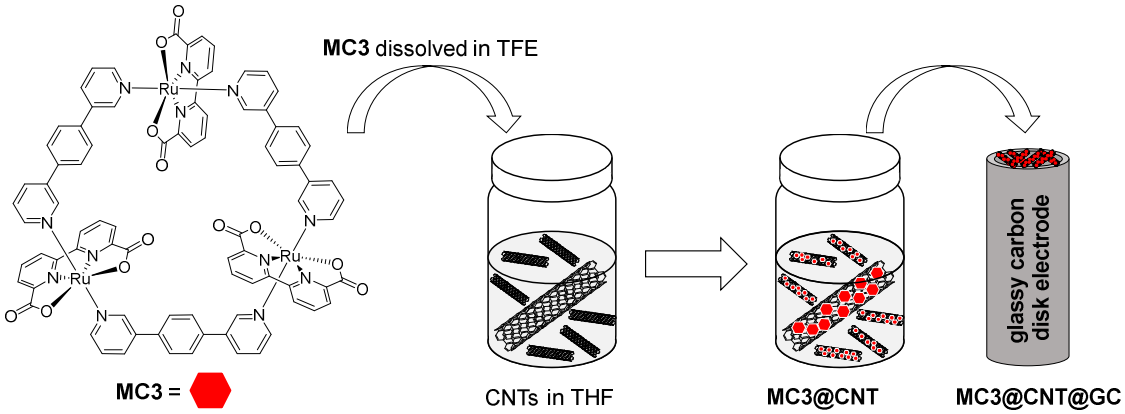

Figure 40: Structure of the Ru(bda) macrocycle **MC3** and schematic illustration of its immobilization on CNTs and subsequent deposition onto a glassy carbon disk.

To anchor trinuclear Ru(bda) catalyst **MC3** on MWCNT surface, 0.1 mL of a solution of **MC3** in trifluoroethanol (TFE) was added to a freshly prepared dispersion of MWCNTs in THF (Figure 40). Immediate decolorization of the mixture indicated the binding of the catalyst onto the surface of the CNTs. To confirm that catalyst **MC3** is indeed attached to the CNTs, AFM measurements[2] were performed by spin-coating a dispersion of **MC3@CNT** onto a silicon wafer (Figure 41). is shown in Figure S49. Thus, the direct anchoring of an unfunctionalized Ru(bda) complex to CNTs through non-covalent interactions could be proofed by a microscopic technique.

[2] Measurements performed by Dr. Vladimir Stepanenko, Universität Würzburg.

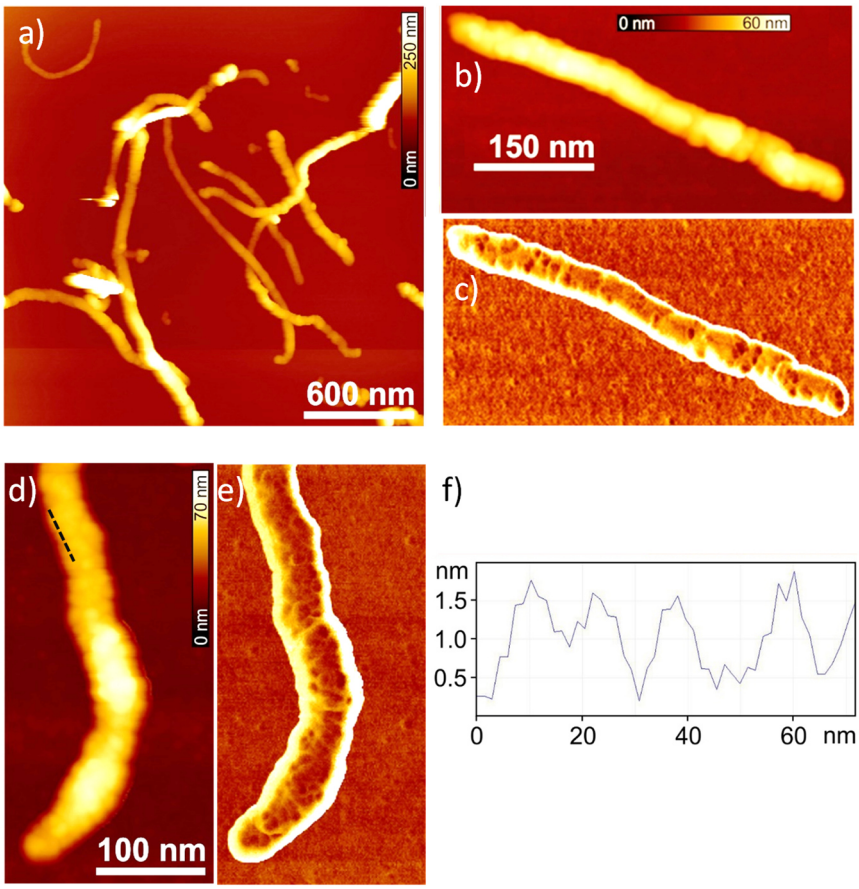

Figure 41: Height (a,b,d) and phase (c,e) AFM images obtained after spin-coating a dispersion of **MC3@CNT** (0.4 mL of **MC3** in TFE (c = 1 mg/mL) in 1 mL of MWCNTs in THF (c = 1 mg/mL)) onto a silicon wafer. Z scale: 250 nm (a), 60 nm (b) and 70 nm (d). Images in c) and e) show one single magnified nanotube, respectively, decorated with **MC3** molecules. f) Cross-section analysis from the black dashed line in image (d).

Further characterization by scanning electron microscopy (SEM) and energy-dispersive X-ray spectroscopy (EDX) experiments was performed (Figures S50 – S54) to characterize **MC3@CNTs**.[3] For SEM imaging, **MC3@CNTs** was spin-coated onto a silicon wafer. Carbon nanotubes covered with Ru macrocycles **MC3** could be clearly observed (Figure S52). The **MC3** cycles appear much brighter in backscattered electrons (BSE) images which confirms the adsorption of the Ru-macrocycle on the CNT surface. The presence of Ru attached to the CNTs was revealed by EDX analysis (Figure S53). Good detectable signal at 2.558 keV is corresponding to the Ru(*Lα)* X-ray emission peak. Investigations of the coverage on a well-defined glassy carbon disk have demonstrated that 93% of the surface are covered, indicating the formation of a monolayer distribution on the carbon material (Figure S55).

For electrochemical studies, working electrodes (WE) with **MC3@CNTs** were prepared. The glassy carbon (GC) disk electrodes with a surface area of S = 0.07 cm^2 were thoroughly cleaned and dried before applying 4 times drops of 20 µL of a suspension of **MC3@CNT** onto

[3] Measurements performed by Dr. Vladimir Stepanenko, Universität Würzburg.

the GC disk (denoted as **MC3@CNT@GC**). Cyclic voltammetry (CV) experiments were then performed with these electrodes in a 1 M phosphate buffer solution (pH 7) using a three electrode cell. A platinum mesh and $Hg/HgSO_4$ electrode were used as counter (CE) and reference electrodes (RE), respectively. All potentials reported hereinafter are converted and referenced to NHE. No loss of the catalyst was observed in CV experiments as the aqueous phosphate buffer soltuion stayed colorless during all measurements. However, since **MC3** is not soluble in pure water, a 'rinse test' experiment was performed to verify whether the complex is firmly anchored to the CNT support on the GC electrode. The prepared electrode was dipped into a DCM/MeOH (5:3) mixture for 30 seconds and subsequently, a CV of the first redox process in the non-catalytic region was measured before and after (Figure S56) this test. No decrease in intensity indeed demonstrated a stable anchoring of **MC3** to the CNTs.

5.2.2 Electrochemical activation of MC3@CNT@GC

The electrochemical properties of the prepared **MC3@CNT@GC** electrode were investigated by means of CV and DPV measurements (Figure 42). All CV and DPV scans started at the lowest potential and were performed towards the aniodic region (oxidative process) and the scan was reversed and swept back to the cathodic region in case of CV measurements. In the first cycle, current densities of about 50 mA/cm^2 at a potential of E = 1.45 V were observed (Figure 42d, black line). The onset potential of catalytic process was determined as the intersection between the baseline and the slope at the very beginning of the catalytic water oxidation process at E_{onset} = 1.05 V, giving an overpotential of 330 mV for water oxidation (Figure S57). Repetitive CV cycles up to a potential of 1.35 V revealed a steady rise of the catalytic current (Figure 42a, b), along with changes in the non-catalytically active redox waves (Figure 42a, inset). As the number of CV cycles increases, higher catalytic current densities are observed until a plateau is reached after around 100 cycles (Figure 42b).

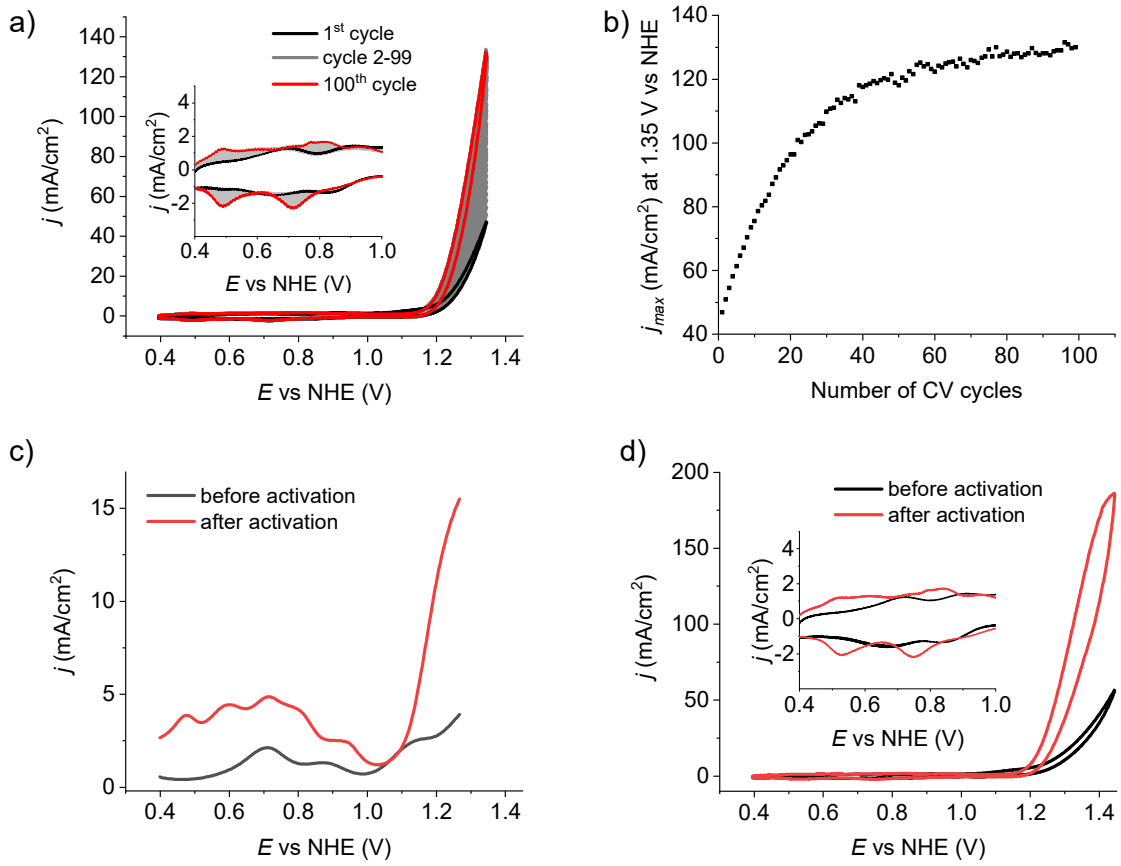

Figure 42: Electrochemical experiments with **MC3@CNT@GC** in 1 M phosphate buffer (pH 7). a) 100 repetitive CV scans (scan rate: 100 mV/s). Inset: Enlarged area of the non-catalytic waves. Initial species in the first cycle is shown in black, 100th cycle is shown in red. Scans 2-99 are depicted in grey. b) Development of the maximal current densities at E = 1.35 V vs NHE with the increasing number of CV scans. c) Comparison of the differential pulse voltammograms of the initial species (black line) and the final species after 100 CV cycles (red line). d) Comparison of the cyclic voltammograms (scan rate: 100 mV/s) of the initial (black line) and the final species (red line) after 100 CV cycles.

Control CV experiments confirmed that a CNT decorated electrode without the catalyst (**CNT@GC**, Figure S58a, blank) does not produce any significant current under identical experimental conditions. Even after 100 CV cycles, no rise in current could be observed (Figure S58e). Interestingly, **MC3** as a homogeneous catalyst in a phosphate buffer/TFE 1:1 mixture (pH 7) does not show any comparable catalytic activity in water oxidation (Figure S58b). Investigations of the redox properties of homogeneous **MC3** by differential pulse voltammetry (DPV) showed three reversible oxidation processes that are assignable to the transitions from the Ru^{II} to Ru^{V} oxidation states.[42] DPV analysis of **MC3@CNT@GC** electrode revealed that the first and the second oxidation waves of immobilized **MC3** correspond to the $Ru^{III/II}$ and $Ru^{IV/III}$ redox couples at E = 0.68 V and 0.85 V, respectively, and are not influenced by the immobilization of the catalyst. The $Ru^{V/IV}$ oxidation is shifted to higher potentials from 1.02 V to 1.11 V in the case of **MC3@CNT@GC** compared to the non-immobilized catalyst (Figure S58c, d).

By DPV analysis, the appearance of additional redox waves of **MC3@CNT@GC** and a rise in the catalytic current can be observed after the final state is reached upon 100 CV cycles (Figure 42c). This indicates the formation of a new and even more active species on the electrode. Five redox processes can be seen before the onset of the water oxidation catalysis, which is now shifted to higher potentials and appears at E_{onset} = 1.15 V (Figure S57). The $Ru^{V/IV}$ oxidation of the initial species is covered by the catalytic slope of the newly formed species and, therefore, not observable any more. The first redox process of the newly formed species arises at 0.50 V, which presumably corresponds to the $Ru^{III/II}$ redox process and is also shifted to lower potentials than in the initial species. Similar electrochemical activation processes have already been described for other Ru catalysts like $Ru(tda)(py)_2$ or $Ru(pdc)(bpy)_2$ (pdc: pyridyl-2,6-dicarboxylate),[207, 209] where the formation of a Ru aqua species as active catalyst was supposed after repetitive CV cycles. However, such activated species has not been reported for Ru(bda) catalysts.

Since the DPV (Figure 42c) shows waves of the initial species in addition to new waves associated with the newly generated and presumably more active one, experiments to transform all of the initial complex were performed. One strategy has been the performance of repetitive CV cycles at higher potential of E = 1.6 V (Figure S59). Faster activation was observed compared to the experiments at 1.3 V, as the plateau maximum current densities has already been reached after 50 cycles (Figure S59b). However, a complete conversion has not been achieved, both initial and activated species could be identified after activation in the DPV (Figure S59c). Also additional 100 CV cycles (Figure S60) did not transform all of the initial species. In contrast, due to the large amount of oxygen generated, oxygen bubbles in the CNT network maximize the risk of losing of some parts of the **MC3@CNT** layer on the GC surface and therefore reduced current densities were observed (Figure S60b). These results indicate that a complete conversion of **MC3** into the activated species might not be possible.

In 2015, Llobet and coworkers presented the direct anchoring of a $Ru(bda)L_2$ catalyst onto a GC electrode.[228] A diazonium salt was introduced in the bipyridine ligand and reduction lead to the generation of a carbon radical resulting in C-C bond formation with the surface of the graphite electrode. Activation by repetitive CV cycles lead to a significant increase in current density (from initially j_{max} = 0.6 mA/cm^2 to finally j_{max} = 1.4 mA/cm^2 after 50 cycles at E = 1.4 V vs NHE). However, it has been revealed by X-ray absorption spectroscopy (XAS) experiments that the increase of the catalytic current originated from the degradation of the catalyst and the formation of RuO_2 as active species on the surface of the electrode. To verify that **MC3@CNT@GC** is indeed stable and does not decompose to RuO_2, XANES (X-ray absorption

near-edge structure spectroscopy) experiments have been performed with the initial and activated electrodes (Figure 43).[4]

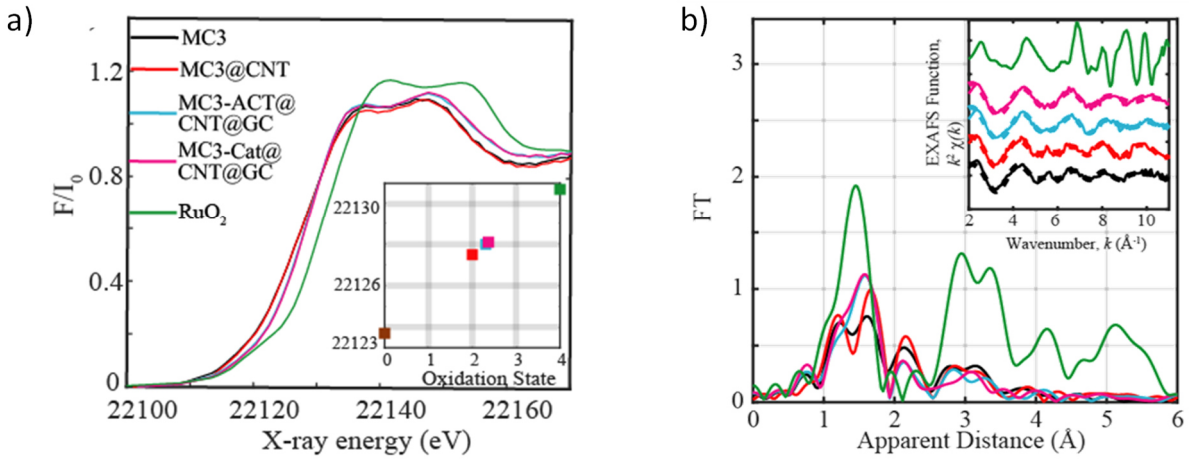

Figure 43: a) Normalized Ru-K-edge XANES, inset: plot of half peak K-edge energy vs oxidation state. b) Fourier transformations for measured samples. Inset: Back Fourier transformed experimental $k_2[\chi(k)]$ of Ru complexes together with RuO_2. Experimental spectra were calculated for k values of 2-11 $Å^{-1}$. **MC3** (black), **MC3@CNT** (red), **act-MC3@CNT@GC** (blue), after catalysis (magenta) and RuO_2 (green).

In XANES spectroscopy, X-rays are used to promote electrons from an atomic core orbital to an unoccupied bound or continuum state with specific energies given by the Fermi Golden Rule.[288] As the excitation probability highly increases when the energy of the incident photon is the same as the binding energy of a core-electron (referred to as edge-energy in XAS), specific spectra are obtained for each compound. Comparison of XANES data (Figure 43a) show very similar spectra of **MC3** (black line) and **MC3@CNT** (red line). The spectra of **act-MC3@CNT@GC** and after catalysis of **act-MC3@CNT@GC** only show slightly differences while the spectrum of RuO_2 (green line) is clearly different. The same trend is reflected in the Fourier transformation of the measured samples (Figure 43b). These measurements provide evidence of the molecularity of the water oxidation active catalyst since no RuO_2 can be detected at the surface of the electrode before and after catalysis. Moreover, the formation of RuO_2 as catalytically active species would lead to a decrease in the catalytically not active waves. This is not the case in **act-MC3@CNT@GC**, where instead the appearance of additional waves is observed (Figure 42c).

After removing all oxygen bubbles from the surface of the activated electrodes (**act-MC3@CNT@GC**), a cyclic voltammogram was recorded and compared to the one of the unactivated electrode (Figure 42d). An exceptionally high current density (j) of 186 mA/cm^2

[4] Measurements performed and evaluated by Dr. Dooshaye Moonshiram, Instituto Madrileño de Estudios Avanzados en Nanociencia (IMDEA Nanociencia), 28049 Madrid (Spain).

was reached at E = 1.45 V after the activation process, which is about four times higher than the value observed before activation. Reproducibility has been demonstrated in three independently prepared electrodes and an average current density of 176 mA/cm^2 (Figure S61). Earlier approaches by Sun and coworkers of immobilizing pyrene-functionalized Ru(bda) catalysts on an ITO surface using carbon nanotubes as support resulted in current densities of only 720 µA/cm^2.[233] Thus, the observed j_{max} value for anchored and activated **MC3** is the highest one reported so far for Ru(bda) catalysts with confirmed molecular active species and comparable with the very recently observed maximum current density of 240 mA/cm^2 for an immobilized Ru(tda) polymer.[234] CV experiments after activation of the electrode have also been performed at different pH values (Figure S62). The highest current density was observed at pH 9, however, all further experiments were also performed at pH 7 for comparability to literature. Nevertheless, it is worth to notice that no significant catalytic current was observed at pH below 5. This once more supports that no RuO_2 is formed at the GC surface, as RuO_2 is known to be highly active under acidic conditions in electrocatalysis.[289]

5.2.3 Stability and efficiency of act-MC3@CNT@GC

Proven to be highly efficient, the stability and efficiency of the **act-MC3@CNT@GC** electrodes was then investigated by controlled potential electrolysis (CPE) experiments. To avoid disturbance by the evolving hydrogen in the cathode, a two-compartment setup was used, where the working and the reference electrodes were placed in one chamber and the counter electrode in the other one.

To verify that no side processes other than water oxidation take place during this electrochemical reaction, the Faraday efficiency of **act-MC3@CNT@GC** was determined. The Faraday efficiency is used to describe how efficient charge is transferred in a system and how electrons are taking place in a specific electrochemical reaction. Faradaic loss can be assigned to the participation of electrons or ions in unwanted side reactions and are observed as chemical by-products and/or heat.[290]

The amount of charge passing through the system was recorded by the potentiostat and the actual amount of oxygen produced during one CPE experiment was measured by a gas phase Clark electrode in the head-space of the chamber containing the working electrode (Figure 44). The whole setup has been degassed and carefully sealed air-tight before the measurement. To produce a sufficient amount of oxygen to be detectable in the gas phase by the Clark electrode, a glassy carbon plate was used as a working electrode due to its increased surface area. With the standard drop-casting procedure, amounts of **MC3@CNT** were applied to the surface of the GC plate until it completely covered. After activation by 100 CV cycles to 1.35 V, a constant potential of 1.3 V was applied and after few seconds bubbles of oxygen could be

seen by the naked eye on the working electrode. The huge amount of generated oxygen was clearly observable by an increased level of the gas phase in the anionic chamber. The CPE experiment was stopped after 45 minutes.

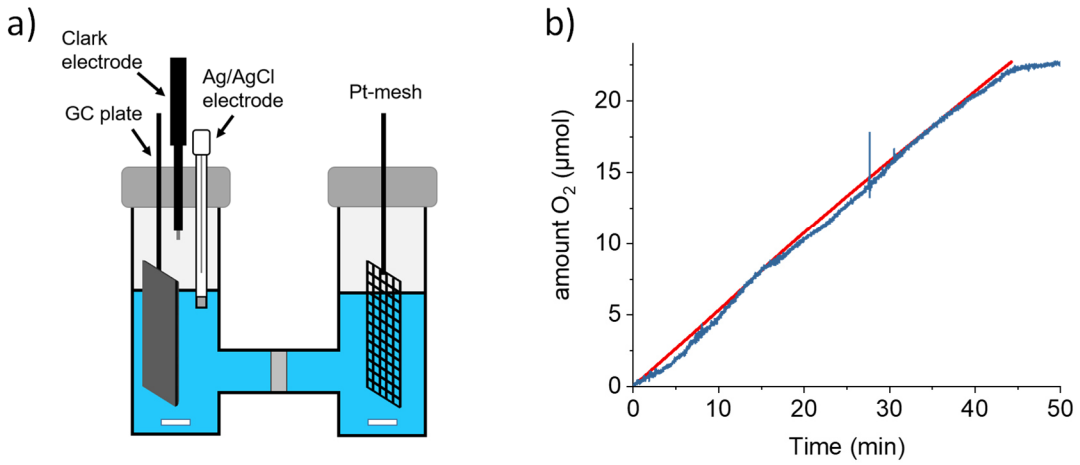

Figure 44: a) Experimental setup for determining the Faraday efficiency in a two-compartment cell with a Clark electrode in the anodic chamber. b) Determination of the Faraday efficiency of **MC3@CNT@GC**-plate. The red line shows the theoretical amount of produced oxygen calculated from the passed charge in a CPE experiment assuming a Faraday efficiency of 100%. The blue line corresponds to the head-space analysis of the amount of oxygen detected by a Clark electrode.

With four electrons involved in the water oxidation process (according to the water oxidation reaction equation $H_2O \rightarrow O_2 + 2H^+ + 4e^-$), the amount of passed electrons detected by the potentiostat during the CPE experiment was converted into the maximal amount of produced oxygen applying Faraday's law:

$$n\,(mol) = \frac{Q}{F * z} \qquad \text{(eq. 11)}$$

where Q is the charge passed in the CPE during 45 min, F is the Faraday constant and z reflects the amount of electrons in the process of water oxidation. After subtracting the values from a blank experiment, the value obtained according to Faraday law was compared with the amount of detected oxygen (after blank subtraction) by a Clark electrode in the headspace of the anodic compartment. The quantity of detected oxygen was compared to the theoretical maximum calculated one assuming a Faraday efficiency of 100% (equation 11). Almost no deviations between these values (Figure 44) imply a Faraday efficiency of 99%.

Electrochemically, the TON and therefore the stability of the hybrid anode can be determined as following: a constant potential is applied over a certain time and the responsive current as well as the flowing charge is monitored. No degradation is indicated by a stable current and a

linear increase of the flowing charge. For this purpose, the surface of a glassy carbon disk was sufficient and accordingly an electrode was prepared as described before. A constant potential of 1.6 V was applied in this experiment. No decrease in the catalytic current during 6 hours confirms that the immobilized catalyst does not undergo any considerable degradation or detachment from the electrode during continuous catalytic water oxidation process (Figure 45a).

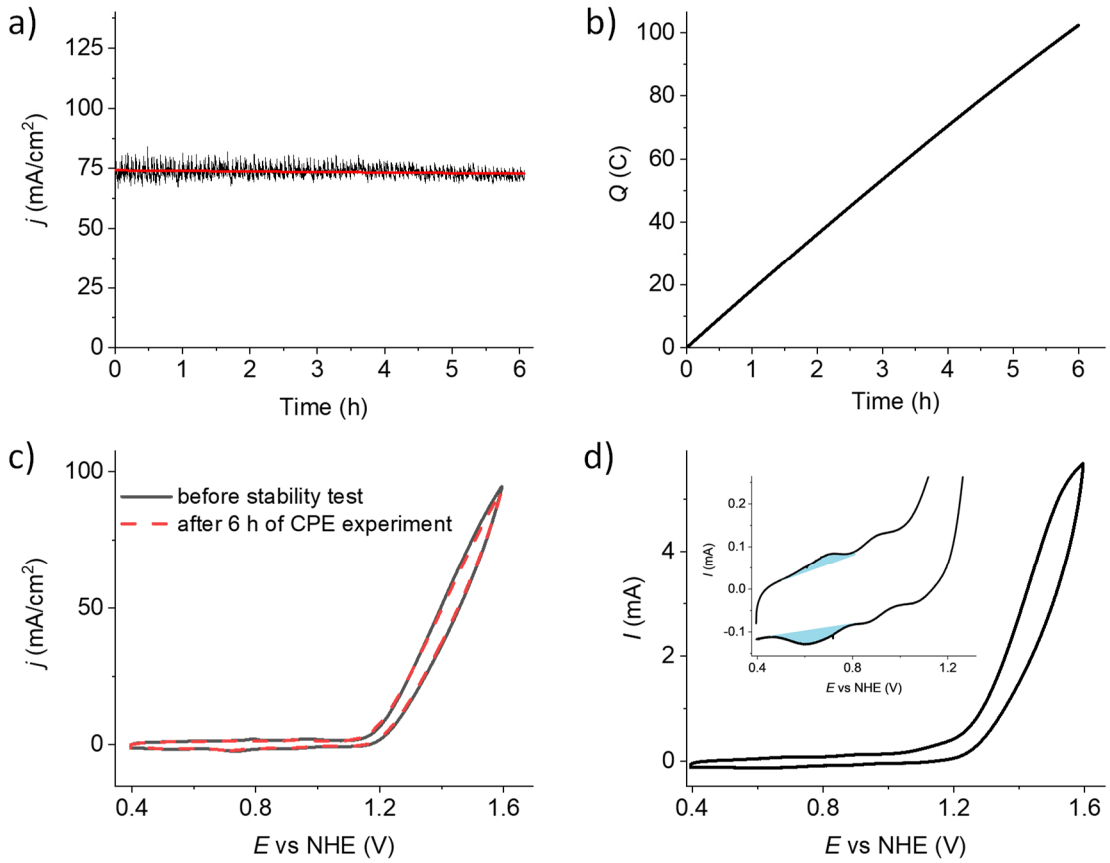

Figure 45: a) Stability test by controlled potential electrolysis (CPE) experiment of activated electrode **act-MC3@CNT@GC** in a 1 M phosphate buffer (pH 7) at 1.6 V vs NHE for 6 h. Red line shows the average current density. b) Charge flowing through the system during CPE for 6 h. c) CV of **act-MC3@CNT@GC** electrode before (black line) and after (red dotted line) CPE experiment (scan rate: 100 mV/s). d) CV of **MC3@CNT** electrode before activation. The amount of total Ru on the surface of the electrode was determined by integration of regions marked in blue.

As illustrated with the red line in Figure 45a, the average current density is highly stable. Only a negligible loss can be observed and 97% of the initial current density still remains after 6 hours. This is further demonstrated by the linear increase of the current flowing through the system (Figure 45b). CVs recorded before and after the CPE shows that no significant changes can be observed after 6 hours and the maximum current densities remain equal, confirming the high stability of the prepared electrode (Figure 45c).

Assuming that all electrons passing through the system are involved in the catalytic reaction, the amount of generated oxygen can be calculated from the charge after 6 hours (Figure 45b).

According to the water oxidation reaction and assuming 100% Faraday efficiency, four electrons are used to generate one molecule of oxygen. Therefore, the amount of generated oxygen was calculated from the passed charge by employing Faraday law (equation 11). For the presented experiment, $2.6*10^{-4}$ mol of oxygen have been generated. To calculate the TON, this value needs to be set in relation to the amount of catalyst on the electrode. Assigning the first wave in the initial CV before activation to the one-electron transfer process of the $Ru^{III/II}$ oxidation in every Ru(bda) center of the trinuclear Ru(bda) complex **MC3**, the initial amount of Ru on the surface of the **MC3@CNT@GC** electrode can be determined by integrating the area under the wave as described in equation 12:

$$Q_{av}(C) = \frac{Q_{ap,Ru^{III/II}} + Q_{cp,Ru^{III/II}}}{2} \qquad \text{(eq. 12)}$$

where Q_{av} is the average of the charge in the $Ru^{III/II}$ redox process by taking the charge under the anionic (ap) and cathodic peak (cp) (as shown by the blue area in Figure 45d) and dividing by sum of the number of electrons involved in the process. Applying this method, the amount of Ru centers on the electrode before the activation was determined to be 5.35×10^{-10} mol. By dividing the amount of generated oxygen by the number of Ru centers on the electrode, a remarkably high TON of 0.5 million is obtained. Referring to the amount of activated Ru centers on the electrode (1.44×10^{-10} mol, for the determination see Figure 46) which should be mainly responsible for the catalysis, a TON as high as 1.8×10^{6} was obtained. Ru(tda) polymers anchored onto CNTs by the same approach result in a TON of 2×10^{5} (applied current: 1.45 V, time = 12 h), [234] while a TON of 1×10^{4} has been reported for Ru(bda) complexed anchored to CNTs by pyrene-modified pyridine ligands.[233]

5.2.4 FOWA for the determination of TOF

The foot of the wave analysis (FOWA), first developed by Savéant and coworkers[291] and applied for electrocatalytic reduction processes[292-296] and later adapted to the electrochemical water oxidation,[161] was performed to gain more insights into the kinetics of the electrocatalytic water oxidation reaction performed by **act-MC3@CNT@GC**. Since the high activity of the latter is attributed to the newly formed active species, only the amount of activated catalyst on the electrodes surface was taken into account. For the estimation of the concentration of the active species, the integration of the first wave in the anodic scan of the CV experiments was used. As it could be identified by comparing CV and DPV measurements of the initial and activated species, this wave could be clearly assigned to the $Ru^{III/II}$ electron transfer process of activated Ru centers and is not present in the unactivated state (Figure 46a,b; signal used for

determining the charge is marked in orange box). Due to an overlap of the signals of both species in the cathodic scan, only the anodic peak could be used for integration.

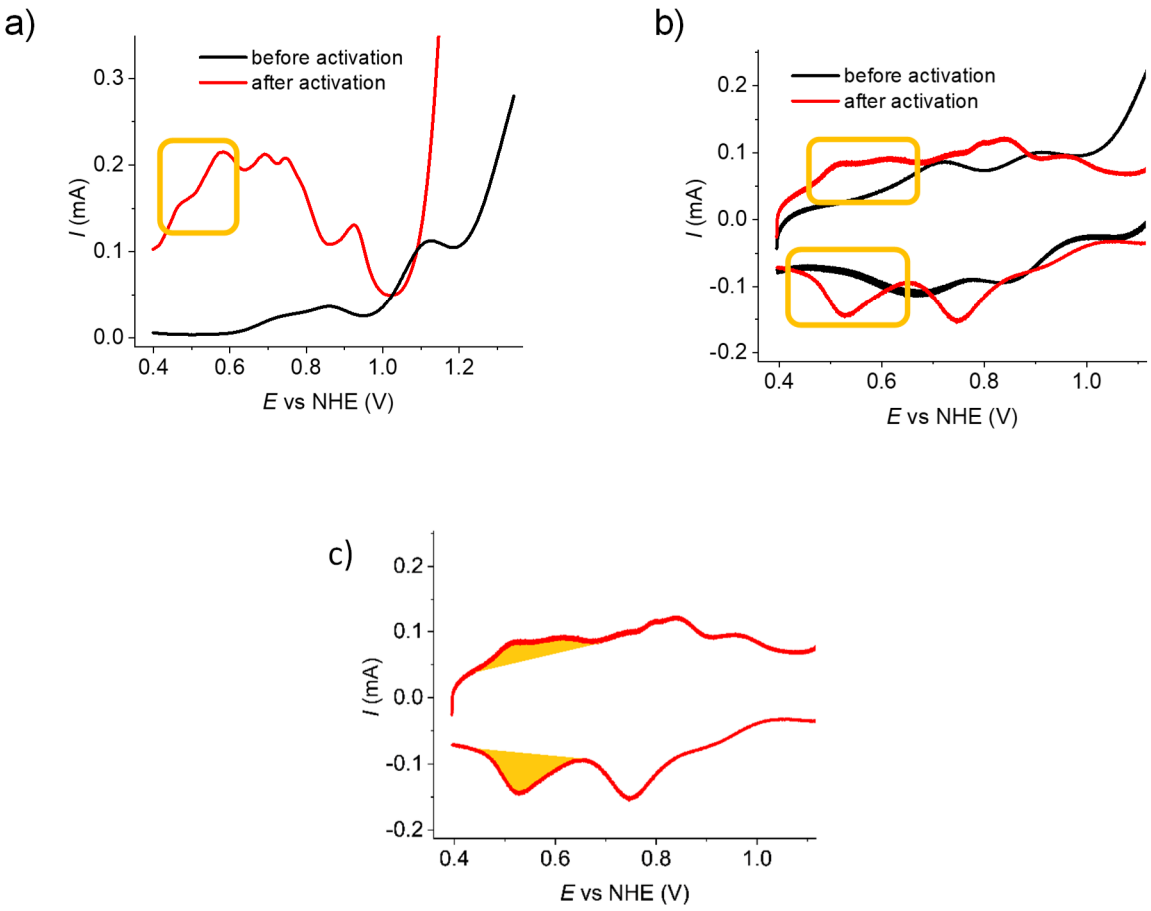

Figure 46: a) DPV and b) CV of **MC3@CNT@GC** before activation (black line) and after activation (red line) in a 1 M phosphate buffer (pH 7) with a CV scan rate of 100 mV/s. The orange frames show the signal used for the integration of activated species. c) An example of the area of the CV (red curve) which was used for the estimation of the charge. The charge of the $Ru^{III/II}$ couple of the activated species was determined by taking the average of the charge under the anodic and cathodic scan (area marked in orange).

For the estimation of the loading of the active species, the average of the integration of the first waves in the anodic scan and the last wave of the cathodic scan of the CV experiments was used to calculate the charge (*Q*) corresponding to the $Ru^{III/II}$ electron transfer process of activated Ru centers (Figure 46). Due to a slightly overlap of the redox waves, values of activated catalyst might have been overestimated. The corresponding charge belonging to the activated Ru centers was converted to moles of Ru according to the Faraday law as described above (equation 11).

Electrodes with different loadings of the catalyst were prepared, activated and subsequently CV experiments were performed (Figure 47a) in order to apply the FOWA methodology.

The surface coverage Γ of the electrode of was determined using the following equation:

$$\Gamma(mol * cm^{-2}) = \frac{Q}{x\ S\ F} \quad (7)$$

where Q is the charge corresponding to the $Ru^{III/II}$ electron transfer process of the activated Ru centers, x is the number of electrons involved in the oxidation process, S is the geometric surface area and F is the Faraday constant. The amount of active catalyst on the electrodes surface proved to be in a linear relationship with the maximum current densities determined at 1.45 V (Figure 47b). This is in accordance with expected behavior of catalysts functioning via WNA mechanism.

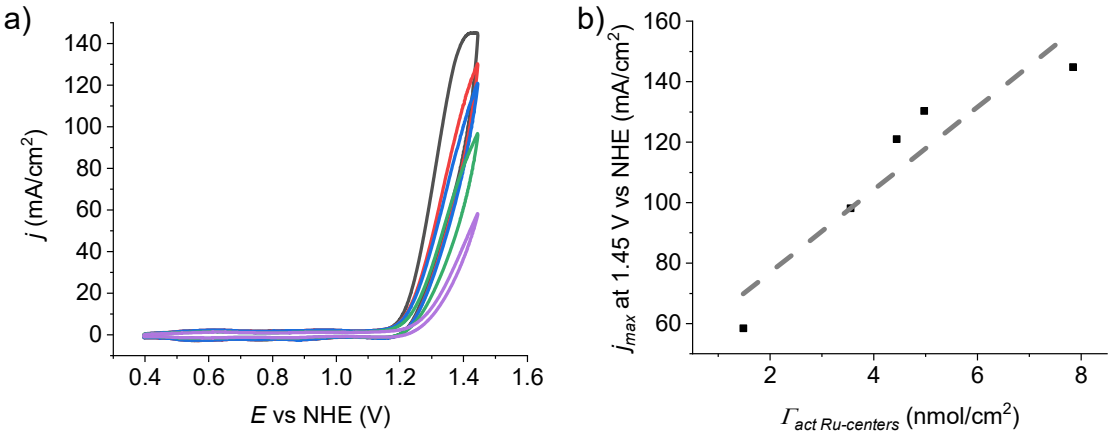

Figure 47: a) CVs (scan rate: 100 mV/s) of **MC3@CNT@GC** electrodes after activation with different loadings of activated Ru-centers (purple: 1.0 nmol/cm², green: 2.4 nmol/cm², blue: 2.9 nmol/cm², red: 3.4 nmol/cm², black: 5.3 nmol/cm²) in a 1 M phosphate buffer solution (pH 7). b) Plot of the maximum current densities versus the surface concentration of activated Ru centers.

To investigate the mechanism in detail and extract kinetic data, the first data points of the catalytic slope of one CV cycle (Figure 48, blue dots) were used. By assuming a hetero-WNA mechanism taking place on the electrodes' surface, these data points were plotted according to:

$$\frac{i}{Q_{Ru}} = \frac{k_{WNA}}{1 + (\frac{F(E^{0,ap} - E)}{R\ T})} \quad \text{(eq. 13)}$$

$$TOF_{max} = k_{WNA} \quad \text{(eq. 14)}$$

In these equations, *i* is the current intensity in the CV, Q_{Ru} is the charge under the anodic wave of the activated Ru^{III}/Ru^{II} couple, *R* is the gas constant, *T* is the temperature, *F* is the Faraday

constant and $E^{0,ap}$ is the apparent potential of the precatalytic wave extracted from the DPV. The obtained k_{WNA} values for each electrode correspond to the apparent maximum TOF (s^{-1}). The gradient of the received curve from equation (13) was fitted by linear regression (Figure 48a, inset; red line). Its slope represents the apparent pseudo-rate constant (k_{WNA} value) at the foot of the catalytic wave for each electrode with different catalyst concentrations, which equals the TOF_{max} value (equation 14) The independence of k_{WNA} values versus loading of the activated Ru centers (Figure 48b) is a clear indication of a single mechanism operating in this system.

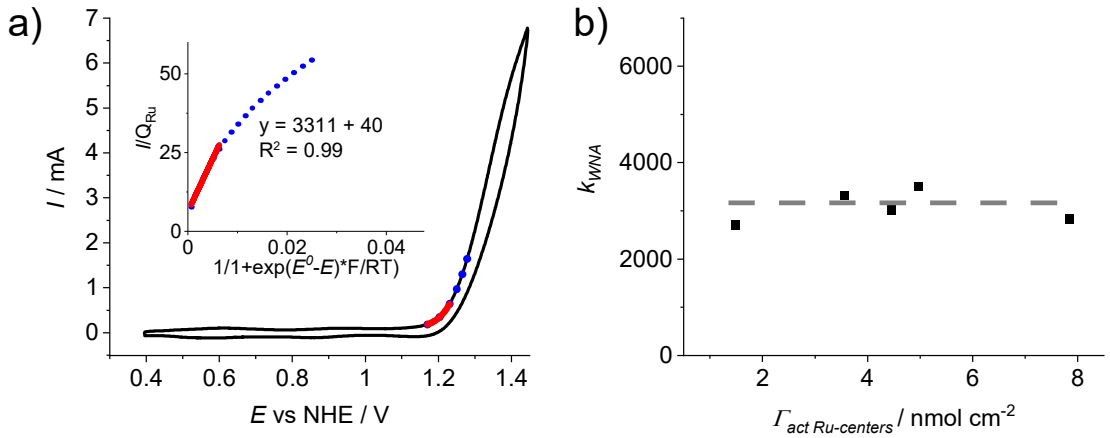

Figure 48: a) The solid black line shows the second cycle of the CV of **act-MC3@CNT@GC** in a 1 M phosphate buffer (pH 7) for a surface concentration of the active species of $\Gamma_{act\ cat}$ = 2.4 * 10^{-9} mol/cm^2. The region used for the FOWA is indicated by the blue dotted line. The red solid line at the foot of the wave shows the area which is used for the determination of the apparent rate constant. Inset: i/Q_{Ru} vs 1/(1+exp(E^0-E)*F/RT) plot assuming a WNA mechanism for the immobilized macrocyclic catalyst. The apparent rate constant k_{WNA} at the foot of the wave was obtained by fitting the points represented by the solid red line. b) The k_{WNA} values obtained from i/Q_{Ru} vs 1/(1+exp(E^0-E)*F/RT) plot (a, inset) at the corresponding surface concentrations of the active species are shown as black data points. Independence of the k_{WNA} values of the surface concentration indicated by the grey dashed line is in agreement with the assumption of a WNA mechanism on the surface.

Further, the first-order kinetics with regards to the catalyst's concentration agrees with a WNA mechanism taking place for **act-MC3@CNT@GC**. An average apparent rate constant of k_{WNA} = TOF_{max} = (3197 ± 395) s^{-1} was obtained (Figure 48b). Table S5 shows an comparison of different Ru based WOCs immobilized on anodes. It has been reported in literature that a $Ru(bda)(L)_2$ catalyst (L = functionalized pyridine ligand), which oxidizes water via a bimolecular I2M O-O bond formation step in homogeneous catalysis, not only drops in activity when immobilized on an electrode surface changing to a WNA mechanism (FOWA: TOF_{max} = 53 s^{-1} homogeneous; TOF_{max} = 1.9 s^{-1} heterogeneous), but also ends up decomposing to RuO_2.[161, 228, 286] In contrast, a $Ru(tda)(L)_2$ catalyst which functions through a WNA mechanism in homogeneous catalysis does not undergo any significant change upon immobilization (FOWA: TOF_{max} = 8000 s^{-1} homogeneous; TOF_{max} = 9000 s^{-1} heterogeneous).[278, 286] The latter is also

the case for our trinuclear Ru(bda) macrocycle **MC3**, which was previously reported to function through a WNA mechanism.[42]

5.3 Discussion

Since activation of **MC3** is only observed upon its adsorption on MWCNTs, the strength of non-covalent interactions with the CNT surface is assumed to play a crucial role during this process. Therefore, semiempirical calculations using graphene-like surface as a model have been performed.[5] These theroretical calculation indicated that structural changes of **MC3** upon activation are key steps in forming a more active species. For the following calculations, a hexagonal graphene sheet was used as a model for the interactions of the catalyst with the CNT surface. Semiempirically optimized structures of **MC3** in different relevant conformations have been optimized (Figure 49).

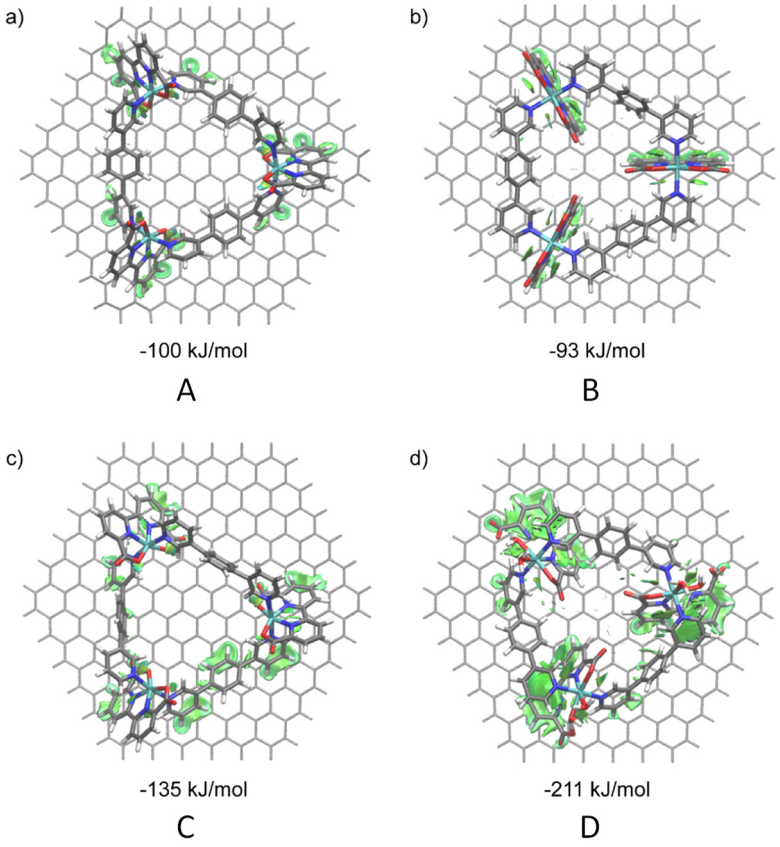

Figure 49: Optimized structures of a)-c) different conformations of **MC3** on a hexagonal graphene sheet and d) proposed activated species as also depicted in Figure 50. Under each structure, the interaction energy between the catalyst and the surface model is provided as determined by relaxed scans of the catalyst-surface distance. Intermolecular interactions are displayed using the NCIPLOT.

[5] Structure optimizations and calculations shown in Figures 49 – 51 have been performed by Dr. Joachim Lindner, Universität Würzburg.

Structure **A** corresponds to the C3-symmetric structure of **MC3**, which represents the conformation that has been found to be the lowest-energy structure in solution. Structure **B** results from a rotation of 90° of all three Ru(bda) units in such a way that four CH-pi interactions are generated per Ru(bda) unit. This structure corresponds to the interaction scheme as postulated by the Llobet group for 1D-Ru(tda) polymers.[234] However, distances between bridging ligands and the surface are unfavorably large in the **MC3** molecule. A closer contact to the surface is achieved in structure **C** for one of the three bridging ligands, while symmetry is lifted. Structure **D** represents a symmetric structure in which all three bda ligands are twisted around their central C-C bonds. Accordingly, one carboxy and one pyridine unit are removed from the ligand sphere of every Ru center. The free coordination sites are filled with water to yield three Ru centers of 6-coordinate diaqua complex centers. Remarkably, the rotated parts of the bda ligands can interact with the surface and bridging ligands. A detailed side view of this structure is presented in Figure 50.

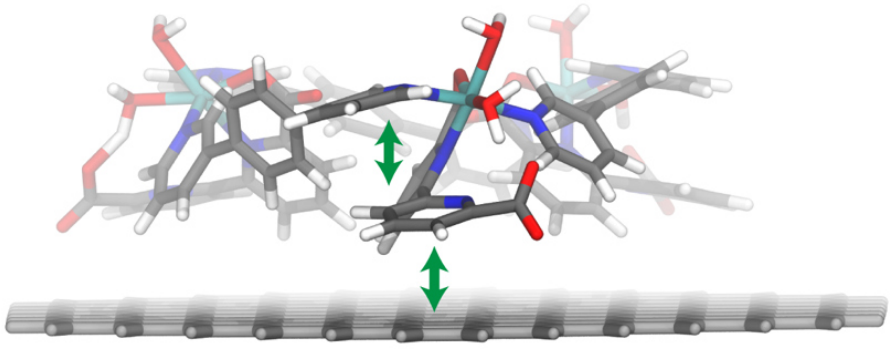

Figure 50: Optimized structure based on semiempirical calculations of the proposed activated species **act-MC3@CNT@GC** (grey: carbon, white: hydrogen, blue: nitrogen, red: oxygen, turquoise: ruthenium). A hexagonal graphene sheet has been used as a model for the graphitic surface of MWCNTs. Green double-headed arrows indicate attractive π-π interactions.

The partial decoordination of the bda ligands as shown in Figure 50 and Figure S63, allowing for the coordination of additional water molecules to Ru, introduces additional stabilizing π-π interactions compared to different possible conformations of **MC3** (Figure 49). Owing to the presence of multiple acidic protons in the environment of aqua-coordinated Ru, oxidation of this species up to Ru^{V} is possible without total charge buildup (Figure S64). Such diaqua species would explain the observed, notably changed redox behavior of **act-MC3@CNT@GC** compared to the non-activated **MC3@CNT@GC** and can play a role in electrochemical heterogeneous water oxidation by Ru(bda) macrocycle.

A diaqua species of a Ru-based water oxidation catalyst has already been reported in 2010 by Llobet and co-workers.[297] In the catalytic cycle of $Ru(bpy)_2(H_2O)_2^{2+}$, a formal four-step oxidation up to a Ru^{VI} state is suggested, stabilized by two coordinated $-O^{2-}$ species. A water nucleophilic attack mechanism was proposed to be the lowest energy path based on

calculations. To investigate the mechanism of water oxidation with the Ru(bda) diaqua species generated on the surface, a monomeric *cis*-$Ru^{II}(H_2O)_2$(bda-*κ*-NO)$(py)_2$ model compound has been applied. A proposed mechanism based on DFT calculations is presented in Figure 51.[298]

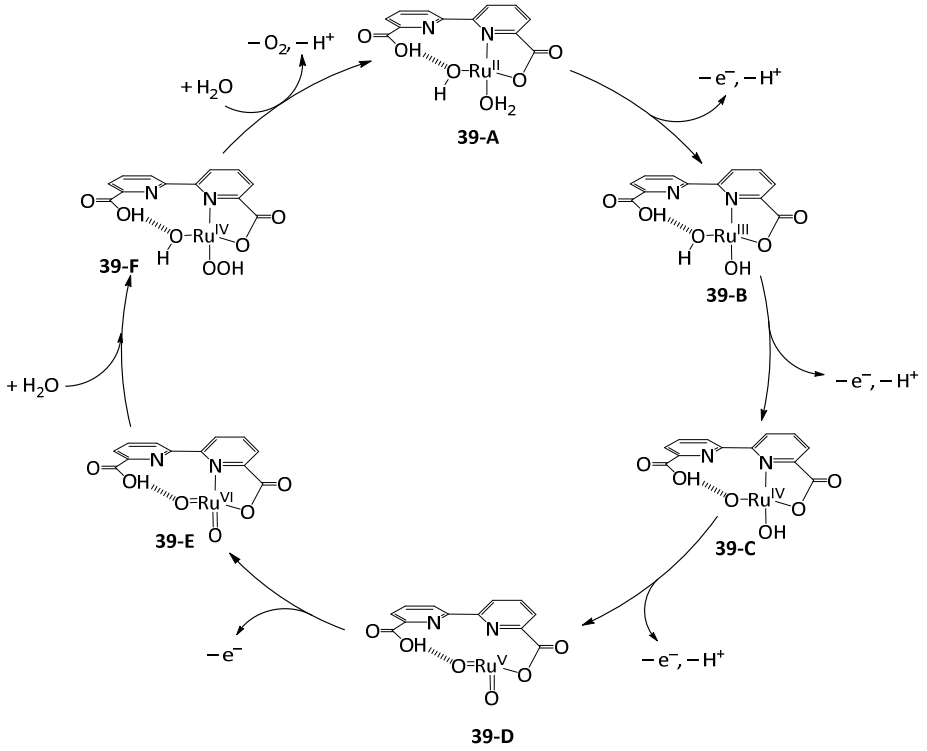

Figure 51: Proposed catalytic cycle of water oxidation with the Ru(bda) diaqua species **39-A** generated on the surface. Axial pyridine ligands are omitted for clarity.

The coordination of two aqua ligands in the Ru^{II} state (**39-A**) leads to a decoordination of one nitrogen atom of the equatorial bipyridine ligand stabilized by interactions with the graphitic surface, while the dangling carboxyl group can stabilize one of the aqua ligands by hydrogen bonding. After three consecutive proton-coupled electron transfers, a Ru^{V} state (**39-D**) is reached with a completely decoordinated bipyridine unit and two oxo-groups coordinated to the Ru center. A following one-electron oxidation to the formal Ru^{VI} state (**39-E**) is attacked in a nucleophilic fashion by a water molecule and the oxidation state is reduced to Ru^{IV} (**39-F**). The interaction of a second water molecule with species **39-F** generates oxygen while the starting complex is regenerated. The important role of the dangling carboxy groups for stabilizing intermediates in the suggested catalytic cycle would explain the inactivity of the catalyst at pH below 5, as the carboxylate would be protonated and not available for proton sharing.

5.4 Conculsions

In conclusion, it has been shown that the immobilization of the **MC3** macrocycle on CNTs is possile without any further fuctionalization of the catalyst. AFM and SEM images supported by EDX analysis comfirmed for the first time the direct anchoring to the graphene-like surface. Taking advantage of the intrinsic properties of CNTs, glassy carbon electrodes with anchored **MC3** catalyst were prepared. Electrochemical investigations have shown that the redox potentials of the anchored catalyst compared to homogeneous measurements do not undergo any significant changes. However, upon performing multiple CV cycles to a potential high enough to initiate the water oxidation process, changes can be observed. After 100 cycles at 1.3 V, an equilibrium state was reached and a newly formed species with much higher catalytic activities was obtained. Such electrochemical activation of a Ru(bda) complex that has been transformed into a more active species by repetitive CV cycles was indeed unprecedented and opens up a new perspective for R(bda) WOCs. A current density as high as 186 mA/cm^2 was observed, which is among the highest values reported so far for molecular Ru catalysts anchored on solid state anodes. A Faraday efficiency of 99% demonstrated that all electrons flowing through the system are indeed participating in the water oxidation reaction and no other side processes take place. The absence of RuO_2 as a highly active degradation product of **MC3** could be excluded unambiguously by XAS spectroscopy. A remarkably high TON value of half a million obtained by CPE experiments confirmed the stability of the hydride anode. The observed TOF_{max} of 3200 s^{-1} demonstrates that the **act-MC3@CNT@GC** electrodes are efficient devices for electrochemically driven heterogeneous water oxidation.

Chapter 6

—

Summary

Climate change as the major challenge of the 21st century has gained increasingly more public attention in the last years particularly through activities of the younger generation. Their commitment in climate movements rises public awareness to the urgency of replacing fossil fuels as predominant origin of harmful emissions. In view of the need for environmentally benign renewable and storable energy sources, production of hydrogen by using sunlight to split water into its components is a promising approach (*Chapter 2.1*). However, the water oxidation reaction providing the required reducing equivalents for transforming protons into molecular hydrogen comprises a challenging four electron transfer process, which demands for robust and efficient catalysts (*Chapter 2.2*). Intensive research on molecular water oxidation catalysts (WOCs) in the last decades revealed that catalysts containing the catalytically active Ru(bda) fragment (bda: 2,2'-bipyridine-6,6'-dicarboxylate) exhibits high efficiencies in water oxidation.[41] Based on these findings, Würthner and co-workers developed a supramolecular approach of combining three Ru(bda) units in a macrocyclic fashion.[42] These macrocyclic Ru(bda) complexes exhibit outstanding catalytic activities with significantly higher turnover frequency (TOF) and turnover number (TON) values as well as improved stability compared to the mononuclear reference catalyst Ru(bda)$(pic)_2$. Interestingly, a hydrogen-bonded water network in the cavity of the macrocycle was presumed to be responsible for fast proton-coupled electron transfer (PCET) steps and accelerated reaction rates. Furthermore, mechanistic investigations revealed a change of catalytic pathway from a bimolecular I2M (interaction of two M-O units) for the mononuclear reference complex Ru(bda)$(pic)_2$ to a monomolecular WNA (water nucleophilic attack) mechanism in trinuclear macrocyclic WOC **MC3** (*Chapter 2.3*), which make the latter particularly interesting for use in devices.

One of the aims of this thesis was the study of axial ligand exchange processes in Ru(bda)-type complexes to gain insight into kinetic and thermodynamic reaction conditions in the synthesis of macrocyclic Ru(bda) WOCs. Based on the results, a new di- and a new tetranuclear Ru(bda) macrocycle and their properties in homogeneous water oxidation have

been explored. A major goal of this thesis was the investigation of electrochemically-driven heterogeneous water oxidation of the **MC3** macrocycle, which has been previously well-characterized in structure as well as in homogeneous catalysis.[42, 216]

To investigate the formation of **MC3**, ^{1}H NMR experiments monitoring the reaction of Ru(bda)(dmso)$_2$ with respective dipyridyl ligands were performed. By following the increase of product formation based on an internal standard, it was found that under the applied reaction conditions (CD_2Cl_2/MeOD 5:1, 55°C, 12 h), the desired products are formed in a kinetic pathway. Thus, to study axial ligand exchange processes in Ru(bda) complexes, different mononuclear Ru(bda)L_2 model compounds were deployed. An underlying dissociative exchange mechanism was verified, being beneficial for building up large structures in a thermodynamic equilibrium as the rate of the ligand exchange is independent of the amount of free exchanging ligand in the reaction mixture. Conditions for fast ligand exchange have been explored and applied for the synthesis of new di- and tetranuclear Ru(bda) macrocycles **OEG-MC2** and **OEG-MC4** at elevated temperatures (Figure 52a). **OEG-MC4** represents the only tetrameric as well as the largest macrocyclic WOC known to date. Oligoethylene glycol chains (OEG) were introduced into the axial ligands for improved solubility. The highly symmetrical and thus cyclic structure of the new macrocycles could be verified by the complete absence of signals assignable to end groups of possible linear coordination polymers in ^{1}H NMR spectra. The complementary **OEG-MC3** macrocycle containing three Ru(bda) units and identical side chains in the bridging ligands was synthesized for comparison. Analysis of the redox potentials showed little deviation in the three macrocycles. However, spectroelectrochemically investigations revealed a strong transition at 700 nm in the Ru^{III} state, previously explained based on theoretical and experimental evidence by a water network within the cavity of the **MC3** macrocycle[43], only for the tri- and tetranuclear macrocycles, but not for dinuclear one (spectroelectrochemically investigations exemplarily shown for **OEG-MC4** in Figure 52b).

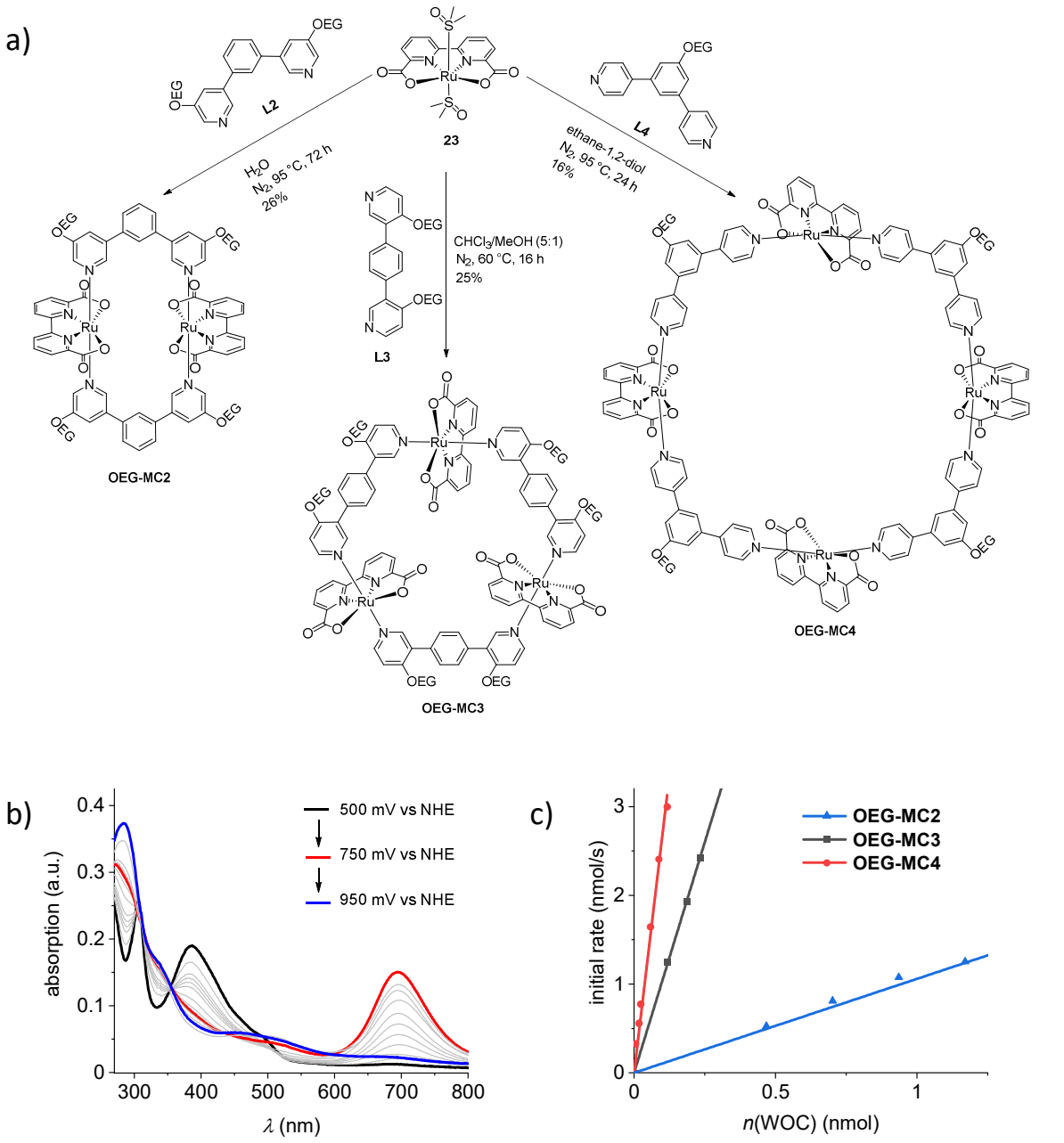

Figure 52: a) Chemical structures of di-, tri-, and tetranuclear macrocycles **OEG-MC2**, **OEG-MC3** and **OEG-MC4**. b) Spectroelectrochemical investigations of **OEG-MC4** indicating the presence of a hydrogen-bonded water network in the cavity as observed for **MC3** macrocycles. c) Initial rates of **OEG-MC2**, **OEG-MC3** and **OEG-MC4** in photocatalytic water oxidation. For detailed experimental conditions, see *Chapter 4*.

The largest tetranuclear macrocycle **OEG-MC4** showed superior catalytic activity with a total value of TOF = 42 s^{-1} in chemical water oxidation (TOF per Ru unit: 10.5 s^{-1}) at pH 1 driven by cerium(IV) ammonium nitrate (CAN) in comparison to the tri- and dinuclear WOCs. While the activity of **OEG-MC3**[215] was found to be in a similar range (total TOF of 26 s^{-1}, TOF per Ru unit: 8.7 s^{-1}), a lower TOF was observed for **OEG-MC2** (total TOF of 12 s^{-1}, TOF per Ru unit: 6 s^{-1}). All three OEG-functionalized macrocycles are less stable than the unfunctionalized parent macrocycle **MC3**.[216] The observed TONs of for tri- and tetranuclear complexes, 2200

and 2870, respectively, are similar to **MC3** (5300),[216] whereas the TON of **OEG-MC2** (200) is more than one order of magnitude lower. Furthermore, investigations in photocatalytic water oxidation applying a three-component system with $Ru(bpy)_3^{2+}$ as a photosensitizer and sodium persulfate as electron acceptor at pH 7 were performed (Figure 52c). A similar trend in efficiency as in chemical water oxidation was observed. An excellent TOF value of 23 s^{-1} (5.8 s^{-1} per Ru unit) was observed for **OEG-MC4**, being one of the highest TOF values reported so far for Ru(bda) catalysts in photocatalysis, while **OEG-MC3** showed a lower TOF of 10 s^{-1} (3.3 s^{-1} per Ru unit), which is almost identical to that of **MC3** (TOF of 11 s^{-1}, 3.7 s^{-1} per Ru unit).[216] Moreover, TON values of tetra- and trinuclear WOCs (500 and 400, respectively) are in the same range as unfunctionalized **MC3** (TON = 430).[216] Interestingly, in contrast to the larger complexes, the catalytic activity of the dinuclear **OEG-MC2** did not show any benefit of the macrocyclic structure as an identical TOF of 0.55 s^{-1} per Ru unit to that of mononuclear $Ru(bda)pic_2$ (TOF = 0.6 s^{-1}) was observed. It was presumed that the presence of a hydrogen-bonded water network in the cavity of the tri- and tetranuclear WOCs is responsible for their good performance, whereas the absence of these feature in the dinuclear complex results in inferior efficiency. As in chemical water oxidation, the dimeric complex **OEG-MC2** also lacks in stability (TON = 36) by about one order of magnitude compared to the larger WOCs (TON = 400 and 500 for **OEG-MC3** and **OEG-MC4**, respectively).

In the context of going beyond fundamental laboratory research, the investigations on electrochemically-driven heterogeneous water oxidation with the WOC **MC3** reported in *Chapter 5* represents a step forward to practical application. These experiments were performed in collaboration with Prof. Antoni Llobet at the *Institut Català d'Investigació Química* in Tarragona, Spain. Multi-walled carbon nanotubes (MWCNTs) were applied as supporting materials for immobilizing the catalyst **MC3** to a glassy carbon electrode (Figure 53a). Drop casting of the **MC3@CNT**s dispersion on glassy carbon electrodes resulted in hydride anodes. Presumably, due to the fact of having multiple Ru(bda) units connected by aromatic bridging ligands, the trimeric macrocycle **MC3** has a strong affinity to adhere to the CNT surface through CH-π and π-π interactions. Indeed, this approach demonstrated for the first time that immobilization of Ru(bda) catalysts on surfaces is possible without special functionalization of catalysts. AMF images clearly showed that the **MC3** molecules are anchored to the surface of the CNTs (Figure 53b).

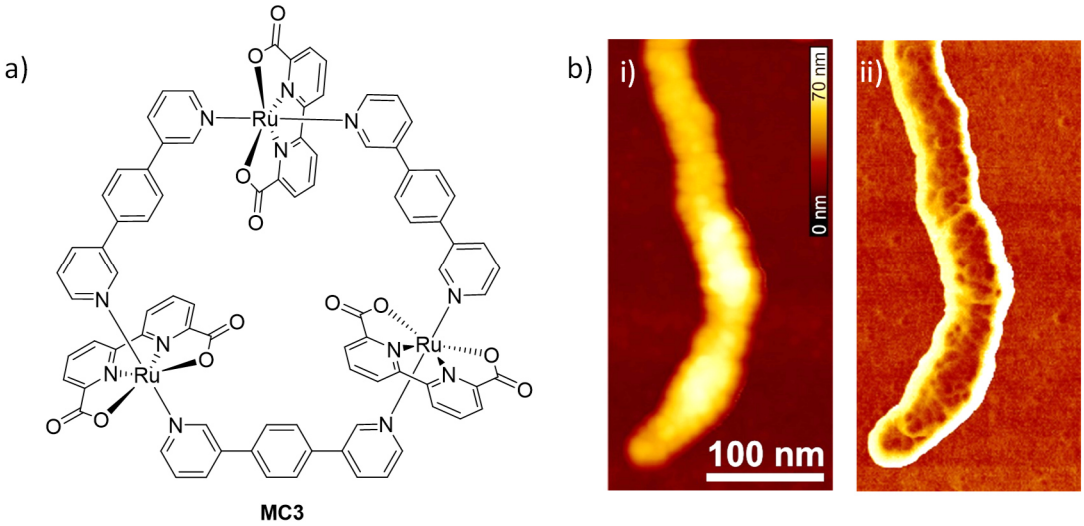

Figure 53: a) Structure of the trimeric Ru(bda) macrocycle **MC3**. b) AFM images obtained after spin coating a dispersion of **MC3@CNT** in a THF/TFE (1:0.1) mixture onto a silicon waver: i) height of CNT decorated with **MC3**, *Z* scale is 70 nm, ii) phase image of CNT decorated with **MC3**.

It was found that upon repetitive CV cycling experiments, the anchored catalyst was partly transformed into an activated species. Hereby, a four-fold increase in catalytic current towards water oxidation was achieved (Figure 54a). A remarkable maximum current density (*j*) of 186 mA/cm^2 was observed, being to the best of my knowledge the highest value reported so far for immobilized molecular Ru(bda) WOCs. Stability of the obtained anode was investigated in controlled potential electrolysis (CPE) experiments. A constant potential was applied and the remarkable stability of the activated electrode was demonstrated by only negligible decrease in the corresponding current density observed over 6 hours, while 97% of the initial activity was sustained (Figure 54b). Furthermore, the stability of the activated catalyst during the CPE experiment was determined based on the amount of catalyst present at the electrode. An impressive TON of more than a million turnovers was obtained when referring to the amount of activated catalyst.

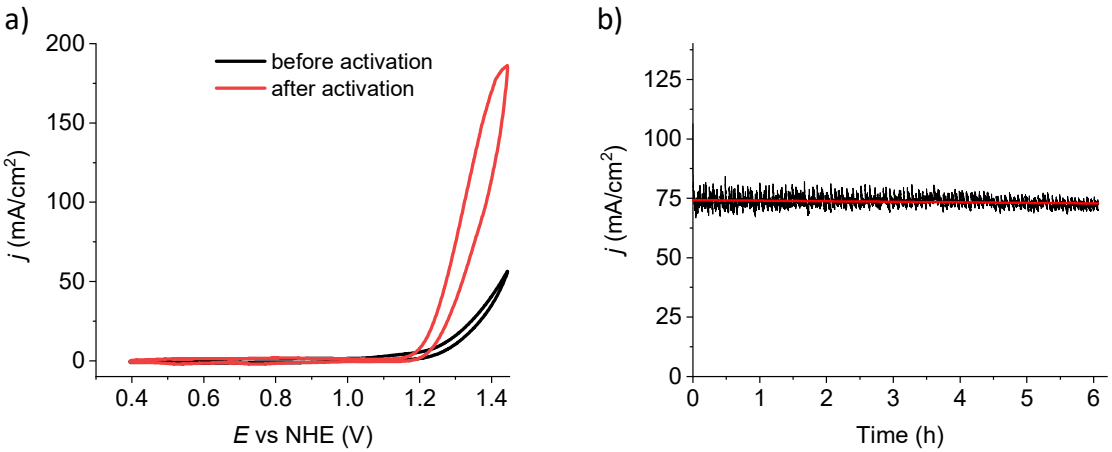

Figure 54: a) CV of **MC3@CNT**s before (black line) and after (red line) activation in 1 M phosphate buffer solution (pH 7). b) Stability test by CPE experiment at 1.6 V in a 1 M phosphate buffer solution (pH 7). Red line indicates the average current density (*j*) during 6 h. For detailed experimental conditions, see *Chapter 5*.

Moreover, to determine the efficiency of the catalyst and exclude that currents originate from any undesirable side reactions, the Faraday efficiency of the activated electrode was determined. Given only a minor deviation, the result of Faraday efficiency of 99% demonstrates selective and quantitative water oxidation without side reactions. Applying the Foot of the Wave Analysis (FOWA) and studying the very begining of the catalytic process of the activated species revealed that the efficiency of the activated catalyst with a TOF of 3200 s^{-1} ranks among the highest reported values for immobilized Ru catalysts.

To investigate the nature of the activation process and the underlying transformation, which takes place during consecutive CV cycles, theoretical calculations were performed in by Dr. Joachim Lindner. These studies, which were interpreted in collaboration in agreement with the electrochemical data, revealed that the addition of two water molecules to the ruthenium center during the activation process, as shown in optimized calculated structure in Figure 55, is responsible for the observed shift in the redox potentials compared to unactivated **MC3** as well as higher catalytic currents.

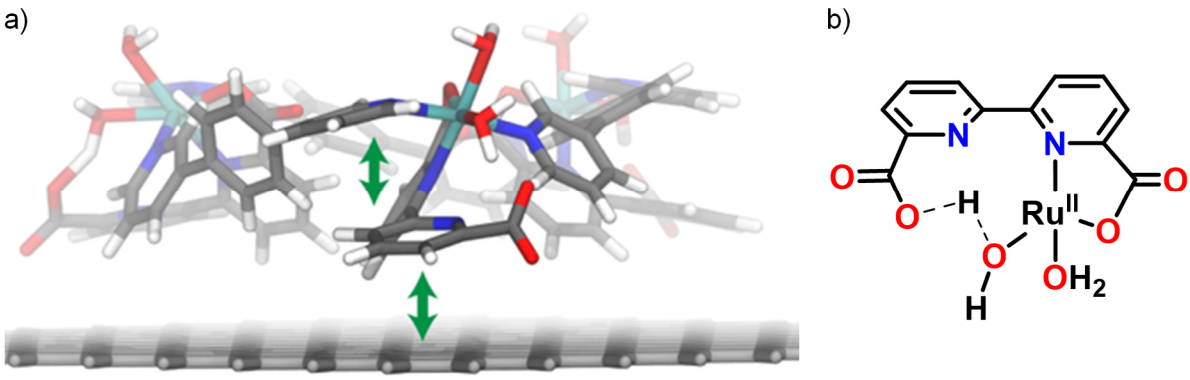

Figure 55: a) Side view on optimized activated **MC3** species anchored to graphitic surface based on semiempirical calculations. b) Schematic illustration of activated Ru-diaqua species. Axial ligands have been omitted for clarity.

Thus, for the first time, the activation of Ru(bda) species by formation of highly efficient Ru(bda)-diaqua species in electrocatalysis could be demonstrated. Moreover, based on theoretical calculations, a new reaction pathway for water oxidation following the WNA-type mechanism could be proposed that comprises decoordination of one pyridyl unit of the equatorial bda ligand enabling coordination of additional water molecules to the Ru center.

In conclusion, this work presents detailed ^{1}H NMR studies on the ligand exchange process of Ru(bda)L_2 complexes providing valuable mechanistic insights. Based on these studies, reaction conditions for the formation of Ru(bda) macrocycles in thermodynamic equilibrium could be explored and two novel supramolecular di- and tetranuclear macrocyclic Ru(bda) complexes could be synthesized. It was found that the largest tetranuclear Ru(bda) macrocycle is the most efficient one in the present homologous series in homogeneous water oxidation catalysis with an excellent TOF in photocatalysis, being among the best values reported for Ru(bda) WOCs in light-driven water oxidation. The high photocatalytic efficiency of the tetranuclear WOC is presumably due to the formation of a hydrogen-bonded water network in the macrocyclic cavity. Extending water splitting investigations to heterogeneous systems, trinuclear macrocycle **MC3** was immobilized on glassy carbon electrodes by applying CNTs as a supporting semiconducting material. A transformation into an activated species was observed upon multiple CV cycles, going along with remarkably high efficiencies for water splitting. A new catalytic pathway with the proposed Ru(bda)-diaqua species generated by electrochemical activation was suggested based on theoretical calculations. Undoubtedly, these investigations of activation processes with resulting high activities in heterogeneous catalysis contribute to a deeper understanding of operating modes in molecular WOCs and open the doors to new approaches for the design of efficient catalysts. Combined with strong anchoring strategies as presented in this work, this will allow for promising applications in water-splitting devices.

Chapter 7

—

Zusammenfassung

Der Klimawandel als die gesellschaftliche Herausforderung des 21. Jahrhunderts ist der Allgemeinheit in den letzten Jahren insbesondere durch Aktivitäten der jüngeren Generation mehr und mehr ins Bewusstsein gerückt. Mit ihrem Engagement in Klimabewegungen machen sie auf die Dringlichkeit aufmerksam, fossile Brennstoffe als Hauptverursacher schädlicher Emissionen zu ersetzen. Angesichts des Bedarfs an umweltfreundlichen erneuerbaren und zugleich speicherbaren Energiequellen ist die Erzeugung von Wasserstoff unter Verwendung von Sonnenlicht zur Spaltung von Wasser in seine Bestandteile ein vielversprechender Ansatz (*Kapitel 2.1*). Die Wasseroxidationsreaktion, die die erforderlichen Reduktionsäquivalenten für die Umwandlung von Protonen in molekularen Wasserstoff liefert, umfasst jedoch einen herausfordernden Vier-Elektronen-Transferprozess, der robuste und effiziente Katalysatoren unverzichtbar macht (*Kapitel 2.2*). In den letzten Jahrzehnten durchgeführte ausführliche Untersuchungen an molekularen Wasseroxidationskatalysatoren (WOCs, engl: water oxidation catalysts) haben gezeigt, dass Katalysatoren, die das katalytisch aktive Ru(bda) Fragment (bda: 2,2'-bipyridin-6,6'-dicarbonsäure) enthalten, eine hohe Effizienz in der Wasseroxidation aufweisen.[41] Basierend auf diesen Erkenntnissen entwickelten Würthner und Mitarbeiter einen supramolekularen Ansatz, bei dem drei Ru(bda) Einheiten makrozyklisch organisiert werden.[42] Diese makrozyklischen Ru(bda) Komplexe zeigten außerordentlich hohe katalytische Aktivitäten mit bedeutend höherer Umsatzfrequenz (TOF, engl: turnover frequency) und Umsatzzahl (TON, engl: turnover number) sowie einer verbesserten Stabilität des Katalysators im Vergleich zur einkernigen Referenzverbindung $Ru(bda)(pic)_2$.[40] Interessanterweise wurde herausgefunden, dass vermutlich ein wasserstoffverbrücktes Wassernetzwerk in der Kavität des Makrozyklus für schnelle Protonen-gekoppelte Elektronen-Transfer-Schritte (PCET, engl: protonen-coupled electron transfer) und somit beschleunigte Reaktionsgeschwindigkeiten verantwortlich ist. Darüber hinaus belegten mechanistische Untersuchungen einen Wechsel des katalytischen Weges von einem bimolekularen I2M (Interaktion von zwei M-O Einheiten, engl: interaction of two M-O units) Mechanismus im

einkernigen Ru(bda)pic_2 Referenzkomplex zu einem mononuklearen WNA (nukleophiler Wasserangriff, engl: water nucleophiilic attack) Mechanismus im dreikernigen makrozyklischen WOC **MC3** (*Kapitel 2.3*), was letzteren besonders interessant für anwendungsbezogene Untersuchungen macht.

Eines der Ziele dieser Arbeit war die Untersuchung axialer Ligandenaustauschprozesse in Ru(bda) Komplexen, um Einblicke in kinetische und thermodynamische Reaktionsbedingungen bei der Synthese makrozyklischer Ru(bda) WOCs zu erhalten. Basierend auf den Erkentnissen konnten neue zwei- und vierkernige Ru(bda) Makrozyklen erhalten werden, deren Eigenschaften in der homogenen Wasseroxidationskatalyse untersucht wurden. Um die Bildung von **MC3** zu untersuchen, wurden ^{1}H NMR Experimente durchgeführt, bei denen die Reaktion von Ru(bda)$(dmso)_2$ mit entsprechenden Dipyridylliganden beobachtet wurde. Durch das Verfolgen der Produktzunahme basierend auf einem internen Standard wurde herausgefunden, dass unter den angewendeten Reaktionsbedingungen (CD_2Cl_2/MeOD 5:1, 55°C, 12 h) das gewünschte Produkt auf einem kinetischen Weg gebildet wird. Um axiale Ligandenaustauschprozesse in Ru(bda) Komplexen zu erforschen wurden verschiedene einkernige Ru(bda)L_2 Modellverbindungen eingesetzt. Ein zugrundeliegender dissoziativer Austauschmechanismus wurde beobachtet, was für den Aufbau großer Strukturen in einem thermodynamischen Gleichgewicht von Vorteil ist, da hier die Geschwindigkeit des Ligandenaustauschs unabhängig von der Menge an freiem auszutauschenden Liganden im Reaktionsgemisch ist. Bedingungen für einen schnellen Ligandenaustausch wurden untersucht und entsprechend erhöhte Temperaturen in der Synthese der neuen zwei- und vierkernigen Ru(bda) Makrozyklen **OEG-MC2** und **OEG-MC4** angewendet (Abbildung 52a). **OEG-MC4** stellt den bis heute einzigen vierkernigen und zudem größten bisher bekannten makrozyklischen WOC dar. Zur Verbesserung der Löslichkeit der WOCs wurden in die axialen Liganden Oligoethylenglykol-Ketten (OEG) eingeführt. Die hochsymmetrische und damit zyklische Struktur der neuen Komplexe konnte anhand von ^{1}H NMR Spektren verifiziert werden. Lineare Koordinationspolymere konnten aufgrund der Abwesenheit von zusätzlichen Signalen, welche offenen Endgruppen zugeordnet werden würden, ausgeschlossen werden. Zum Vergleich mit den neuen Makrozyklen wurde der komplementäre **OEG-MC3** Makrozyklus synthetisiert, welcher drei Ru(bda) Einheiten und identische Seitenketten in den Brückenliganden enthält. Die Analyse der Redoxpotentiale zeigte nur geringe Unterschiede zwischen den drei Makrozyklen. Spektroelektrochemische Untersuchungen ergaben jedoch, dass nur in den drei- und vierkernigen Makrozyklen eine deutliche Absorptionsbande bei 700 nm im Ru^{III}-Zustand zu beobachten ist, jedoch nicht in zweikernigen Komplex (spektroelektrochemische Untersuchungen sind exemplarisch für **OEG-MC4** in Abbildung 52b gezeigt). Dieser Übergang wurde zuvor im **MC3** Makrozyklus beobachtet und basierend auf

theoretischen Beobachtungen und experimentellen Indizien mit einem in der Kavität des Makrozyklus vorhandenen Wassernetzwerk in Verbindung gebracht.[43]

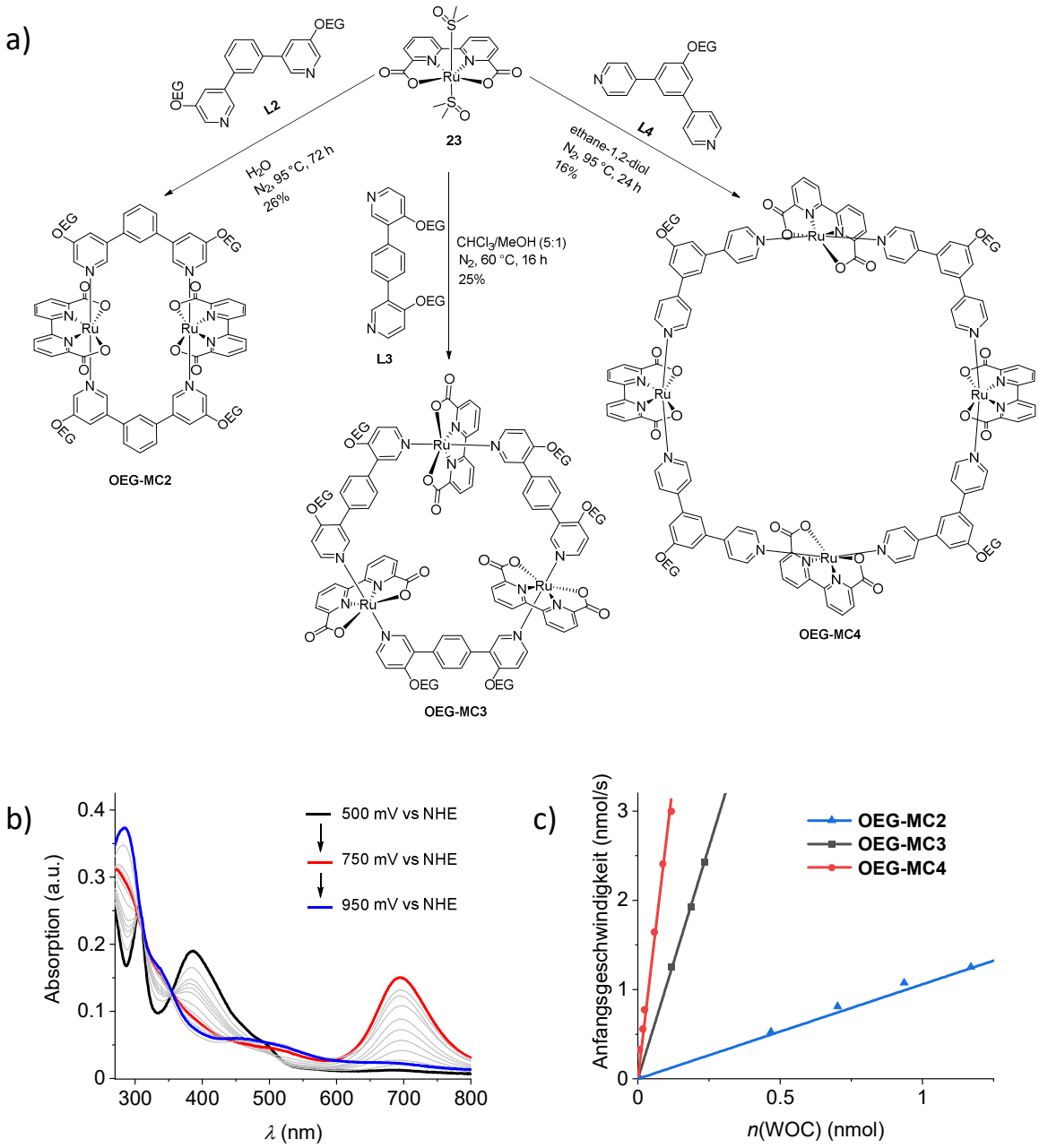

Abbildung 52: a) Chemische Struktur der di-, tri- und tetranuklearen Makrozyklen **OEG-MC2**, **OEG-MC3** und **OEG-MC4**. b) Spektroelektrochemische Untersuchungen von **OEG-MC4** weisen auf die Anwesenheit eines wie zuvor in **MC3** beobachteten Netzwerks aus über Wasserstoffbrücken verbundenen Wassermolekülen hin. c) Anfangsgeschwindigkeiten von **OEG-MC2**, **OEG-MC3** und **OEG-MC4** in der photokatalytischen Wasseroxidation. Detaillierte experimentelle Bedingungen können *Kapitel 4* entnommen werden.

Der größte vierkernige Makrozyklus der Reihe, **OEG-MC4**, zeigte bei Untersuchungen in der chemischen Wasseroxidation bei pH 1 angetrieben durch Cer(IV)-ammoniumnitrat (CAN) im Vergleich zu den kleineren zwei- und dreikernigen WOCs überlegene Leistungen mit einer Gesamt-TOF von 42 s^{-1} (TOF pro Ru-Einheit: 10.5 s^{-1}). Während die Aktivität von **OEG-MC3**

(Gesamt-TOF = 26 s^{-1}, TOF pro Ru-Einheit: 8.7 s^{-1})[215] in einem ähnlichen Bereich liegt, wurde für **OEG-MC2** eine niedrigere Gesamt-TOF von 12 s^{-1} (TOF pro Ru-Einheit: 6 s^{-1}) beobachtet. Zudem zeigten sich alle drei hier vorgestellten OEG-funktionalisierten WOCs in Bezug auf ihre Stabilität dem unfunktionalisierten Makrozyklus **MC3** unterlegen.[216] Die TONs für die drei und vierkernigen Komplexe, 2200 und 2870, sind dabei noch vergleichbar mit dem erhaltenen Wert für **MC3** (5300),[216] während die TON vom **OEG-MC2** (200) mehr als eine Größenordnung darunter liegt. Neben Untersuchungen der chemischen Wasseroxidationskatalyse wurden Studien zur photokatalytischen Wasseroxidation durchgeführt. Hierbei wurde ein Drei-Komponenten-System bestehend aus dem WOC, $Ru(bpy)_3^{2+}$ als Photosensibilisator und Natriumpersulfat als Elektronenakzeptor bei pH 7 verwendet (Abbildung 52c). Ein ähnlicher Effizienztrend wie in der chemischen Wasseroxidation wurde beobachtet. Ein ausgezeichneter Wert für die TOF von 23 s^{-1} wurde für **OEG-MC4** bestimmt (5.8 s^{-1} pro Ru Einheit), welcher zu den höchsten bisher veröffentlichten Aktivitätswerten unter den Ru(bda) WOCs in der homogenen Photokatalyse gehört, während **OEG-MC3** mit einer leicht niedrigeren TOF von 10 s^{-1} (3.3 s^{-1} pro Ru Einheit) einen fast identischen Wert wie **MC3** zeigt (TOF = 11 s^{-1}, pro Ru-Einheit: 3.7 s^{-1}).[216] Darüber hinaus liegen die TON-Werte der drei- und vierkernigen WOCs (TON = 400 bzw. 500) im gleichen Bereich wie der des nicht funktionalisierten **MC3** (TON = 430).[216] Interessanterweise konnte im Gegensatz zu den größeren WOCs im zweikernigen **OEG-MC2** in Bezug auf die Aktivität kein Gewinn an der makrozyklischen Struktur beobachtet werden. Die erhaltene TOF von 0.55 s^{-1} pro Ru-Einheit ist identisch zu der für den einkernigen $Ru(bda)pic_2$ Komplex erhaltenen (TOF = 0.6 s^{-1}). Es wurde angenommen, dass das Vorhandensein eines wasserstoffverbrückten Wassernetzwerks in der makrozyklischen Kavität der drei- und vierkernigen WOCs für ihre gute Effizienzen verantwortlich ist, während der zweikernigen Komplex nicht von dessen Anwesenheit profitiert und entsprechend geringere Aktivitäten aufweist. Die um etwa eine Größenordnung geringere TON der dimeren Verbindung (TON = 36) im Vergleich zu den größeren WOCs weist auf eine deutlich geringere Stabilität von **OEG-MC2** hin (TON = 400 und 500 für den dreikernigen und vierkernigen WOC).

Vor dem Hintergrund der Erweiterung bisheriger grundlegender Erforschung von Wasseroxidationskatalysatoren im Labor sind die in *Kapitel 5* beschriebenen elektrochemischen Untersuchungen von WOC **MC3** in der heterogenen elektrochemischen Wasseroxidation ein Fortschritt in Richtung Anwendung. Diese Untersuchungen wurden in Kooperation mit Prof. Antoni Llobet am *Institut Català d'Investigació Química* in Tarragona (Spanien) durchgeführt. Mehrwandige Kohlenstoffnanoröhren (MWCNTs, engl: multi-walled carbon nanotubes) wurden hierbei als Trägermaterial für die Immobilisierung des Katalysators **MC3** auf eine glasartige Kohlenstoffelektrode (engl: glassy carbon electrode) verwendet (Abbildung 53a). Das tropfenweise Auftragen (engl: drop-casting) der Suspension von **MC3@CNT**s auf die glasartigen Kohlenstoffelektroden führte zu Hybridanoden. Vermutlich aufgrund der Tatsache,

dass mehrere Ru(bda) Einheiten durch aromatische Brückenliganden verbunden sind, hat der trimere Makrozyklus eine starke Fähigkeit durch CH-π- und π-π-Wechselwirkungen mit den CNT an deren Oberfläche zu haften. In der Tat konnte mit diesem Ansatz erstmals die Immobilisierung von Ru(bda) Katalysatoren auf Oberflächen ohne spezielle Funktionalisierung der WOCs demonstriert werden. AFM-Aufnahmen bestätigen, dass die **MC3** Moleküle an der Oberfläche der CNTs verankert sind (Abbildung 57b).

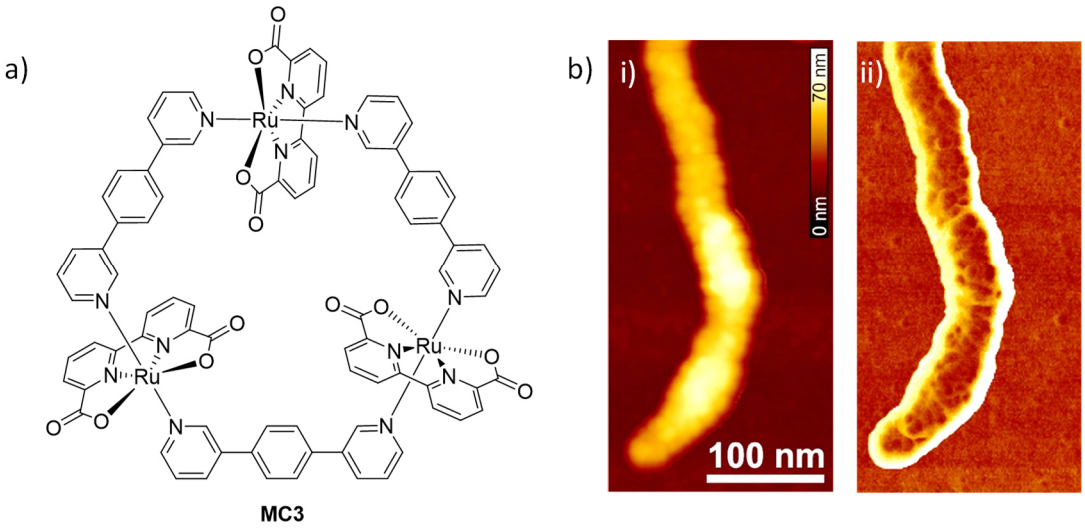

Abbildung 53: a) Struktur des trimeren Ru(bda) Makrozyklus MC3. b) Erhaltene AFM-Aufnahmen nach Rotationsbeschichtung eines Silikon-Plättchens mit einer Dispersion von **MC3@CNT** in einer THF/TFE (10:0.1) Mischung: i) Höhe der CNTs bestückt mit **MC3**, *Z* Achse ist 70 nm, ii) Phasenbild von CNT mit immobilisierten **MC3**.

Bei der Durchführung mehrerer aufeinanderfolgender CV-Zyklen konnte beobachtet werden, dass der verankerte Katalysator teilweise in eine aktivierte Spezies umgewandelt wurde. Hierbei wurde ein Anstieg des katalytischen Stroms der Wasseroxidation um das vierfache des anfänglichen Wertes beobachtet (Abbildung 54a). Die dabei gemessene maximale Stromdichte (*j*) von 186 mA/cm^2 ist meines Wissens die höchste jemals für molekulare immobilisierte Ru(bda) WOCs erreichte. Die Stabilität der hergestellten Anoden wurde in Experimenten mit einem kontrolliert angelegten Potential (CPE, engl: controlled potentials electrolysis) untersucht. Hierbei wurde bei einer ausgewählten konstanten Spannung der Verlauf des fließenden Stroms analysiert. Es wurde beobachtet, dass die Stromdichte an den aktivierten Elektroden während 6 Stunden nur geringfügig abnimmt. 97% der anfänglichen Aktivität wurden aufrecht erhalten, was auf eine bemerkenswerte Stabilität der Elektroden schließen lässt (Abbildung 54b). Basierend auf der Menge des auf der Elektrode vorhandenen Katalysators wurde die TON während des CPE-Experiments bestimmt. Bezogen auf den aktiven Katalysator wurde hierbei ein eindrucksvoller Wert von über einer Millionen erhalten.

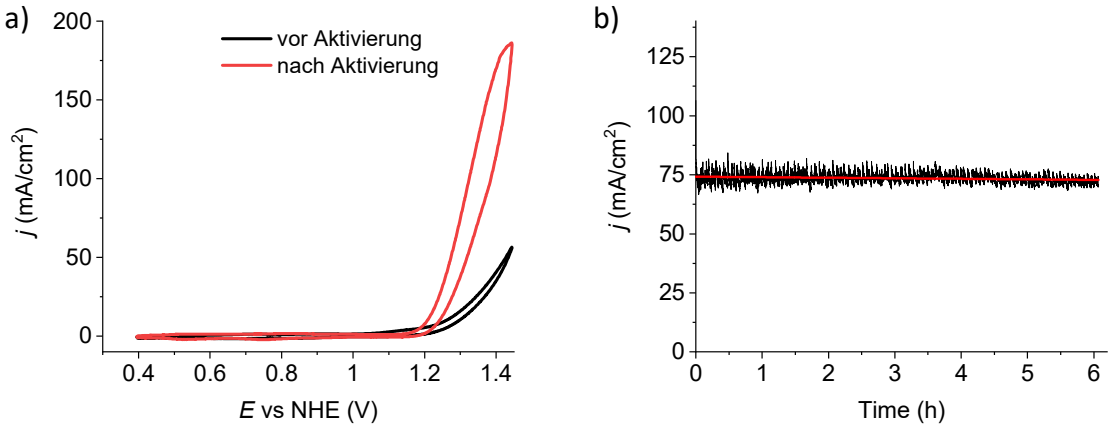

Abbildung 54: a) CV von **MC3@CNT**s vor (schwarze Linie) und nach (rote Linie der Aktivierung in einer 1 M Phosphatpuffer-Lösung (pH 7). b) Stabilitätsmessung mittels CPE Experiment bei 1.6 V in einer 1 M Phosphatpufferlösung (pH). Die rote Linie zeigt die durchschnittliche Stromdichte (*j*) während des sechsstündigen Experiments an. Detaillierte experimentelle Bedingungen sind in *Kapitel 5* zu finden.

Des Weiteren wurde die Faraday-Effizienz der aktivierten Elektrode ermittelt, um die Effizienz des Katalysators zu bestimmen und auszuschließen, dass Ströme aus unerwünschten Nebenreaktionen zu der gemessenen Stromdichte beitragen. Die gefundene nur geringe Abweichung dieser Werte führte zu einer Faraday-Effizienz von 99%, was eine selektive und quantitative Wasseroxidation ohne Nebenreaktionen bestätigt. Die Untersuchung des Beginns des katalytischen Prozesses der aktivierten Spezies am Fuß der katalytischen Welle (FOWA Analyse, engl: Foot of the Wave Analysis) ergab, dass die Aktivität des aktivierten Katalysators mit einer TOF von 3200 s^{-1} unter den höchsten liegt, die je für immobilisierte Ru Katalysatoren gemessen wurden (siehe *Chapter 9*, Table S5).

Um die Art des Aktivierungsprozesses und die zugrunde liegende Transformation in eine aktivere Spezies während aufeinanderfolgender CV-Zyklen näher zu untersuchen wurden theoretische Berechungen von Dr. Joachim Lindner durchgeführt. Die erhaltenen Ergebnisse, welche gemeinsam in Übereinstimmung mit den experimentellen Daten interpretiert wurden, haben gezeigt, dass die Anlagerung von zwei Wassermolekülen an das Rutheniumzentrum (siehe optimierte Struktur in Abbildung 55) während des Aktivierungsprozesses für eine Verschiebung der Redoxpotentiale sowie höhere katalytische Ströme verantwortlich ist.

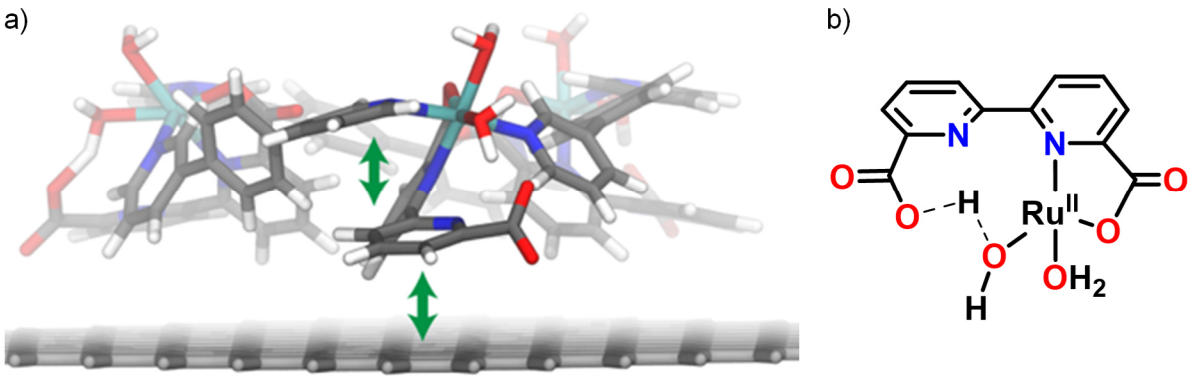

Abbildung 55: a) Seitenansicht der optimierten Struktur der aktivierten **MC3**-diaqua Spezies auf einer Grafitoberfläche basierend auf semiempirischen Berechnungen. b) Schematische Abbildung der aktiven Ru-Diaqua-Spezies. Axiale Liganden wurden aus Gründen der Übersicht nicht dargestellt.

Diese Ergebnisse zeigen zum ersten Mal die Aktivierung eines Ru(bda) Komplexes durch Bildung einer hocheffizienten Ru(bda)-Diaqua-Spezies während der Elektrokatalyse. Darüber hinaus wurde basierend auf theoretischen Berechnungen ein Vorschlag für einen neuen Reaktionsweg für die Wasseroxidation nach dem WNA-Mechanismus präsentiert, welcher durch vollständige Ablösung einer Pyridineinheit des äquatorialen bda-Liganden am Reaktionszentrum die Koordination von zusätzlichen Wassermolekülen an das Ru-Zentrum ermöglicht.

Zusammenfassend präsentiert diese Arbeit zunächst detaillierte ^{1}H NMR Studien zum Ligandenaustauschprozess und dessen Mechanismus in Ru(bda)L_2 Komplexen. Basierend auf diesen Untersuchungen konnten Reaktionsbedingungen für die Bildung makrozyklischer Komplexe im thermodynamischen Gleichgewicht untersucht und zwei neue supramolekulare zwei- und vierkernige makrozyklische Ru(bda) Komplexe synthetisiert werden. Es wurde herausgefunden, dass der größte vierkernige Komplex der effizienteste homogene Wasseroxidationskatalysator der vorliegenden homologen Reihe ist. Sein ausgezeichneter TOF-Wert in der Photokatalyse zählt zu den besten, welche für Ru(bda) Katalysatoren in der lichtgetriebenen Wasseroxidation bekannt sind. Die hohe photokatalytische Effizienz ist vermutlich auf die Bildung eines wasserstoffverbrückten Wassernetzwerks in der Kavität des Makrozyklus zurückzuführen. Für erweiterte Untersuchungen der Wasserspaltung in der heterogenen Katalyse wurde der dreikernige Makrozyklus **MC3** nach Aufbringen auf halbleitende CNTs als Trägermaterial auf Glaskohlenstoffelektroden immobilisiert. Während mehrfachen CV-Zyklen wurde eine Umwandlung in eine aktivierte Spezies beobachtet, die mit bemerkenswert hohen Effizienzen in der Wasserspaltung einherging. Basierend auf theoretischen Untersuchungen wurde ein neuer katalytischer Mechanismus mit einer während der elektrochemischen Aktivierung gebildeten Ru(bda)-Diaqua Spezies vorgeschlagen. Zweifellos tragen diese Studien zu Aktivierungsprozessen mit resultierenden hohen Aktivitäten

in der heterogenen Katalyse zu einem besseren Verständnis der Funktionsweise der molekularen Katalysatoren bei und öffnen damit Türen zu neuen Ansätzen für die Entwicklung weiterer effizienter WOCs. In Kombination mit stabilen Verankerungsstrategien, wie sie in dieser Arbeit vorgestellt wurden, ermöglicht dies zukünftig vielversprechende Anwendungen in photovoltaisch gekoppelten Elektrolysezellen oder photoelektrochemischen Zellen.

Chapter 8

—

Experimental Section

8.1 Materials and Methods

All chemicals and reagents were purchased from commercial suppliers and used without any further purification, unless noted otherwise. Compounds 2,2'-bipyridine-6,6'-dicarboxylic acid (bda),[299-300] $RuCl_2(dmso)_4$,[301-302] $Ru(bda)(dmso)_2$,[125, 233] $Ru(bda)(pic)_2$,[40] **OEG-1,4-bpb**,[215] **OEG-MC3**[215] and **MC3**[42] were synthesized according to previously published procedures. $[Ru(bpy)_3]Cl_2$ was purchased from Sigma Aldrich with 99.95% purity. Deuterated solvents for NMR analysis were purchased from Deutero (pyridine-d5, MeOD, CD_2Cl_2, DMF-d7) or Eurisotop (TFE-d3). Unless otherwise noted, reactions were carried out under normal laboratory atmosphere. Reactions with oxygen or water sensitive reagents were carried out under a nitrogen atmosphere. For homogeneous CV as well as water oxidation experiments and reactions in aqueous media highly pure water obtained from a PURELAB Classic water purification system (ELGA) was used. Phosphate buffer for light-induced water oxidation experiments and UV/Vis studies at pH 7 was bought from Honeywell. Phosphate buffer for CV experiments was prepared according to the procedure described below. Multi-walled carbon nanotubes (MWCNTs) in bulk with a purity of > 95%, OD > 50 nm, length ~ 50 µm were obtained from HeJi, Inc., China. Glassy carbon plates (GC_p, 20 x 10 x 0.18 mm) were purchased from HTW, Germany. For heterogeneous water oxidation experiments, highly pure water was obtained by filtration of distilled water through a nanopure Mili-Q water purification system. All solvents used in electrochemical studies were of a purity of 99.8% and higher. Electrochemical studies in *Chapter 5* have been performed in the laboratory of Prof. Antoni Llobet at the *Institut Català d'Investigació Química* (ICIQ), Tarragona, Spain.

Thin layer chromatography (TLC) and column chromatography

For analytical TLC, sheets pre-coated with silica gel (ALUGRAM® Xtra SIL G/UV254) or aluminum oxide (POLYGRAM® ALOX N/UV254) purchased from Macherey-Nagel were used. To visualize the substances, the TLC plate was exposed to ultraviolet light (254 and 366 nm). Purification of compounds by column chromatography was performed using silica gel (60M, 0.04-0.063 mm, Macherey-Nagel) or aluminum oxide (EcoChrom MP Alumina N Act. V, MP Biomedicals).

Size exclusion chromatography (GPC)

Size exclusion chromatography was performed in a 9:1 DMC/MeOH mixture on suspended BioBeads particles (S-X1, Bio-Rad). Analytical GPC was performed on a JASCO system (RI-2031 Plus Intelligent RI Detector MD-2015 Plus Multiple wavelength detector, LG-2080-02 Ternary Gradient Unit and one PSS SDV 5µ 8x30 mm linear M column). Preparative GPC purification was performed on a LC-5060 system from Japan Analytical Industries (three columns from Aligent, PLgel, 10 µm, 100 Å; 10 µm, 100 Å; 10 µm, 500 Å). In both cases, a mixture of chloroform (90%) stabilized with ethanol and methanol (10%) was used as eluent.

NMR spectroscopy

1H NMR spectra were recorded at room temperature (ca 22 °C) with a Bruker Avance III HD 400 spectrometer at 400 MHz. ^{13}C NMR spectra are proton decoupled and recorded at 100 MHz using the same instrument. DOSY spectra were recorded on a Bruker Avance III HD 600 spectrometer. Chemical shifts δ are indicated in parts per million (ppm) relative to the solvent peaks and coupling constants J in Hz. Solvent peaks of residual undeuterated solvent were used for calibration of the spectra. The following abbreviations were used to describe the observed multiplicities: s = singlet, d = doublet, t = triplet, m = multiplet, dd = doublet of a doublet. ^{1}H NMR spectra of new compounds were assigned with the help of 2D spectra (COSY, HSQC, NOESY, HMBC).

DOSY NMR

DOSY (diffusion orderd spectroscopy) spectra were recorded at 295.2 K in a mixture of deuterated 2,2,2-triflouroethanol/dichloromethane/methanol (10:3:7). The viscosity of η = 0.99 *10^{-3} $\frac{\mathrm{kg}}{\mathrm{m\,s}}$ of the used solvent mixture was determined using a Ubbelohde Viscometer (type 501 03). The hydrodynamic radius of the sample assuming a spherical character was estimated using the Stokes-Einstein equation (equation 10).

Mass spectrometry

Mass spectra (HR-ESI) were recorded on an ESI microTOF Focus mass spectrometer from Bruker Daltonics GmbH. Measurements were carried out in positive mode and mass signals are reported as fragment mass per charge (*m*/*z*).

Melting points

Melting points were measured in open glass capillaries in a melting point apparatus (Büchi) or a BX41 optical microscope (Olympus) and are not corrected.

UV/Vis absorption spectroscopy

UV/Vis absorption spectra were recorded in 1 cm quartz cuvettes with a Jasco V-670 spectrometer at 25 °C using spectroscopic grade solvents.

Spectroelectrochemistry

Measurements were performed in reflection mode using Agilent Cary 5000 spectrometer. A home built cylindrical PTFF cell with a sapphire window and an adjustable three-in-one electrode setup comprising a 6 mm platinum disk as a working electrode, a 1 mm platinum counter electrode and a pseudo-reference electrode was used. The layer thickness was set to be about 100 µm and experiments were performed in 1:1 TFE/water mixtures (pH 7, phosphate buffer). Potentials were referenced to the first oxidation event determined by DPV.

Chemical water oxidation

For chemically driven water oxidation experiments, gas tight reaction vessels of V = 20.6 mL were connected to pressure transducers (Honeywell, SSCDANN030PAAA5, absolute pressure, 0 to 30 psi). In one single experiment, cer ammonium nitrate (CAN, 1 g, 1.82 mmol) was dissolved in 3 mL of a water/acetonitrile mixture (pH 1, triflic acid, various ratios) in the reaction vessel and 400 µL of a stock solution of the catalyst dissolved in water/acetonitrile (pH 1, trifilic acid, same ratio as in experiment) were injected through a septum using a Hamilton syringe. At the end of each experiment, 500 µL gas of the head space was taken with a gas tight Hamilton syringe and injected into a gas chromatograph GC-2010 Plus (Shimadzu, thermal conductivity detector at 30 mA, argon as carrier gas) for analyzing its composition. For calculating the TON, the total amount of generated oxygen during catalysis was determined and divided by the amount of catalyst present in the experiment. By applying the ideal gas law, the quantity of evolved oxygen was determined from the increase in pressure in the reaction vessel:

$$\Delta p * V = R * T * \Delta n \quad \text{(eq. 15)}$$

where Δp is the pressure increase, V is the volume of the reaction vessels, R is the gas constant, T is the temperature and Δn the amount of generated oxygen. In a series of concentration-dependent measurements, the highest TON obtained at one single concentration was reported. TOFs have been determined for each measurement. In series with varying solvent ratios, TOFs for single experiments at various solvent ratios have been calculated from the obtained initial rates by linear regression through the first linear part of the oxygen evolution curve at the very beginning of catalysis. In series of multiple measurements of different concentration at a fixed solvent ratio, the reported TOF is the slope of the linear regression of the plot of the initial rates vs the amount of catalyst.

Photocatalytic water oxidation

Photocatalytic water oxidation experiments were carried out in a transparent and temperature-controlled reaction chamber at 20 °C. The chamber was equipped with a Clark electrode (Oxygraph Plus Clark-electrode system from Hansatech) for oxygen detection in solution. Irradiation of the samples was performed by a 150 W xenon lamp (Newport) with a 400 nm cutoff filter calibrated to an intensity of 100 mW cm^{-1}. Light intensity calibration inside the reaction chamber was carried out using a PM 200 optical power meter with a S121C sensor (Thorlabs) combined with a CCS 200/M wide range spectrometer (Thorabs). A stock solution of the photosensitizer and sodium persulfate in a 1:1 acetonitrile/water mixture (pH 7, phosphate buffer) was prepared in the dark directly before starting a series of experiments. An aliquant of the stock solution (1.5 mL) was mixed with a varying amount of catalyst concentration (0.5 mL) inside the reaction chamber in the dark for 45 seconds prior to illumination. For all experiments, the amount of photosensitizer (c = 1.5 mM) and sodium persulfate (c = 37 mM) was kept constant and a blank without any catalyst was subtracted before evaluating the data. The TON was determined by evaluating the highest amount of oxygen in solution during each experiment and dividing by the amount of catalyst used. The reported TON value corresponds to the highest TON at one concentration. For the determination of TOF, oxygen evolution was plotted versus the reaction time of the experiment. The oxygen evolution after a short induction period (~1 s) was fitted by linear regression analysis during the first five to ten seconds of catalysis to give the initial rates of catalysis. The slope of a plot of the initial rates versus the catalyst concentration gives the TOF.

Electrochemistry in homogeneous phase

Cyclic voltammetry (CV) or differential pulse voltammetry (DPV) experiments were carried out on a BAS Epsilon (BAS Cellstand C3) potentiostat. A standard three electron configuration was used with a glassy carbon disk (ϕ = 0.3 cm, S = 0.07 cm^2) as working electrode (WE), platinum wire (homogeneous measurements) as a counter electrode (CE) and Ag/AgCl (3 M KCl) as a reference electrode (RE). Samples were measured in homogeneous phase and prepared in 1:1 water/TFE mixtures (pH 7 phosphate buffer, 0.1 M). All potentials were converted and are reported vs normal hydrogen electrode (NHE). For ensuring the same distance of the electrodes in CV and DPV measurements, a glass vial with a self-made Teflon lid with three holes for the electrodes was used. CV experiments were recorded at a scan rate of 100 mV/s with an *iR* compensation of 85%. The following parameters were used in DPV experiments: ΔE = 4 mV, amplitude = 50 mV, pulse width = 0.05 s, sampling width = 0.0167 s and pulse period = 0.2 s.

Heterogeneous water oxidation

Preparation of phosphate buffer for electrochemical experiments

Phosphate buffers used in the electrochemical experiments were prepared by dissolving different amounts of phosphate salts in highly pure Mili-Q water:

i) pH 7, 1 M ionic strength: NaH_2PO_4 (23.1 g, 193 mmol) and Na_2HPO_4 (37.7 g, 266 mmol) in water (1000 mL).
ii) pH 2, 1 M ionic strength: H_3PO_4, 85% (36 mL, 526 mmol) and NaH_2PO_4 (60.2 g, 424 mmol) in water (500 mL).
iii) pH 11, 1 M ionic strength: Na_2HPO_4 (3.90 g, 27.5 mmol) and Na_3PO_4 (11.4 g, 69.5 mmol) in water (1000 mL).

Preparation of **MC3@CNTs@GC**

A dispersion of MWCNTs (5 mg) in THF (5 mL) was prepared by sonicating the mixture for 40 minutes. **MC3** (1 mg) was dissolved in TFE (1 mL) and 0.1 mL of the brown catalyst solution was added to 1 mL of a freshly prepared dispersion of MWCNTs in THF. After immediate decolorization, indicating the anchoring of the catalyst on the CNTs, the dispersion of **MC3@CNT** was used for the preparation of electrodes.

Electrodes for cyclic voltammetry (CV) and differential pulse voltammetry (DPV) experiments were prepared by drop-casting the **MC3@CNT** suspension in THF/TFE (1:0.1) onto the surface of the glassy carbon disk (4 x 20 µL). Only after the solvent of the first drop was evaporated completely, the next drop was placed onto electrode. For verifying that all catalyst was actually

bound to the surface of the CNTs, the electrode was washed with a CH_2Cl_2/MeOH (5:3) mixture in which the catalyst is highly soluble. No loss of the catalyst was observed after washing, as CV experiments before and after showed the same intensities for all redox processes. For foot of the wave analysis (FOWA) experiments, electrodes with different amounts of catalyst were prepared by varying the amount of **MC3** which was added to the CNT dispersion. The amout of active catalyst on the surface was determined after activation of the electrodes. The glassy carbon plate (GC_p) for the determination of the Faraday efficiency was prepared using a tape to control the surface area of the GC_p to 1 cm^2. Drops of 30 µL of **MC3@CNT** in THF were placed on the surface until one side was completely covered with CNTs.

Electrochemistry

All electrochemical experiments were carried out on an IJ-Cambria CHI-730 potentiostat. As working electrodes (WE), glassy carbon disks (GC, ϕ = 0.3 cm, S = 0.07 cm^2) or a glassy carbon plate (GC_p, 20 mm x 10 mm x 0.18 mm) were used. Pt mesh was used as a counter electrode (CE). $Hg/HgSO_4$ (K_2SO_4 sat.) was used as a reference electrode (RE) in CV and DPV experiments. For the determination of the Faraday efficiency, an Ag/AgCl (KCl sat.) electrode was employed as RE. All potentials were converted to normal hydrogen electrode (NHE) by adding 0.65 V to the measured potential (0.20 V in the case of Ag/Ag/Cl reference).

Electrochemical cells

For CV and DPV measurements, a 20 mL glass vial was used. A self-made Teflon cap with three holes was applied to hold the electrodes in the same distance and ensure reproducibility.

Cyclic voltammetry (CV) and differential pulse voltammetry (DPV)

For CV experiments, the scan rate was 100 mV/s unless stated otherwise. *iR* compensation at 85% was applied for single CV and DPV experiments. Parameters in the DPV experiments were: ΔE = 4 mV, amplitude = 50 mV, pulse width = 0.05 s, sampling width = 0.0167 s and pulse period = 0.5 s.

Controlled potential electrolysis (CPE)

For CPE experiments, a two compartment cell was used. The chambers were separated with a frit. The working electrode and the reference electrode were placed in one compartment, the counter electrode in the other one. Both chambers were equipped with a magnetic stirring bar.

Oxygen detection

In the CPE for the Faraday efficiency experiment, both chambers and the solvent were degassed with argon gas and sealed air-tight with septum caps. To have a large enough

surface area for the detection of the generated amount of oxygen, a glassy carbon plate covered with **act-MC3@CNT** was used as a working electrode. An Ag/AgCl (KCl sat.) was employed as reference electrode and Pt mesh as a counter electrode. The generated amount of oxygen during water oxidation was monitored by a Clark electrode (Unisense Ox-N needle microsensor), which was situated in the headspace of the compartment containing the working electrode. Calibration of the Clark electrode was performed by adding different amounts of air at the end of the experiment. A blank experiment with a glassy carbon plate covered with CNTs (without catalyst) was performed under identical conditions.

Foot of the wave analysis (FOWA)

The foot of the wave analysis was performed by applying the adapted equations for a heterogeneous WNA mechanism in water oxidation catalysis as described in the literature, where the catalyst is anchored to the surface of an electrode and translational mobility is suppressed.[161] The current intensity at the foot of the wave, assuming that the bulk concentration of H_2O as well as the gradient of both H_2O and O_2 are constant, is only dependent on the apparent rate of the reaction (k_{WNA}) and can be described as:

$$\frac{i}{4\,F\,S} = \Gamma_Q \; k_{WNA} \qquad \text{(eq. 16)}$$

where i is the CV current intensity, *F* is the Faraday constant, *S* is the geometric surface of the electrode, Γ_Q is the surface concentration of the catalyst in the catalytically active state after multiple oxidation steps. As in the homogeneous case, the equation applied to extract the TOF_{max} at the foot of the wave can be obtained by using the Nernst equation and dividing the moles of the electrons associated with a 1 electron transfer of the immobilized catalyst. For the evaluation of the data, the second cycle of the CV was used.

Surface coverage in GC disk

The surface coverage (%) was calculated as follows:

$$S_{MC3} = \frac{Q_{Ru^{III/II}} \cdot N_A \cdot S_{MC3}}{F \cdot n_{Ru}} \qquad \text{(eq. 17)}$$

$$Coverage\ (\%)_{MC3@GC} = \frac{S_{MC3}}{S} \text{x}\ 100 \qquad \text{(eq. 18)}$$

where $Q_{Ru^{III/II}}$ is the charge under the $Ru^{III/II}$ redox event for **MC3@GC**. *F* is the Faraday constant. n_{Ru} is the number of Ru units per macrocycle (n_{MC3}= 3). N_A is the Avogadro's number, S_{MC3} is the surface area occupied by a single molecule calculated with the approximate triangle

generated by **MC3**, S_{MC3} = [$3^{1/2}$/4 x 2.21^2] = 2.11 nm^2 or 2.11 x 10^{-18} m^2, and *S* is the geometric surface area of the electrode (GC_d, *S* = 0.07 cm^2).

Atomic force microscopy (AFM)

AFM measurements were performed by Dr. Vladimir Stepanenko under ambient conditions using a Bruker Multimode 8 SPM system operating in tapping mode in air. Silica cantilevers (OMCL-AC200TS, Olympus) with a resonance frequency of ~150 kHz and a spring constant of ~10 Nm^{-1} were used. The samples were prepared by spin-coating of a dispersion of **MC3@CNTs** onto silicon wafers under 2000 rpm.

Scanning electron microscopy (SEM) and Energy-dispersive X-ray spectroscopy (EDX)

SEM images were recorded by Dr. Vladimir Stepanenko using a Zeiss Ultra Plus field emission scanning electron microscope equipped with GEMINI e-Beam column operated at 1 or 3 kV with an aperture size set to 30 µm. For the energy dispersive X-ray analysis (EDX), the Oxford X-Max EDX detector and accelerating voltage of 10 kV (with the 120 µM aperture in high current mode) were used. The SEM sample was prepared by spin-coating of the solution **MC3@CNT** in THF/TFE onto silicon wafer under 2000 rpm.

X-ray absorption spectroscopy (XAS)

X-ray absorption spectra were measured by Dr. Dooshaye Moonshiram (IMDEA Nanociencia, Madrid, Spain) on bending magnet beamline 9 at an electron energy of 23 KeV and an average current of 100 mA at the Advanced Photon Source (APS) at Argonne National Laboratory, USA. Radiation monochromatized by a Si(111) crystal monochromator was used. Three ion chambers (I_0, I_1 and I_2) filled with 70% nitrogen and 30% argon and placed before the sample (I_0) and after the sample (I_1 and I_2) were applied to monitor the intensity of the X-rays. The sample with the Ru metal was placed between ion chamber I_1 and I_2 and its absorption was recorded with each scan for the energy calibration. The samples were kept at 20 K in a He atmosphere at ambient pressure and recorded as fluorescence excitation spectra using a 4-element energy-resolving Si-drift detector. A portion of the solid complex **MC3** (~ 4 mg) was diluted with boron nitride pressed between 3 µm polypropylene film and mylar tape and measured in the continuous helium flow cryostat in fluorescence mode. About 25-40 XAS spectra of each sample were measured. Several positions of each sample were measured and no more than five scans were taken at each sample position. In order to reduce the risk of sample damage by X-ray radiation, 80% flux was used (beam size 6000 µm (horizontal) x 1000 µm (vertical)) and no damage was observed after scan in any sample. All samples were protected from the X-ray beam during spectrometer movements by a shutter synchronized with

the scan program. Ru XAS energy was calibrated by the first maxima in the second derivative of the ruthenium metal X-ray Absorption Near Edge Structure (XANES) spectrum.

Extended X-ray absorption fine structure (EXAFS) analysis

For processing the obtained data, Athena software[303] was used by Dr. Dooshaye Moonshiram (IMDEA Nanociencia, Madrid, Spain). The energy scale for each scan was normalized using ruthenium metal standard. Data in energy space were pre-edge corrected, normalized, deglitched (if necessary), and background corrected. The processed data were converted to the photoelectron wave vector (k) space and weighted by k^2. The electron wave number is defined as $k = [2m(E - E_0)/\hbar^2]^{1/2}$, E_0 is the energy origin or the threshold energy. K-space data were truncated near the zero crossings k = 2 to 11 Å^{-1} for the solid and hybrid complexes in Ru EXAFS before Fourier transformation. The k-space data were transferred into the Artemis software for curve fitting. In order to fit the data, the Fourier peaks were isolated separately, grouped together, or the entire (unfiltered) spectrum was used. The individual Fourier peaks were isolated by applying a Hanning window to the first and last 15% of the chosen range, leaving the middle 70% untouched. Curve fitting was performed using *ab initio*-calculated phases and amplitudes from the FEFF8[304] program from the University of Washington. *Ab initio*-calculated phases and amplitudes were used in the EXAFS equation

$$\chi(k) = S_0^2 \sum_j \frac{N_j}{kR_j^2} f_{eff_j}(\pi, k, R_j) e^{-2\sigma_j^2 k^2} e^{\frac{-2R_j}{\lambda_j(k)}} \sin(2kR_j + \phi_{ij}(k)) \qquad \text{(eq. 19)}$$

Here N_j is the number of atoms in the j^{th} shell, R_j the mean distance between the absorbing atom and the atoms in the j^{th} shell; $f_{eff_j}(\pi, k, R_j)$ is the *ab initio* amplitude function for shell *j*, and the Debye-Waller term $e^{-2\sigma_j^2 k^2}$ accounts for damping due to static and thermal disorder in absorber-backscatterer distances. The mean free path term $e^{\frac{-2R_j}{\lambda_j(k)}}$ reflects losses due to inelastic scattering, where $\lambda_j(k)$ is the electron mean free path. The oscillations in the EXAFS spectrum are reflected in the sinusoidal term $\sin(2kR_j + \phi_{ij}(k))$, where $\phi_{ij}(k)$ is the ab initio phase function for shell *j*. This sinusoidal term shows the direct relation between the frequency of the EXAFS oscillations in k-space and the absorber-backscatterer distance. S_0^2 is an amplitude reduction factor. The EXAFS equation[305] (eq. 19) was used to fit the experimental Fourier isolated data (q-space) as well as unfiltered data (k-space) and Fourier transformed data (R-space) using N, S_0^2, E_0, R, and σ^2 as variable parameters. N refers to the number of coordination atoms surrounding Ru for each shell. The quality of fit was evaluated by R-factor and the reduced Chi^2 value. The deviation in E_0 ought to be less than or equal to 10 eV. R-factor less than 2% denotes that the fit is good enough,[305] whereas R-factor between 2 and

5% denotes that the fit is correct within a consistently broad model. The reduced Chi^2 value is used to compare fits as more absorber-backscatter shells are included to fit the data. A smaller reduced Chi^2 value implies a better fit. Similar results were obtained from fits done in *k*, *q*, and R-spaces.

Computational details

As a model of the graphitic surface of MWCNTs, a hexagonal graphene sheet was optimized in D_{6h} symmetry using density functional theory (DFT) and employing the PBE[306] functional together with the def2-SVP[307] basis set, as implemented in Turbomole V6.5.[308] All structure optimizations of **MC3** was performed by Dr. Joachim Lindner on the semiempirical PM6 level,[309] including the D3H4 correction[310] as implemented in MOPAC2016.[311] During the semiempirical catalyst optimizations, coordinates of the preoptimized graphene layer was frozen and the oxidation states set to Ru^{II} in all cases. Since an adequate quantum-chemical description of Ru^{V} species is not possible with semiempirical methods, the same DFT method was employed in this case as described above. Additionally, the def2-ECP effective core potential[312] was used for Ru atoms and D3 dispersion correction[313] was applied. The COSMO model[314] was used to implicitly include solvation in water. Non-covalent interactions were visualized using the NCIPLOT method[315] based on promolecular densities. For this purpose, the intermolecular setting was used in which all bridging ligands of **MC3** as well as the graphene layer were treated as individual molecules.

8.2 Synthesis and Characterization

Synthesis of Ru(bda)L_2 complexes for NMR studies

Ru(bda)(2-picoline)$_2$ (26)

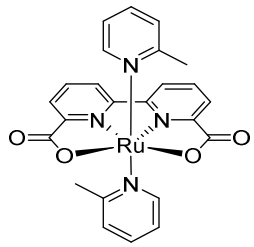

Melting point: >300 °C. Ru(bda)(dmso)$_2$ (50.0 mg, 100 µmol, 1 equiv.) and 2-picoline (180 µL, 2.01 mmol, 20 equiv.) were dissolved in degassed methanol (7 mL) and stirred at 65 °C for 3 h in a nitrogen inert gas atmosphere. The solvent was removed *in vacuo* and the remaining solid was redissolved in DCM/MeOH (5:3) and purified by chromatography (Al_2O_3, DCM/MeOH 9:1 to 1:1) to yield the product as a dark brown solid (43.6 mg, 82.4 µmol, 82%).

Melting point: >300 °C. ^{1}H NMR (400 MHz, MeOD): δ = 8.52 (dd, $^3J_{H-H}$ = 8.01 Hz, $^4J_{H-H}$ = 1.15 Hz, 2H, Ar-*H*), 7.96 (dd, $^3J_{H-H}$ = 7.74 Hz, $^4J_{H-H}$ = 1.12 Hz, 2H, Ar-*H*), 7.80 (t, $^3J_{H-H}$ = 7.83 Hz, 2H, Ar-*H*), 7.40 (dt, $^3J_{H-H}$ = 7.71 Hz, $^4J_{H-H}$ = 1.66 Hz, 2H, Ar-*H*), 7.14 (dd, $^3J_{H-H}$ = 7.81 Hz, $^4J_{H-H}$ = 1.42 Hz, 2H, Ar-*H*), 6.52 (dt, $^3J_{H-H}$ = 5.88 Hz, $^4J_{H-H}$ = 1.48 Hz, 2H, Ar-*H*), 6.20 (dd, $^3J_{H-H}$ = 5.79 Hz, $^4J_{H-H}$ = 1.52 Hz, 2H, Ar-*H*), 3.43 (s, 6H, Ar-CH_3) ppm. HR-MS (ESI$^+$, MeOH/$CHCl_3$ 1:1): *m/z* calculated for [M+Na]$^+$ ([$C_{24}H_{20}N_4O_4RuNa$]$^+$): 553.0425, found: 553.0445.

Ru(bda)(2-isopropylpyridine)$_2$ (27)

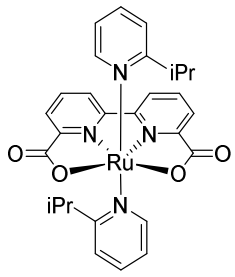

Ru(bda)(dmso)$_2$ (50.0 mg, 100 µmol, 1 equiv.) and 2-isopropylpyridine (258 µL, 2.01 mmol, 20 equiv.) were dissolved in degassed methanol (15 mL) and stirred at 65 °C for 3 h in a nitrogen inert gas atmosphere. The solvent was removed *in vacuo* and the remaining solid was redissolved in DCM/MeOH (5:3) and purified by chromatography (Al_2O_3, DCM/MeOH 9:1 to 1:1) to yield the product as a dark brown solid (39.4 mg, 74.4 µmol, 74%).

Melting point: >300 °C. ^{1}H NMR (400 MHz, MeOD): δ = 8.79 (dd, $^3J_{H-H}$ = 7.98 Hz, $^4J_{H-H}$ = 1.24 Hz, 2H, Ar-*H*), 7.98 (dd, $^3J_{H-H}$ = 7.78 Hz, $^4J_{H-H}$ = 1.19 Hz, 2H, Ar-*H*), 7.91 (t, $^3J_{H-H}$ = 7.89 Hz, 2H, Ar-*H*), 7.59 (dt, $^3J_{H-H}$ = 7.65 Hz, $^4J_{H-H}$ = 1.57 Hz, 2H, Ar-*H*), 7.41 (dd, $^3J_{H-H}$ = 8.05 Hz, $^4J_{H-H}$ = 1.55 Hz, 2H, Ar-*H*), 6.64 (dt, $^3J_{H-H}$ = 5.87 Hz, $^4J_{H-H}$ = 1.53 Hz, 2H, Ar-*H*), 6.33 (dd, $^3J_{H-H}$ = 5.96 Hz, $^4J_{H-H}$ = 1.46 Hz, 2H, Ar-*H*), 3.28 (m, 2H, Ar-C*H*-$(CH_3)_2$) 1.57 (d, $^3J_{H-H}$ = 6.81 Hz, 12H, Ar-CH-(C*H*$_3$)$_2$) ppm. HR-MS (ESI$^+$, MeOH/$CHCl_3$ 1:1): ***m/z*** calculated for $[M]^+$ ($[C_{28}H_{28}N_4O_4Ru]^+$): 586.1154, found: 586.1128.

Synthesis of ligands for macrocyclic WOCs

2-(2-(2-Methoxyethoxy)ethoxy)ethyl-4-methylbenzenesulfonate (33)[316]

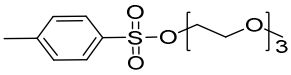

A solution of triethylgylcolmonomethylether (20.0 g, 121 mmol, 1 equiv.) in THF (50 mL) was cooled to 0 °C. Sodium hydroxide (9.75 g, 244 mmol, 2 equiv.) in water (10 mL) was added and the reaction mixture was stirred for 30 min at 0 °C. *p*-Toluluenesulfonyl chloride (34.9 g, 183 mmol, 1.5 eq) dissolved in cold tetrahydrofuran (120 mL, dry) was added dropwise over 2 h and the reaction mixture was left in the cooling bath to warm up to room temperature. After 16 h, water (20 mL) was added. The aqueous layer was separated, the organic layer was dried over anhydrous Na_2SO_4 and the solvent was removed *in vacuo*. The residual liquid was dissolved in diethylether (50 mL) and extracted with water (2 x 20 mL). After flash-column chromatography (SiO_2, cyclohexane:EA 1:1), the product was obtained as colourless liquid (35.0 g, 278 mol, 90%).

^{1}H NMR (400 MHz, $CDCl_3$) δ = 7.34 (d, $^3J_{H-H}$ = 8.38 Hz, 2H, Ar-*H*), 7.35 (d, $^3J_{H-H}$ = 8.50 Hz, 2H, Ar-*H*), 4.15 (t, $^3J_{H-H}$ = 7.42 Hz, 2H, Ar-O-C*H*$_2$-CH_2O), 3.52-3.68 (m, 10H, O-C*H*$_2$-C*H*$_2$-O), 3.36 (s, 3H, O-C*H*$_3$), 1.26 (s, 3H, Ar-CH_3) ppm.

3-Bromo-5-(2-(2-(2-methoxyethoxy)ethoxy)ethoxy)pyridine (34)[263]

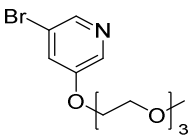

5-Brompyridin-3-ol (4.50 g, 17.9 mmol, 1 equiv.), **33** (6.83 g, 21.4 mmol, 1.2 equiv.) and K_2CO_3 (3.01 g, 21.8 mmol, 1.2 equiv.) were added to dimethylformamide (100 mL) and stirred for 17 h at 50 °C. After filtration, the organic solvent was removed *in vacuo* and chloroform (100 mL)

was added to the residue. The reaction mixture was treated in an ultrasonic bath for 10 min. After a second filtration the organic solvent was removed *in vacuo*. The product was obtained as light brown liquid (7.00 g, 17.6 mmol, 98%).

^{1}H NMR (400 MHz, $CDCl_3$): δ = 8.27 (d, $^4J_{H-H}$ = 1.77 Hz, 1H, Ar-*H*), 8.25 (d, 1H, $^4J_{H-H}$ = 1.77 Hz, Ar-*H*), 7.42 (dd, 1H, $^4J_{H-H}$ = 2.47 Hz, $^5J_{H-H}$ = 1.77 Hz, Ar-*H*), 4.19-4.19 (m, 2H, Ar-O-C*H*$_2$-CH$_2$O-R), 3.88-3.85 (m, 2H, Ar-O-CH$_2$-C*H*$_2$-R), 2.69-3.64 (m, 6H, Ar-(O-C$_2$H$_4$)-O-C*H*$_2$-C*H*$_2$-O-C*H*$_2$-R), 3.56-3.53 (m, 2H, Ar-(O-C$_2$H$_4$)$_2$-O-CH$_2$-C*H*$_2$-R), 3.38 (s, 3H, O-C*H*$_3$) ppm. HR-MS (ESI$^+$, MeCN/$CHCl_3$ 1:1): *m/z* calculated for [M+Na]$^+$ ([$C_{12}H_{18}BrO_4NNa$]$^+$): 342.0311, found: 342.0359.

1,3-Dibromo-5-(2-(2-(2- methoxyethoxy)ethoxy)ethoxy)benzene (37)[317]

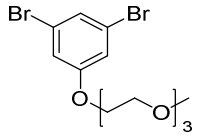

3,5-Dibromophenol (4.50 g, 17.9 mmol, 1 equiv.), **33** (7.90 g, 24.8 mmol, 1.4 equiv.) and K_2CO_3 (3.49 g, 25.2 mmol, 1.4 equiv.) were added to dimethylformamide (100 mL) and stirred for 17 h at 50 °C. After filtration, the organic solvent was removed *in vacuo* and chloroform (100 mL) was added to the residue. The reaction mixture was treated in an ultrasonic bath for 10 min. After a second filtration the organic solvent was removed *in vacuo*. The product was obtained as dark brown liquid (5.20 g, 13.0 mmol, 73%).

^{1}H NMR (400 MHz, $CDCl_3$): δ = 7.23 (t, $^4J_{H-H}$ = 1.70 Hz, 1H, Ar-*H*), 7.01 (d, 2H, $^4J_{H-H}$ = 1.65 Hz, Ar-*H*), 4.09 (t, 2H, Ar-O-C*H*$_2$-CH$_2$O), 3.53-3.83 (m, 10H, Ar-O-CH$_2$-C*H*$_2$-(O-C$_2$H$_4$)$_2$), 3.37 (s, 3H, O-C*H*$_3$) ppm. HR-MS (ESI$^+$, MeCN/$CHCl_3$ 1:1): *m/z* calculated for [M+Na]$^+$ ([$C_{12}H_{18}Br_2O_4Na$]$^+$): 420.9443, found: 420.9436.

1,3-Bis(5-(2-(2-(2-methoxyethoxy)ethoxy)ethoxy)pyridin-3-yl)benzene (L2)

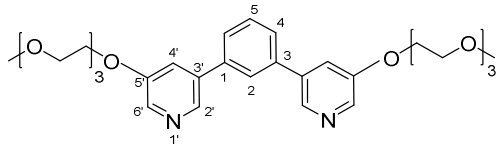

The reaction was carried out in an inert nitrogen gas atmosphere. A mixture of toluene (10.0 mL), ethanol (6.0 mL) and an aqueous sodium carbonate solution (2 M, 10.0 mL) was degassed by "pump-freeze-thaw" cycles. Subsequently, 1,4-Bis(4,4,5,5-tetramethyl-1,3,2-dioxaborolan-2-yl)benzene (515 mg, 1.56 mmol, 1 equiv.), **34** (1.50 g, 4.68 mmol, 3 equiv.)

and $Pd(PPh_3)_4$ (180 mg, 156 mol, 0.10 equiv.) were added and the product was purified by flash-column chromatography (SiO_2, EA 100% to EA:MeOH 8:2). The desired compound **L2** was obtained as an off-white solid (813 mg, 1.46 mmol, 94%).

Melting point: 57-58 °C. ^{1}H NMR (400 MHz, CD_2Cl_2): δ = 8.50 (d, $^4J_{H-H}$ = 1.44 Hz, 2H, Ar-$H_{2'}$), 8.32 (d, $^4J_{H-H}$ = 2.74 Hz, 2H, Ar-$H_{6'}$), 7.82 (dt, $^4J_{H-H}$ = 1.82 Hz, $^5J_{H-H}$ = 0.50 Hz, 1H, Ar-H_5), 7.66-7.57 (m, 3H, Ar-$H_{2,4'}$), 7.50 (dd, 2H, $^4J_{H-H}$ = 2.75 Hz, $^4J_{H-H}$ = 0.50 Hz, Ar-H_4), 4.27-4.25 (m, 4H, Ar-O-CH_2-CH_2-O), 3.88-3.86 (m, 4H, Ar-O-CH_2-CH_2O), 3.70-3.67 (m, 4H, Ar-(O-C_2H_4)-O-CH_2-R), 3.64-3.61 (m, 4H, Ar-(O-C_2H_4)-O-CH_2-CH_2), 3.59-3.57 (m, 4H, Ar-(O-C_2H_4)$_2$-O-CH_2-R), 3.50-3.47 (m, 4H Ar-(O-C_2H_4)$_2$-O-CH_2-CH_2-R), 3.32 (s, 6H, OCH_3) ppm. ^{13}C NMR (100 MHz, CD_2Cl_2): δ = 155.7, 141.3, 139.1, 137.5, 137.4, 130.3, 127.6, 127.7, 120.2, 72.4, 71.4, 71.0, 71.0, 70.1, 68.6, 59.2 ppm. HR-MS (ESI$^+$, MeCN/$CHCl_3$ 1:1): *m/z* calculated for $[M+H]^+$ ($[C_{30}H_{41}N_2O_8]^+$): 557.2857, found: 557.2877.

4,4'-(5-(2-(2-(2-Methoxyethoxy)ethoxy)ethoxy)-1,3- phenylene)dipyridine (L4)

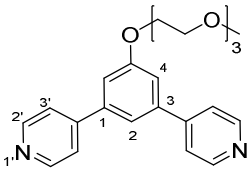

The reaction was carried out in an inert nitrogen gas atmosphere. A mixture of toluene (16.0 mL), ethanol (2.0 mL) and an aqueous sodium carbonate solution (2 M, 16.0 mL) was degassed by "pump-freeze-thaw" cycles. Subsequently, **37** (1.50 g, 3.77 mmol, 0.33 equiv.), **4** (2.34 g, 11.4 mmol, 1 equiv.) and $Pd(PPh_3)_4$ (1.32 g, 1.14 mmol, 0.1 equiv.) were added and the reaction mixture was stirred for 24 h at 100 °C. The solvent was removed *in vacuo* and the product was purified by flash-column chromatography (SiO_2, EA 100% to EA:MeOH 8:2). Compound **L4** was obtained as a pale yellow solid (996 mg, 2.53 mmol, 67%).

Melting point: 65-66 °C. ^{1}H NMR (400 MHz, CD_2Cl_2): δ = 8.67 (dd, $^4J_{H-H}$ = 1.47 Hz, $^3J_{H-H}$ = 4.72 Hz, 4H, Ar-$H_{2'}$), 7.57 (dd, $^4J_{H-H}$ = 1.58 Hz, $^3J_{H-H}$ = 4.73 Hz, 4H, Ar-$H_{3'}$), 7.51 (s, 1H, Ar-H_2), 7.28 (d, $^4J_{H-H}$ = 1.54 Hz, 2H, Ar-H_4), 4.28-4.26 (m, 2H, Ar-O-CH_2-CH_2O), 3.89-3.87 (m, 2H, Ar-O-CH_2-CH_2-(O-C_2H_4)$_2$), 3.72-3.69 (m, 2H, Ar-O-(CH_2)$_2$-(O-C_2H_4)$_2$), 3.64-3.62 (m, 2H, Ar-O-(CH_2)$_2$-(O-C_2H_4)$_2$), 3.60-3.58 (m, 2H, Ar-O-(CH_2)$_2$-(O-C_2H_4)$_2$), 3.50-3.48 (m, 2H, Ar-O-(CH_2)$_2$-(O-C_2H_4)$_2$), 3.32 (s, 3H, O-CH_3) ppm. ^{13}C NMR (100 MHz, CD_2Cl_2): δ = 160.4, 150.7, 148.0, 140.9, 122.1, 118.8, 114.2, 72.3, 71.2, 70.9, 70.8, 70.0, 68.4, 59.0 ppm. HR-MS (ESI$^+$, MeCN/$CHCl_3$ 1:1): *m/z* calculated for $[M+H]^+$ ($[C_{23}H_{27}N_2O_4]^+$): 395.1965, found: 395.1967.

Synthesis of Ru(bda) macrocycles

OEG-MC2

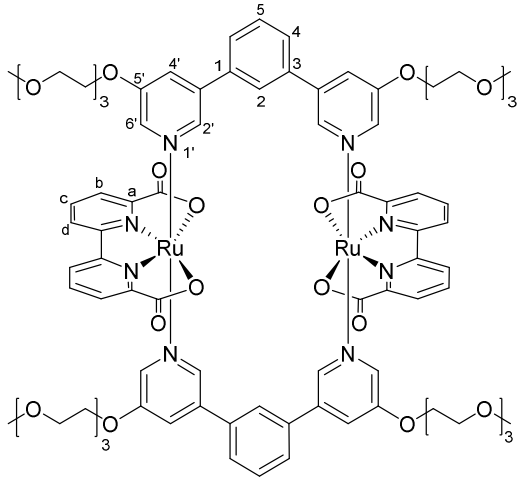

$Ru(bda)(dmso)_2$ (15.0 mg, 30.0 µmol, 1 equiv.) and ligand **L2** (16.7 mg, 30.0 µmol, 1 equiv.) were dissolved in degassed H_2O (12 mL) and stirred at 95 °C for 72 h in a nitrogen inert gas atmosphere. The solvent was removed by filtration and the remaining solid was redissolved in DCM/MeOH (5:3) and filtered over aluminum oxide (neutral, 15% w/w H_2O). Further purification by size exclusion chromatography (BioBeads S-X1, DCM/MeOH 9:1) and subsequent recycling GPC cycles ($CHCl_3$/MeOH 9:1) yielded in 7.0 mg (3.9 µmol, 26%) of macrocycle **OEG-MC2**.

Melting point: > 300 °C. ^{1}H NMR (400 MHz, CD_2Cl_2 / MeOD): δ = 9.41 (s, 2H, Ar-H_d), 8.12-8.11 (m, 6H, Ar-$H_{b,6',2'}$), 7.49-7.45 (m, 3H, Ar-$H_{c,2}$), 7.35 (s, 2H, Ar-$H_{4'}$), 7.21 (s, 2H, Ar-H_4), 7.12 (s, 1H, Ar-H_5), 4.44 (s, 4H, Ar-O-CH_2-CH_2-O), 4.06-4.03 (m, 4H, Ar-O-CH_2-CH_2-O), 3.73-3.71 (m, 4H, Ar-O-$(CH_2)_2$-(O-$C_2H_4)_2$), 3.58-3.52 (m, 8H, Ar-O-$(CH_2)_2$-(O-$C_2H_4)_2$), 3.46-3.44 (m, 4H, -(O-C_2H_4)-OCH_3), 3.28 (s, 6H, OCH_3) ppm. ^{13}C NMR (100 MHz, CD_2Cl_2 / MeOD): δ = 174.7, 160.9, 157.6, 156.6, 143.4, 140.5, 138.7, 137.8, 134.4, 134.1, 131.1, 129.3, 127.0, 125.3, 121.6, 72.4, 71.3, 71.1, 70.9, 69.9, 69.1, 59.1 ppm. HR-MS (ESI$^+$, MeCN/$CHCl_3$ 1:1): *m/z* calculated for $[M+Na]^+$ ($[C_{84}H_{92}N_8O_{24}Ru_2]^+$): 1823.4204, found: 1823.4219.

OEG-MC4

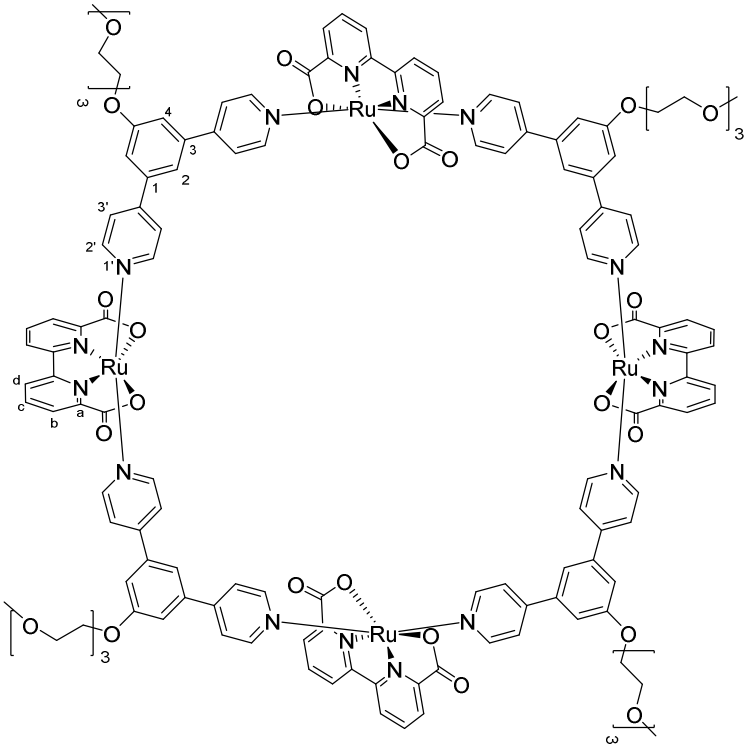

Ru(bda)(dmso)$_2$ (31.5 mg, 63.5 µmol, 1 equiv.) and ligand **L4** (25 mg, 63.5 µmol, 1 equiv.) were dissolved in degassed ethane-1,2-diol (15 mL) and stirred at 95 °C for 24 h in a nitrogen inert gas atmosphere. The solvent was removed by filtration and the remaining solid was redissolved in DCM/MeOH (5:3) and filtered over aluminum oxide (neutral, 15% w/w H_2O). Further purification by size exclusion chromatography (BioBeads S-X1, DCM/MeOH 9:1) and subsequent recycling GPC cycles ($CHCl_3$/MeOH 9:1) yielded in 7.5 mg (2.54 µmol, 16%) of **OEG-MC4**.

Melting point: > 300 °C. ^{1}H NMR (400 MHz, CD_2Cl_2 / MeOD / CF_3CD_2OD): δ = 8.46 (d, $^3J_{H-H}$ = 7.40 Hz, 8H, Ar-*H$_d$*), 7.98 (d, $^3J_{H-H}$ = 6.66 Hz, 8H, Ar-*H$_b$*), 7.83-7.78 (m, 24H, Ar-*H$_{c,2'}$*), 7.32 (d, $^3J_{H-H}$ = 6.66 Hz, 16H, Ar-*H$_{3'}$*), 7.23 (s, 4H, Ar-*H$_2$*), 7.10 (s, $^3J_{H-H}$ = 6.66 Hz, 8H, Ar-*H$_4$*), 4.11-4.07 (m, 8H, Ar-O-C*H$_2$*-CH$_2$-O), 3.76-3.72 (m, 8H, Ar-O-CH$_2$-C*H$_2$*-O), 3.60-3.65 (m, 8H, Ar-O-(CH$_2$)$_2$-(O-C$_2$*H$_4$*)$_2$), 3.54-3.48 (m, 16H, Ar-O-(CH$_2$)$_2$-(O-C$_2$*H$_4$*)$_2$), 3.41-3.39 (m, 8H, Ar-O-(CH$_2$)$_2$-(O-C$_2$*H$_4$*)$_2$), 3.22 (s, 12H, O-C*H$_3$*) ppm. ^{13}C NMR (100 MHz, CD_2Cl_2 / MeOD / CF_3CD_2OD): δ = 174.1, 160.7, 160.3, 157.3, 152.8, 148.5, 139.4, 132.3, 126.6, 125.1, 123.2, 118.7, 114.9, 72.3, 71.1, 70.9, 70.8, 70.0, 68.4, 58.9 ppm. HR-MS (ESI$^+$, MeCN/$CHCl_3$ 1:1): *m/z* calculated for $[M]^+$ ($[C_{140}H_{128}N_{16}O_{32}Ru_4]^+$): 2952.5055, found: 2950.4640.

Chapter 9

—

Appendix

9.1 Supporting Information for Chapter 3

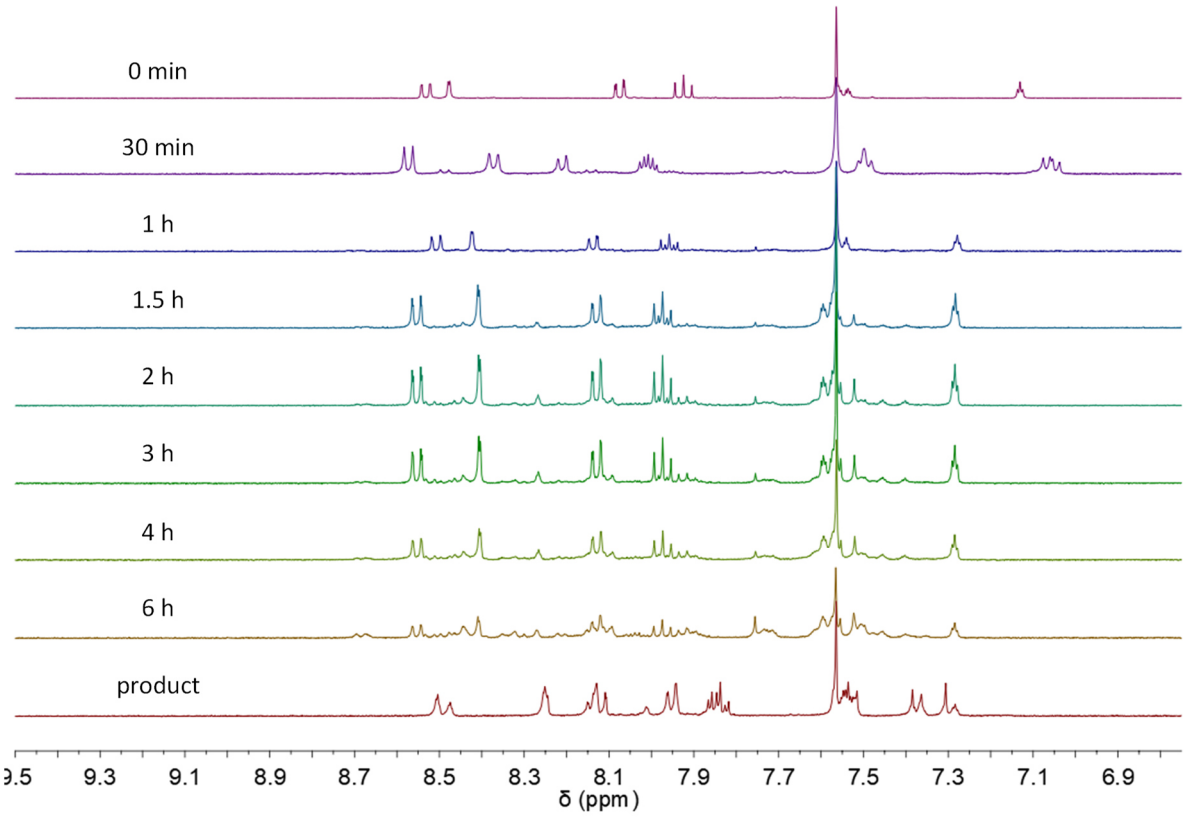

Figure S1: Time-dependent ^{1}H NMR spectra for the formation of ***m*-F-MC3** in CD_2Cl_2/MeOD (5:1). Reaction was performed in a NMR tube in an oil bath at 55 °C and the NMR spectra were recorded at room temperature at 400 MHz.

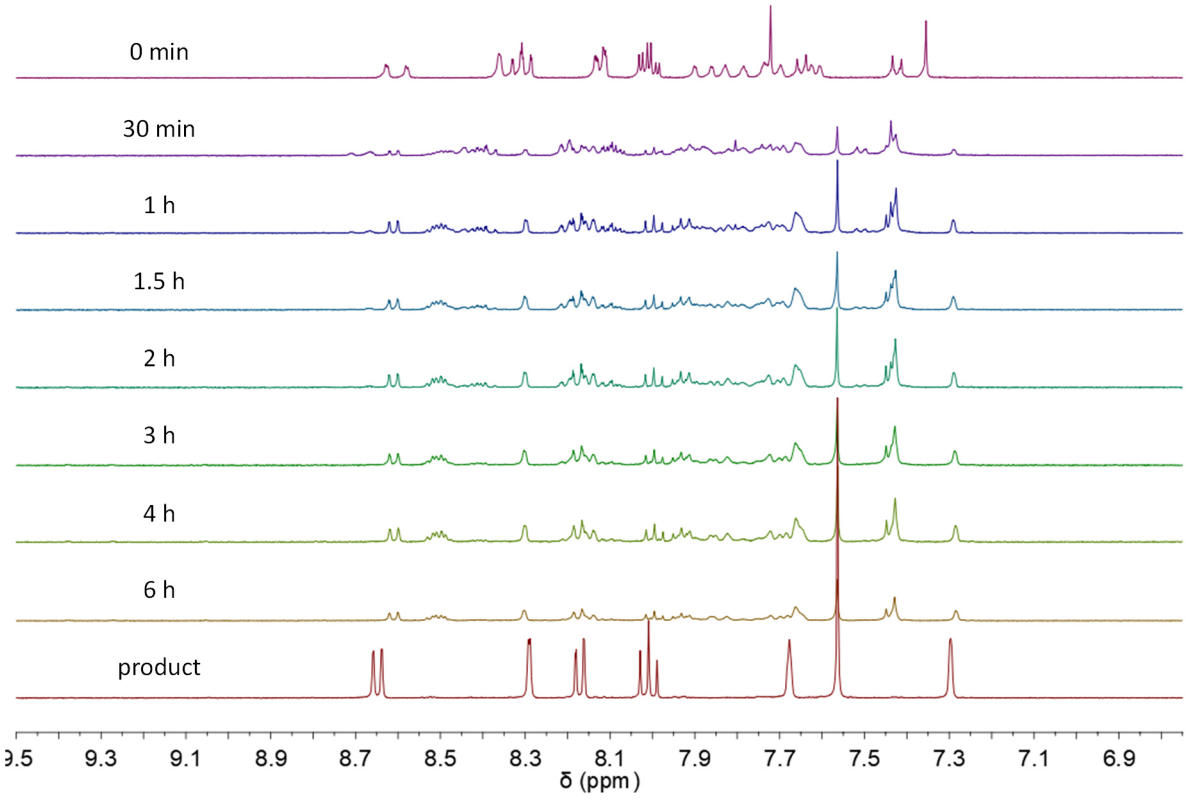

.

Figure S2: Time-dependent ^{1}H NMR spectra for the formation of ***m*-Me-MC3** in CD_2Cl_2/MeOD (5:1). Reaction was performed in a NMR tube in an oil bath at 55 °C and the NMR spectra were recorded at room temperature at 400 MHz.

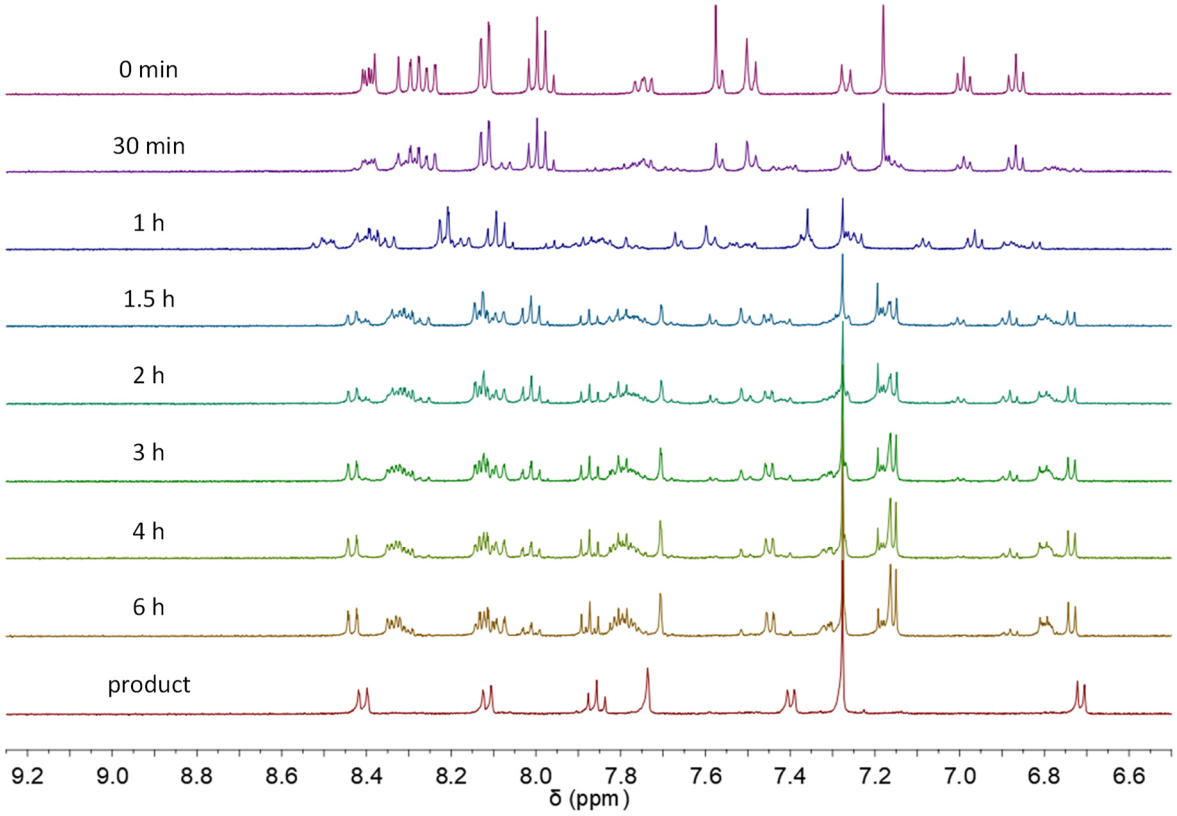

Figure S3: Time-dependent ^{1}H NMR spectra for the formation of ***p*-OMe-MC3** in CD_2Cl_2/MeOD (5:1). Reaction was performed in a NMR tube in an oil bath at 55 °C and the NMR spectra were recorded at room temperature at 400 MHz.

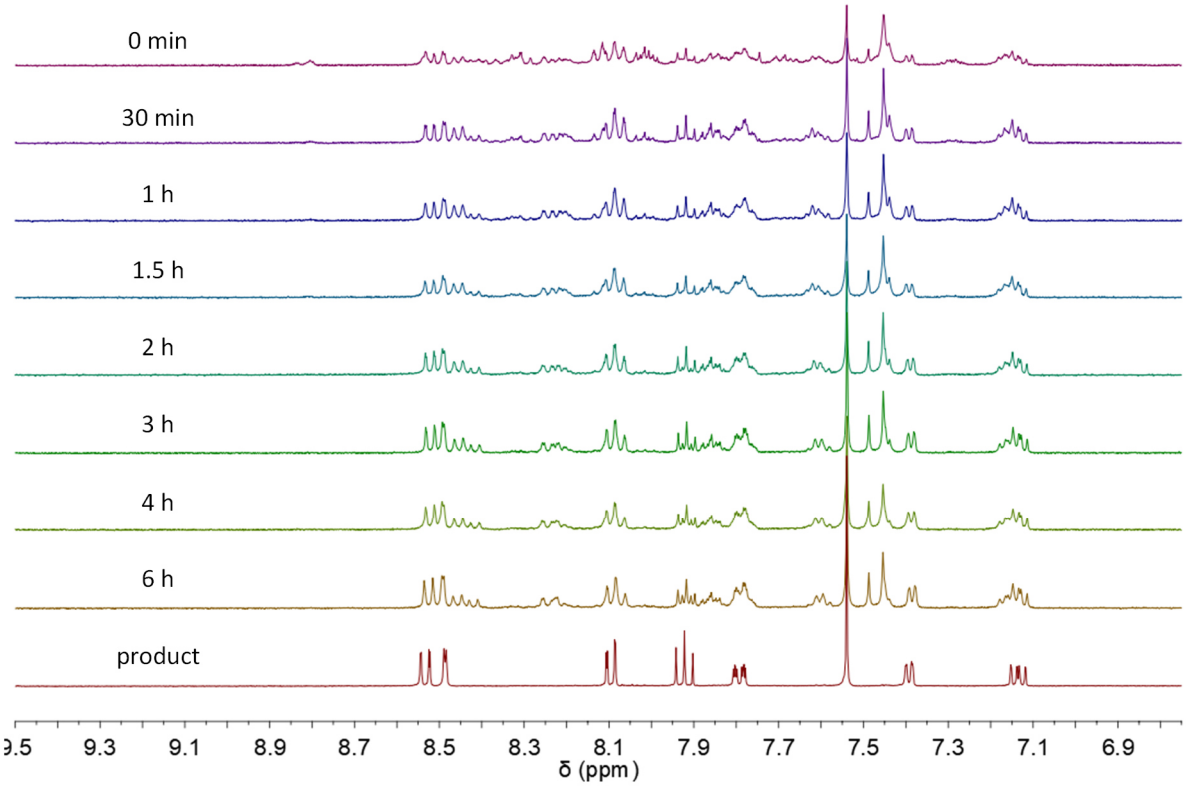

Figure S4: Time-dependent ^{1}H NMR spectra for the formation of **MC3** in CD_2Cl_2/MeOD (5:1). Reaction was performed in a NMR tube in an oil bath at 55 °C and the NMR spectra were recorded at room temperature at 400 MHz.

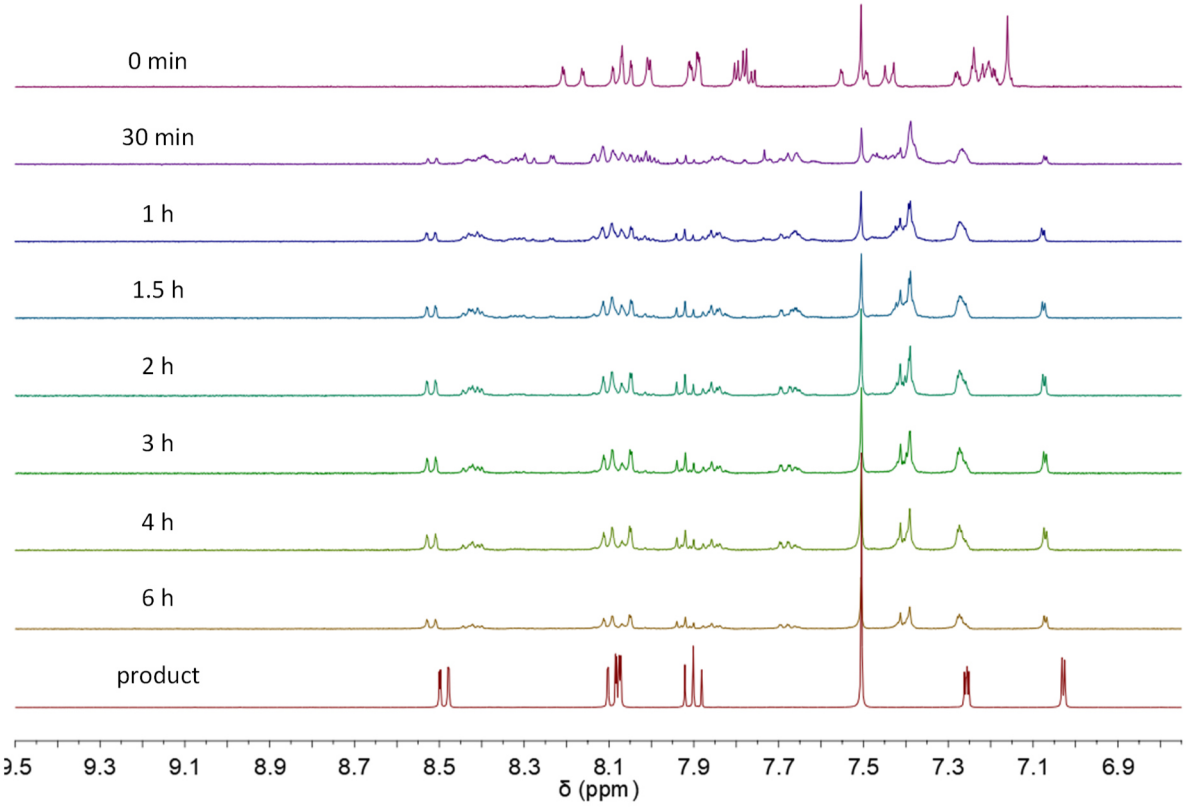

Figure S5: Time-dependent ^{1}H NMR spectra for the formation of ***m*-OMe-MC3** in CD_2Cl_2/MeOD (5:1). Reaction was performed in a NMR tube in an oil bath at 55 °C and the NMR spectra were recorded at room temperature at 400 MHz.

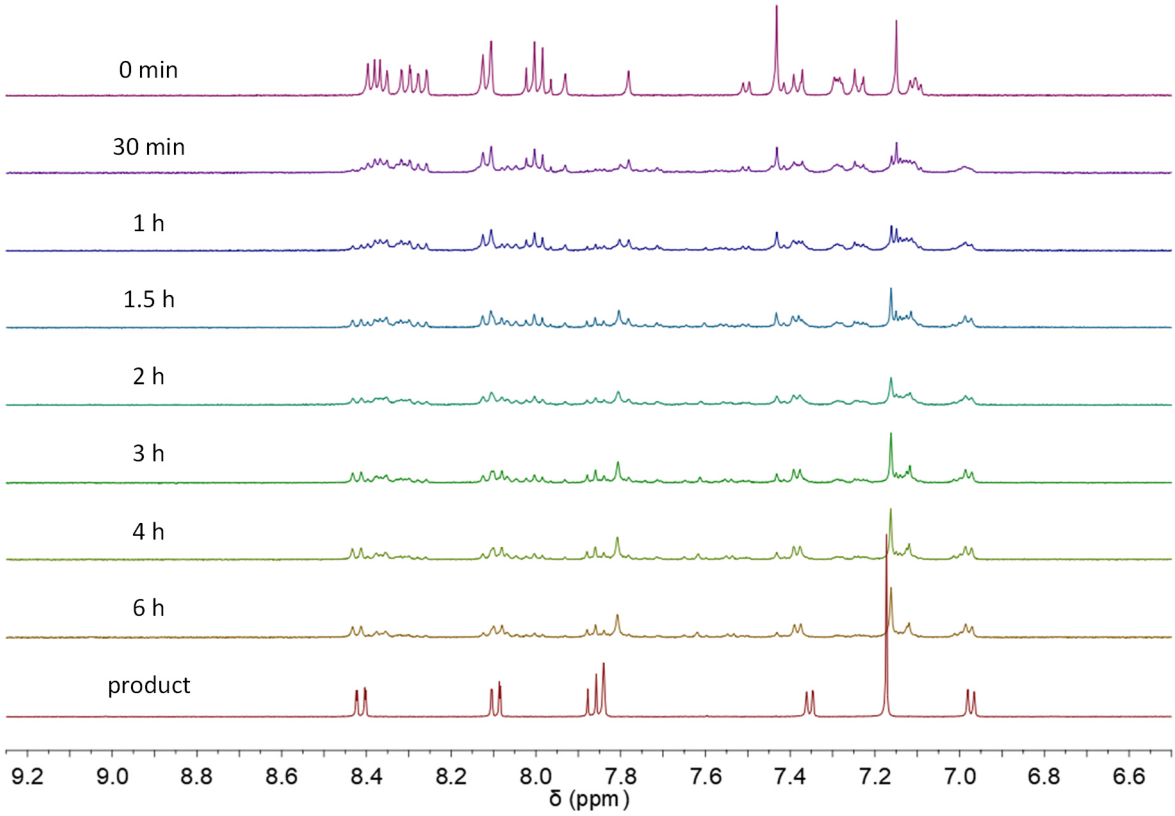

Figure S6: Time-dependent ^{1}H NMR spectra for the formation of ***p*-Me-MC3** in CD_2Cl_2/MeOD (5:1). Reaction was performed in a NMR tube in an oil bath at 55 °C and the NMR spectra were recorded at room temperature at 400 MHz.

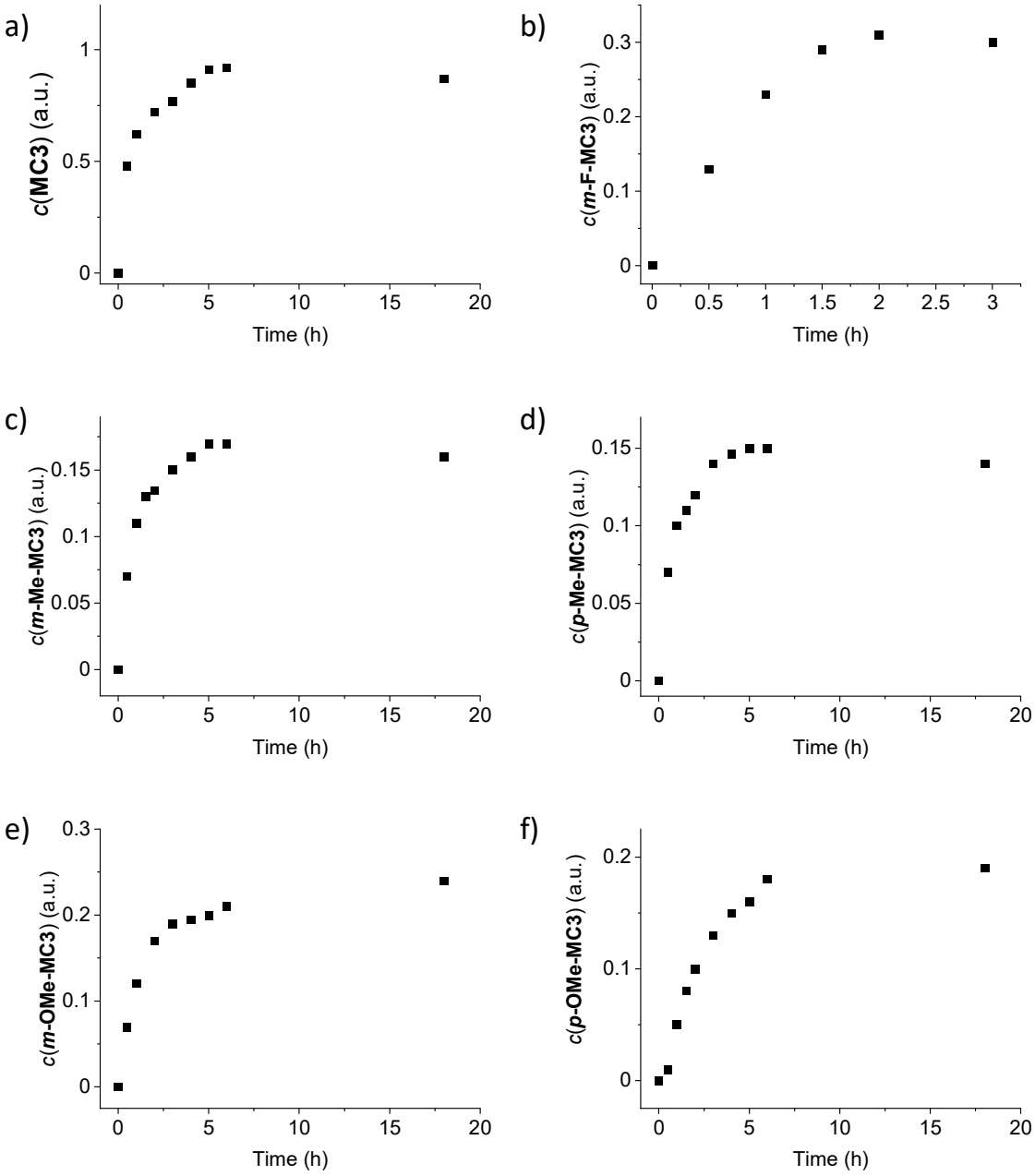

Figure S7: Time-dependent product formation of **MC3** and its determined by ^{1}H NMR spectroscopy in reference to an internal standard in the reaction mixture. ^{1}H NMR spectra (400 MHz) were recorded in CD_2Cl_2/MeOD (5:1) at room temperature.

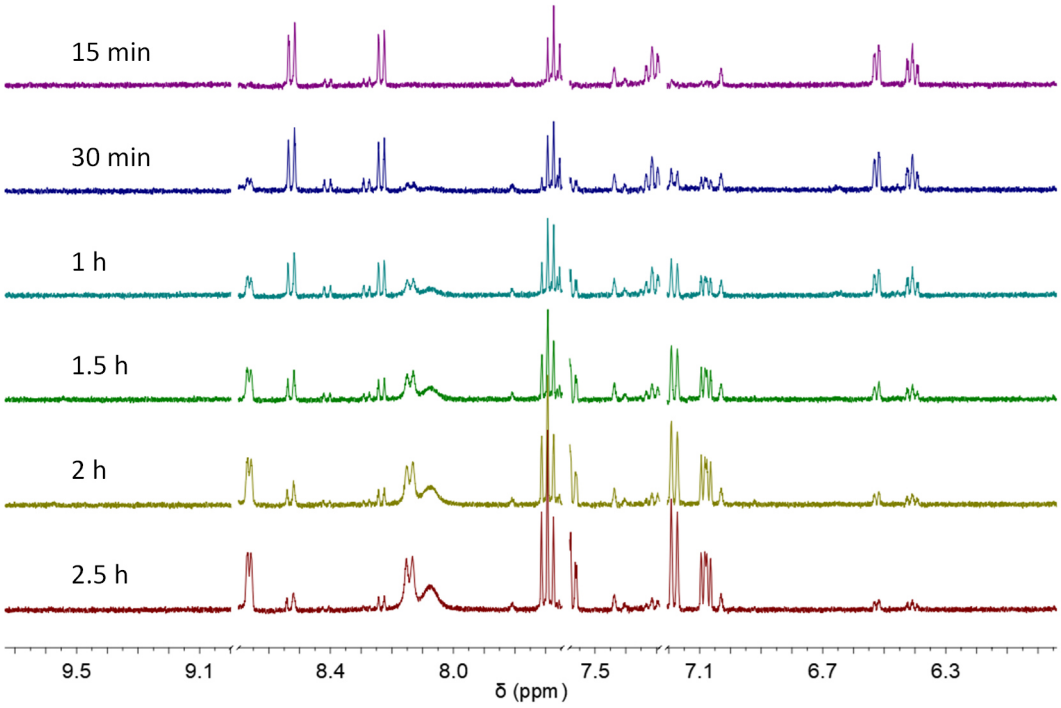

Figure S8: Time-dependent ^{1}H NMR spectra (400 MHz) of ligand exchange reaction with Ru(bda)(2-isopropylpyridine)$_2$ **27** in pyridine-d_5 at 71 °C.

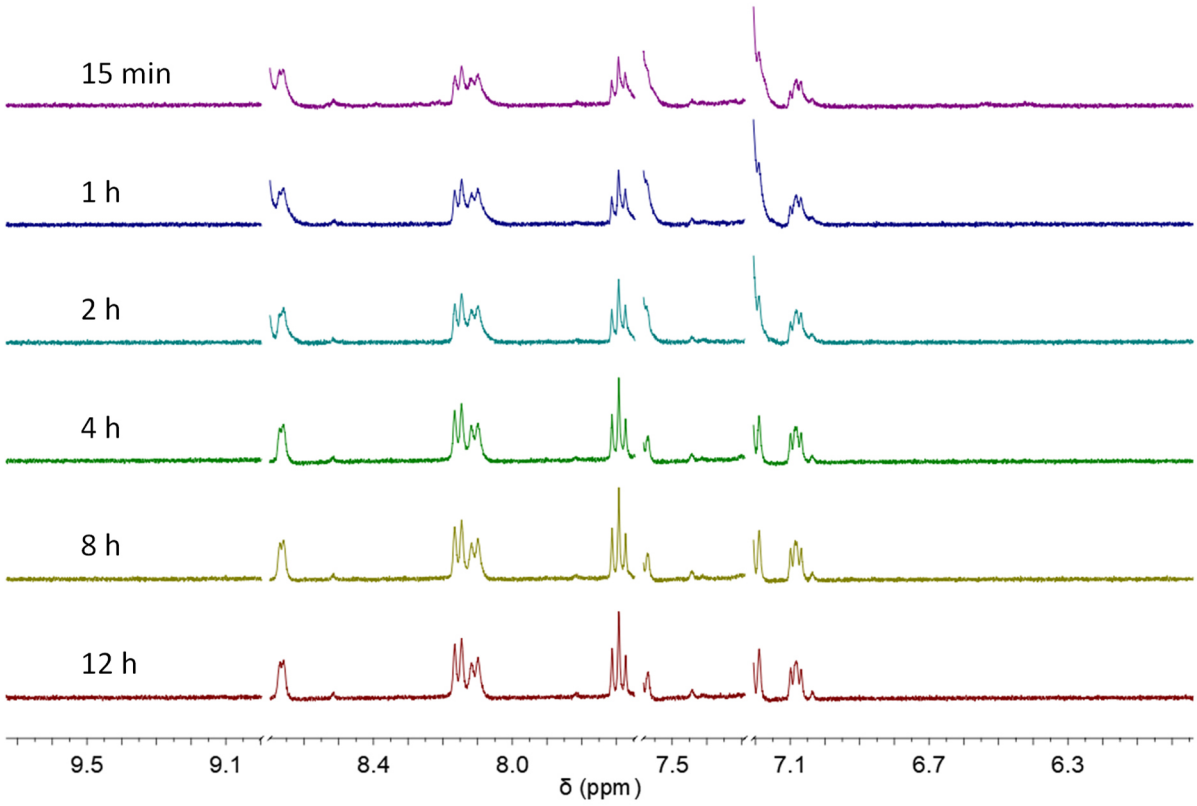

Figure S9: Time-dependent ^{1}H NMR spectra (400 MHz) of ligand exchange reaction with Ru(bda)(2-isopropylpyridine)$_2$ **27** in pyridine-d_5 at 81 °C.

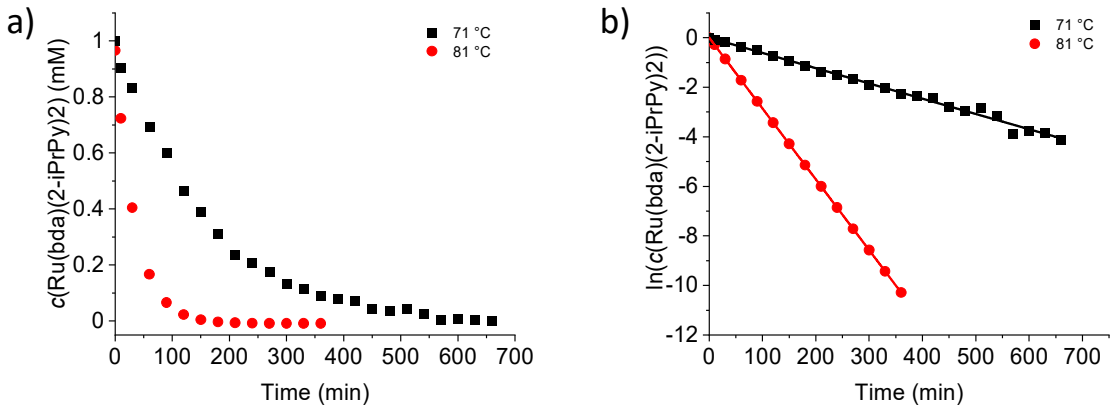

Figure S10: a) Concentration changes of Ru(bda)(2-isopropypyridine)$_2$ **27** for the reaction in pyridine-d$_5$ at two temperatures (T_1 = 71 °C and T_2 = 81 °C). b) Determination of the individual reaction rates (k_1 = 6.16 * 10^{-3} min^{-1}, k_2 = 14.9 * 10^{-3} min^{-1}) for determination of the activation energy (E_a).

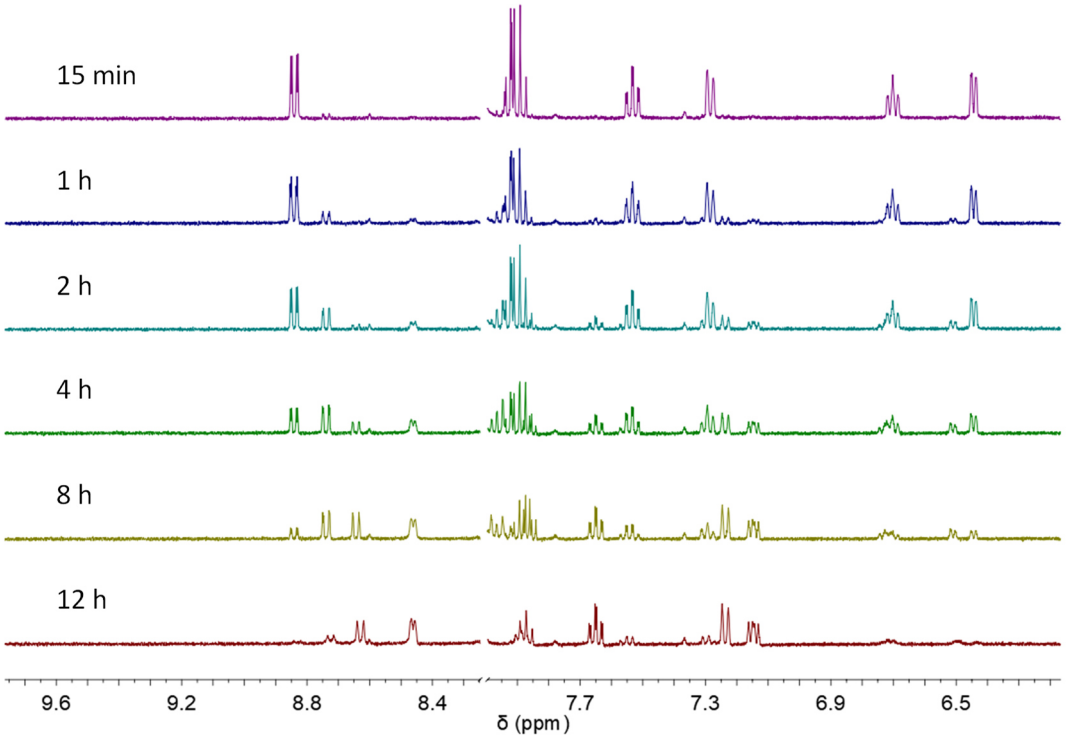

Figure S11: Time-dependent ^{1}H NMR spectra (400 MHz) of ligand exchange reaction of Ru(bda)(2-picoline)$_2$ **26** with 5 eqiv. pyridine-d$_5$ in DMF-d$_7$ at 92 °C.

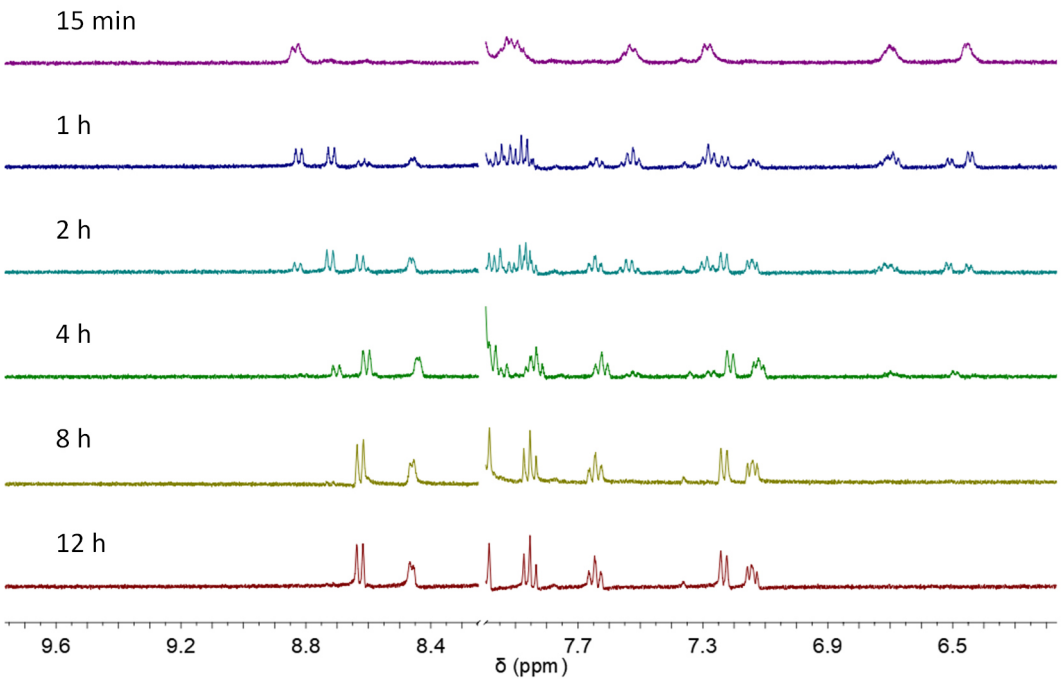

Figure S12: Time-dependent ^{1}H NMR spectra (400 MHz) of ligand exchange reaction of Ru(bda)(2-picoline)$_2$ **26** with 5 eqiv. pyridine-d_5 in DMF-d_7 at 104 °C.

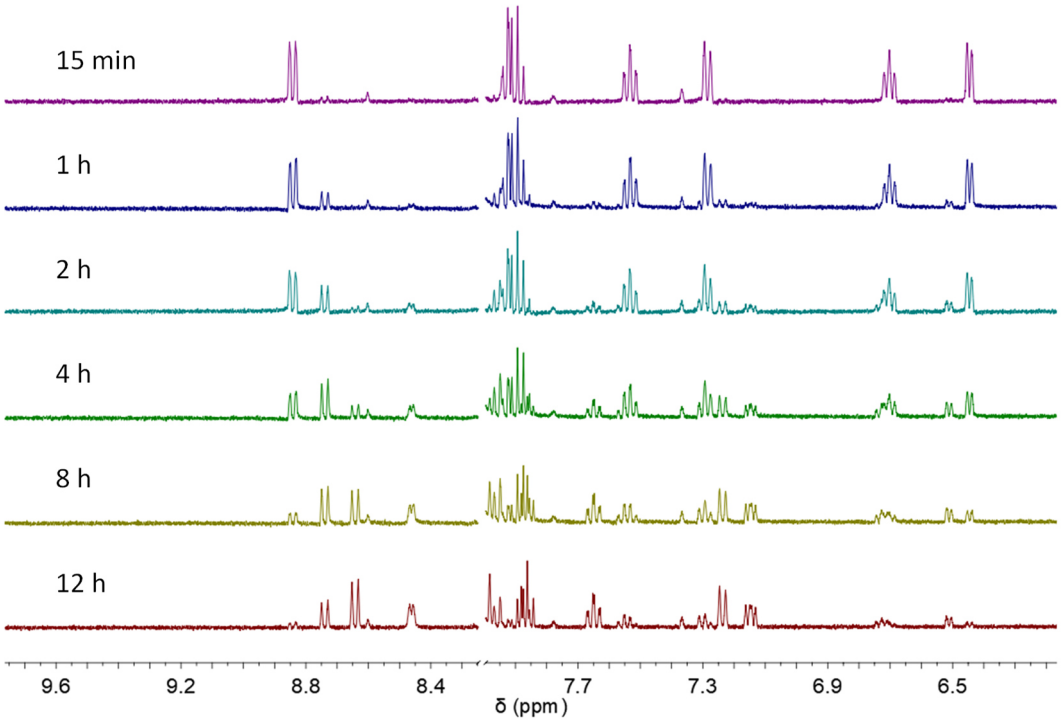

Figure S13: Time-dependent ^{1}H NMR spectra (400 MHz) of ligand exchange reaction of Ru(bda)(2-picoline)$_2$ **26** with 10 eqiv. pyridine-d_5 in DMF-d_7 at 92 °C.

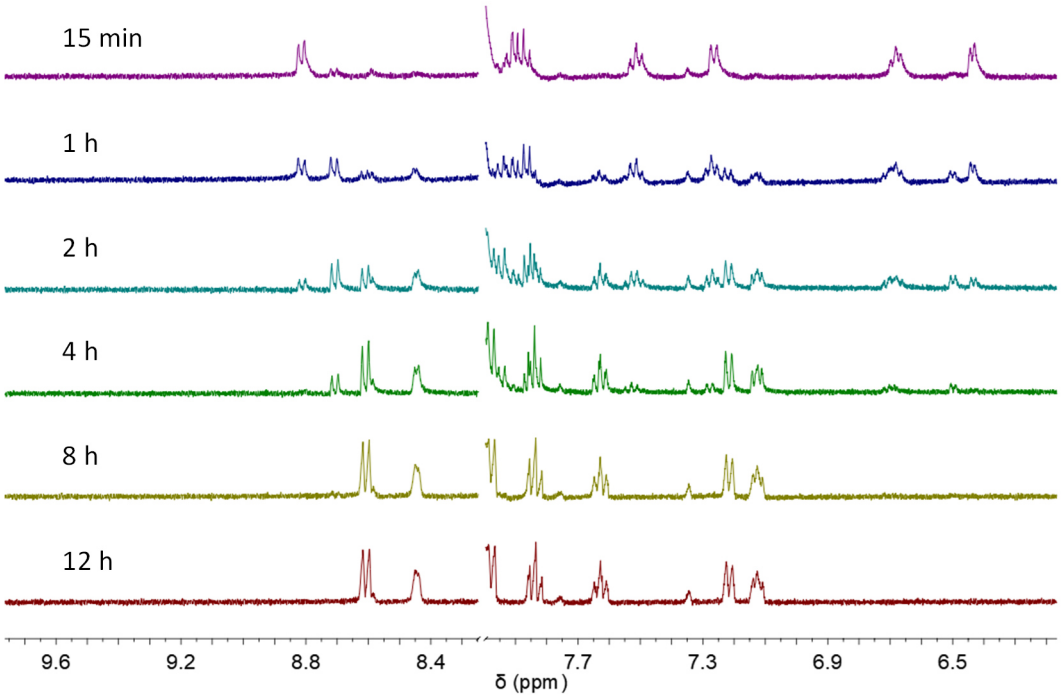

Figure S14: Time-dependent ^{1}H NMR spectra (400 MHz) of ligand exchange reaction of Ru(bda)(2-picoline)$_2$ **26** with 10 eqiv. pyridine-d_5 in DMF-d_7 at 104 °C.

9.2 Supporting Information for Chapter 4

NMR spectra of **L2** and **L4** and complexes **OEG-MC2** and **OEG-MC4**

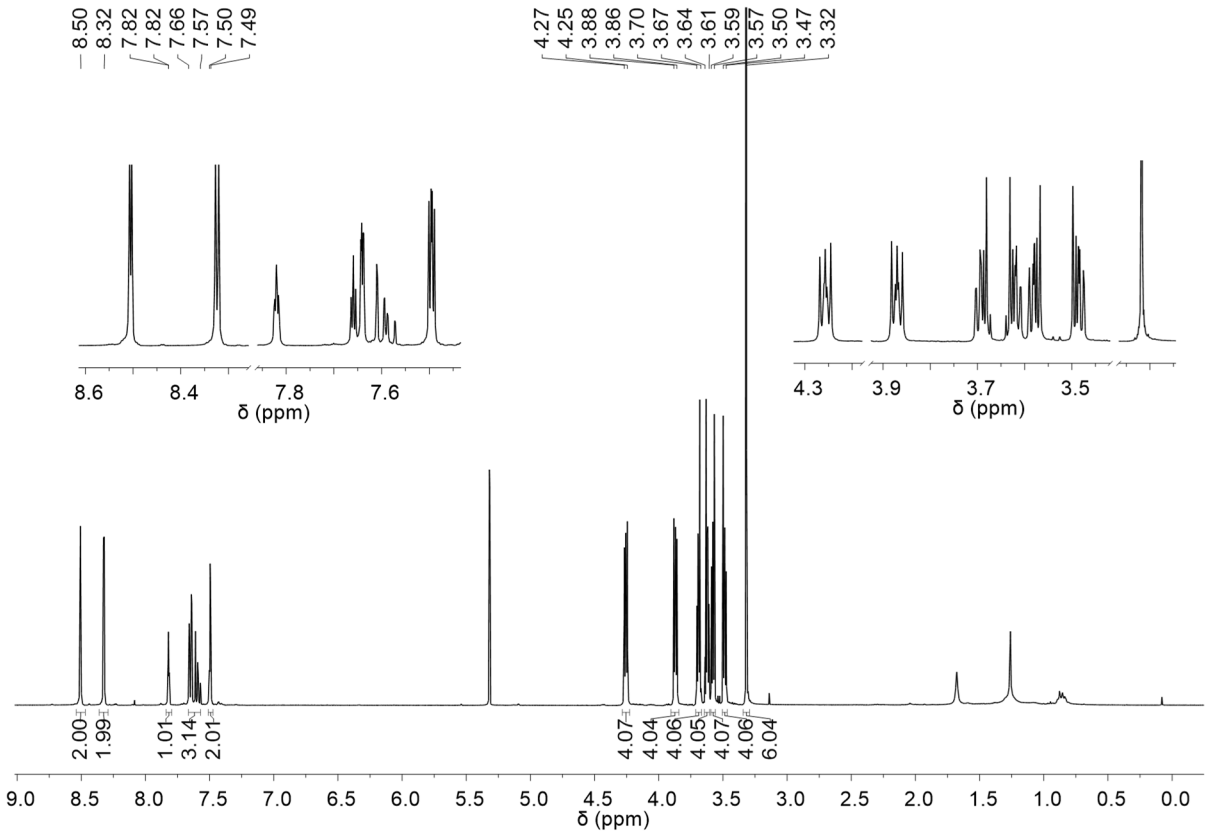

Figure S15: ^{1}H NMR spectrum (400 MHz, CD_2Cl_2) of **L2**.

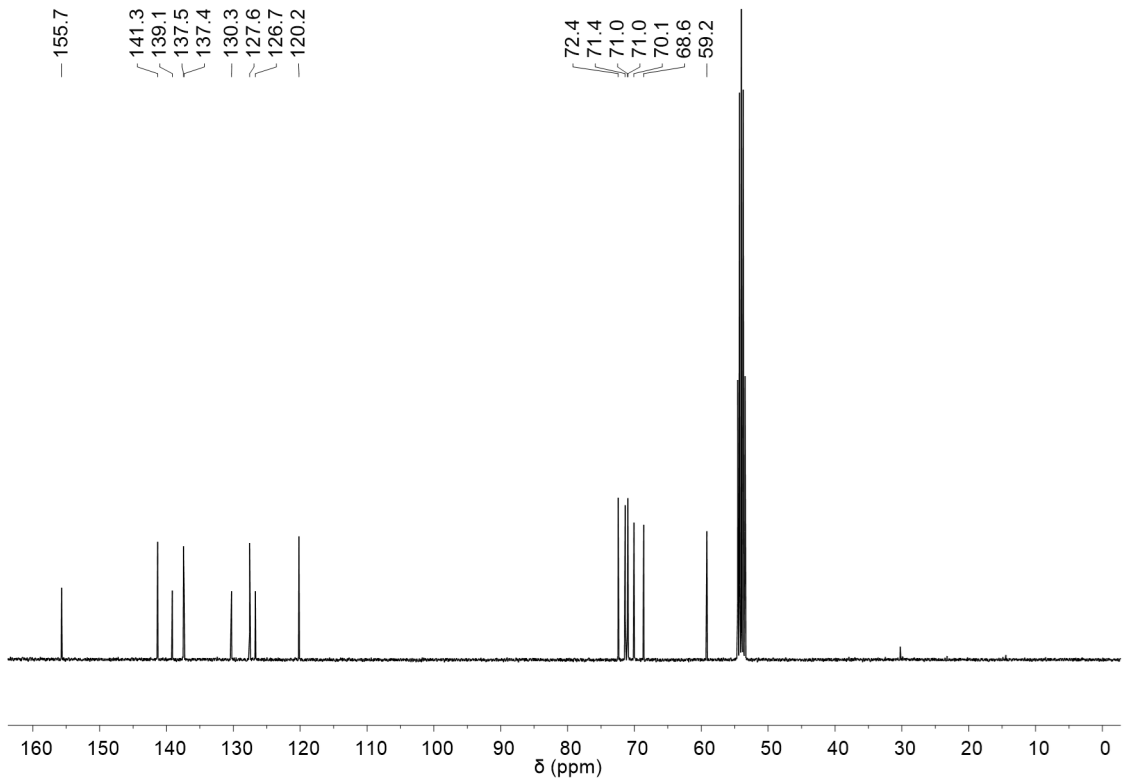

Figure S16: ^{13}C NMR spectrum (100 MHz, CD_2Cl_2) of **L2**.

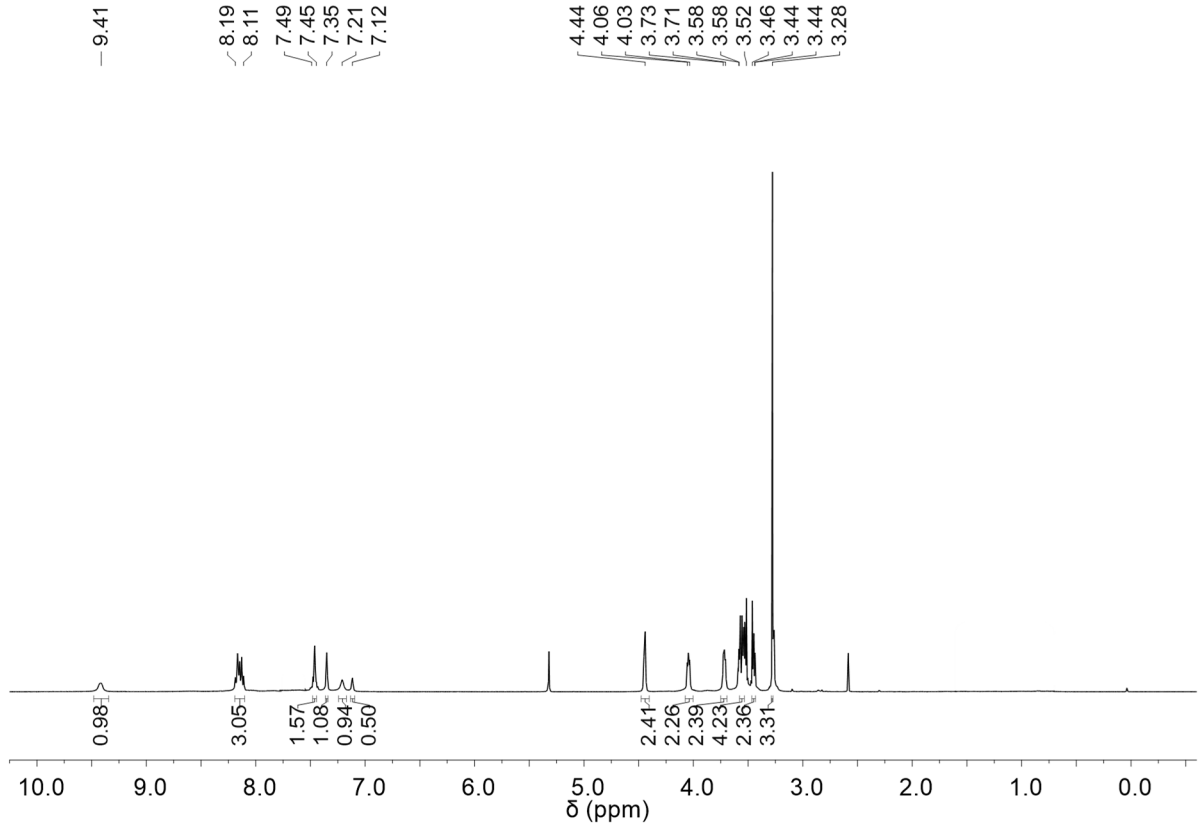

Figure S17: ^{1}H NMR spectrum (400 MHz, CD_2Cl_2/MeOD 5:3) of **OEG-MC2**. The integration of the signals is normalized for a monomeric unit.

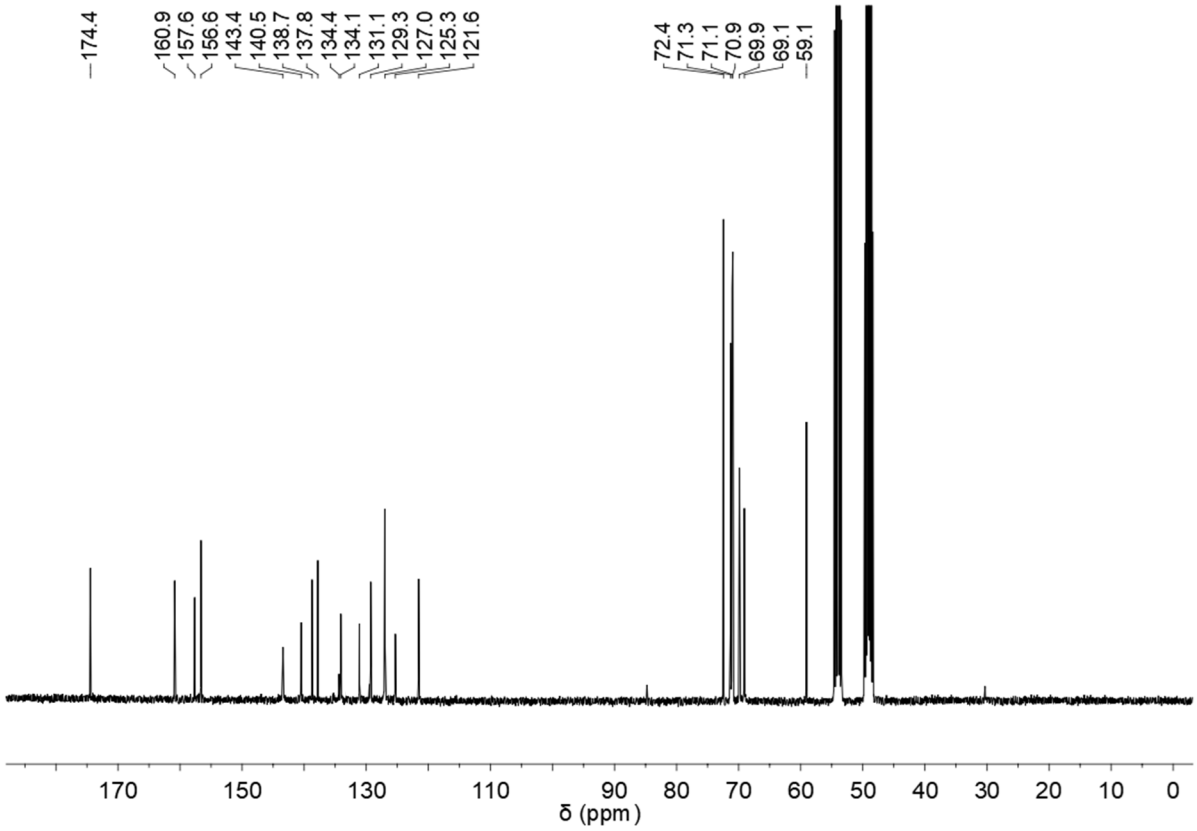

Figure S18: ^{13}C NMR spectrum (100 MHz, CD_2Cl_2/MeOD 5:3) of **OEG-MC2**.

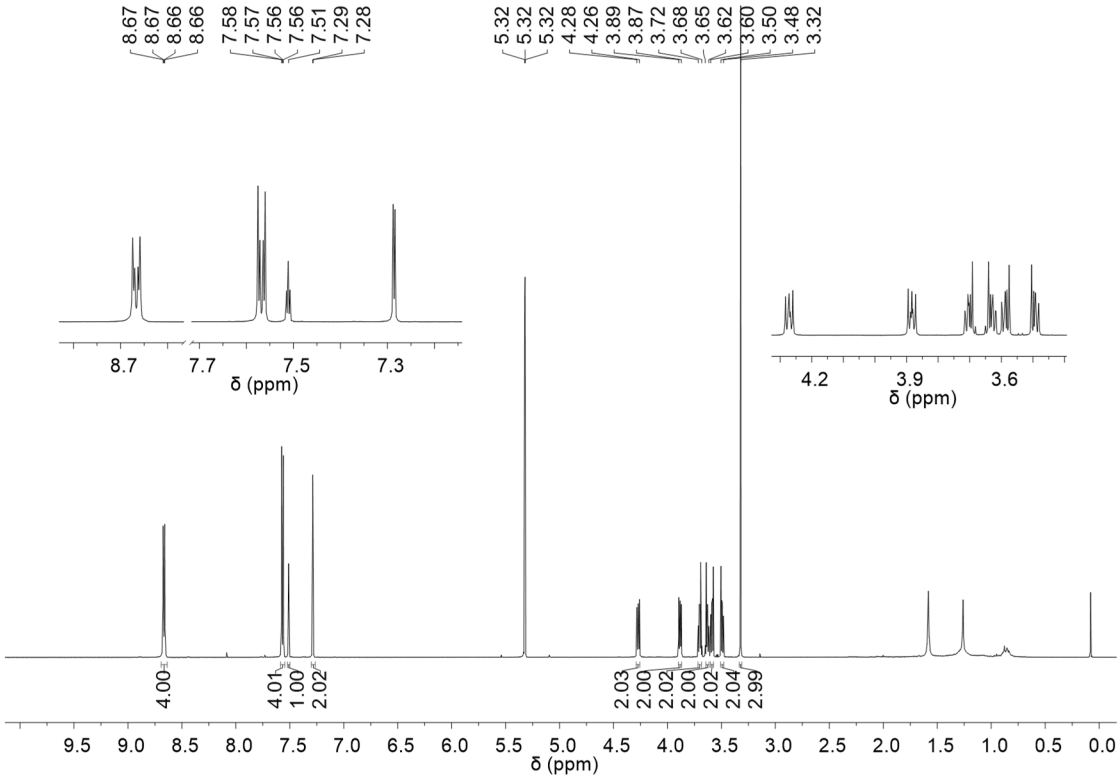

Figure S19: ^{1}H NMR spectrum (400 MHz, CD_2Cl_2) of **L4**.

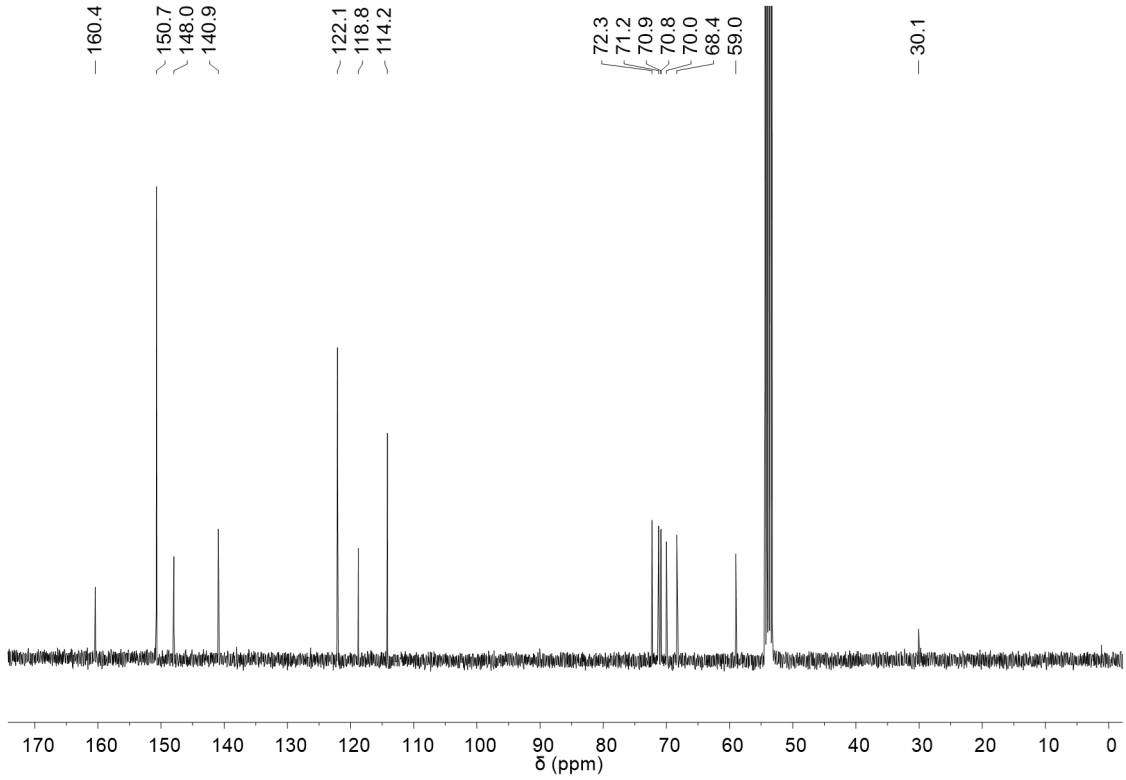

Figure S20: ^{13}C NMR spectrum (100 MHz, CD_2Cl_2) of **L4**.

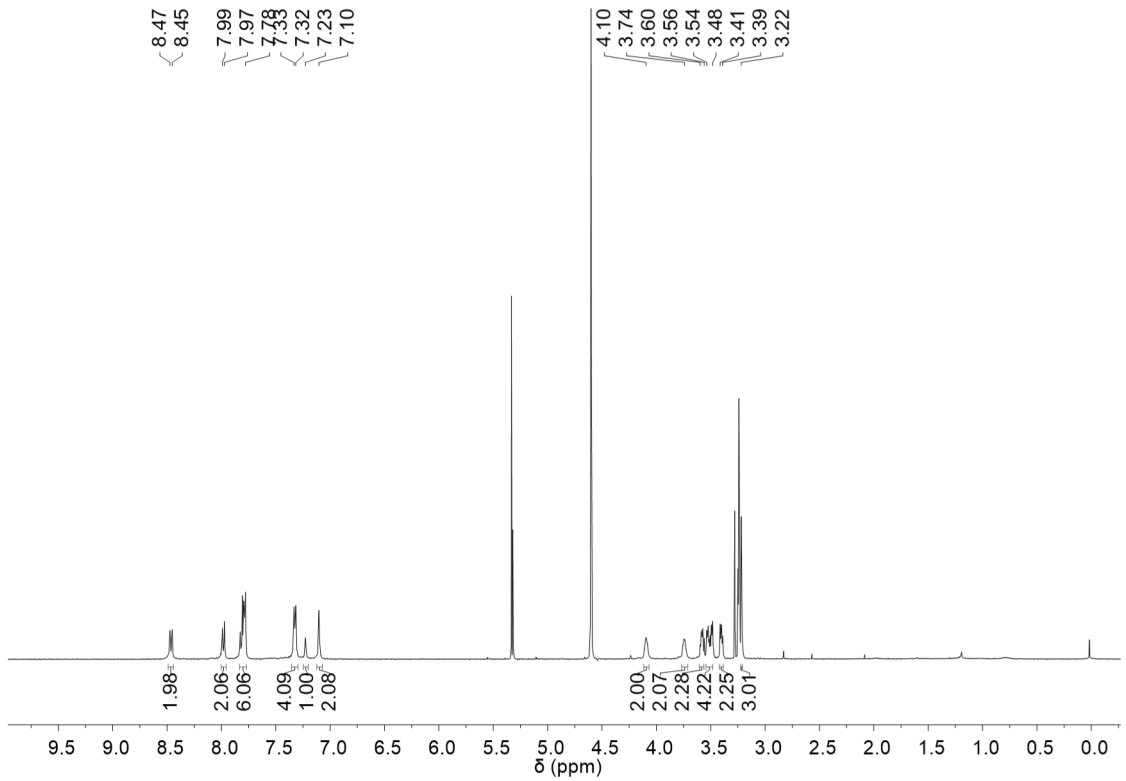

Figure S21: ^{1}H NMR spectrum (400 MHz, CD_2Cl_2/MeOD/TFE-d_3 5:3:2) of **OEG-MC4**. The integration of the signals is normalized for a monomeric unit.

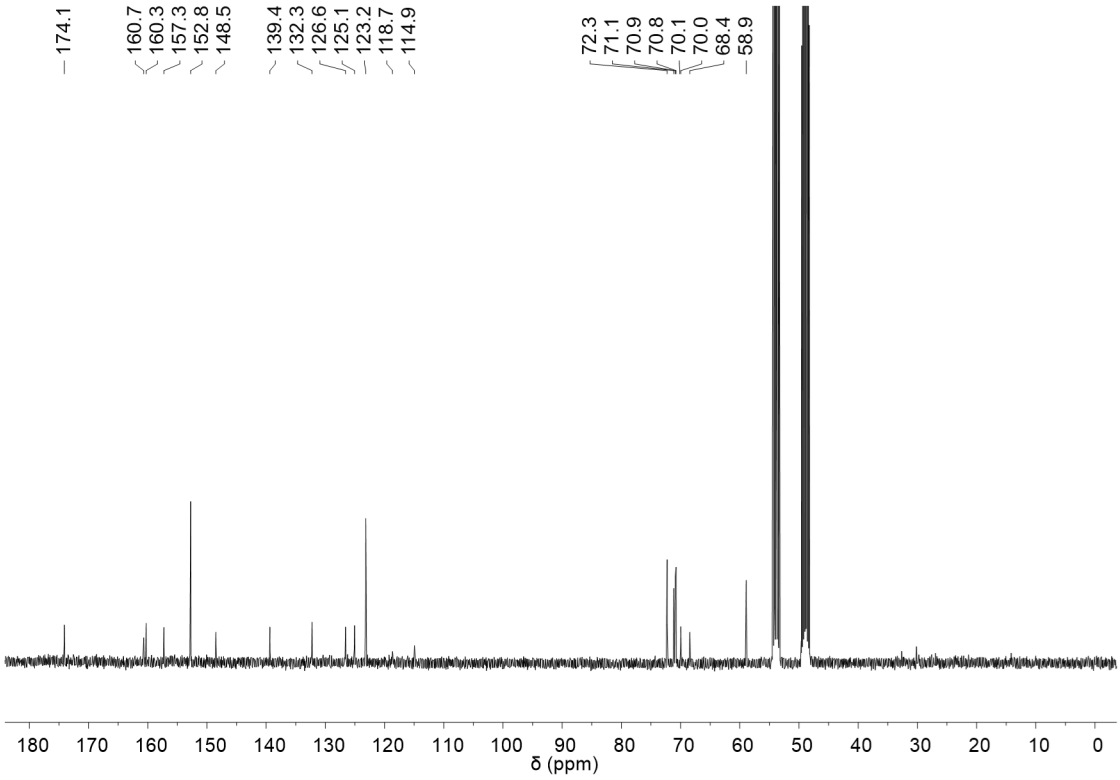

Figure S22: ^{13}C NMR spectrum (100 MHz, CD_2Cl_2/MeOD/TFE-d_3 5:3:2) of **OEG-MC4**.

HR mass spectra of **L2** and **L4** and complexes **OEG-MC2** and **OEG-MC4**

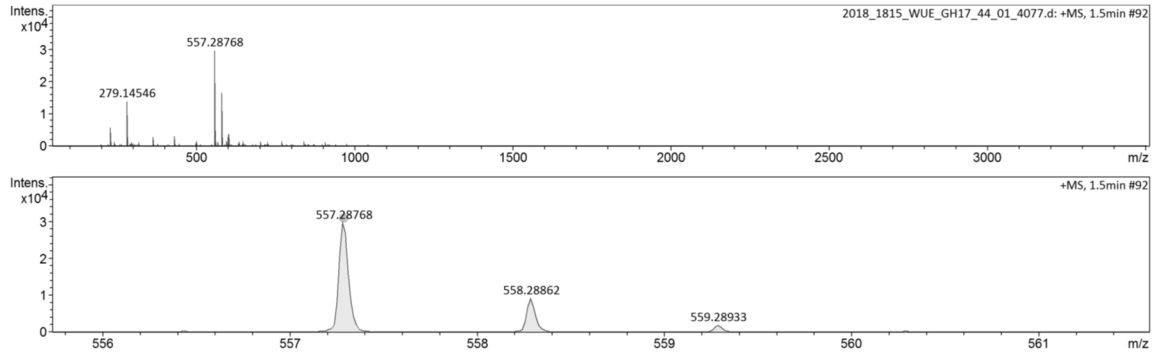

Figure S23: HR ESI mass spectrum (MeCN/$CHCl_3$ 1:1, positive mode) of **L2**.

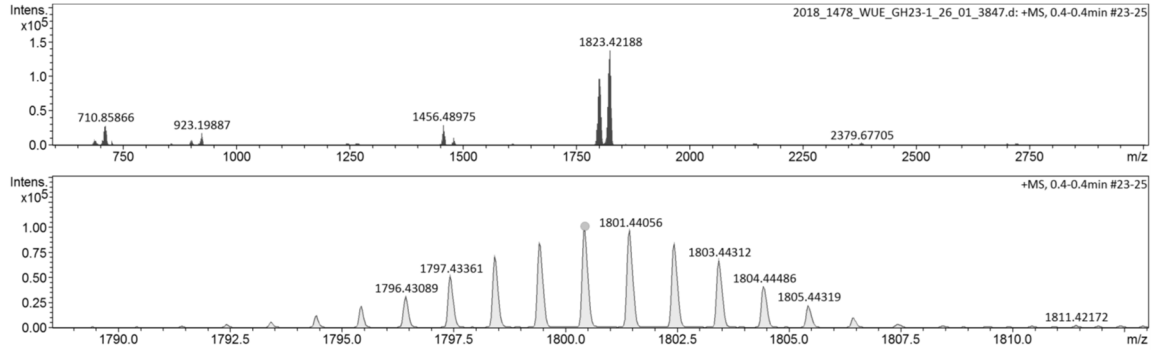

Figure S24: HR ESI mass spectrum (MeCN/$CHCl_3$ 1:1, positive mode) of **OEG-MC2**.

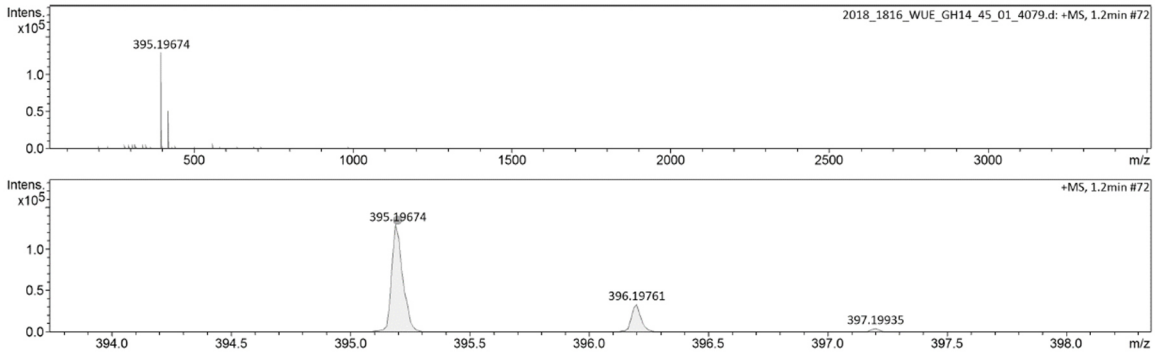

Figure S25: HR ESI mass spectrum (MeCN/$CHCl_3$ 1:1, positive mode) of **L4**.

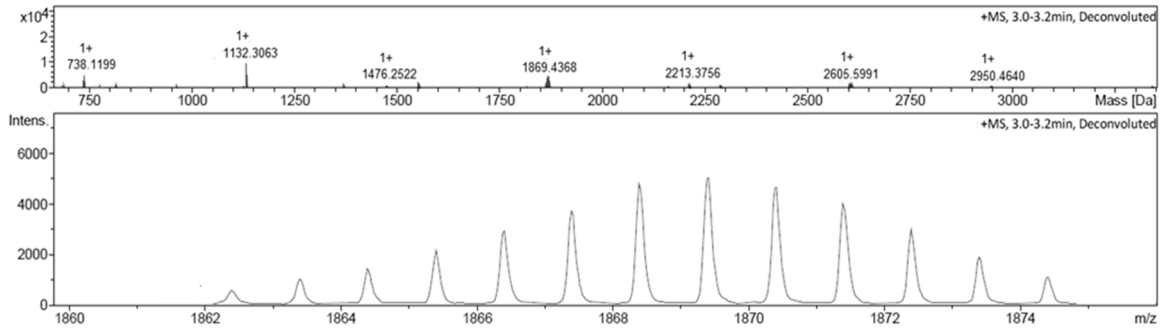

Figure S26: HR ESI mass spectrum (MeCN/$CHCl_3$ 1:1, positive mode) of **OEG-MC4**. Signal on the bottom belongs to $[Ru(bda)_2(L4)_3]$ fragment. Calculated: *m*/*z* = 1869.8985, found: *m*/*z* = 1869.4368.

Electrochemical Data for WOCs and Ligands

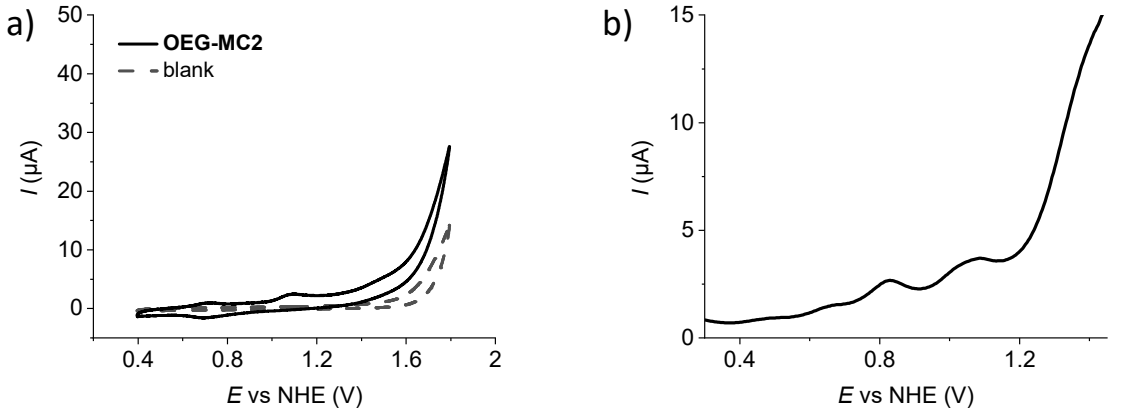

Figure S27: CV (scan rate: 100 mV/s) (a) and DPV (b) of **OEG-MC2** in TFE/H_2O 1:1 (pH 7, phosphate buffer), c = 0.25 mM.

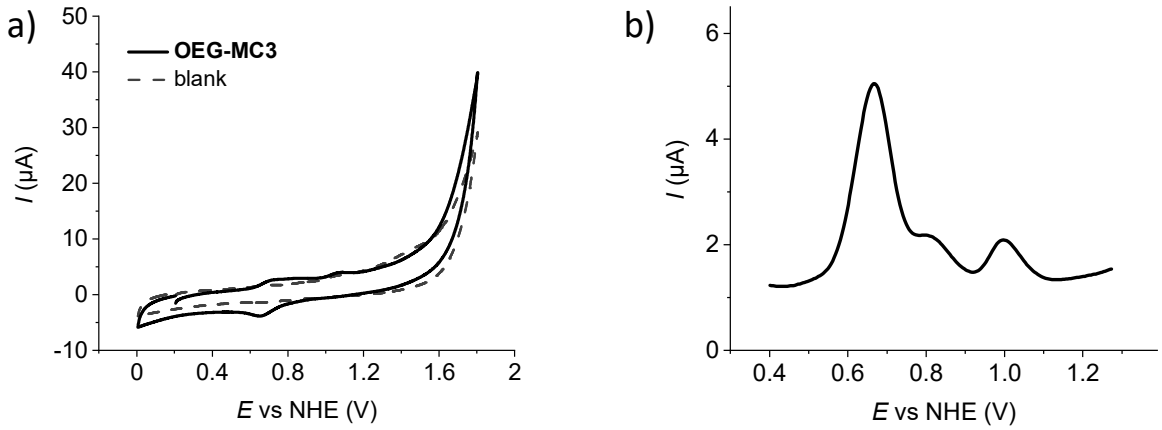

Figure S28: CV (scan rate: 100 mV/s) (a) and DPV (b) of **OEG-MC3** in TFE/H_2O 1:1 (pH 7, phosphate buffer), c = 0.25 mM.

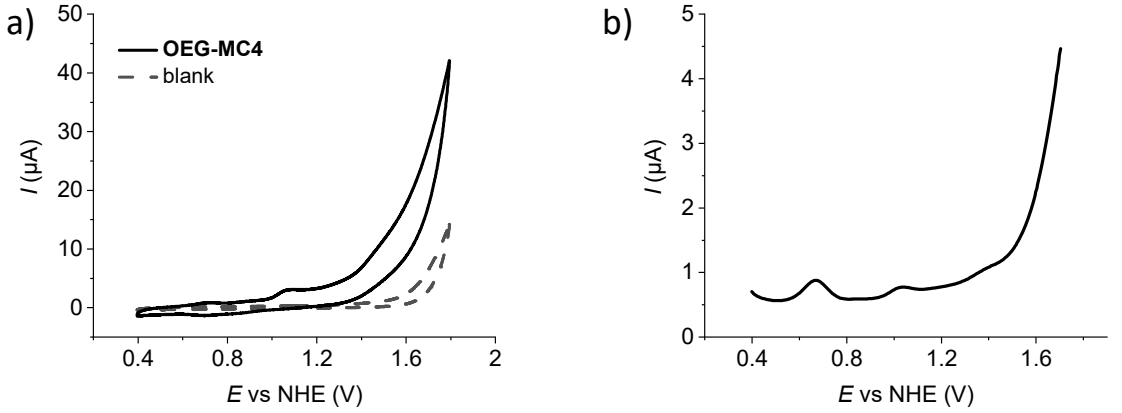

Figure S29: CV (scan rate: 100 mV/s) (a) and DPV (b) of **OEG-MC4** in TFE/H_2O 1:1 (pH 7, phosphate buffer), c = 0.25 mM.

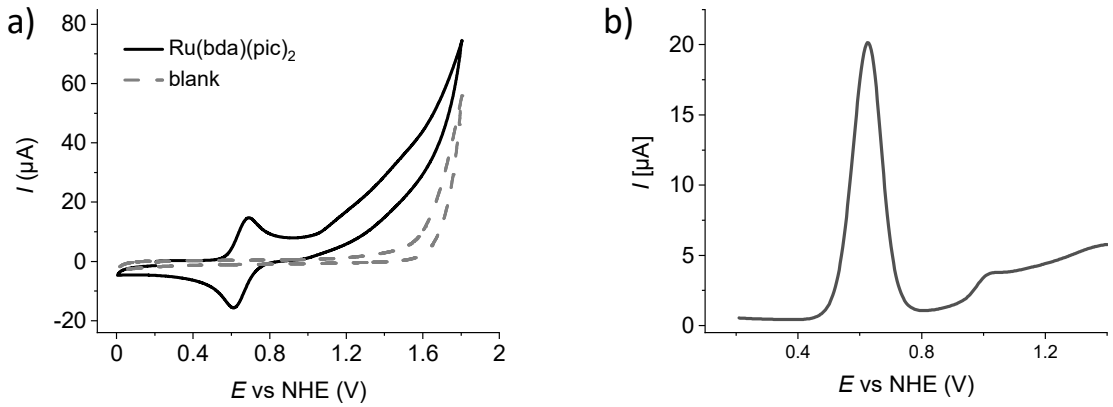

Figure S30: CV (scan rate: 100 mV/s) (a) and DPV (b) of Ru(bda)(pic)$_2$ in TFE/H$_2$O 1:1 (pH 7, phosphate buffer), c = 0.25 mM.

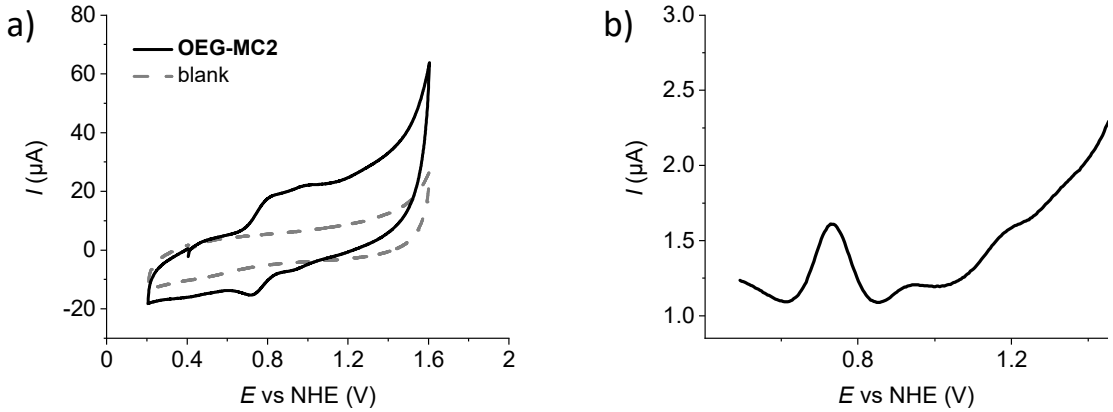

Figure S31: CV (scan rate: 100 mV/s) (a) and DPV (b) of **OEG-MC2** in TFE/H$_2$O 1:1 (pH 1, triflic acid), c = 0.25 mM.

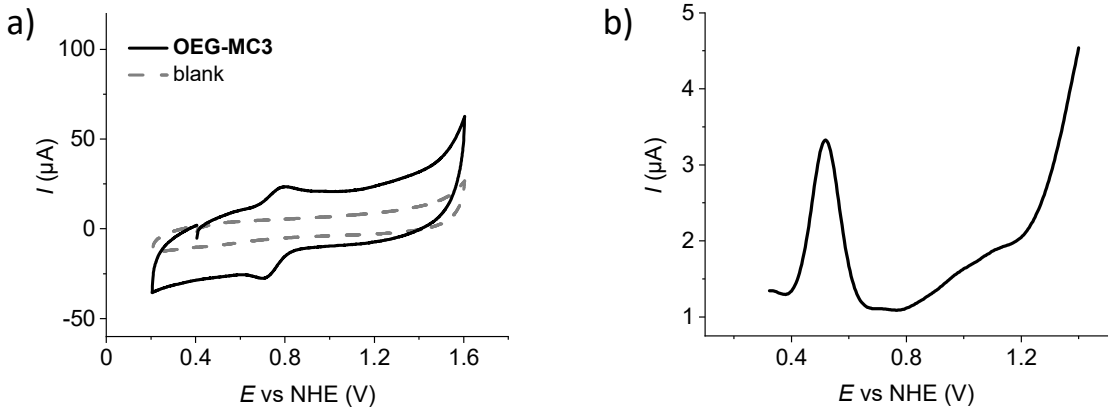

Figure S32: CV (scan rate: 100 mV/s) (a) and DPV (b) of **OEG-MC3** in TFE/H$_2$O 1:1 (pH 1, triflic acid), c = 0.25 mM.

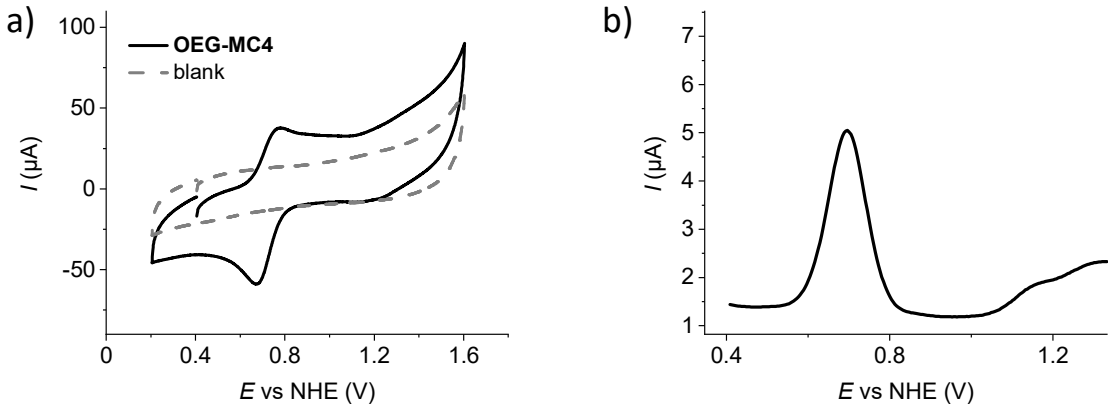

Figure S33: CV (scan rate: 100 mV/s) (a) and DPV (b) of **OEG-MC4** in TFE/H_2O 1:1 (pH 1, triflic acid), *c* = 0.25 mM.

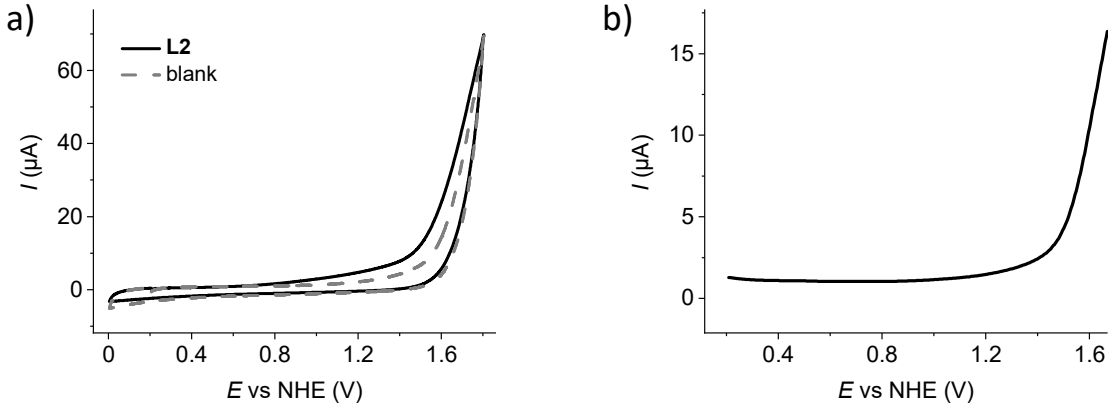

Figure S34: CV (scan rate: 100 mV/s) (a) and DPV (b) of **L2** in TFE/H_2O 1:1 (pH 7, phosphate buffer), *c* = 0.25 mM.

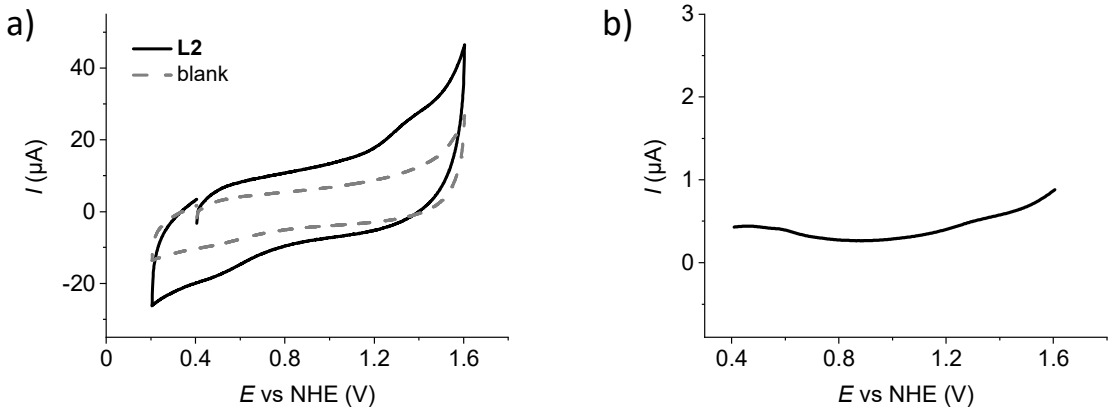

Figure S35: CV (scan rate: 100 mV/s) (a) and DPV (b) of **L2** in TFE/H_2O 1:1 (pH 1, triflic acid), *c* = 0.25 mM.

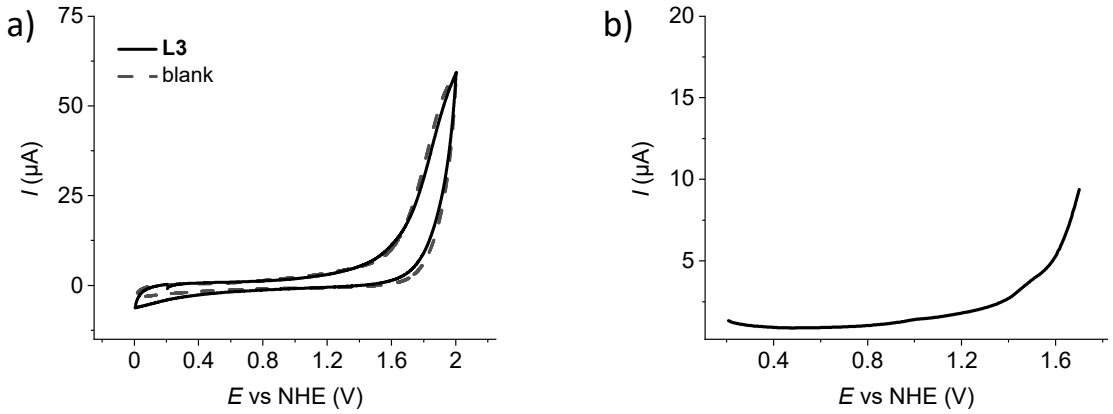

Figure S36: CV (scan rate: 100 mV/s) (a) and DPV (b) of **L3** in TFE/H_2O 1:1 (pH 7, phosphate buffer), *c* = 0.25 mM.

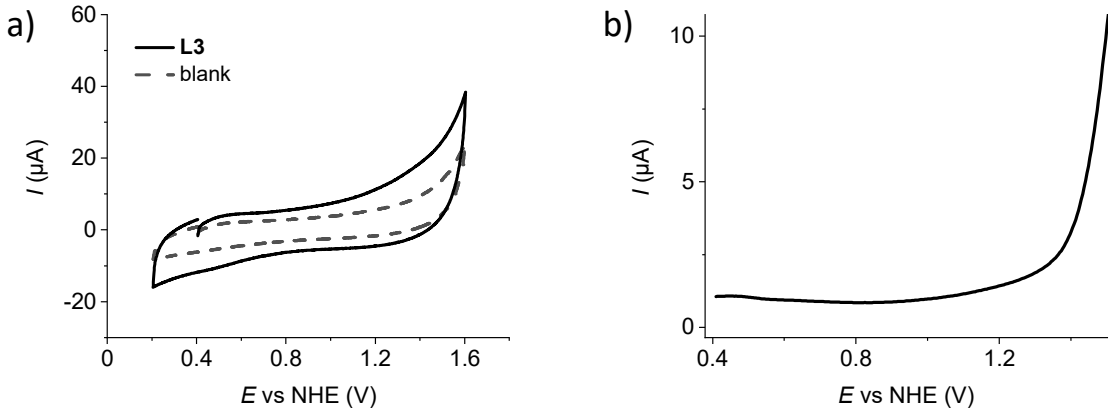

Figure S37: CV (scan rate: 100 mV/s) (a) and DPV (b) of **L3** in TFE/H_2O 1:1 (pH 1, triflic acid), *c* = 0.25 mM.

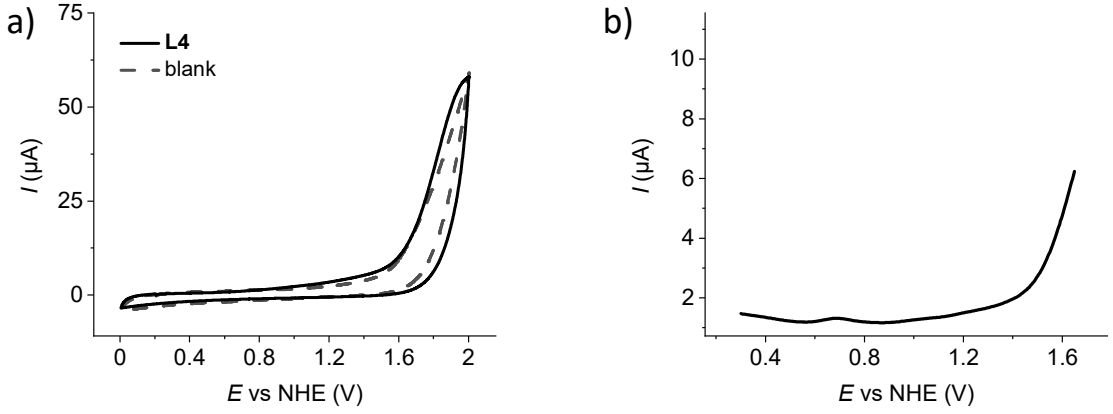

Figure S38: CV (scan rate: 100 mV/s) (a) and DPV (b) of **L4** in TFE/H_2O 1:1 (pH 7, phosphate buffer), *c* = 0.25 mM.

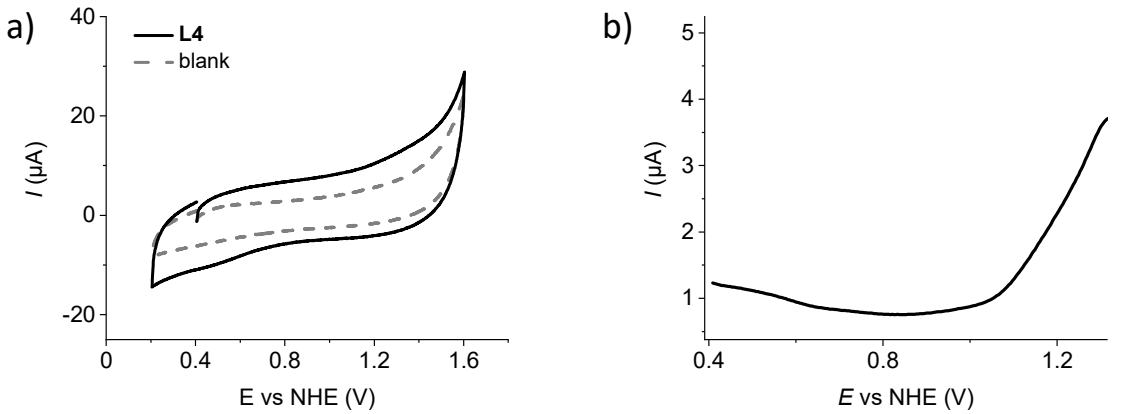

Figure S39: CV (scan rate: 100 mV/s) (a) and DPV (b) of **L4** in TFE/H_2O 1:1 (pH 1, triflic acid), *c* = 0.25 mM.

Spectroelectrochemical Data for **OEG-MC3**

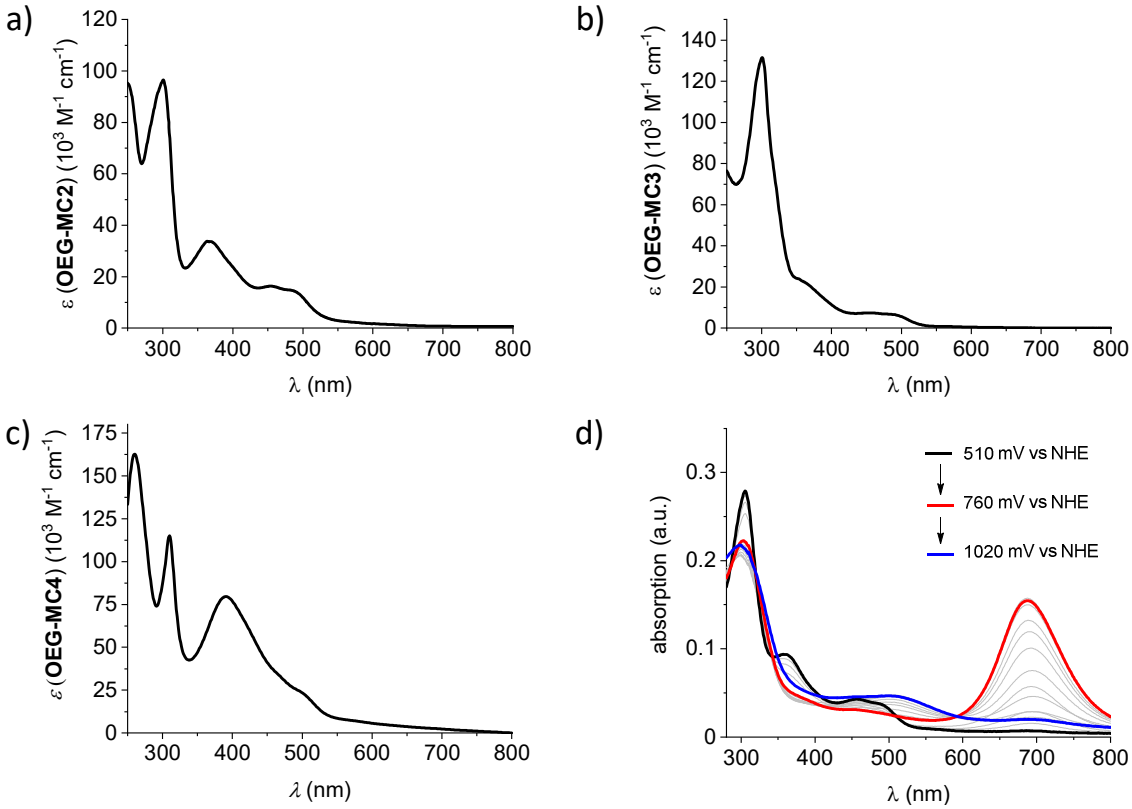

Figure S40: UV/Vis absorption spectra in MeCN/H_2O (phosphate buffer, pH 7, 0.1 M) (1:1) of a) **OEG-MC2** (*c* = 11 µM), b) **OEG-MC3** (*c* = 10 µM), c) **OEG-MC4** (*c* = 8 µM). d) Spectroelectrochemical studies of **OEG-MC3** (*c* = 219 µM) in a 1:1 mixture of TFE/H_2O (phosphate buffer, pH 7, 0.1 M).

Chemical Water Oxidation

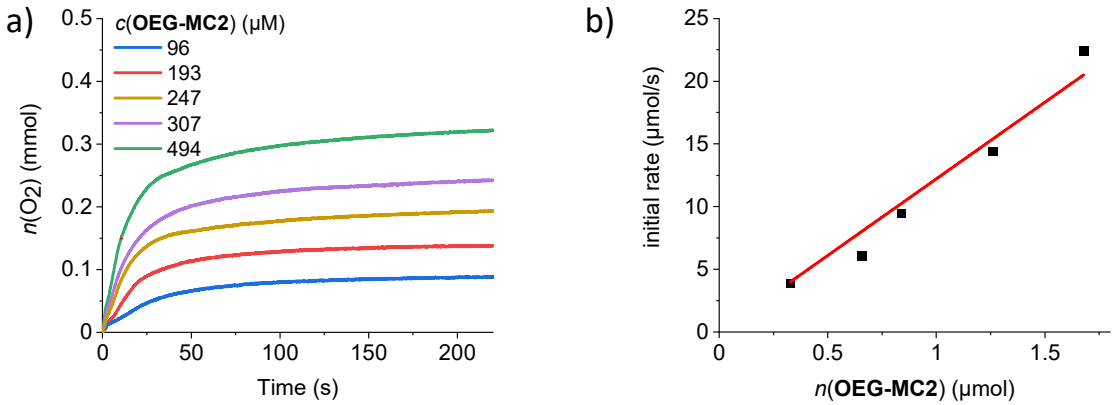

Figure S41: a) Concentration-dependent oxygen evolution curves for **OEG-MC2** in MeCN/H_2O 1:1 (pH 1, triflic acid). b) Plot of initial rates vs. catalyst amount with linear regression for the determination of TOF.

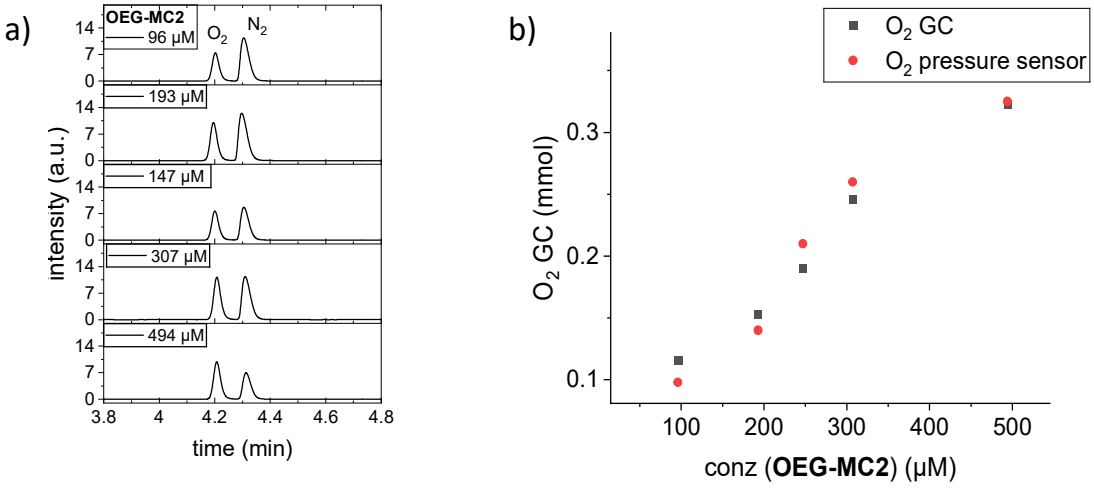

Figure S42: a) Chromatogram of headspace at the end of water oxidation experiments with **OEG-MC2** as WOC. b) Comparison of the amount of evolved oxygen determined by GC and with pressure sensor.

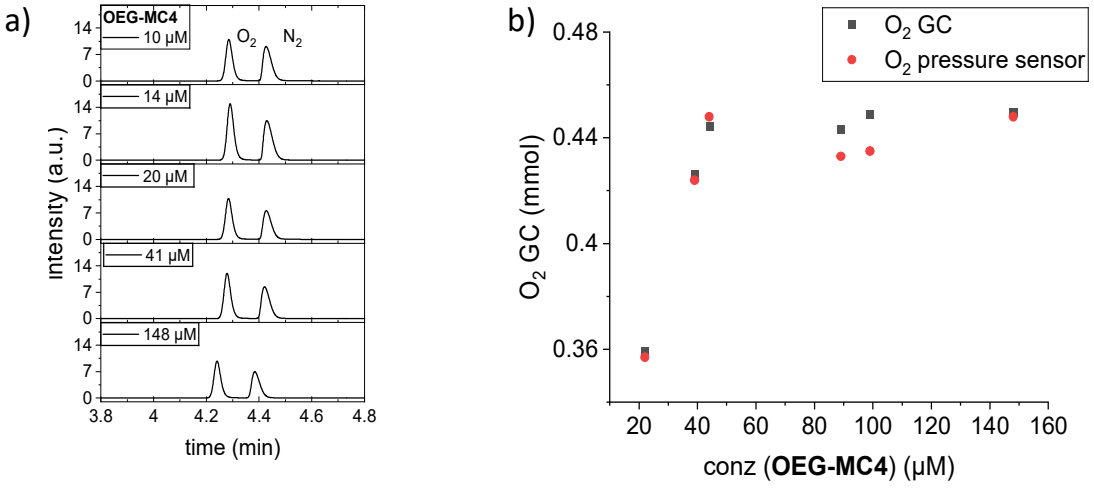

Figure S43: a) Chromatogram of headspace at the end of water oxidation experiments with **OEG-MC4** as WOC. b) Comparison of the amount of evolved oxygen determined by GC and with pressure sensor.

Photocatalytic Water Oxidation

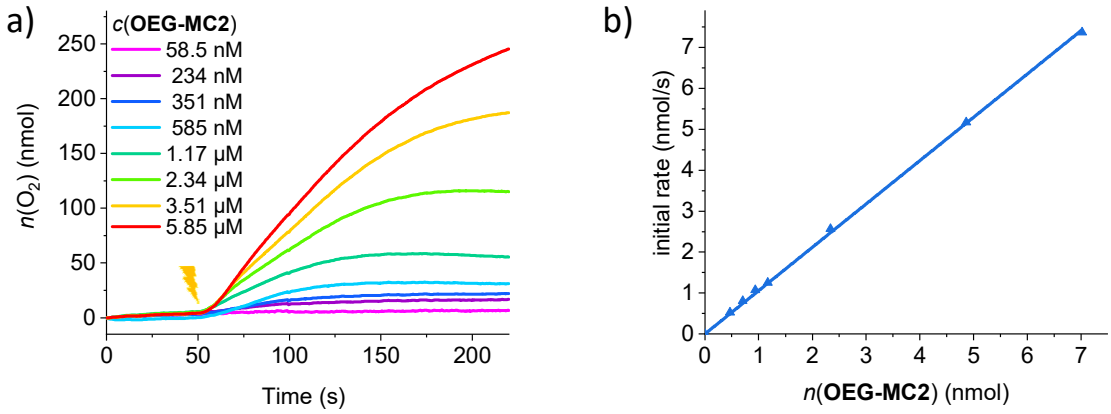

Figure S44: Concentration-dependent oxygen evolution curves for **OEG-MC2** in MeCN/H_2O 1:1 (phosphate buffer, pH 7). b) Plot of initial rates vs. catalyst amount with linear regression for the determination of TOF.

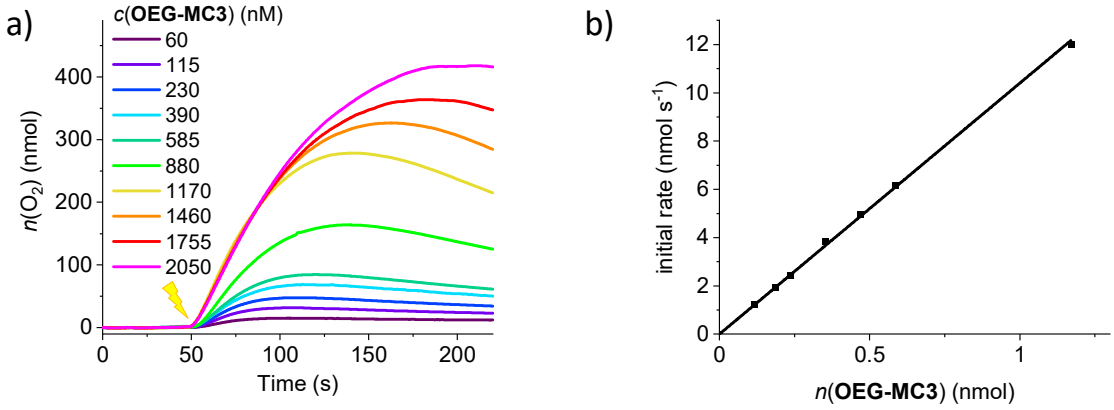

Figure S45: Concentration-dependent oxygen evolution curves for **OEG-MC3** in MeCN/H_2O 1:1 (phosphate buffer, pH 7). b) Plot of initial rates vs. catalyst amount with linear regression for the determination of TOF.

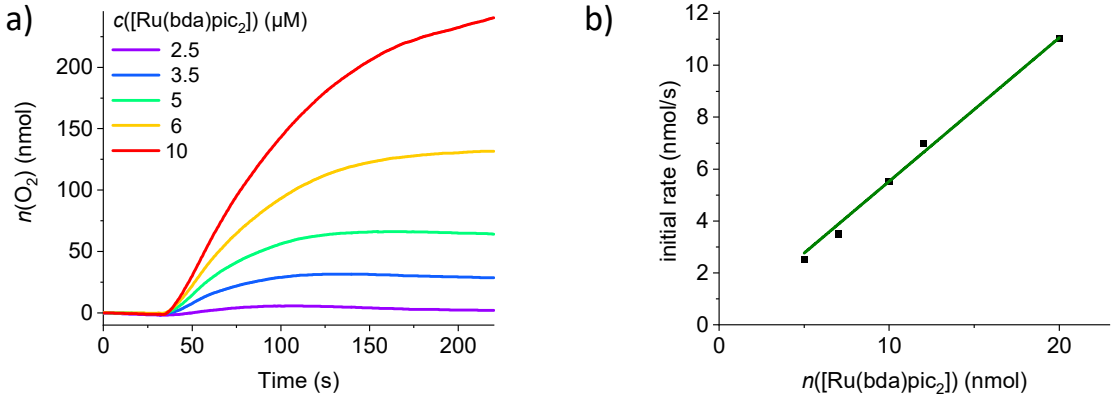

Figure S46: Concentration-dependent oxygen evolution curves for Ru(bda)$(pic)_2$ in MeCN/H_2O 1:1 (phosphate buffer, pH 7). b) Plot of initial rates vs. catalyst amount with linear regression for the determination of TOF.

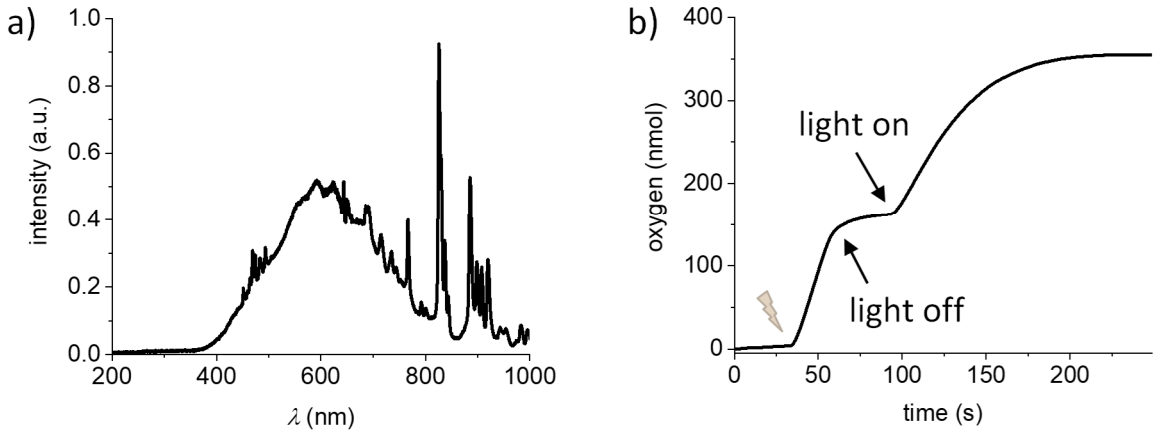

Figure S47: a) Emission profile of xenon lamp used for photocatalytic water oxidation experiments. b) Oxygen evolution curve vs time in photocatalytic water oxidation with **OEG-MC4** (*c* = 2000 nM) using $Ru(bpy)_3$ (*c* = 1.5 mM) as a photosensitizer and $Na_2S_2O_4$ (*c* = 37 mM) as a sacrificial electron acceptor. The lighting symbol indicates the time at which the sample was exposed to light for the first time after stirring for 30 seconds in the dark. The light was turned off after 30 seconds of illumination and no further oxygen was produced. After 30 seconds in the dark, the light was again turned on and the catalytic process was re-initiated, indicated by the rise in oxygen detected by the Clark electrode.

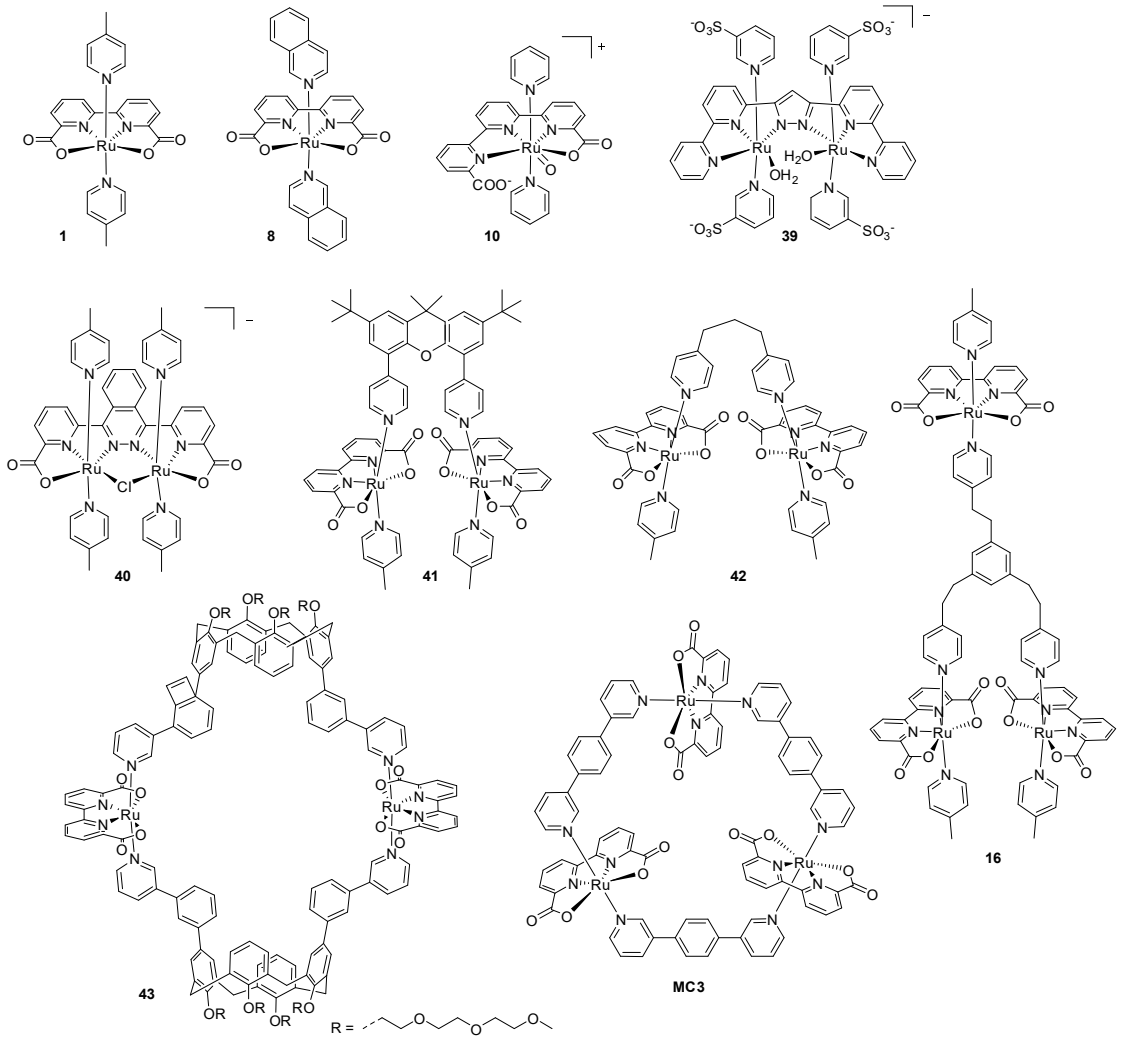

Figure S48: Chemical structures of WOCs presented in Table S1.

Table S1: Catalytic activities of selected Ru WOCs in chemical and photocatalytic water oxidation.

Catalyst	chemical water oxidation		photocatalytic water oxidation	
	TOF (s^{-1})	TON	TOF (s^{-1})	TON
1[a] [318]	41	2000	0.6	13
8[b] [269, 319]	303	8360	0.24	140
10[c] [206]	inactive	inactive	50	1050
39[d] [273]	0.068	211	11	5300
40[e] [320]	1.2	10400	0.83	580
41[f] [321]	n.d.	900	n.d.	n.d.
42[g] [213, 322]	n.d.	20800	n.d.	640
16[h] [214]	126	86500	n.d.	540
43[i] [272]	19	820	15.5	460
MC3[j] [216]	136	5300	11	430

Experimental conditions: [a]: Chemical WO:[318] H_2O (pH 1, triflic acid), *c*(CAN) = 0.4 M, *c*(**1**) = 12–216 µM; photocat. WO:(*) H_2O (pH 7.2, phosphate buffer), *c*($[Ru(bpy)_3]^{2+}$) = 1.5 mM, *c*($Na_2S_2O_8$) = 37 mM, *c*(**1**) = 2.5-10 µM. [b]: Chemical WO:[269] H_2O (pH 1, triflic acid), *c*(CAN) = 0.5 M, *c*(**8**) = 114–216 µM; Photocat. WO:[319] H_2O (pH 1, perchloric acid), *c*($[Ru(5\text{-}CF_3\text{-}bpy)_3]^{2+}$) = 0.2 mM, *c*($Na_2S_2O_8$) = 1 M, *c*(**8**) = 20 µM. [c]: Photocat. WO:[206] H_2O (pH 7, phosphate buffer), *c*($[Ru(4,4'\text{-}COOEt\text{-}bpy)_2bpy]^{2+}$) = 0.2 mM, *c*($Na_2S_2O_8$) = 10 mM, *c*(**10**) = 1–16 µM. [d]: Chemical WO: H_2O (pH 1, triflic acid), *c*(CAN) = 0.1 M, *c*(**39**) = 0.1–1 mM; Photocat. WO: H_2O (pH 7, phosphate buffer), *c*($[Ru(4,4'\text{-}COOEt\text{-}bpy)_2bpy]^{2+}$) = 0.2 mM, *c*($Na_2S_2O_8$) = 20 mM, *c*(**39**) = 0.2 µM. [e]: Chemical WO:[320] H_2O (pH 1, triflic acid), *c*(CAN) = 0.02–5 mM, *c*(**40**) = 0.05–0.5 µM; Photocat. WO:[320] H_2O (pH 7, phosphate buffer), *c*($[Ru(4,4'\text{-}COOEt\text{-}bpy)_2bpy]^{2+}$) = 0.62 mM, *c*($Na_2S_2O_8$) = 10 mM, *c*(**40**) = 2.5 µM. [f]: Chemical WO:[321] 1:9 CF_3CH_2OH/H_2O (pH 1, triflic acid), *c*(CAN) = 0.5 M, *c*(**41**) = 59 µM. Photocatalytic WO:[273] H_2O (pH 7, phosphate buffer), *c*($[Ru(4,4'\text{-}COOEt\text{-}bpy)_2bpy]^{2+}$) = 0.2 mM, *c*($Na_2S_2O_8$) = 20 mM, *c*(**41**) = 0.2 µM. [g] Chemical WO:[213] H_2O (pH 1, triflic acid), *c*(CAN) = 5 mM, *c*(**42**) = 50 nM; Photocat WO:[322] 6:4 MeCN/H_2O (pH 6.8, phosphate buffer), *c*($[Ru(bpy)_3]^{2+}$) = 1 mM, *c*(NaS_2O_8) = 45 mM, *c*(**42**) = 2 µM. [h]: Chemical WO:[214] H_2O (pH 1, triflic acid), *c*(CAN) = 50 mM, *c*(**16**) = 33 nM; Photocatalytic WO:[214] H_2O (pH 7, phosphate buffer), *c*($[Ru(4,4'\text{-}COOEt\text{-}bpy)_2bpy]^{2+}$) = 1 mM, *c*($Na_2S_2O_8$) = 10 mM, *c*(**16**) = 0.5 µM. [i]: Chemical WO:[272] 4:6 MeCN/H_2O (pH 1, triflic acid), *c*(CAN) = 0.6 M, *c*(**43**) = 50-300 µM; Photocat. WO:[272] 4:6 MeCN/H_2O (pH 7, phosphate buffer), *c*($[Ru(bpy)_3]^{2+}$) = 1.5 mM, *c*($Na_2S_2O_8$) = 37 mM, *c*(**43**) = 12-200 nM. [j]: Chemical WO:[216] 1:1 MeCN/H_2O (pH 1, triflic acid), *c*(CAN) = 0.6 M, *c*(**MC3**) = 5–322 µM; Photocat. WO:[216] 1:1 MeCN/H_2O (pH 7, phosphate buffer), *c*($[Ru(bpy)_3]^{2+}$) = 1.5 mM, *c*($Na_2S_2O_8$) = 37 mM, *c*(**MC3**) = 60–600 nM. (*) measured in this work

9.3 Supporting Information for Chapter 5

Microscopic studies[6]

AFM microscopy

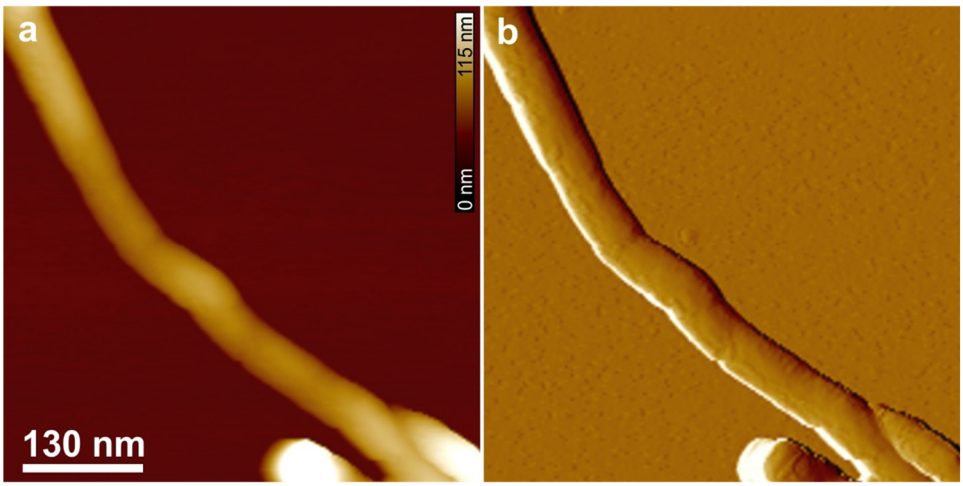

Figure S49: AFM images of bare CNT suspended in THF and spin-coated on silicon waver SiO_x with 2000 rpm. a) Height and b) phase image. *Z* scale is 115 nm.

Scanning electron microscopy (SEM) and Energy-dispersive X-ray spectroscopy (EDX)

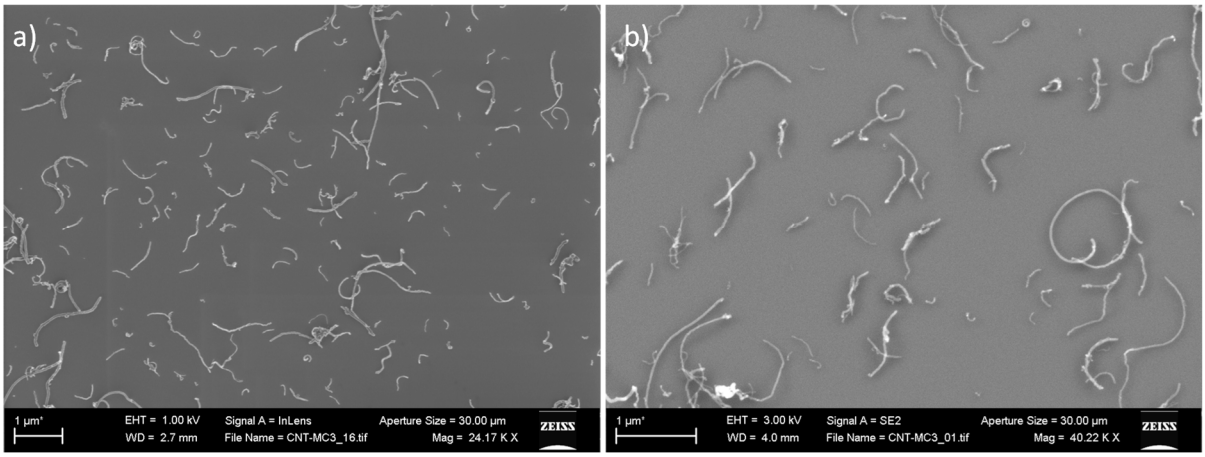

Figure S50: Secondary electrons SEM images (SE) of **MC3@CNTs** on silicon wafer show a thin film consisting of the carbon nanotubes.

[6] AFM, SEM and EDX measurements shown in Figures S49 – S54 were performed by Dr. Vladimir Stepanenko, Universität Würzburg.

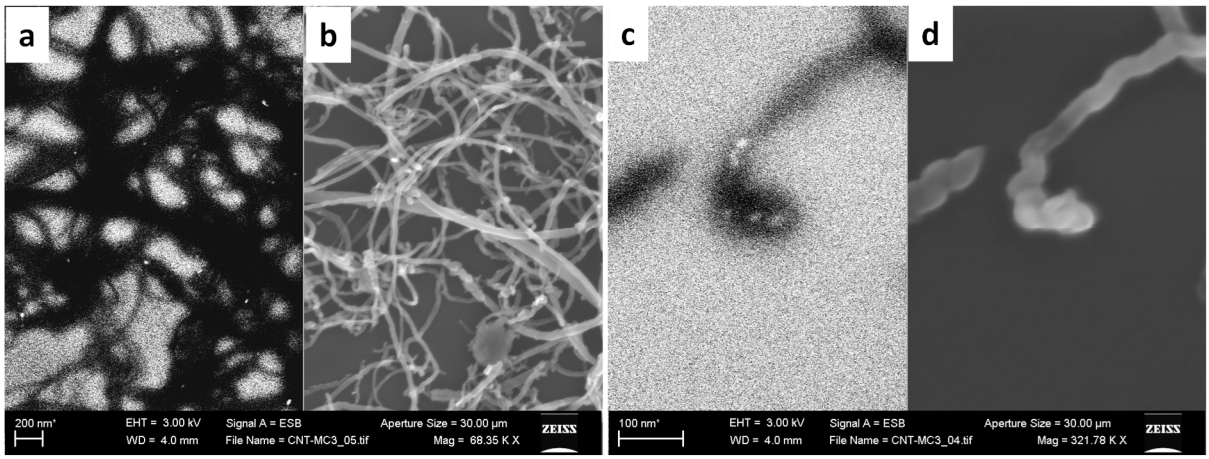

Figure S51: SEM images of the **MC3@CNTs** sample on silicon wafer: (a,c) backscattered electrons (BSE) images and (b,d) corresponding secondary electrons (SE) images.

The SEM images provide visualization of the 3D structure on the surface, while the BSE images give information on chemical composition. Heavy elements with the high atomic number backscatter electrons more strongly than light elements with the low atomic number, and thus appear brighter in the image (the particle-like structures in images (a,c)).

Some parts of the carbon nanotubes are covered with the spherical particles that probably correspond to Ru-complexes **MC3**.

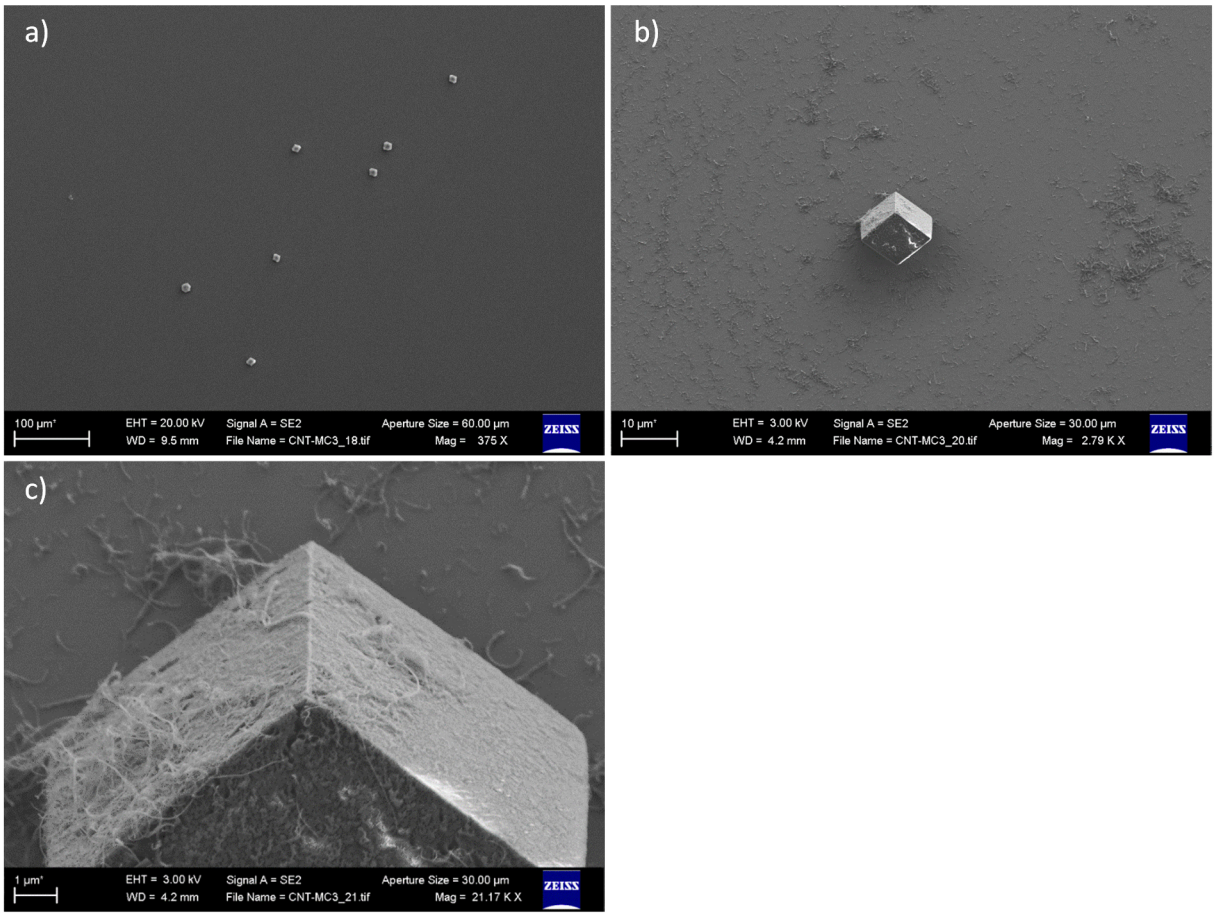

Figure S52: SEM images of **MC3@CNTs** sample. The large-scale images (b, c) reveal the presence of the crystalline structures on silicon surface. The structures have a cube-like shape and, using EDX data, can be assigned to the ruthenium complexes (see Figure S53).

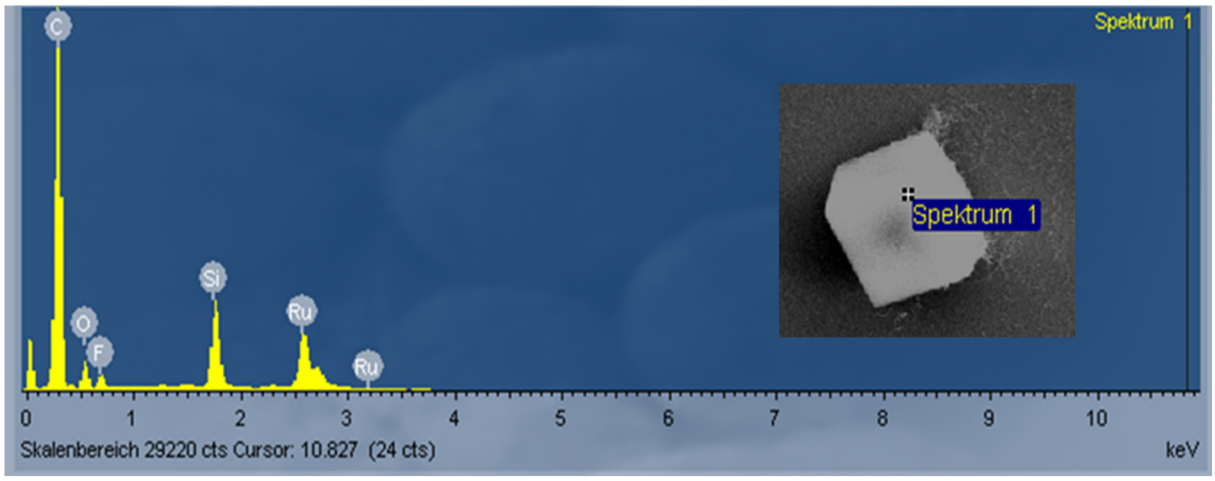

Figure S53: EDX was used to determine which chemical elements are present in the sample. EDX spectrum shows the prominent X-ray peaks for carbon (C), silicon (Si) and ruthenium (Ru). The Si peak was produced from substrate (SiOx).

EDX spectrum shows a prominent peak for Si (substrate). The carbon (C) and ruthenium (Ru) elements are also good detectable and visible in the spectrum as well as in the chemical

mapping. The Ru element is concentrated densely in the lower part of the image, where the carbon nanotubes form the co-agglomerates (Figure S54, marked with yellow circle in image b,c).

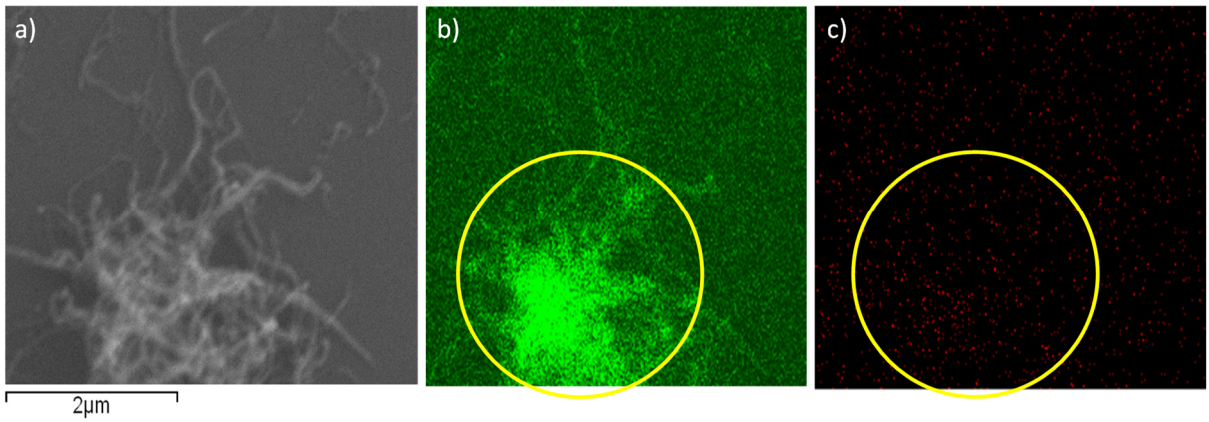

Figure S54: EDX spectrum (a) from **MC3@CNTs** co-agglomerates. b) and c) represent the mapping of chemical elements: carbon (green) and ruthenium (red).

Electrochemical Data

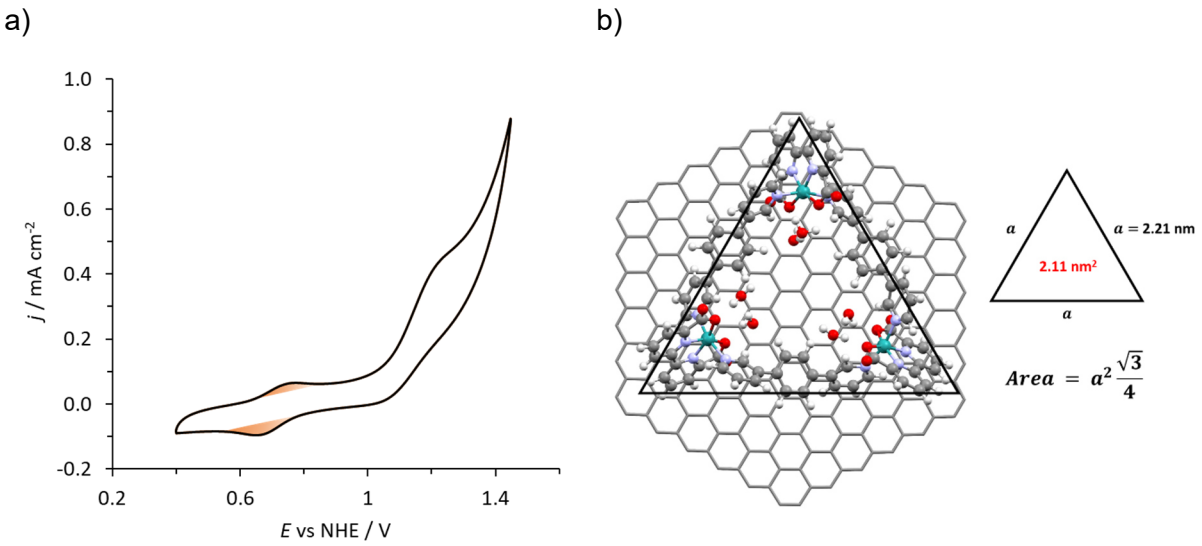

Figure S55: a) CV (scan rate: 100 mV/s) of **MC3@GC** in a 1 M phosphate buffer (pH 7) solution using a GC_d (S = 0.07 cm^2) as a working electrode. $Q(Ru^{III/II})$ = 1.5 x 10^{-6} C. b) Structure of **MC3** with key metric parameters and drawing of the approximate triangle generated by the **MC3** on the surface S_{MC3} = [$3^{1/2}$/4 x 2.21^2] = 2.11 nm^2, giving a surface coverage of approximately 93%.

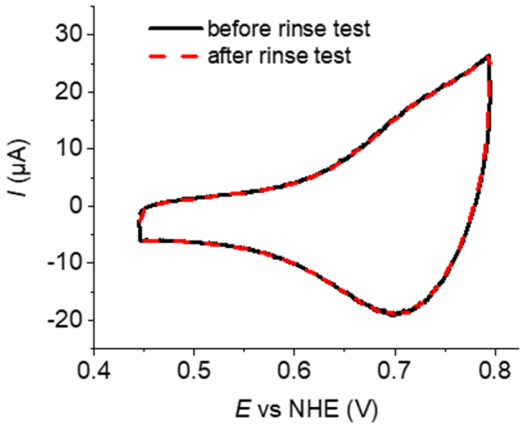

Figure S56: CV (scan rate: 100 mV/s) of the first redox process of **MC3@CNT@GC** in 1 M phosphate buffer (pH 7) before (back line) and after (red line) washing the electrode with DCM/MeOH (5:3). No deviation in intensity demonstrate the stable anchoring of the catalyst. Only the first redox process has been considered to exclude possible changes from an activation process.

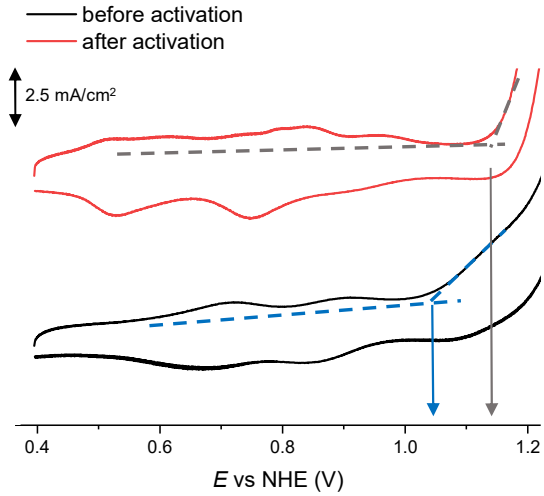

Figure S57: Section of CV (scan rate: 100 mV/s) of **MC3@CNT@GC** (black line) and **act-MC3@CNT@GC** (red line) in phosphate buffer (1 M) at pH 7. The onset potential was determined as the crossing point between the baseline and the slope (dotted lines) of the catalytic water oxidation at the beginning of the process.

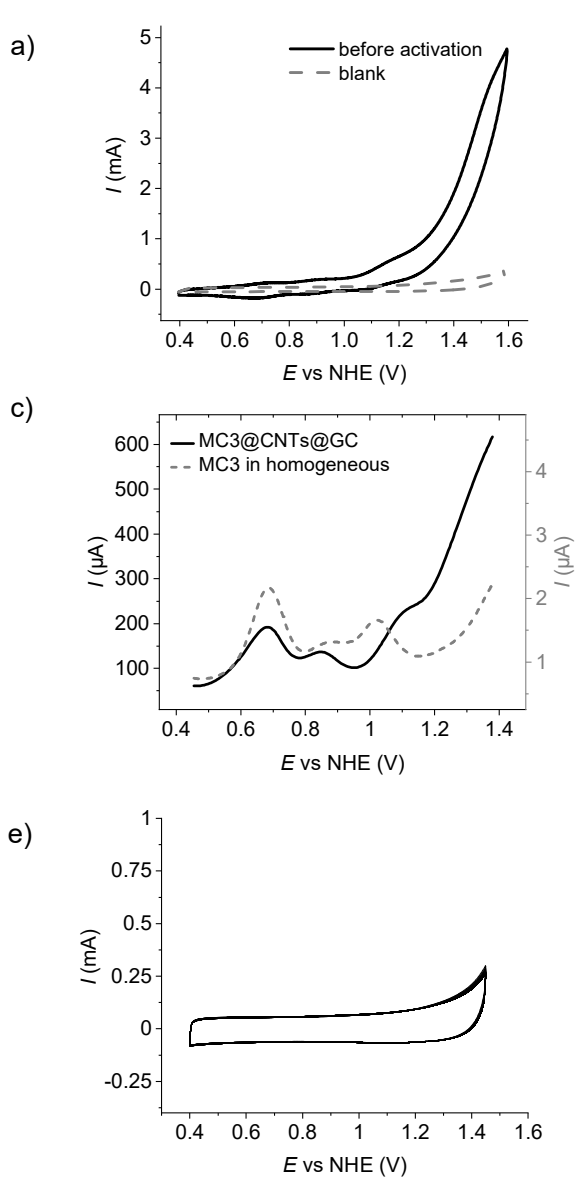

d)

MC3	E^{ox} vs NHE (V)		
	$Ru^{III/II}$	$Ru^{IV/III}$	$Ru^{V/IV}$
homogeneous **MC3**[a]	0.67	0.87	1.02
MC3@CNT@GC[b]	0.68	0.85	1.11

[a]: TFE/H_2O (1:1), (0.1 M, pH 7), [b]: H_2O, (1 M, pH 7).

Figure S58: a) CV of a blank (dotted line, CNT@GC) and **MC3@CNT@GC** (black line) in a 1 M phosphate buffer (pH 7) with a scan rate of 100 mV/s. b) CV of solvent mixture without catalyst (blank, dotted line) and with **MC3** (*c* = 0.25 mM, blue line) in a phosphate buffered TFE/H2O 1:1 mixture (0.1 M, pH 7) with a scan rate of 100 mV/s. c) DPV of **MC3@CNT@GC** (black line, in a 1 M phosphate buffer, pH 7) and **MC3** (*c* = 0.25 mM, blue line, in a 1:1 TFE/phosphate buffer (0.1 M, pH 7). d) Table with the oxidation potentials of **MC3** under homogeneous and heterogeneous conditions deduced from the corresponding DPVs. e) Blank experiment of **CNT@GC** during 100 CV cycles (0.4-1.45 V) in a 1 M phosphate buffer (pH 7) with a scan rate of 100 mV s^{-1}. No increase in current during 100 cycles demonstrates that oxygen evolution is solely attributed to the anchored catalyst.

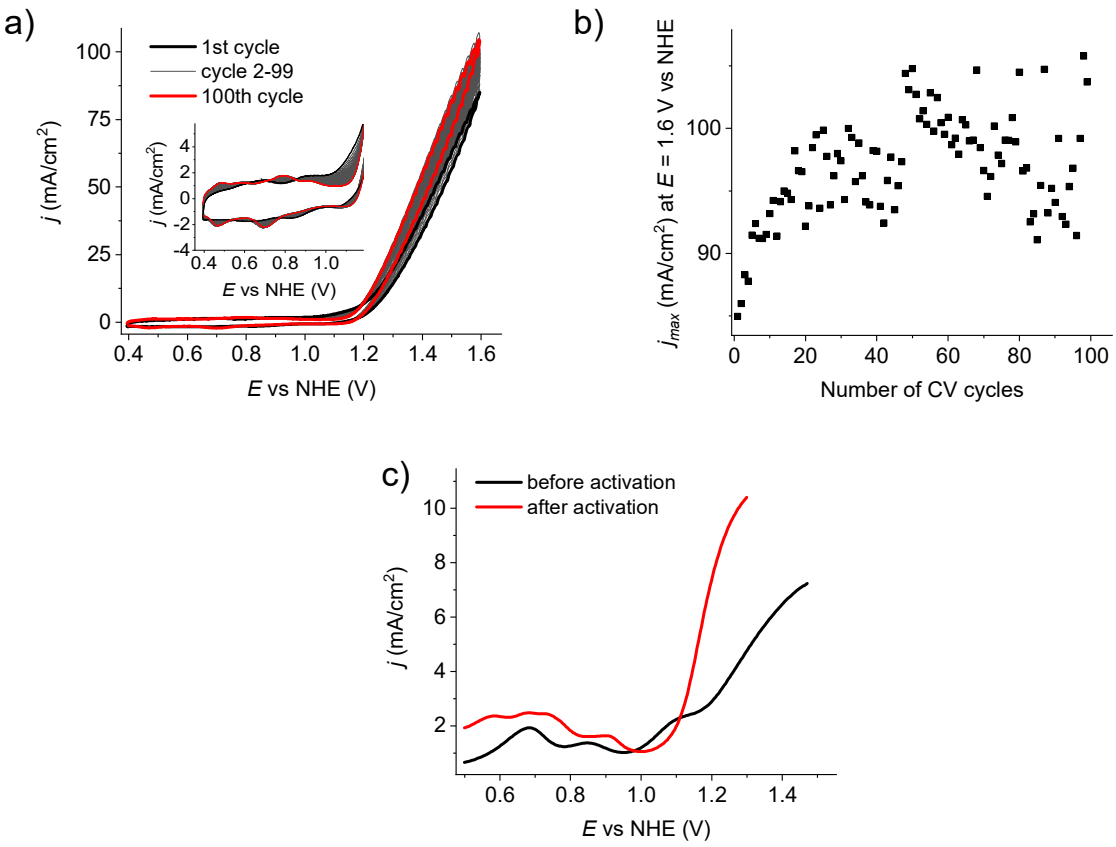

Figure S59: Electrochemical experiments with **MC3@CNT@GC** in 1 M phosphate buffer (pH 7). a) 100 repetitive CV cycles /scan rate: 100 mV/s) to a potential of *E* = 1.6 V vs NHE. Inset: Enlarged area of the non-catalytic waves. b) Development of the maximal current densities at *E* = 1.6 V vs NHE with the increasing number of CV scans. c) Comparison of the DPV of the initial (black line) and the final species (red line) after 100 CV cycles.

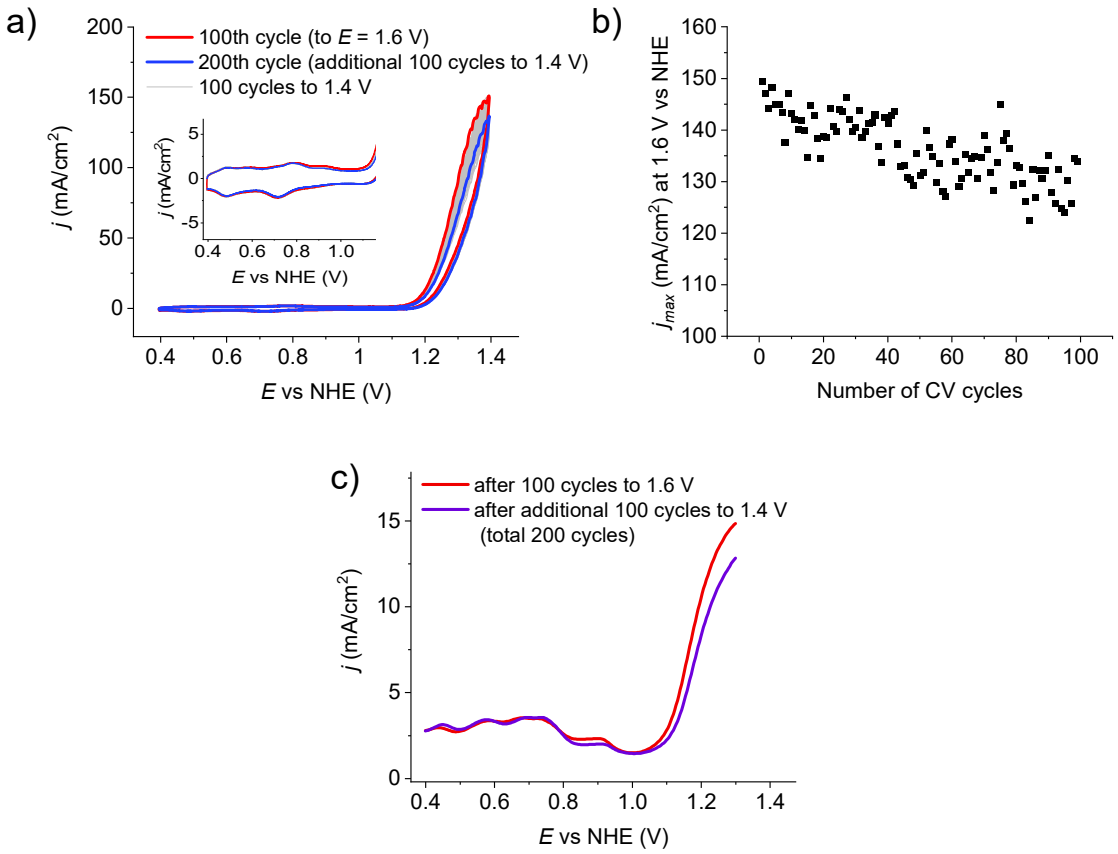

Figure S60: Electrochemical experiments with **act-MC3@CNT@GC** in 1 M phosphate buffer (pH 7). a) 100 repetitive CV cycles (scan rate: 100 mV/s) of activated electrode to a potential of *E* = 1.4 V (after 100 cycles to *E* = 1.6 V vs NHE). Inset: Enlarged area of the non-catalytic waves. b) Development of the maximal current densities at *E* = 1.4 V vs NHE with the increasing number of CV scans. c) Comparison of the DPV of the activated electrode (red line) and the final species after 200 CV cycles (purple line).

XAS Data[7]

Table S2: Summary of the bond distances (Å)

Sample	Bond distances (Å)
MC3 Powder	Ru-N,2: 1.90 Ru-N/O,4: 2.08
MC3@CNT Powder	Ru-N,2: 1.90 Ru-N/O,4: 2.10
act-MC3@CNT	Ru-N/O,6: 2.10
act-MC3@CNT (after catalysis)	Ru-N/O,6: 2.10

Table S3: Comparison of XANES energies of different Ru species

Sample	Energy at Normalized Fluorescence 0.6 (eV)	Percentage Presence of Ru(II), Ru(III) and Ru(IV)	Oxidation State
Ru(0)	22123.7	-	0
$Ru^{III}(tda)py_2$[207]	22129.1	100% Ru(III)	3
RuO_2	22130.7	100% Ru(IV)	4
MC3 Powder	22127.5	100% Ru(II)	2
MC3@CNT Powder	22127.5	100% Ru(II)	2
act-MC3@CNT	22128.0	69% Ru(II) + 31% Ru(III)	2.31
act-MC3@CNT after catalysis	22128.1	63% Ru(II) + 37% Ru(III)	2.37

[7] All XAS, XANES and EXAFS data shown in Tables S2 – S4 was obtained by Dr. Dooshaye Moonshiram, Instituto Madrileño de Estudios Avanzados en Nanociencia (IMDEA Nanociencia), 28049 Madrid (Spain).

Table S4: EXAFS Fit parameters

Sample	Fit	Reg-ion	Shell,N	R, Å	E_0	ss.^{2} (10^{-3})	R-factor	Reduced Chi-square
MC3 Powder	1	I	Ru-N,2 Ru-O,4	1.90 2.08	-1.7	1.4 4.4	0.0533	169
	2	I,II	Ru-N,2 Ru-O,4 Ru-C,10	1.89 2.07 2.87	-1.2	3.3 6.4 14.9	0.0326	48
	3	I,II,III	Ru-N,2 Ru-O,4 Ru-C,10 Ru-C,24	1.90 2.08 2.91 3.14	-0.57	1.4 4.5 8.2 5.1	0.0212	39
MC3@CNT Powder	4	I	Ru-N,2 Ru-O,4	1.88 2.08	-1.4	1.7 1.5	0.0187	75
	5	I,II	Ru-N,2 Ru-O,4 Ru-C,10	1.88 2.09 2.81	0.44	0.7 2.7 14.6	0.0249	47
	6	I,II	Ru-N,2 Ru-O,4 Ru-C,10 Ru-C,24	1.90 2.10 2.93 3.14	1.5	1.2 1.6 7.1 7.9	0.0080	19
act-MC3@CNT	7	I	Ru-N,2 Ru-O,4	1.91 2.07	1.7	5.4 2.5	0.0061	30
	8	I,II	Ru-N/O, 6 Ru-C,10	2.10 3.26	6.5	8.1 53.3	0.0156	27
	9	I,II,III	Ru-N/O,6 Ru-C,10 Ru-C,24	2.10 3.05 3.21	8.4	8.0 15.7 2.6	0.0171	23
act-MC3@CNT (after catalysis)	10	I	Ru-N,2 Ru-O,4	1.91 2.07	1.1	2.3 1.8	0.0099	63
	11	I	Ru-N/O,6	2.09	5.9	7.7	0.0160	114
	12	I,II	Ru-N/O,6 Ru-C,10	2.10 3.22	7.0	7.7 45.2	0.0180	29
	13	I,II,III	Ru-N/O,6 Ru-C,10 Ru-C,24	2.10 3.08 3.24	7.9 19.9 12.1	7.5	0.0160	28

Electrochemical Data

a)

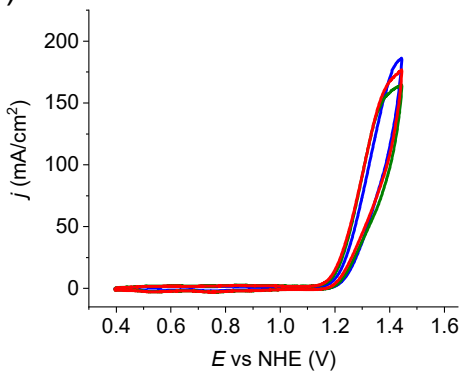

b)

	blue	red	green
j_{max} (mA/cm^2)	186	178	166
$j_{max,\ average}$	(176 ± 8) mA/cm^2		

Figure S61: a) Electrochemical experiments with **act-MC3@CNT@GC** in 1 M phosphate buffer (pH 7). Three independent electrodes were prepared, activated by 100 CV cycles to E = 1.35 V and CVs are compared for demonstrating reproducibility. b) Maximum current densities observed for **act-MC3@CNT@GC** in a).

a)

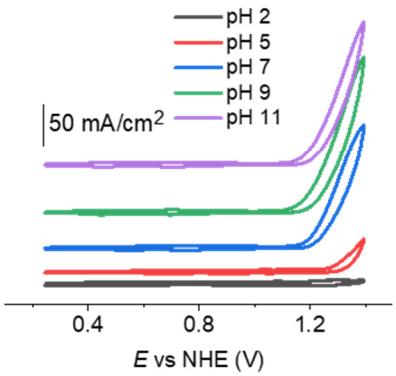

b)

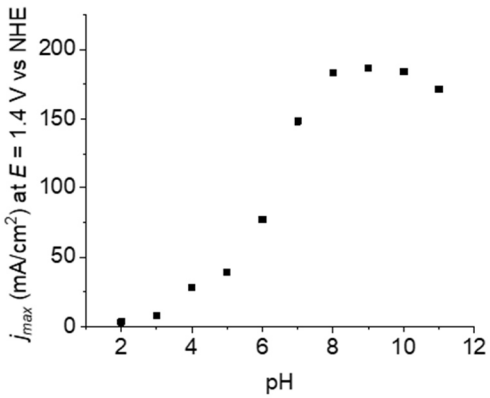

Figure S62: a) CVs (scan rate: 100 mV/s) of **act-MC3@CNT@GC** in a 1 M phosphate buffer at different pH values. b) Dependency of maximum current densities at E = 1.4 V vs NHE of **act-MC3@CNT@GC** on the pH value measured in phosphate buffer solutions.

Table S5: Comparison of selected Ru based water oxidation catalysts.

#	Compound[a]	Anchored via[b]	Support material[c]	pH	Γ_M (nmol cm^{-2})	E (V vs NHE)	j_{max} (mA cm^{-2})	TOF[d] (s^{-1})
1	**MC3@CNT**	CH-π, π-π	GC	7	8.4	1.45	186	3200
2[233]	Ru(bda)(pyn)$_2$@CNT	π-π	ITO	7	2	1.8	0.72	0.3
3[232]	Ru(bda)(4-(C_5H_{11})-py)$_2$	SAB	nanoITO/FTO	4.65	21	1.4	2.2	-
4[161]	Ru(bda)(phpy)$_2$	[R-Ar]-M	GC	7	0.1	1.2	0.2	1.9
5[262]	Ru(bda)(vpy)$_2$@TiO_2	p-vinyl	FTO	7	-	~1.55	~3.6	-
6[219]	Ru(bda)(F-isoq)(py-thiophene)]	p-thiophene	GC	7.2	0.96	1.3	4	5.7
7[278]	Ru(tda)(Pyr-Py)$_2$@CNT	π-π	GC	7	0.03	1.45	2.2	8076
8[278]	Ru(tda)(pyn)$_2$@CNT	π-π	GC	7	0.55	1.45	10.5	8935
9[234]	[Ru^{II}(OH_2)(tda))(4,4'-bpy)]$_5$(4,4'-bpy)@CNT	CH-π	GC	7	9.5	1.45	190	8054
10[234]	[Ru^{II}(OH_2)(tda))(4,4'-bpy)]$_{15}$(4,4'-bpy)]CNT	CH-π	GC	7	17.5	1.45	240	8060
11[224]	(bpy-$CH_2PO_3H_2$)Ru(Mebimpy)(OH_2)$^{2+}$	[R-PO_3H^-]-M	ITO/FTO	5	0.12	1.85	0.6	0.36
12[323]	(pdc-tta)Ru(pic)$_3$	[R-Ar]-M	GC	7	0.1	1.12	~0.05	0.07
13[230]	(pdc-O-(CH_2)$_{11}$-CH_3)Ru(pic)$_3$@CNT	hydrophilic interactions	GDL	7	0.85	1.3	2.2	7.6
14[324]	Ru(Mebimpy)(dvbpy)(OH_2)$^{2+}$	p-vinyl	VTMS-FTO/nanoITO	7.5	32	1.6	0.4	0.12

[a]: CNT is carbon nanotubes, bda is [2,2'-bipyridine]-6,6'-dicarboxylate, pyn is 4-(pyren-2-yl)-*N*-(pyridin-4-ylmethyl)butanamide, phpy is 4-phenylpyridine, vpy is 4-vinylpyridine, F-isoq is 6-fluoroisoquinoline, py-thiophene is 4-(2-(thiophen-3-yl)ethyl)pyridine, tda is [2,2':6',2''-terpyridine]-6,6''-dicarboxylate, pyr-py is 4-(pyren-2-yl)pyridine, bpy is 2,2′-bipyridine, Mebimpy is 2,6-bis(1-methylbenzimidazol-2-yl)pyridine, pdc is 2,6-pyridinedicarboxylate, pic is 4-picoline, tta is 1-(*p*-tolyl)-1*H*-1,2,3-triazole, Mebimpy is 2,6-bis(1-methyl-1H-benzo[*d*]imidazol-2-yl)pyridine; dvbpy is 5,5′-divinyl-2,2′-bipyridine. [b]: SAB self-assembles bilayers, p-vinyl is *in situ* polymerization of vinyl groups on the electrode, p-thiophene is *in situ* polymerization of thiophene groups on the electrode. [c]: GC is glassy carbon, ITI is indium tin oxide, FTO is fluorinated tin oxide, GLD is gas diffusion layer, VTMS is vinyltrimethoxysilane-functionalized. [d]: entry 1 and 7-10 determined by foot of the wave analysis.

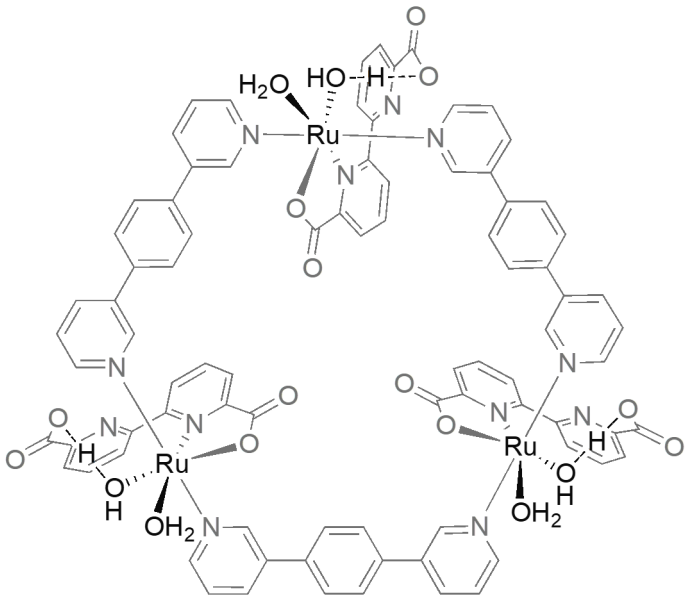

Figure S63: Chemical structure representation of activated species of **act-MC3@CNT@GC** proposed based on semiempirical calculations.

Calculated data[8]

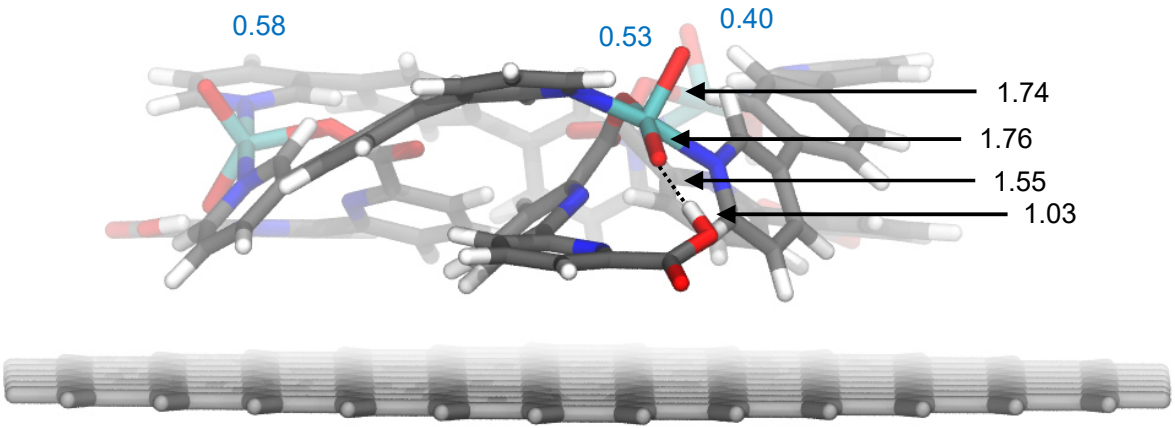

Figure S64: DFT-optimized structure in Ru^{V} state obtained assuming three consecutive PCET processes on each Ru center of the proposed **act-MC3@CNT@GC**. Due to the presence of two aqua ligands per Ru in the latter system, it is possible to oxidize up to Ru^{V} without total charge buildup. This is reflected in remarkably low Mulliken charges on Ru atoms (blue numbers) and, therefore, can explain the notably changing redox behavior during activation. Relevant Ru-O and O-H distances in optimized structure in Ru^{V} state are provided (black arrows and numbers) in Å.

[8] Structure in Figure S64 was optimized by Dr. Joachim Lindner, Universität Würzburg.

Screening of activities in heterogeneous water oxidation of catalysts presented in *Chapter 4*

Additionally, catalysts **OEG-MC2**, **OEG-MC3**, **OEG-MC4** presented in *Chapter 4* have been investigated to assess their behavior in heterogeneous water oxidation. Electrodes were prepared and experiments on activation were performed as described for **MC3**. Results are briefly discussed and details of activation are shown in Figures S66 – S68. It can be observed that the anchoring onto the CNTs seems less efficient with molecules comprising solubilizing OEG-chains, since maximum current densities of these catalysts decrease after about 10 – 20 CV cycles. This might either be due to a less stable anchoring of the catalyst to the CNTs, or due to unfavorable interactions of the OEG-chains between the CNT layers and the GC-electrode surface. Maximum current densities of **dfb-Dimer** also decrease fast, but might also be caused by oxidizing ligands, as much lower current densities are observed. Figure S65 shows an overview of the CVs in which the maximum current densities have been achieved during the activation process.

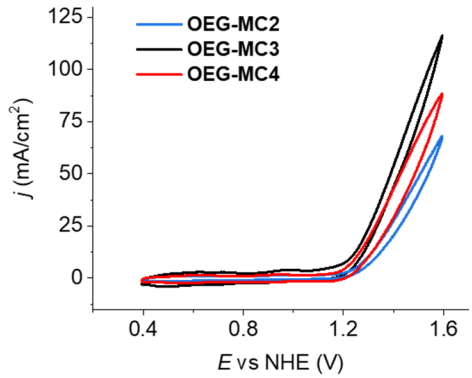

Figure S65: CV cycles (scan rate: 100 mV/s) of maximum current densitiey during activation process. **OEG-MC2** (14th cycle, blue), **OEG-MC3** (9th cycle, black) and **OEG-MC4** (24th cycle, red).

The maximum current density of **MC3** is comparable with the one of **OEG-MC3** when cycling to 1.6 V (j_{max} = 106 mA/cm^2 and j_{max} = 116 mA/cm^2, respectively, see Figure S59). However, stability of the hybrid anode is much lower in the latter as the current drops significantly during the 100 cycles. **OEG-MC4** reaches a maximum current density of j_{max} = 92 mA/cm^2, while **OEG-MC2** is much less active with j_{max} = 68 mA/cm^2.

OEG-MC2

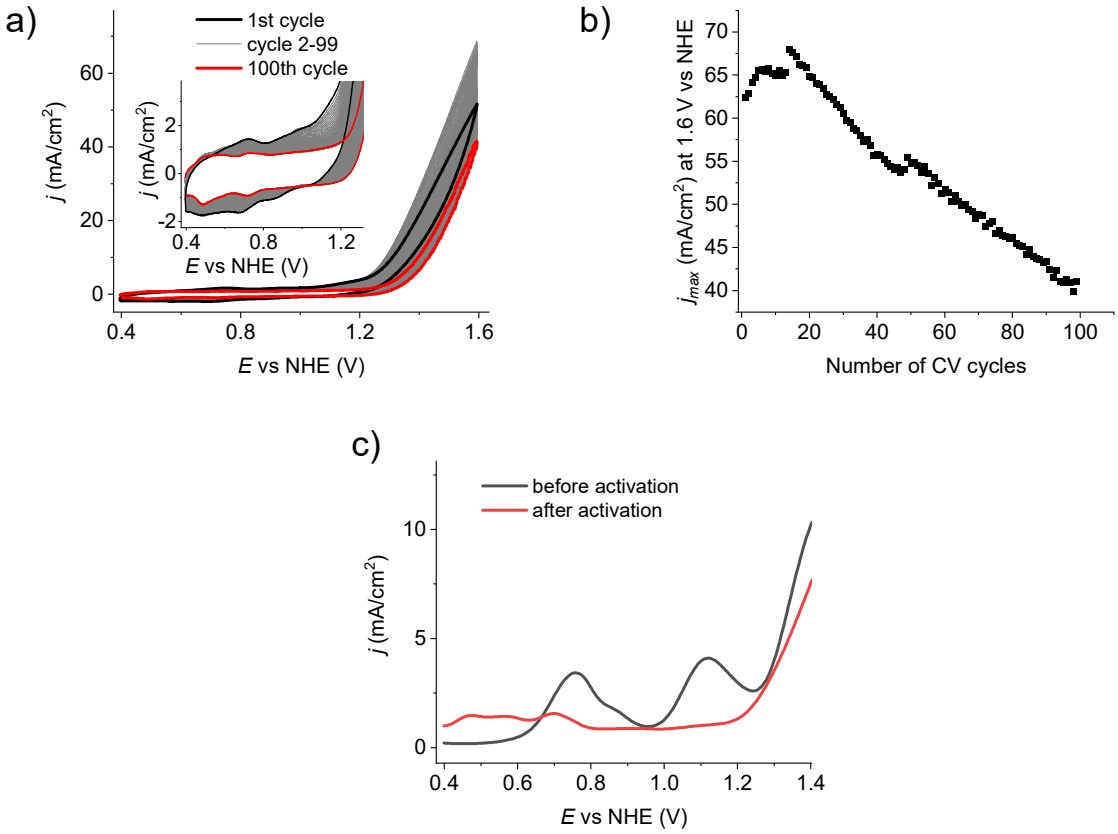

Figure S66: Electrochemical experiments (CV scan rate: 100 mV/s) with **OEG-MC2@CNT@GC** in 1 M phosphate buffer (pH 7). a) 100 repetitive CV cycles to a potential of *E* = 1.6 V vs NHE. Inset: Enlarged area of the non-catalytic waves. b) Development of the maximal current densities at *E* = 1.6 V vs NHE with the increasing number of CV scans. c) Comparison of the DPV of the initial (black line) and the final species (red line) after 100 CV cycles.

OEG-MC3

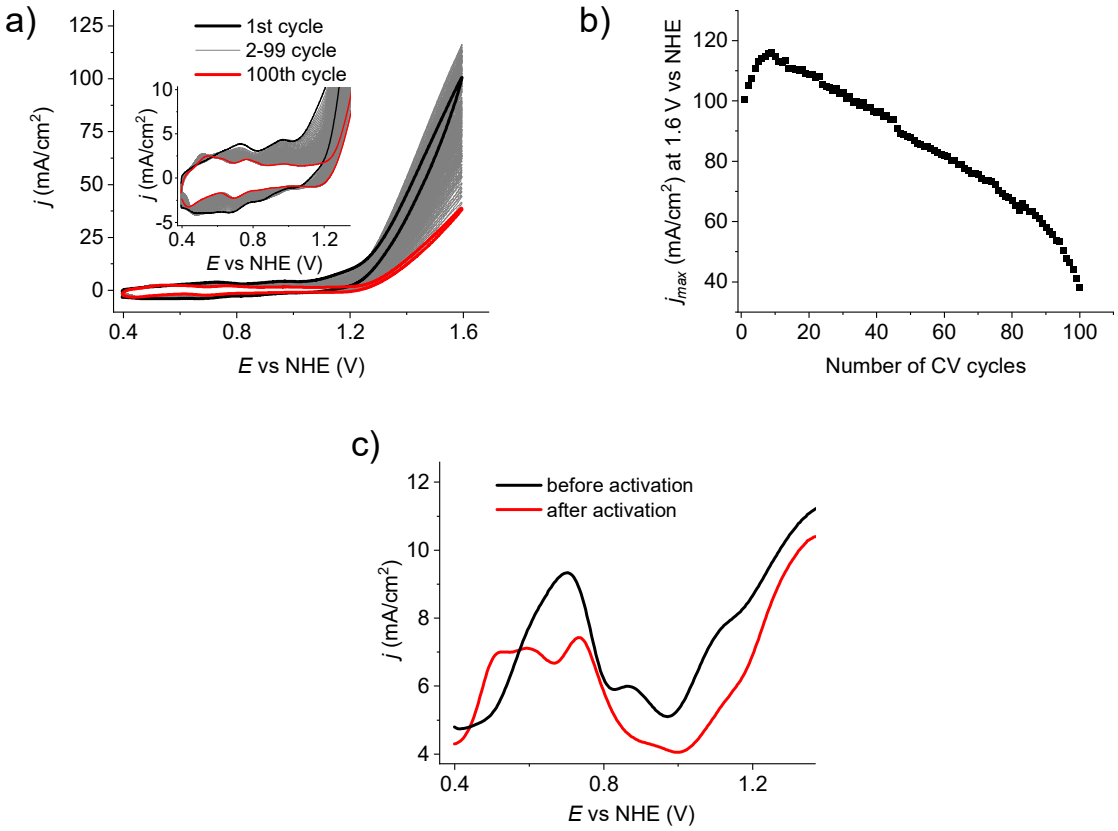

Figure S67: Electrochemical experiments (CV scan rate: 100 mV/s) with **OEG-MC3@CNT@GC** in 1 M phosphate buffer (pH 7). a) 100 repetitive CV cycles to a potential of *E* = 1.6 V vs NHE. Inset: Enlarged area of the non-catalytic waves. b) Development of the maximal current densities at *E* = 1.6 V vs NHE with the increasing number of CV scans. c) Comparison of the DPV of the initial (black line) and the final species (red line) after 100 CV cycles.

OEG-MC4

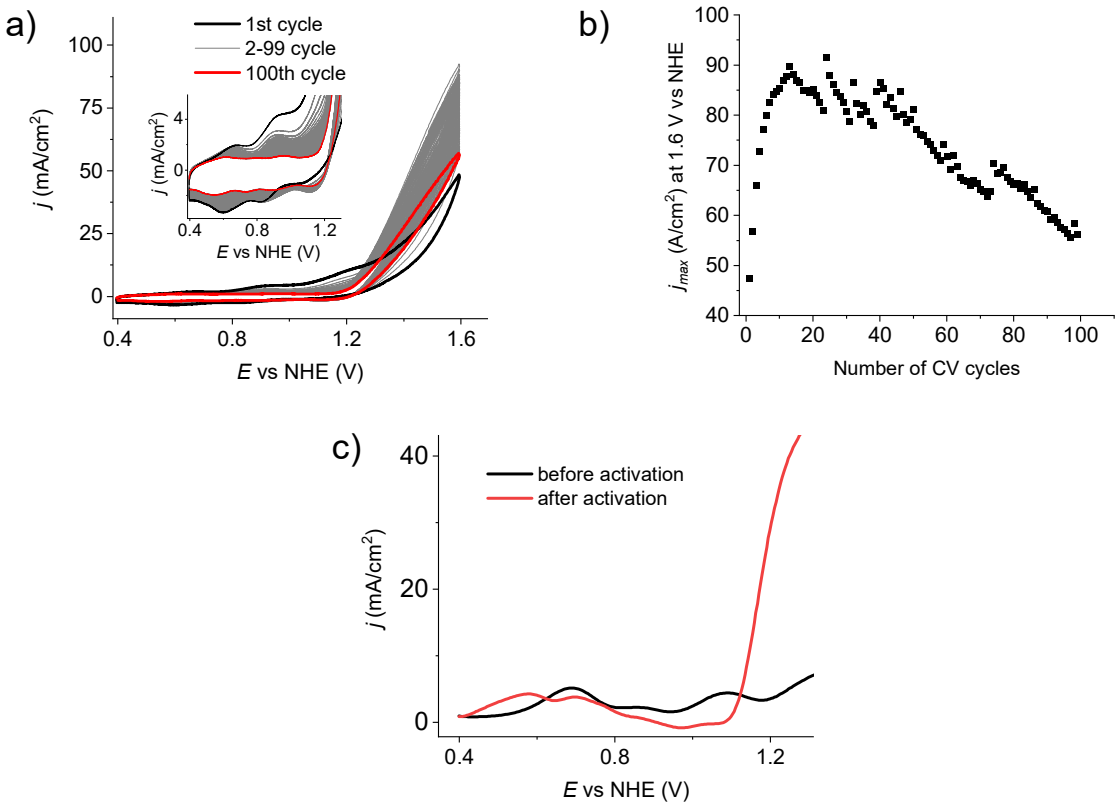

Figure S68: Electrochemical experiments (CV scan rate: 100 mV/s) with **OEG-MC4@CNT@GC** in 1 M phosphate buffer (pH 7). a) 100 repetitive CV cycles to a potential of *E* = 1.6 V vs NHE. Inset: Enlarged area of the non-catalytic waves. b) Development of the maximal current densities at *E* = 1.6 V vs NHE with the increasing number of CV scans. c) Comparison of the DPV of the initial (black line) and the final species (red line) after 100 CV cycles.

Danksagung

An erster Stelle gilt mein besonderer Dank meinem Doktorvater Prof. Dr. Frank Würthner. Ich bedanke mich für die Aufnahme in seinen Arbeitskreis, die Vergabe des interessanten Forschungsthemas, seine Unterstützung und wissenschaftliche Betreuung sowie die Bereitstellung exzellenter Forschungs- und Arbeitsbedingungen. Zudem danke ich für die Möglichkeit der Teilnahme an wissenschaftlichen Konferenzen und für die Ermöglichung meines Forschungsaufenthalts am *Institut Català d'Investigació Química* (ICIQ) in Tarragona, Spanien.

Zudem möchte ich Prof. Dr. Antoni Llobet für die freundliche Aufnahme in seine Arbeitsgruppe am ICIQ und seine Betreuung während meines Aufenthalts dort danken. Dank seiner Expertise und Zeit für viele ausführliche wissenschaftliche Diskussionen ist es erstmalig gelungen, elektrochemische Aktivierungsprozesse an Ru(bda) Komplexen zu analysieren. Für die Unterstützung, gute Zusammenarbeit und angenehme Arbeitsatmosphäre möchte ich allen Mitgliedern der Gruppe und insbesondere Dr. Marcos Gil-Sepulcre, Nataliia Vereshchuk, Marta Ventosa und Dr. Jan Oldengott danken.

Mein ausdrücklicher Dank gilt zudem Dr. Chantu Saha-Möller für wertvolle wissenschaftliche Diskussionen und dafür, dass er mir stets mit seinem Rat zur Seite stand. Ich bedanke mich für die Überarbeitung der aus Kapitel 5 hervorgegangenen Publikation und besonders für die mühevolle Arbeit des Korrekturlesens der Doktorarbeit.

Dr. David Schmidt danke ich für seine fortwährende Unterstützung und positive Art während meiner ersten Zeit im Arbeitskreis sowie für seine Ratschläge, auch nachdem er nicht mehr in Würzburg als mein Subgroup-Leiter tätig war.

Ich bedanke mich bei Dr. Matthias Stolte für seine Hilfe bezüglich des Aufbaus der photokatalytischen Wasseroxidation sowie seine Unterstützung in organisatorischen Angelegenheiten. Bei Prof. Dr. Roland Mitrić und Dr. Merle Röhr bedanke ich mich für ihre Zeit zur Teilnahme an Subgroup-Meetings und anschließende wertvolle wissenschaftliche Diskussionen.

Dr. Vladimir Stepanenko danke ich für die Aufnahme von AFM, SEM und EDX Bildern sowie fachliche Diskussion zu den erhaltenen Ergebnissen. Dr. Dooshaye Moonshiram vom *Instituto Madrileño de Estudios Avanzados en Nanociencia* (IMDEA Nanociencia) in Madrid, Spanien danke ich für die Kooperation bei der Aufnahme von XAS Spektren.

Dem Team der NMR-Abteilung unter Dr. Matthias Grüne danke ich für ihre Hilfestellungen bei Problemen während Probenmessungen sowie für ihre fachlichen Ratschläge. Insbesondere bedanke ich mich bei Marvin Grüne und Patricia Altenberger für das Aufnehmen von DOSY und 2D-NMR Spektren. Bei der Abteilung für Massenspektrometrie unter Dr. Michael Büchner und speziell bei Juliane Adelmann bedanke ich mich für die Einführung in das eigenständige Probenmessen sowie Ratschläge und tatkräftige Unterstützung.

Sarah Bullnheimer, Christiana Toussaint und Ellen Klaus danke ich von Herzen für ihre immer freundliche Art und Hilfe bei organisatorischen Fragen während meiner Zeit in Würzburg. Besonders danke ich auch Petra Seufert-Baumbach, Anja Rausch und Maximilian Roth für ihre Unterstützung bei jeglichen Anliegen im Laboralltag.

Den aktuellen und ehemaligen Mitgliedern der Ru-Subgroup, Dr. Ana Lucía Meza, Niklas Noll, Dr. Joachim Lindner, Dr. Suvendu Karak und Maximilian Roth danke ich für die angenehme Arbeitsatmosphäre und gute Zusammenarbeit. Insbesondere danke ich Dr. Ana Lucía Meza und Dr. Joachim Lindner für zahllose wissenschaftliche Diskussionen zu verschiedensten Problemen und ihre stetige Hilfsbereitschaft. Mein ausdrücklicher Dank gilt zudem Maximilian Roth für seine synthetische Unterstützung und Geduld auch bei schwierigen Aufgaben. Meinen Masterpraktikanten Samuel Nees, Günther Horrer und Samuel Trimble sowie meiner Auszubildenden Jennifer Walter danke ich für ihre gute Arbeit im Labor. Ich bedanke mich zudem bei meinen Vorgängern auf dem Thema der Wasseroxidationskatalyse, Dr. Valentin Kunz und Dr. Marcus Schulze, für ihre Hilfe bei der Einarbeitung in das Forschungsgebiet.

Mein ausdrücklicher Dank gilt zudem dem ganzen Arbeitskreis für die freundliche Atmosphäre, gute Zusammenarbeit und die schöne Zeit in Würzburg.

Ganz besonders bedanke ich mich bei meiner Familie für ihre stetige Unterstützung, Förderung, Geduld und Motivation nicht nur während dieser Arbeit, sondern während des gesamten Studiums. Ich bin sehr dankbar, dass ihr immer für mich da seid. Danke für alles.

References

[1] N. Armaroli, V. Balzani, *Angew. Chem. Int. Ed.* **2007**, *46*, 52-66.
[2] *World Population Clock: 7.8 Billion People (2020) - Worldometer*, https://www.worldometers.info/world-population/, accessed: July 23, 2020.
[3] N. Abas, A. Kalair, N. Khan, *Futures* **2015**, *69*, 31-49.
[4] M. Asif, T. Muneer, *Renew. Sust. Energ. Rev.* **2007**, *11*, 1388-1413.
[5] H. Daly, *Appl. Energy* **1994**, *47*, 101-121.
[6] F. Johnsson, J. Kjärstad, J. Rootzén, *Clim. Policy* **2019**, *19*, 258-274.
[7] D. J. Wuebbles, A. K. Jain, *Fuel Process. Technol.* **2001**, *71*, 99-119.
[8] M. Höök, X. Tang, *Energy Policy* **2013**, *52*, 797-809.
[9] B. p.l.c., *BP Statistical Review of World Energy 2020*, 69th edition.
[10] A. A. Alola, D. Kirikkaleli, *Air Qual. Atmos. Health* **2020**, DOI: 10.1007/s11869-11020-00962-z.
[11] *U.S. Global Change Research Program*, globalchange.gov, **2018**.
[12] A. G. Olabi, *Energy* **2017**, *136*, 1-6.
[13] G. C. Dismukes, V. V. Klimov, S. V. Baranov, Y. N. Kozlov, J. DasGupta, A. Tyryshkin, *Proc. Natl. Acad. Sci. USA* **2001**, *98*, 2170-2175.
[14] K. Handayani, Y. Krozer, T. Filatova, *Energy Policy* **2019**, *127*, 134-146.
[15] P. J. D. Janssen, M. D. Lambreva, N. Plumeré, C. Bartolucci, A. Antonacci, K. Buonasera, R. N. Frese, V. Scognamiglio, G. Rea, *Front. Chem.* **2014**, *2*.
[16] D. J. Des Marais, **2000**, *289*, 1703-1705.
[17] D. S. Bendall, C. J. Howe, E. G. Nisbet, R. E. R. Nisbet, *Phil. Trans. R. Soc. B* **2008**, *363*, 2625-2628.
[18] T. Cardona, *Open Biol.* **2019**, *9*, 180246.
[19] N. S. Lewis, *Science* **2016**, *351*, aad1920.
[20] T. R. Cook, D. K. Dogutan, S. Y. Reece, Y. Surendranath, T. S. Teets, D. G. Nocera, *Chem. Rev.* **2010**, *110*, 6474-6502.
[21] V. Etacheri, R. Marom, R. Elazari, G. Salitra, D. Aurbach, *Energy Environ. Sci.* **2011**, *4*, 3243-3262.
[22] J. P. Rivera-Barrera, N. Muñoz-Galeano, H. O. Sarmiento-Maldonado, *Electronics* **2017**, *6*.
[23] G. J. May, A. Davidson, B. Monahov, *J. Energy Storage* **2018**, *15*, 145-157.
[24] Y. Yang, S. Bremner, C. Menictas, M. Kay, *Renew. Sust. Energ. Rev.* **2018**, *91*, 109-125.
[25] D. Gust, T. A. Moore, A. L. Moore, *Acc. Chem. Res.* **2009**, *42*, 1890-1898.
[26] S. Styring, *Faraday Discuss.* **2012**, *155*, 357-376.
[27] J. R. Bolton, *Science* **1978**, *202*, 705-711.
[28] R. E. Blankenship, *Plant Physiol.* **2010**, *154*, 434-438.
[29] N. S. Lewis, D. G. Nocera, *Proc. Natl. Acad. Sci. USA* **2006**, *103*, 15729-15735.
[30] V. Balzani, A. Credi, M. Venturi, *ChemSusChem* **2008**, *1*, 26-58.
[31] W. Song, Z. Chen, M. K. Brennaman, J. J. Concepcion, A. O. T. Patrocinio, N. Y. M. Iha, T. J. Meyer, *Pure Appl. Chem.* **2011**, *83*, 749.
[32] A. Züttel, A. Remhof, A. Borgschulte, O. Friedrichs, *Phil. Trans. R. Soc. A* **2010**, *368*, 3329-3342.
[33] W. Lubitz, W. Tumas, *Chem. Rev.* **2007**, *107*, 3900-3903.

[34] *International Energy Agency: The clean hydrogen future has already begun (2019),* https://www.iea.org/commentaries/the-clean-hydrogen-future-has-already-begun, accessed: July 23, 2020.
[35] R. J. Cogdell, T. H. P. Brotosudarmo, A. T. Gardiner, P. M. Sanchez, L. Cronin, *Biofuels* **2010**, *1*, 861-876.
[36] K. J. Young, L. A. Martini, R. L. Milot, R. C. Snoeberger, V. S. Batista, C. A. Schmuttenmaer, R. H. Crabtree, G. W. Brudvig, *Coord. Chem. Rev.* **2012**, *256*, 2503-2520.
[37] G. Thomas, *Overview of Storage Development DOE Hydrogen Program*, Sandia National Laboratories, Livermore, California, **2000**.
[38] A. Fujishima, K. Honda, *Nature* **1972**, *238*, 37-38.
[39] S. W. Gersten, G. J. Samuels, T. J. Meyer, *J. Am. Chem. Soc.* **1982**, *104*, 4029-4030.
[40] L. Duan, A. Fischer, Y. Xu, L. Sun, *J. Am. Chem. Soc.* **2009**, *131*, 10397-10399.
[41] B. Zhang, L. Sun, *J. Am. Chem. Soc.* **2019**, *141*, 5565-5580.
[42] M. Schulze, V. Kunz, P. D. Frischmann, F. Würthner, *Nat. Chem.* **2016**, *8*, 576-583.
[43] V. Kunz, J. O. Lindner, M. Schulze, M. I. S. Rohr, D. Schmidt, R. Mitric, F. Wurthner, *Energy Environ. Sci.* **2017**, *10*, 2137-2153.
[44] V. Kunz, D. Schmidt, M. I. S. Röhr, R. Mitrić, F. Würthner, *Adv. Energy Mater.* **2017**, *7*, 1602939.
[45] B. M. Griffin, J. Schott, B. Schink, *Science* **2007**, *316*, 1870-1870.
[46] M. T. Madigan, J. M. Martinko, *Brock Mikrobiologie*, Pearson Studium, **2009**.
[47] J. D. J. Olmos, J. Kargul, *Acta Soc. Bot. Pol.* **2014**, *83*, 423-440.
[48] M. F. Hohmann-Marriott, R. E. Blankenship, *Annu. Rev. Plant Biol.* **2011**, *62*, 515-548.
[49] R. E. Blankenship, *Molecular Mechanisms of Photosynthesis*, WILEY, Blackwell, UK, **2014**.
[50] J. Barber, W. Kühlbrandt, *Curr. Opin. Struct. Bio.* **1999**, *9*, 469-475.
[51] R. Bassi, P. Dainese, *Eur. J. Biochem.* **1992**, *204*, 317-326.
[52] T. Pullerits, V. Sundström, *Acc. Chem. Res.* **1996**, *29*, 381-389.
[53] X. Wei, X. Su, P. Cao, X. Liu, W. Chang, M. Li, X. Zhang, Z. Liu, *Nature* **2016**, *534*, 69-74.
[54] X. Qin, M. Suga, T. Kuang, J. R. Shen, *Science* **2015**, *348*, 989-995.
[55] H. Ishikita, W. Saenger, J. Biesiadka, B. Loll, E.-W. Knapp, *Proc. Natl. Acad. Sci. USA* **2006**, *103*, 9855-9860.
[56] K.-H. Tang, R. E. Blankenship, in *Encyclopedia of Biophysics* (Ed.: G. C. K. Roberts), Springer, Berlin, Heidelberg, **2013**, pp. 1868-1873.
[57] M. Rott, N. F. Martins, W. Thiele, W. Lein, R. Bock, D. M. Kramer, M. A. Schöttler, *Plant Cell* **2011**, *23*, 304-321.
[58] M. Shin, *Photosynthesis research* **2004**, *80*, 307-313.
[59] J. A. Bassham, A. A. Benson, L. D. Kay, A. Z. Harris, A. T. Wilson, M. Calvin, *J. Am. Chem. Soc.* **1954**, *76*, 1760-1770.
[60] C. A. Raines, *Photosynthesis research* **2003**, *75*, 1-10.
[61] J. A. Bassham, M. Calvin, in *The Assimilation of Carbon Dioxide. Encyclopedia of Plant Physiology*, Springer, Berlin, Heidelberg, **1960**.
[62] N. A. Campbell, J. B. Reece, M. R. Taylor, E. J. Simon, *Biology: Concepts & Connections*, Pearson/Benjamin Cummings, **2008**.
[63] K. Miyamoto, in *Renewable biological systems for alternative sustainable energy production*, Food and Agriculture Organization of the United Nations, **2009**.

[64] K. Munk, *Grundstudium Biologie. Botanik*, Spektrum Akademischer Verlag, Heidelberg, **2001**.
[65] E. Weiler, L. Nover, W. Nultsch, *Allgemeine und molekulare Botanik*, Thieme Verlag, Stuttgart, **2008**.
[66] S. Zeki, K. H. Nealson, P. G. Conrad, *Phil. Trans. R. Soc. Lond. B* **1999**, *354*, 1923-1939.
[67] J. Whitmarsh, Govindjee, *Photosynthesis, Vol. 13*, VCH Publishers, Inc., **1995**.
[68] J. Whitmarsh, Govindjee, in *Concepts in photobiology: photosynthesis and photomorphogenesis*, Boston: Kluwer Academic Publishers, **1999**.
[69] C. B. Field, M. J. Behrenfeld, J. T. Randerson, P. Falkowski, *Science* **1998**, *281*, 237-240.
[70] Govindjee, R. E. Blankenship, G. A. Berkowitz, A. R. Portis, Jr., R. J. Shopes, *AccessScience, McGraw-Hill Education* **2019**.
[71] W. Lubitz, E. J. Reijerse, J. Messinger, *Energy Environ. Sci.* **2008**, *1*, 15-31.
[72] M. M. Najafpour, I. Zaharieva, Z. Zand, S. Maedeh Hosseini, M. Kouzmanova, M. Hołyńska, I. Tranca, A. W. Larkum, J.-R. Shen, S. I. Allakhverdiev, *Coord. Chem. Rev.* **2020**, *409*, 213183.
[73] J. Barber, B. Andersson, *Trends Biochem. Sci.* **1992**, *17*, 61-66.
[74] W. Lubitz, M. Chrysina, N. Cox, *Photosynth. Res.* **2019**, *142*, 105-125.
[75] F. A. Armstrong, *Philos. Trans. R. Soc. B* **2008**, *363*, 1263-1270.
[76] J. Limburg, J. S. Vrettos, L. M. Liable-Sands, A. L. Rheingold, R. H. Crabtree, G. W. Brudvig, *Science* **1999**, *283*, 1524-1527.
[77] M. Suga, F. Akita, K. Hirata, G. Ueno, H. Murakami, Y. Nakajima, T. Shimizu, K. Yamashita, M. Yamamoto, H. Ago, J.-R. Shen, *Nature* **2015**, *517*, 99-103.
[78] J. Barber, *Inorg. Chem.* **2008**, *47*, 1700-1710.
[79] L. Vogt, D. J. Vinyard, S. Khan, G. W. Brudvig, *Curr. Opin. Chem. Biol.* **2015**, *25*, 152-158.
[80] L. Sun, *Science* **2015**, *348*, 635-636.
[81] C. Zhang, C. Chen, H. Dong, J.-R. Shen, H. Dau, J. Zhao, *Science* **2015**, *348*, 690-693.
[82] K. Reiss, U. N. Morzan, A. T. Grigas, V. S. Batista, *Inorganics* **2019**, 39.
[83] B. Kok, B. Forbush, M. McGloin, *Photochem. Photobiol.* **1970**, *11*, 457-475.
[84] J. Barber, *Nat. Plants* **2017**, *3*, 17041.
[85] D. J. Vinyard, G. W. Brudvig, *Annu. Rev. Phys. Chem.* **2017**, *68*, 101-116.
[86] V. L. Pecoraro, M. J. Baldwin, M. T. Caudle, W.-Y. Hsieh, N. A. Law, *Pure Appl. Chem.* **1998**, 925-929.
[87] P. E. M. Siegbahn, *Acc. Chem. Res.* **2009**, *42*, 1871-1880.
[88] P. E. M. Siegbahn, *Proc. Natl. Acad. Sci. USA* **2017**, *114*, 4966-4968.
[89] B. Zhang, L. Sun, *Dalton Trans.* **2018**, *47*, 14381-14387.
[90] B. Zhang, L. Sun, *ChemSusChem* **2019**, *12*, 3401-3404.
[91] P. W. Atkins, *Physical Chemistry*, W. H. Freeman & Co, **1997**.
[92] A. D. McNaught, A. Wilkinson, *IUPAC. Compendium of Chemical Terminology, 2nd ed. (the "Gold Book").* Blackwell Scientific Publications, Oxford, **1997**.
[93] J. Russell, R. Cohn, *Nernst Equation*, Book on Demand, **2012**.
[94] M. Ammam, *Applications of Nernst Equation: Basic Concepts with Resolved Questions and Problems*, CreateSpace Independent Publishing Platform, **2018**.
[95] L. Duan, L. Wang, A. K. Inge, A. Fischer, X. Zou, L. Sun, *Inorg. Chem.* **2013**, *52*, 7844-7852.
[96] E. M. Stuve, in *J. Appl. Electrochem.* (Eds.: G. Kreysa, K.-i. Ota, R. F. Savinell), Springer New York, **2014**, pp. 1445-1453.
[97] E. K. Rideal, *J. Am. Chem. Soc.* **1920**, *42*, 94-105.

[98] L. Tong, R. P. Thummel, *Chem. Sci.* **2016**, *7*, 6591-6603.
[99] T. Takahashi, in *Solar-Hydrogen Energy Systems* (Ed.: T. Ohta), Pergamon, **1979**, pp. 25-33.
[100] B. Zhang, L. Sun, *Chem. Soc. Rev.* **2019**, *48*, 2216-2264.
[101] P. D. Frischmann, K. Mahata, F. Würthner, *Chem. Soc. Rev.* **2013**, *42*, 1847-1870.
[102] R. Brimblecombe, G. C. Dismukes, G. F. Swiegers, L. Spiccia, *Dalton Trans.* **2009**, *43*, 9374-9384.
[103] *acatech – National Academy of Science and Engineering, German National Academy of Sciences Leopoldina, Union of the German Academies of Sciences and Humanities, in Artificial Photosynthesis* **2018**, Munich, 1-74.
[104] H. Zhou, F. Yu, Q. Zhu, J. Sun, F. Qin, L. Yu, J. Bao, Y. Yu, S. Chen, Z. Ren, *Energy Environ. Sci.* **2018**, *11*, 2858-2864.
[105] V. Subramani, A. Basile, T. N. Veziroğlu, *Compendium of Hydrogen Energy: : Hydrogen Production and Purification*, Woodhead Publishing, **2015**.
[106] J. Jia, L. C. Seitz, J. D. Benck, Y. Huo, Y. Chen, J. W. D. Ng, T. Bilir, J. S. Harris, T. F. Jaramillo, *Nat. Commun.* **2016**, *7*, 13237.
[107] N. G, D. R. A, A. I. A, J. R.L, *Optik* **2019**, *179*, 889-894.
[108] M. I. Dar, A. K. Chandiran, M. Grätzel, M. K. Nazeeruddin, S. A. Shivashankar, *J. Mater. Chem. A* **2014**, *2*, 1662-1667.
[109] Z. Yu, F. Li, L. Sun, *Energy Environ. Sci.* **2015**, *8*, 760-775.
[110] S. Zhang, H. Ye, J. Hua, H. Tian, *EnergyChem* **2019**, *1*, 100015.
[111] K. Sivula, R. van de Krol, *Nat. Rev. Mater.* **2016**, *1*, 15010.
[112] S. Yun, N. Vlachopoulos, A. Qurashi, S. Ahmad, A. Hagfeldt, *Chem. Soc. Rev.* **2019**, *48*, 3705-3722.
[113] M. K. Brennaman, R. J. Dillon, L. Alibabaei, M. K. Gish, C. J. Dares, D. L. Ashford, R. L. House, G. J. Meyer, J. M. Papanikolas, T. J. Meyer, *J. Am. Chem. Soc.* **2016**, *138*, 13085-13102.
[114] X. Ding, Y. Gao, L. Ye, L. Zhang, L. Sun, *ChemSusChem* **2015**, *8*, 3992-3995.
[115] M. Gratzel, *Nature* **2001**, *414*, 338-344.
[116] A. Hagfeldt, G. Boschloo, L. Sun, L. Kloo, H. Pettersson, *Chem. Rev.* **2010**, *110*, 6595-6663.
[117] B. O'Regan, M. Grätzel, *Nature* **1991**, *353*, 737-740.
[118] L. Hammarström, *Acc. Chem. Res.* **2015**, *48*, 840-850.
[119] N. Manfredi, C. L. Boldrini, A. Abbotto, *ChemElectroChem* **2018**, *5*, 2395-2402.
[120] X. Ding, L. Zhang, Y. Wang, A. Liu, Y. Gao, *Coord. Chem. Rev.* **2018**, *357*, 130-143.
[121] W. J. Youngblood, S.-H. A. Lee, Y. Kobayashi, E. A. Hernandez-Pagan, P. G. Hoertz, T. A. Moore, A. L. Moore, D. Gust, T. E. Mallouk, *J. Am. Chem. Soc.* **2009**, *131*, 926-927.
[122] R. Brimblecombe, A. Koo, G. C. Dismukes, G. F. Swiegers, L. Spiccia, *J. Am. Chem. Soc.* **2010**, *132*, 2892-2894.
[123] L. Li, L. Duan, Y. Xu, M. Gorlov, A. Hagfeldt, L. Sun, *Chem. Commun.* **2010**, *46*, 7307-7309.
[124] L. Zhang, Y. Gao, X. Ding, Z. Yu, L. Sun, *ChemSusChem* **2014**, *7*, 2801-2804.
[125] Y. Gao, X. Ding, J. Liu, L. Wang, Z. Lu, L. Li, L. Sun, *J. Am. Chem. Soc.* **2013**, *135*, 4219-4222.
[126] X. Ding, Y. Gao, L. Zhang, Z. Yu, J. Liu, L. Sun, *ACS Catal.* **2014**, *4*, 2347-2350.
[127] M. Yamamoto, L. Wang, F. Li, T. Fukushima, K. Tanaka, L. Sun, H. Imahori, *Chem. Sci.* **2016**, *7*, 1430-1439.

[128] F. Li, K. Fan, L. Wang, Q. Daniel, L. Duan, L. Sun, *ACS Catal.* **2015**, *5*, 3786-3790.
[129] D. Wang, J. Hu, B. D. Sherman, M. V. Sheridan, L. Yan, C. J. Dares, Y. Zhu, F. Li, Q. Huang, W. You, T. J. Meyer, *Proc. Natl. Acad. Sci. USA* **2020**, *117*, 13256-13260.
[130] L. Li, L. Duan, F. Wen, C. Li, M. Wang, A. Hagfeldt, L. Sun, *Chem. Commun.* **2012**, *48*, 988-990.
[131] Z. Ji, M. He, Z. Huang, U. Ozkan, Y. Wu, *J. Am. Chem. Soc.* **2013**, *135*, 11696-11699.
[132] B. van den Bosch, J. A. Rombouts, R. V. A. Orru, J. N. H. Reek, R. J. Detz, *ChemCatChem* **2016**, *8*, 1392-1398.
[133] H.-L. Wu, X.-B. Li, C.-H. Tung, L.-Z. Wu, *Adv. Sci.* **2018**, *5*, 1700684.
[134] K. Fan, F. Li, L. Wang, Q. Daniel, E. Gabrielssona, L. Sun, *Phys.Chem.Chem.Phys.* **2014**, *16*, 25234 - 25240.
[135] F. Li, K. Fan, B. Xu, E. Gabrielsson, Q. Daniel, L. Li, L. Sun, *J. Am. Chem. Soc.* **2015**, *137*, 9153-9159.
[136] M. G. Walter, E. L. Warren, J. R. McKone, S. W. Boettcher, Q. Mi, E. A. Santori, N. S. Lewis, *Chem. Rev.* **2010**, *110*, 6446-6473.
[137] D. Gao, I. Trentin, L. Schwiedrzik, L. González, C. Streb, *Molecules* **2020**, 157.
[138] Y. Park, K. J. McDonald, K.-S. Choi, *Chem. Soc. Rev.* **2013**, *42*, 2321-2337.
[139] F. F. Abdi, N. Firet, A. Dabirian, R. van de Krol, *MRS Online Proc. Libr.* **2012**, *1446*, 7-12.
[140] A. Kudo, K. Ueda, H. Kato, I. Mikami, *Catal. Lett.* **1998**, *53*, 229-230.
[141] B. M. Hunter, H. B. Gray, A. M. Müller, *Chem. Rev.* **2016**, *116*, 14120-14136.
[142] N. Yuan, Q. Jiang, J. Li, J. Tang, *Arab. J. Chem.* **2020**, *13*, 4294-4309.
[143] D. B. Rogers, R. D. Shannon, A. W. Sleight, J. L. Gillson, *Inorg. Chem.* **1969**, *8*, 841-849.
[144] Y. Matsumoto, E. Sato, *Mater. Chem. Phys.* **1986**, *14*, 397-426.
[145] A. Harriman, I. J. Pickering, J. M. Thomas, P. A. Christensen, *J. Chem. Soc., Faraday Trans. 1* **1988**, *84*, 2795-2806.
[146] S. Cherevko, S. Geiger, O. Kasian, N. Kulyk, J.-P. Grote, A. Savan, B. R. Shrestha, S. Merzlikin, B. Breitbach, A. Ludwig, K. J. J. Mayrhofer, *Catal. Today* **2016**, *262*, 170-180.
[147] T. Audichon, T. W. Napporn, C. Canaff, C. Morais, C. Comminges, K. B. Kokoh, *J. Phys. Chem. C* **2016**, *120*, 2562-2573.
[148] J. Shan, C. Guo, Y. Zhu, S. Chen, L. Song, M. Jaroniec, Y. Zheng, S.-Z. Qiao, *Chem* **2019**, *5*, 445-459.
[149] S. Tsubaki, S. Hayakawa, T. Ueda, S. Fujii, E.-i. Suzuki, J. Zhang, A. Bond, Y. Wada, *Chem. Commun.* **2019**, *55*, 1032-1035.
[150] F. A. Garcés-Pineda, M. Blasco-Ahicart, D. Nieto-Castro, N. López, J. R. Galán-Mascarós, *Nat. Energy* **2019**, *4*, 519-525.
[151] J. Xu, S. Murphy, D. Xiong, R. Cai, X.-K. Wei, M. Heggen, E. Barborini, S. Vinati, R. E. Dunin-Borkowski, R. E. Palmer, L. Liu, *ACS Appl. Energy Mater.* **2018**, *1*, 3013-3018.
[152] Y. Qu, X. Duan, *Chem. Soc. Rev.* **2013**, *42*, 2568-2580.
[153] M. Beller, G. Centi, L. Sun, *ChemSusChem* **2017**, *10*, 6-13.
[154] A. R. Parent, R. H. Crabtree, G. W. Brudvig, *Chem. Soc. Rev.* **2013**, *42*, 2247-2252.
[155] H. N. Kagalwala, L. Tong, R. Zong, L. Kohler, M. S. G. Ahlquist, T. Fan, K. J. Gagnon, R. P. Thummel, *ACS Catal.* **2017**, *7*, 2607-2615.
[156] L. Duan, Y. Xu, P. Zhang, M. Wang, L. Sun, *Inorg. Chem.* **2010**, *49*, 209-215.

[157] M. D. Kärkäs, O. Verho, E. V. Johnston, B. Åkermark, *Chem. Rev.* **2014**, *114*, 11863-12001.
[158] M. Natali, F. Nastasi, F. Puntoriero, A. Sartorel, *Eur. J. Inorg. Chem.* **2019**, *15*, 227-2039.
[159] V. G. Artemov, *Meas. Sci. Technol.* **2016**, *28*, 014013.
[160] T. S. Light, S. Licht, A. C. Bevilacqua, K. R. Morash, *Electrochem. Solid-State Lett.* **2005**, *8*, E16.
[161] R. Matheu, S. Neudeck, F. Meyer, X. Sala, A. Llobet, *ChemSusChem* **2016**, *9*, 3361-3369.
[162] R. G. Ehl, A. J. Ihde, *J. Chem. Educ.* **1954**, *31*, 226.
[163] M. Faraday, *Philos. Trans. Royal Soc.* **1834**, *124*, 77-122.
[164] X. Sala, S. Maji, R. Bofill, J. García-Antón, L. Escriche, A. Llobet, *Acc. Chem. Res.* **2014**, *47*, 504-516.
[165] B. Zhang, S. Zhan, T. Liu, L. Wang, A. Ken Inge, L. Duan, B. J. J. Timmer, O. Kravchenko, F. Li, M. S. G. Ahlquist, L. Sun, *J. Energy Chem.* **2021**, *54*, 815-821.
[166] D. J. Gulliver, W. Levason, *Coord. Chem. Rev.* **1982**, *46*, 1-127.
[167] R. Matheu, M. Z. Ertem, C. Gimbert-Suriñach, X. Sala, A. Llobet, *Chem. Rev.* **2019**, *119*, 3453-3471.
[168] D. Moonshiram, J. W. Jurss, J. J. Concepcion, T. Zakharova, I. Alperovich, T. J. Meyer, Y. Pushkar, *J. Am. Chem. Soc.* **2012**, *134*, 4625-4636.
[169] D. Moonshiram, V. Purohit, J. J. Concepcion, T. J. Meyer, Y. Pushkar, *Materials* **2013**, *6*, 392-409.
[170] J. J. Concepcion, D. K. Zhong, D. J. Szalda, J. T. Muckerman, E. Fujita, *Chem. Commun.* **2015**, *51*, 4105-4108.
[171] E. A. Karlsson, B.-L. Lee, T. Åkermark, E. V. Johnston, M. D. Kärkäs, J. Sun, Ö. Hansson, J.-E. Bäckvall, B. Åkermark, *Angew. Chem. Int. Ed.* **2011**, *50*, 11715-11718.
[172] M. Okamura, M. Kondo, R. Kuga, Y. Kurashige, T. Yanai, S. Hayami, V. K. Praneeth, M. Yoshida, K. Yoneda, S. Kawata, S. Masaoka, *Nature* **2016**, *530*, 465-468.
[173] J. L. Fillol, Z. Codolà, I. Garcia-Bosch, L. Gómez, J. J. Pla, M. Costas, *Nat. Chem.* **2011**, *3*, 807-813.
[174] V. K. K. Praneeth, M. Kondo, M. Okamura, T. Akai, H. Izu, S. Masaoka, *Chem. Sci.* **2019**, *10*, 4628-4639.
[175] S. I. Shylin, M. V. Pavliuk, L. D'Amario, F. Mamedov, J. Sá, G. Berggren, I. O. Fritsky, *Chem. Commun.* **2019**, *55*, 3335-3338.
[176] D. Wang, J. T. Groves, *Proc. Natl. Acad. Sci. USA* **2013**, *110*, 15579-15584.
[177] T. Nakazono, A. R. Parent, K. Sakai, *Chem. Commun.* **2013**, *49*, 6325-6327.
[178] M. L. Rigsby, S. Mandal, W. Nam, L. C. Spencer, A. Llobet, S. S. Stahl, *Chem. Sci.* **2012**, *3*, 3058-3062.
[179] Y. Han, Y. Wu, W. Lai, R. Cao, *Inorg. Chem.* **2015**, *54*, 5604-5613.
[180] P. Garrido-Barros, S. Grau, S. Drouet, J. Benet-Buchholz, C. Gimbert-Suriñach, A. Llobet, *ACS Catal.* **2019**, *9*, 3936-3945.
[181] L. Wang, L. Duan, R. B. Ambre, Q. Daniel, H. Chen, J. Sun, B. Das, A. Thapper, J. Uhlig, P. Dinér, L. Sun, *J. Catal.* **2016**, *335*, 72-78.
[182] P. Garrido-Barros, C. Gimbert-Suriñach, D. Moonshiram, A. Picón, P. Monge, V. S. Batista, A. Llobet, *J. Am. Chem. Soc.* **2017**, *139*, 12907-12910.
[183] S. J. Koepke, K. M. Light, P. E. VanNatta, K. M. Wiley, M. T. Kieber-Emmons, *J. Am. Chem. Soc.* **2017**, *139*, 8586-8600.
[184] H. Lee, X. Wu, L. Sun, *Nanoscale* **2020**, *12*, 4187-4218.

[185] A. Savini, G. Bellachioma, G. Ciancaleoni, C. Zuccaccia, D. Zuccaccia, A. Macchioni, *Chem. Commun.* **2010**, *46*, 9218-9219.
[186] T. K. Michaelos, D. Y. Shopov, S. B. Sinha, L. S. Sharninghausen, K. J. Fisher, H. M. C. Lant, R. H. Crabtree, G. W. Brudvig, *Acc. Chem. Res.* **2017**, *50*, 952-959.
[187] G. Menendez Rodriguez, A. Bucci, R. Hutchinson, G. Bellachioma, C. Zuccaccia, S. Giovagnoli, H. Idriss, A. Macchioni, *ACS Energy Lett.* **2017**, *2*, 105-110.
[188] J. W. Jurss, J. J. Concepcion, J. M. Butler, K. M. Omberg, L. M. Baraldo, D. G. Thompson, E. L. Lebeau, B. Hornstein, J. R. Schoonover, H. Jude, J. D. Thompson, D. M. Dattelbaum, R. C. Rocha, J. L. Templeton, T. J. Meyer, *Inorg. Chem.* **2012**, *51*, 1345-1358.
[189] X. Yang, M.-H. Baik, *J. Am. Chem. Soc.* **2004**, *126*, 13222-13223.
[190] J. A. Stull, R. D. Britt, J. L. McHale, F. J. Knorr, S. V. Lymar, J. K. Hurst, *J. Am. Chem. Soc.* **2012**, *134*, 19973-19976.
[191] D. Geselowitz, T. J. Meyer, *Inorg. Chem.* **1990**, *29*, 3894-3896.
[192] X. Yang, M.-H. Baik, *J. Am. Chem. Soc.* **2006**, *128*, 7476-7485.
[193] F. Liu, J. J. Concepcion, J. W. Jurss, T. Cardolaccia, J. L. Templeton, T. J. Meyer, *Inorg. Chem.* **2008**, *47*, 1727-1752.
[194] D. Moonshiram, I. Alperovich, J. J. Concepcion, T. J. Meyer, Y. Pushkar, *Proc. Natl. Acad. Sci. USA* **2013**, *110*, 3765-3770.
[195] S. Roeser, M. Z. Ertem, C. Cady, R. Lomoth, J. Benet-Buchholz, L. Hammarström, B. Sarkar, W. Kaim, C. J. Cramer, A. Llobet, *Inorg. Chem.* **2012**, *51*, 320-327.
[196] C. Sens, I. Romero, M. Rodríguez, A. Llobet, T. Parella, J. Benet-Buchholz, *J. Am. Chem. Soc.* **2004**, *126*, 7798-7799.
[197] S. Romain, F. Bozoglian, X. Sala, A. Llobet, *J. Am. Chem. Soc.* **2009**, *131*, 2768-2769.
[198] F. Bozoglian, S. Romain, M. Z. Ertem, T. K. Todorova, C. Sens, J. Mola, M. Rodríguez, I. Romero, J. Benet-Buchholz, X. Fontrodona, C. J. Cramer, L. Gagliardi, A. Llobet, *J. Am. Chem. Soc.* **2009**, *131*, 15176-15187.
[199] H.-W. Tseng, R. Zong, J. T. Muckerman, R. Thummel, *Inorg. Chem.* **2008**, *47*, 11763-11773.
[200] J. J. Concepcion, J. W. Jurss, J. L. Templeton, T. J. Meyer, *J. Am. Chem. Soc.* **2008**, *130*, 16462-16463.
[201] R. Zong, R. P. Thummel, *J. Am. Chem. Soc.* **2005**, *127*, 12802-12803.
[202] D. J. Wasylenko, C. Ganesamoorthy, M. A. Henderson, B. D. Koivisto, H. D. Osthoff, C. P. Berlinguette, *J. Am. Chem. Soc.* **2010**, *132*, 16094-16106.
[203] L. Tong, L. Duan, Y. Xu, T. Privalov, L. Sun, *Angew. Chem. Int. Ed.* **2011**, *50*, 445-449.
[204] L. Duan, C. M. Araujo, M. S. G. Ahlquist, L. Sun, *Proc. Natl. Acad. Sci. USA* **2012**, *109*, 15584-15588.
[205] L. Wang, L. Duan, Y. Wang, M. S. G. Ahlquist, L. Sun, *Chem. Commun.* **2014**, *50*, 12947-12950.
[206] L. Francàs, R. Matheu, E. Pastor, A. Reynal, S. Berardi, X. Sala, A. Llobet, J. R. Durrant, *ACS Catal.* **2017**, *7*, 5142-5150.
[207] R. Matheu, M. Z. Ertem, J. Benet-Buchholz, E. Coronado, V. S. Batista, X. Sala, A. Llobet, *J. Am. Chem. Soc.* **2015**, *137*, 10786-10795.
[208] N. Vereshchuk, R. Matheu, J. Benet-Buchholz, M. Pipelier, J. Lebreton, D. Dubreuil, A. Tessier, C. Gimbert-Suriñach, M. Z. Ertem, A. Llobet, *J. Am. Chem. Soc.* **2020**, *142*, 5068-5077.

[209] M. A. Hoque, J. Benet-Buchholz, A. Llobet, C. Gimbert-Suriñach, *ChemSusChem* **2019**, *12*, 1949-1957.
[210] M. Yoshida, M. Kondo, S. Torii, K. Sakai, S. Masaoka, *Angew. Chem. Int. Ed.* **2015**, *54*, 7981-7984.
[211] D. W. Shaffer, Y. Xie, D. J. Szalda, J. J. Concepcion, *J. Am. Chem. Soc.* **2017**, *139*, 15347-15355.
[212] Y. Xie, D. W. Shaffer, J. J. Concepcion, *Inorg. Chem.* **2018**.
[213] Y. Jiang, F. Li, B. Zhang, X. Li, X. Wang, F. Huang, L. Sun, *Angew. Chem. Int. Ed.* **2013**, *52*, 3398-3401.
[214] L. L. Zhang, Y. Gao, Z. Liu, X. Ding, Z. Yu, L. C. Sun, *Dalton Trans.* **2016**, *45*, 3814-3819.
[215] V. Kunz, M. Schulze, D. Schmidt, F. Würthner, *ACS Energy Lett.* **2017**, *2*, 288-293.
[216] A.-L. Meza-Chincha, J. O. Lindner, D. Schindler, D. Schmidt, A.-M. Krause, M. I. S. Röhr, R. Mitrić, F. Würthner, *Chem. Sci.* **2020**, *11*, 7654-7664.
[217] J. Hessels, R. J. Detz, M. T. M. Koper, J. N. H. Reek, *Chem. Eur. J.* **2017**, *23*, 16413-16418.
[218] R. M. Bullock, A. K. Das, A. M. Appel, *Chem. Eur. J.* **2017**, *23*, 7626-7641.
[219] L. Wang, K. Fan, H. Chen, Q. Daniel, B. Philippe, H. Rensmo, L. Sun, *Catal. Today* **2017**, *290*, 73-77.
[220] J. Odrobina, J. Scholz, A. Pannwitz, L. Francàs, S. Dechert, A. Llobet, C. Jooss, F. Meyer, *ACS Catal.* **2017**, *7*, 2116-2125.
[221] S. P. Pujari, L. Scheres, A. T. M. Marcelis, H. Zuilhof, *Angew. Chem. Int. Ed.* **2014**, *53*, 6322-6356.
[222] K. L. Materna, R. H. Crabtree, G. W. Brudvig, *Chem. Soc. Rev.* **2017**, *46*, 6099-6110.
[223] L. Wu, M. Eberhart, A. Nayak, M. K. Brennaman, B. Shan, T. J. Meyer, *J. Am. Chem. Soc.* **2018**, *140*, 15062-15069.
[224] Z. Chen, J. J. Concepcion, J. W. Jurss, T. J. Meyer, *J. Am. Chem. Soc.* **2009**, *131*, 15580-15581.
[225] M. Yamamoto, Y. Nishizawa, P. Chabera, F. Li, T. Pascher, V. Sundstrom, L. Sun, H. Imahori, *Chem. Commun.* **2016**, *52*, 13702-13705.
[226] Y. Zhu, D. Wang, Q. Huang, J. Du, L. Sun, F. Li, T. J. Meyer, *Nat. Commun.* **2020**, *11*, 4610.
[227] D. Wang, S. L. Marquard, L. Troian-Gautier, M. V. Sheridan, B. D. Sherman, Y. Wang, M. S. Eberhart, B. H. Farnum, C. J. Dares, T. J. Meyer, *J. Am. Chem. Soc.* **2018**, *140*, 719-726.
[228] R. Matheu, L. Francàs, P. Chernev, M. Z. Ertem, V. Batista, M. Haumann, X. Sala, A. Llobet, *ACS Catal.* **2015**, *5*, 3422-3429.
[229] H. E. Zittel, F. J. Miller, *Anal. Chem.* **1965**, *37*.
[230] F. Li, L. Li, L. Tong, Q. Daniel, M. Gothelid, L. Sun, *Chem. Commun.* **2014**, *50*, 13948-13951.
[231] L. Wang, D. E. Polyansky, J. J. Concepcion, *J. Am. Chem. Soc.* **2019**, *141*, 8020-8024.
[232] D. Wang, L. Wang, M. D. Brady, C. J. Dares, G. J. Meyer, T. J. Meyer, J. J. Concepcion, *J. Phys. Chem. C* **2019**, *123*, 30039-30045.
[233] F. Li, B. Zhang, X. Li, Y. Jiang, L. Chen, Y. Li, L. Sun, *Angew. Chem. Int. Ed.* **2011**, 12276-12279.
[234] M. A. Hoque, M. Gil-Sepulcre, A. d. Aguirre, J. A. A. W. Elemans, D. Moonshiram, Y. S. R. Matheu, J. Benet-Buchholz, X. Sala, M. Malfois, E.

Solano, J. Lim, A. Garzón-Manjón, C. Scheu, M. Lanza, F. Maseras, C. Gimbert-Suriñach, A. Llobet, *Nat. Chem.* **2020**, *12*, 1060-1066.
[235] R. Chakrabarty, P. S. Mukherjee, P. J. Stang, *Chem. Rev.* **2011**, *111*, 6810-6918.
[236] J.-M. Lehn, *Chem. Eur. J.* **1999**, *5*, 2455-2463.
[237] M. Mastalerz, *Angew. Chem. Int. Ed.* **2010**, *49*, 5042-5053.
[238] S.-K. Lin, *J. Chem. Inf. Comput. Sci.* **1996**, *36*, 367-376.
[239] S. J. Rowan, S. J. Cantrill, G. R. L. Cousins, J. K. M. Sanders, J. F. Stoddart, *Angew. Chem. Int. Ed.* **2002**, *41*, 898-952.
[240] V. Kunz, PhD thesis, Universität Würzburg **2017**.
[241] E. Riedel, *Anorganische Chemie*, Walter de Gruyter, Berlin, **2004**.
[242] I. Bratsos, E. Alessio, *Eur. J. Inorg. Chem.* **2018**, *2018*, 2996-3013.
[243] G. L. Miessler, P. J. Fischer, D. A. Tarr, *Inorganic Chemistry*, Pearson, **2013**.
[244] Y. N. Kukushkin, *Chem. Zvesti* **1971**, *25*, 380-384.
[245] H. V. Huynh, *The Organometallic Chemistry of N-Heterocyclic Carbenes*, WILEY, **2016**.
[246] D. Astruc, *Organometallic Chemistry and Catalysis*, Springer, **2007**.
[247] S. Pal, *Pyridine: A Useful Ligand in Transition Metal Complexes*, IntechOpen, DOI: 10.5772/intechopen.76986, **2018**.
[248] F. Basolo, R. G. Pearson, *Mechanisms of Inorganic Reactions: A Study of Metal Complexes in Solution*, J. Wiley and Sons, **1967**.
[249] A. Masaaki, S. Yoichi, N. Akira, I. Tasuku, *Bull. Chem. Soc. Jpn.* **1992**, *65*, 1411-1414.
[250] M. Abe, A. Mitani, A. Ohsawa, M. Herai, M. Tanaka, Y. Sasaki, *Inorg. Chim. Acta* **2002**, *331*, 158-167.
[251] K. J. Laidler, *J. Chem. Educ.* **1984**, *61*, 494.
[252] S. R. Logan, *J. Chem. Educ.* **1982**, *59*, 279.
[253] E. A. K. J. E. Huheey, Richard L. Keiter, *Inorganic Chemistry: Principles of Structure and Reactivity*, HarperCollins College Publishers, **1993**.
[254] L. Helm, A. E. Merbach, *Chem. Rev.* **2005**, *105*, 1923-1960.
[255] R. G. Wilkins, *Acc. Chem. Res.* **1970**, *3*, 408-416.
[256] M. A. Khalifa, A. A. El-Awady, *Indian J. Chem.* **1989**, *28A*, 774-778.
[257] P. V. Grundler, G. Laurenczy, A. E. Merbach, *Helv. Chim. Acta* **2001**, *84*, 2854-2867.
[258] N. Aebischer, G. Laurenczy, A. Ludi, A. E. Merbach, *Inorg. Chem.* **1993**, *32*, 2810-2814.
[259] D. De Vito, H. Sidorenkova, F. P. Rotzinger, J. Weber, A. E. Merbach, *Inorg. Chem.* **2000**, *39*, 5547-5552.
[260] R. A. Leising, J. S. Ohman, K. J. Takeuchi, *Inorg. Chem.* **1988**, *27*, 3804-3809.
[261] T. Zheng, L. Li, *New J. Chem.* **2018**.
[262] L. Wang, K. Fan, Q. Daniel, L. Duan, F. Li, B. Philippe, H. Rensmo, H. Chen, J. Sun, L. Sun, *Chem. Commun.* **2015**, *51*, 7883-7886.
[263] W. Sun, Y. Wang, L. Ma, L. Zheng, W. Fang, X. Chen, H. Jiang, *J. Org. Chem.* **2018**, *83*, 14667-14675.
[264] P. Groves, *Polym. Chem.* **2017**, *8*, 6700-6708.
[265] Y. Jiang, F. Li, F. Huang, B. Zhang, L. Sun, *Chinese J. Catal.* **2013**, *34*, 1489-1495.
[266] J. J. Concepcion, M.-K. Tsai, J. T. Muckerman, T. J. Meyer, *J. Am. Chem. Soc.* **2010**, *132*, 1545-1557.

[267] Q. Daniel, P. Huang, T. Fan, Y. Wang, L. Duan, L. Wang, F. Li, Z. Rinkevicius, F. Mamedov, M. S. G. Ahlquist, S. Styring, L. Sun, *Coord. Chem. Rev.* **2017**, *346*, 206-215.
[268] M. Ogawa, B. Balan, G. Ajayakumar, S. Masaoka, H.-B. Kraatz, M. Muramatsu, S. Ito, Y. Nagasawa, H. Miyasaka, K. Sakai, *Dalton Trans.* **2010**, *39*, 4421-4434.
[269] L. Duan, F. Bozoglian, S. Mandal, B. Stewart, T. Privalov, A. Llobet, L. Sun, *Nat. Chem.* **2012**, *4*, 418-423.
[270] D. W. Thompson, A. Ito, T. J. Meyer, *Pure Appl. Chem.* **2013**, *85*, 1257.
[271] S. D. Tilley, *Adv. Energy Mater.* **2019**, *9*, 1802877.
[272] N. Noll, F. Würthner, *Chem. Eur. J.* **2021**, *27*, 444-450.
[273] S. Berardi, L. Francàs, S. Neudeck, S. Maji, J. Benet-Buchholz, F. Meyer, A. Llobet, *ChemSusChem* **2015**, *8*, 3688-3696.
[274] J. J. Concepcion, J. W. Jurss, P. G. Hoertz, T. J. Meyer, *Angew. Chem. Int. Ed.* **2009**, *48*, 9473-9476.
[275] D. L. Ashford, A. M. Lapides, A. K. Vannucci, K. Hanson, D. A. Torelli, D. P. Harrison, J. L. Templeton, T. J. Meyer, *J. Am. Chem. Soc.* **2014**, *136*, 6578-6581.
[276] K. E. deKrafft, C. Wang, Z. Xie, X. Su, B. J. Hinds, W. Lin, *ACS Appl. Mater. Interfaces* **2012**, *4*, 608-613.
[277] J. Odrobina, J. Scholz, M. Risch, S. Dechert, C. Jooss, F. Meyer, *ACS Catal.* **2017**, *7*, 6235-6244.
[278] J. Creus, R. Matheu, I. Peñafiel, D. Moonshiram, P. Blondeau, J. Benet-Buchholz, J. García-Antón, X. Sala, C. Godard, A. Llobet, *Angew. Chem. Int. Ed.* **2016**, *55*, 15382-15386.
[279] J. M. Koelewijn, M. Lutz, R. J. Detz, J. N. H. Reek, *ChemPlusChem* **2016**, *81*, 1098-1106.
[280] N. Karousis, N. Tagmatarchis, D. Tasis, *Chem. Rev.* **2010**, *110*, 5366-5397.
[281] V. Strauss, A. Roth, M. Sekita, Dirk M. Guldi, *Chem* **2016**, *1*, 531-556.
[282] V. Sgobba, D. M. Guldi, *Chem. Soc. Rev.* **2009**, *38*, 165-184.
[283] T. Umeyama, H. Imahori, *Energy Environ. Sci.* **2008**, *1*, 120-133.
[284] X. Li, H. Lei, J. Liu, X. Zhao, S. Ding, Z. Zhang, X. Tao, W. Zhang, W. Wang, X. Zheng, R. Cao, *Angew. Chem. Int. Ed.* **2018**, *57*, 15070-15075.
[285] J. Meng, H. Lei, X. Li, J. Qi, W. Zhang, R. Cao, *ACS Catal.* **2019**, *9*, 4551-4560.
[286] P. Garrido-Barros, R. Matheu, C. Gimbert-Suriñach, A. Llobet, *Curr. Opin. Electrochem.* **2019**, *15*, 140-147.
[287] D. W. Shaffer, Y. Xie, J. J. Concepcion, *Chem. Soc. Rev.* **2017**, *46*, 6170-6193.
[288] D. J., F. R., in *Fermi Golden Rule and Open Quantum Systems*, Springer, Berlin, Heidelberg, **2006**.
[289] C.-J. Chang, Y.-C. Chu, H.-Y. Yan, Y.-F. Liao, H. M. Chen, *Dalton Trans.* **2019**, *48*, 7122-7129.
[290] J. E. Jones, L. D. Hansen, S. E. Jones, D. S. Shelton, J. M. Thorne, *J. Phys. Chem.* **1995**, *99*, 6973-6979.
[291] C. Costentin, S. Drouet, M. Robert, J.-M. Savéant, *J. Am. Chem. Soc.* **2012**, *134*, 11235-11242.
[292] C. Costentin, S. Drouet, M. Robert, J.-M. Savéant, *Science* **2012**, *338*, 90-94.
[293] V. Artero, J.-M. Savéant, *Energy Environ. Sci.* **2014**, *7*, 3808-3814.
[294] C. Costentin, J.-M. Savéant, *ChemElectroChem* **2014**, *1*, 1226-1236.
[295] C. Costentin, H. Dridi, J.-M. Savéant, *J. Am. Chem. Soc.* **2014**, *136*, 13727-13734.
[296] C. Costentin, G. Passard, J.-M. Savéant, *J. Am. Chem. Soc.* **2015**, *137*, 5461-5467.

[297] X. Sala, M. Z. Ertem, L. Vigara, T. K. Todorova, W. Chen, R. C. Rocha, F. Aquilante, C. J. Cramer, L. Gagliardi, A. Llobet, *Angew. Chem. Int. Ed.* **2010**, *49*, 7745-7747.
[298] M. Gil-Sepulcre, J. O. Lindner, D. Schindler, L. Velasco, D. Moonshiram, V. Stepanenko, F. Würthner, A. Llobet, *unpublished results*.
[299] C. L. Donnici, D. H. Máximo Filho, L. L. C. Moreira, G. T. d. Reis, E. S. Cordeiro, I. M. F. d. Oliveira, S. Carvalho, E. B. Paniago, *J. Braz. Chem. Soc.* **1998**, *9*, 455-460.
[300] T. M. Cassol, F. W. J. Demnitz, M. Navarro, E. A. d. Neves, *Tetrahedron Lett.* **2000**, *41*, 8203-8206.
[301] I. P. Evans, A. Spencer, G. Wilkinson, *J. Chem. Soc., Dalton Trans.* **1973**, 204-209.
[302] E. Dulière, M. Devillers, J. Marchand-Brynaert, *Organometallics* **2003**, *22*, 804-811.
[303] B. Ravel, M. Newville, *J. Synchrotron Radiat.* **2005**, 537-541.
[304] J. J. Rehr, R. C. Albers, *Rev. Mod. Phys.* **2000**, 621-654.
[305] D. C. Koningsberger, R. Prins, *X Ray Absorption: Principles, Applications, Techniques of EXAFS, SEXAFS and XANES*, John Wiley & Sons, **1988**.
[306] J. P. Perdew, K. Burke, M. Ernzerhof, *Phys. Rev. Lett.* **1997**, *78*, 3865-3868.
[307] F. Weigend, R. Ahlrichs, *Phys. Chem. Chem. Phys.* **2005**, *7*, 3297-3305.
[308] TURBOMOLE V6.5 2013, a development of University of Karlsruhe and Forschungszentrum Karlsruhe GmbH, 1989-2007, TURBOMOLE GmbH, since 2007; available from http://www.turbomole.com.
[309] J. J. P. Stewart, *J. Mol. Model.* **2007**, *13*, 1173-1213.
[310] J. Řezáč, P. Hobza, *J. Chem. Theor. Comput.* **2012**, *8*, 141-151.
[311] MOPAC2016, James J. P. Stewart, Stewart Computational Chemistry, Colorado Springs, CO, USA, HTTP://OpenMOPAC.net (2016).
[312] D. Andrae, U. Häußermann, M. Dolg, H. Stoll, H. Preuß, *Theoret. Chim. Acta* **1990**, *77*, 123-141.
[313] S. Grimme, J. Antony, S. Ehrlich, H. Krieg, *J. Chem. Phys.* **2010**, *132*, 154104.
[314] A. Klamt, G. Schüürmann, *J. Chem. Soc., Perkin Trans. 2* **1993**, 799-805.
[315] J. Contreras-García, E. R. Johnson, S. Keinan, R. Chaudret, J.-P. Piquemal, D. N. Beratan, W. Yang, *J. Chem. Theor. Comput.* **2011**, *7*, 625-632.
[316] Z. Liu, B. X. Dong, M. Misra, Y. Sun, J. Strzalka, S. N. Patel, F. A. Escobedo, P. F. Nealey, C. K. Ober, *Adv. Funct. Mater.* **2019**, *29*, 1805220.
[317] S. Chen, S. Zhang, C. Bao, C. Wang, Q. Lin, L. Zhu, *Chem. Commun.* **2016**, *52*, 13132-13135.
[318] L. Wang, L. Duan, B. Stewart, M. Pu, J. Liu, T. Privalov, L. Sun, *J. Am. Chem. Soc.* **2012**, *134*, 18868-18880.
[319] L. Wang, D. W. Shaffer, G. F. Manbeck, D. E. Polyansky, J. J. Concepcion, *ACS Catal.* **2020**, *10*, 580-585.
[320] Y. Xu, A. Fischer, L. Duan, L. Tong, E. Gabrielsson, B. Åkermark, L. Sun, *Angew. Chem. Int. Ed.* **2010**, *49*, 8934-8937.
[321] S. Neudeck, S. Maji, I. López, S. Meyer, F. Meyer, A. Llobet, *J. Am. Chem. Soc.* **2014**, *136*, 24-27.
[322] F. Li, C. Xu, X. Wang, Y. Wang, J. Du, L. Sun, *Chinese J. Catal.* **2018**, *39*, 446-452.
[323] L. Tong, M. Göthelid, L. Sun, *Chem. Commun.* **2012**, *48*, 10025-10027.
[324] L. Wu, A. Nayak, J. Shao, T. J. Meyer, *Proc. Natl. Acad. Sci. USA* **2019**, *116*, 11153-11158.